

**THÈSE DE DOCTORAT DE
L'UNIVERSITÉ PIERRE ET MARIE CURIE**

Spécialité :
Astronomie et Astrophysique

Présenté par
Sunghye BAEK

pour obtenir la grade de :
DOCTEUR DE L'UNIVERSITÉ PIERRE ET MARIE CURIE

sujet de thèse :
**SIMULATION DE L'ÉPOQUE DE LA RÉIONISATION :
TRANSFERT RADIATIF**

Soutenue le 24 Juin 2009

devant le jury composé de :

Patrick Boissé	Président de Jury
Françoise Combes	Directrice de thèse
Benoît Semelin	Directeur de thèse
Andrea Ferrara	Rapporteur
Romain Teyssier	Rapporteur
Juan Uson	Examineur
Saleem Zaroubi	Examineur

Remerciements

Mes premiers remerciements iront à Benoît Semelin et Françoise Combes pour ces trois années particulièrement enrichissantes. Je tiens à leur exprimer ici toute ma gratitude pour leurs encouragements et leur soutien.

Je remercie mes collaborateurs Paola Di Matteo et Yvez Revaz pour les nombreux et productifs échanges.

Très proches de moi également Alain Coulais, Mohammad Heydari-Malayeri, Jean-François Lestrade, Thibaut Le Bertre, Benjamin L’Huillier, Yannick Libert, Chiara Mastropietro, et Anne-Laure Melchior, pour leur présence chaleureuse. Ainsi que l’ensemble de l’équipe du LERMA pour toute la sympathie qu’elle m’a manifestée.

Je tiens à remercier Patrick Boissé, Juan Uson et Saleem Zaroubi pour m’avoir fait l’honneur de faire partie du jury de thèse, et tout particulièrement Andrea Ferrara et Romain Teyssier pour avoir accepté d’être les rapporteurs de mon manuscrit de thèse.

Je terminerai en exprimant l’amour, la gratitude et le respect que j’ai pour mon mari, Euihun.

Abstract

Keywords : radiative transfer, early Universe, large-scale structure of Universe, HII regions, galaxy formation

The 21-cm hyperfine line of neutral hydrogen from the high-redshift Universe ($6 < z < 20$) promises to probe a new era in cosmology, the epoch of reionization (EoR). It will provide more detailed, less ambiguous and more complete three-dimensional informations than other observations of the EoR (such as the QSO absorption lines, or the secondary scattering of CMB). It also traces many different physical processes. The next generation radio telescopes, SKA and its precursors, will start to operate within one decade, and will observe this signal. Numerical simulations predicting the 21-cm emission are important to optimize the design of the instruments, and interpret the observations.

In this work, we develop a continuum radiative transfer part for the LICORICE cosmological code to study the epoch of reionization, where radiative transfer is an essential tool. We use a Monte-Carlo ray-tracing algorithm on an adaptive grid. Several tests, both for static density field cases and radiative hydrodynamic cases have been performed to validate the code.

Then we compute the 21-cm signal during the EoR, which provides a direct probe on reionization and contains a lot of informations on the sources of ionization and heating. Usually the Ly- α flux, which influences the strength of the 21-cm signal, is assumed to be strong and homogeneous during the whole cosmic reionization, but this assumption is not valid during the early stage of EoR. We evaluate exactly the local Ly- α flux using the Lyman line radiative transfer module of LICORICE and show that using the local Ly- α flux modifies the power spectrum of the 21-cm signal, especially during the early reionization. We also find a strong signal in absorption which can not be predicted with the usual assumptions.

Even a small amount of X-rays can affect the physical state of the neutral intergalactic medium since X-rays have a very long mean free path. X-ray heating is an important factor to evaluate the strength of the 21-cm signal in the neutral regions,

so we implemented the corresponding ray-tracing in LICORICE. We find that X-rays need time to increase the gas temperature in the IGM above the CMB temperature, so with a reasonable level of X-rays we can still see the signal in strong absorption during the early phase of reionization.

In addition, we study the formation of galaxies in a cosmological context. The goal is to explore the physics of primordial galaxies considering radiative feedback on hydrodynamics. In a preliminary way, we find that including non-equilibrium ionization modifies the temperature of the diffuse gas, and its accretion history.

Résumé

Mots clés : transfert radiatif, Univers primordial, structure à grande échelle de l'Univers, régions HII, formation de galaxies

La raie hyperfine à 21-cm de l'hydrogène atomique émise dans l'univers à grand redshift ($6 < z < 20$) permettra de sonder une nouvelle ère de la cosmologie, l'époque de la réionisation (EoR). Elle fournira des informations plus détaillées, moins ambiguës et plus complètes en 3D que les autres observations possibles de l'EoR (comme les raies d'absorption des quasars, ou le CMB). Son intensité dépend de nombreux processus physiques. Les radiotélescopes de nouvelle génération, SKA et ses précurseurs, entreront en service dans les prochaines années pour observer ce signal. La simulation numérique du 21-cm est importante pour optimiser le design des instruments et interpréter les observations futures.

Dans ce travail, nous avons développé un module de transfert radiatif pour le continuum ionisant dans le code LICORICE dans le but de simuler l'époque de la réionisation, pour laquelle le transfert radiatif est un outil essentiel. Nous utilisons un algorithme de ray-tracing de type Monte Carlo sur une grille adaptative. Plusieurs tests sont réalisés pour valider le code dans deux cas, celui d'un champ de densité statique et dans le cas de l'hydrodynamique radiative.

Nous produisons ensuite le signal à 21-cm émis pendant l'EoR, qui nous fournit une sonde directe de la réionisation et contient de nombreuses informations sur les sources d'ionisation et de chauffage. Habituellement, on suppose que le flux Ly- α , qui influence la puissance du signal à 21-cm, est fort et homogène pendant toute la réionisation, mais cette hypothèse n'est pas valable durant la première phase de l'EoR. Nous évaluons exactement le flux Ly- α local en utilisant le module de transfert radiatif de la raie Lyman α et montrons que ce flux modifie le spectre de puissance du signal à 21-cm, particulièrement pendant la première phase de la réionisation. Nous trouvons également que le signal est en absorption forte ce qui ne peut pas être simulé avec les hypothèses habituelles.

Même une faible quantité de rayons X peut affecter l'état physique du gaz neutre dans le milieu inter galactique, puisque ceux-ci ont un libre parcours moyen très long.

Le chauffage par les rayons X est un facteur important pour évaluer la puissance du signal à 21-cm dans les régions neutres, aussi avons nous inclus le ray-tracing correspondant dans LICORICE. Nous constatons que les rayons X ont besoin de temps pour élever la température du gaz au-dessus de la température du CMB. Ainsi, avec un niveau de rayons X raisonnable, nous continuons à observer le signal en absorption pendant la première phase de la réionisation.

De plus, nous étudions la formation des galaxies dans un contexte cosmologique. Le but est d'explorer la physique des galaxies primordiales en considérant la rétroaction radiative sur l'hydrodynamique. Nos résultats préliminaires montrent que le calcul de l'ionisation hors équilibre modifie la température du gaz diffus, et son histoire d'accrétion.

Contents

1	Introduction	11
1.1	The epoch of reionization	11
1.1.1	A brief thermal history of the Universe	11
1.2	Observational constraints on reionization	13
1.2.1	Gunn-Peterson Troughs : Quasar absorption spectra	13
1.2.2	CMB polarization and temperature anisotropy	15
1.2.3	Other probes of reionization	18
1.3	21 cm line and reionization	18
1.3.1	The HI 21-cm probe	19
1.3.2	Brief review of numerical simulations of the EoR	19
1.4	Observing the 21 cm line	24
1.4.1	Tomography	24
1.4.2	Global signal	27
1.4.3	Power spectrum	28
1.4.4	Foreground Contamination	30
2	Numerical code - LICORICE	33
2.1	Tree SPH algorithm for dynamics	33
2.1.1	Tree algorithm for gravitation	33
2.1.2	The SPH algorithm for hydrodynamics	34
2.1.3	Additional physics	35
2.2	Monte Carlo on an adaptive grid - continuum	36
2.2.1	Adaptive grid	36
2.2.2	Ionizing radiation field	37
2.2.3	Absorption probability of photon packets	38
2.2.4	Updating physical quantities	41
2.2.5	Adaptive time integration	44
2.2.6	X-ray radiative transfer	44
2.3	Lyman line transfer	46
2.3.1	The optical depth	47

2.3.2	Hubble Expansion	48
2.3.3	Scattering off atoms	48
2.3.4	Propagation	48
2.3.5	Acceleration scheme	49
2.3.6	Further improvements for future	50
2.4	Radiative Transfer Comparison Test	51
2.4.1	Static density field cases	51
2.4.2	Radiative-hydrodynamics cases	61
2.5	Performance	99
3	The simulated 21 cm signal I	101
3.1	Physics of the 21 cm signal	101
3.1.1	Basic equations	101
3.1.2	The spin temperature	103
3.2	Lyman-alpha radiative transfer during the EoR	104
3.3	The simulated 21 cm signal during the EoR	117
4	The simulated 21 cm signal II	137
4.1	Source Model	137
4.1.1	Star Formation Rate	138
4.1.2	Luminosity and SED of the stellar sources	138
4.1.3	X-ray source model	139
4.2	Simulations	141
4.2.1	Initial condition	141
4.2.2	Global history of reionization	142
4.3	Helium reionization	146
4.4	QSO index	148
4.5	Luminosity of the QSO	150
4.6	The 21-cm signal	151
5	Galaxy formation with LICORICE	157
5.1	Initial conditions	157
5.2	Cooling rate and collisional equilibrium	159
5.3	Snapshot of the simulation	160
5.4	Discussion and prospects	160
6	Conclusion	163
A	Cross-sections and rate coefficients	167

Chapter 1

Introduction

1.1 The epoch of reionization

1.1.1 A brief thermal history of the Universe

According to the standard Λ CDM cosmology, the history of the universe started from the Big Bang, 13.7 billion years ago. The early universe is very hot and dense, but it gets cooler and more diffuse as expansion proceeds. The temperature is high enough to maintain hydrogen in the plasma state until the age of the universe is equal to 380,000 years. However, as the temperature of the universe cools to 1 eV, the electrons get captured by the protons making them neutral atoms. The photons which were previously coupled to electrons via Compton and Thomson scattering can now propagate freely through the universe since almost all free electrons have been captured by protons. The photons emitted at this moment (redshift about $z \sim 1000$) propagate ever after almost without absorption, they form the Cosmic Microwave Background (CMB) Radiation. The observed CMB anisotropies tells us that the structure formation in the universe originated from very small density fluctuations ($\Delta\rho/\rho \sim 10^{-5}$).

After the recombination, the universe enters the Dark Age which proceeds until the first bound objects are formed and emit the first light. During this era ($z \leq 50$), baryonic density perturbations grow more and more due to gravitational instability. Baryons fall in the deeper potential wells formed by the Cold Dark Matter (CDM). However most of the modes remain linear and measurements from this era would be very helpful to constrain the cosmology because the IGM is no longer affected by photon scattering. Unfortunately, there is no way to observe this era with present technology.

The baryon fluctuations on scales of the Jeans mass ($\sim 10^6 M_\odot$, Jeans (1928)) begin to collapse and form bound objects. These bound objects become the building

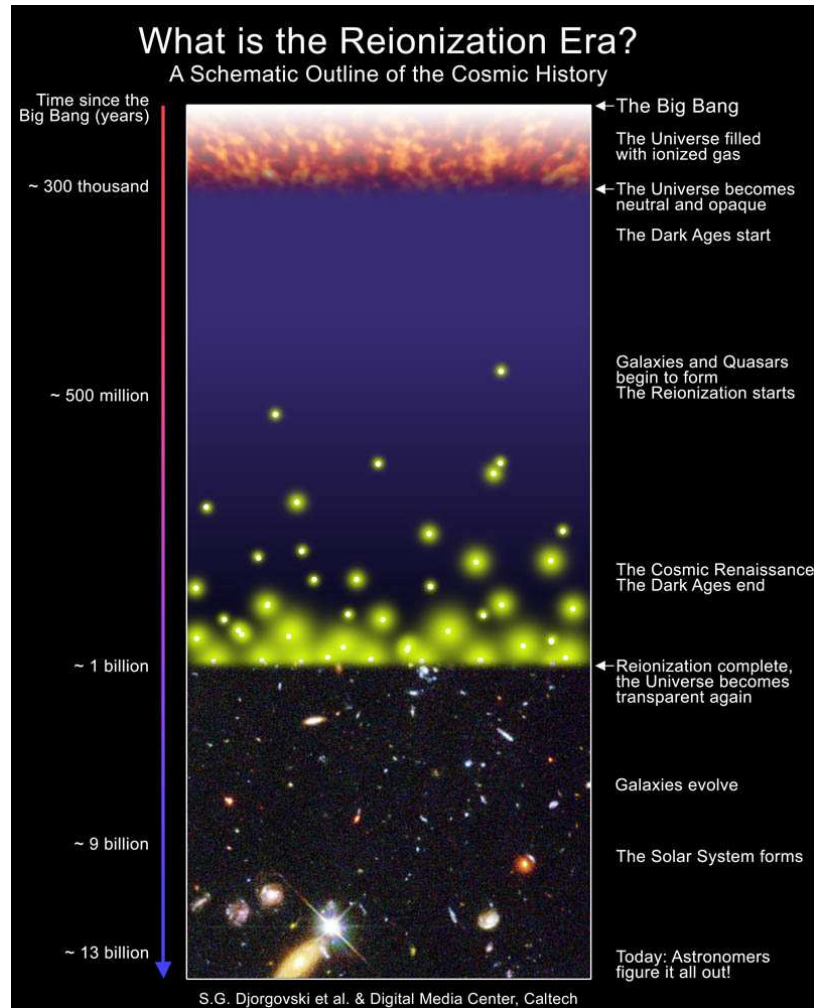


Figure 1.1: A schematic outline of the cosmic history from S.G. Djorgovski et al. & Digital Media Center, Caltech. INSU

blocks in the hierarchical cold dark matter cosmology at a redshift about $z \geq 30$. The exact time when this new cosmic era begins varies depending on the cosmological models and parameters as well as the baryonic process. The properties of the sources, such as initial mass function, star formation rate and metallicities during this epoch are uncertain. The successor to the Hubble space telescope, called the James Webb Space Telescope, planned for launch in 2013, and also the millimeter array ALMA in Chajnantor will observe the first galaxies and alleviate some of the uncertainties on the first sources' properties.

The ionizing radiation from the first sources ionizes hydrogen in a growing volume, soon encompassing the IGM within a single HII bubble. In the early stage of this process, each galaxy produces a distinct HII bubble. Neighbouring HII regions begin to overlap whenever two ionized bubbles connect, leading to the “overlap phase” of the

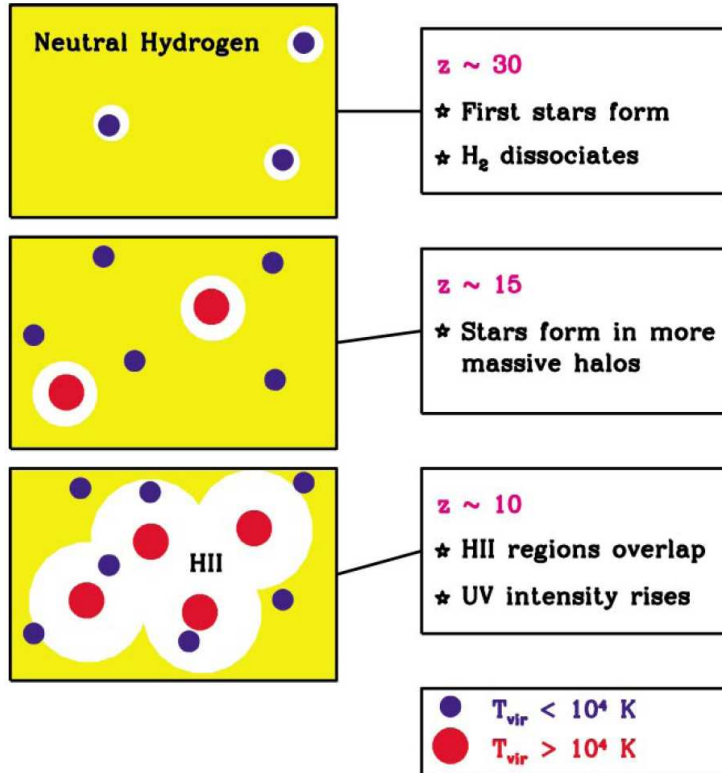


Figure 1.2: Stage in the reionization of hydrogen in the intergalactic medium (From Loeb & Barkana (2001))

EoR as shown in Fig. 1.2. By the end of this stage, most regions in the IGM are able to see several unshielded sources, and therefore the ionizing intensity is much higher than before. Although the beginning of the reionization epoch is uncertain, the end of this age is constrained by the quasar absorption spectra at $z \sim 6$. Later the IGM is ionized. Some neutral gas remains in high density regions which create Lyman limit systems or damped Lyman- α systems. This “post-overlap” stage continues indefinitely because collapsed objects retain neutral gas even in the current universe.

1.2 Observational constraints on reionization

1.2.1 Gunn-Peterson Troughs : Quasar absorption spectra

Gunn-Peterson Troughs

Gunn & Peterson (1965) showed that even a tiny neutral fraction can produce a high Ly- α scattering rate; indeed the optical depth of Ly- α scattering τ_α is about $\sim 10^6$ in

a fully neutral Universe at $z \sim 10$. The Gunn-Peterson optical depth for Ly α photons is

$$\tau_{GP} = \frac{\pi e^2}{m_e c} f_e \lambda_\alpha H^{-1}(z) n_{\text{HI}}, \quad (1.1)$$

where f_e is the oscillator strength of the Ly α transition, $\lambda_\alpha = 1216\text{\AA}$, $H(z)$ is the Hubble constant at redshift z , and n_{HI} is the density of neutral hydrogen in the IGM. At high redshifts,

$$\tau_{GP} = 4.9 \times 10^5 \left(\frac{\Omega_m h^2}{0.13} \right)^{-1/2} \left(\frac{\Omega_b h^2}{0.02} \right) \left(\frac{1+z}{7} \right)^{3/2} \left(\frac{n_{\text{HI}}}{n_{\text{H}}} \right) \quad (1.2)$$

for a uniform IGM (Fan et al 2006).

The spectra of high-redshift quasars provide a powerful probe of the neutral IGM in the universe. Since even a tiny neutral fraction $\sim 10^{-4}$ is sufficient to produce complete GP absorption, the GP troughs have been studied for a long time as a probe of the EoR. The ionizing photons which have wavelength longer than Ly α ($\lambda_\alpha = 1216\text{\AA}$) never resonate with neutral hydrogen atoms on their way to the observer. On the contrary, the ionizing photons in the range of $(1+z_i)\lambda \leq \lambda_{obs} \leq (1+z_s)\lambda_\alpha$ will be scattered out of the line of sight by the large Ly- α resonance cross section, where z_s is the redshift of the source and z_i is the redshift of the end of EoR.

SDSS quasar spectra at high redshift

At lower redshift ($z \lesssim 5$), the Ly α forest system of the quasar absorption spectra offers a powerful tool to investigate the ionization fraction of the IGM. The Sloan Digital Sky Survey (SDSS) with its large sky coverage provides a large sample of quasars over the $0 < z < 6.5$ range. Songaila (2004) noticed that the neutral fraction evolves rapidly at $z \geq 5$ and the transmitted flux approaches zero at $z \geq 5.5$. Among the 19 quasars observed at $z \geq 5.7$ (Fig. 1.3), SDSSJ1030+0524 ($z \sim 6.2$, Becker et al. (2001); Fan et al. (2001)) shows complete GP trough in both Ly α and Ly β flux. Fan et al. (2006) found an empirical fit of the optical depth $\tau \propto (1+z)^{4.3}$ at $z_{abs} < 5.5$ which increase rapidly $\tau \propto (1+z)^\alpha$; where $\alpha > 10$ at $z > 5.5$.

The rapidly decreasing transmitted flux blueward of Ly α around $z \sim 5.5$ and complete GP trough at $z \sim 6.28$ indicate the end of reionization. However, inferring the neutral fraction from these measurements is not straightforward. Only the rarest voids in the IGM allow light to pass through, thus only the tail of the IGM density distribution is directly sampled, and its properties must be extrapolated to the bulk of matter (Songaila & Cowie, 2002; Oh & Furlanetto, 2005).

Fan et al.(2002, 2006b), Lidz et al. (2002) and Cen & McDonald (2002) find that the volume-averaged neutral fraction increases to $10^{-3.5}$ at $z > 6$ (Fig. 1.4).

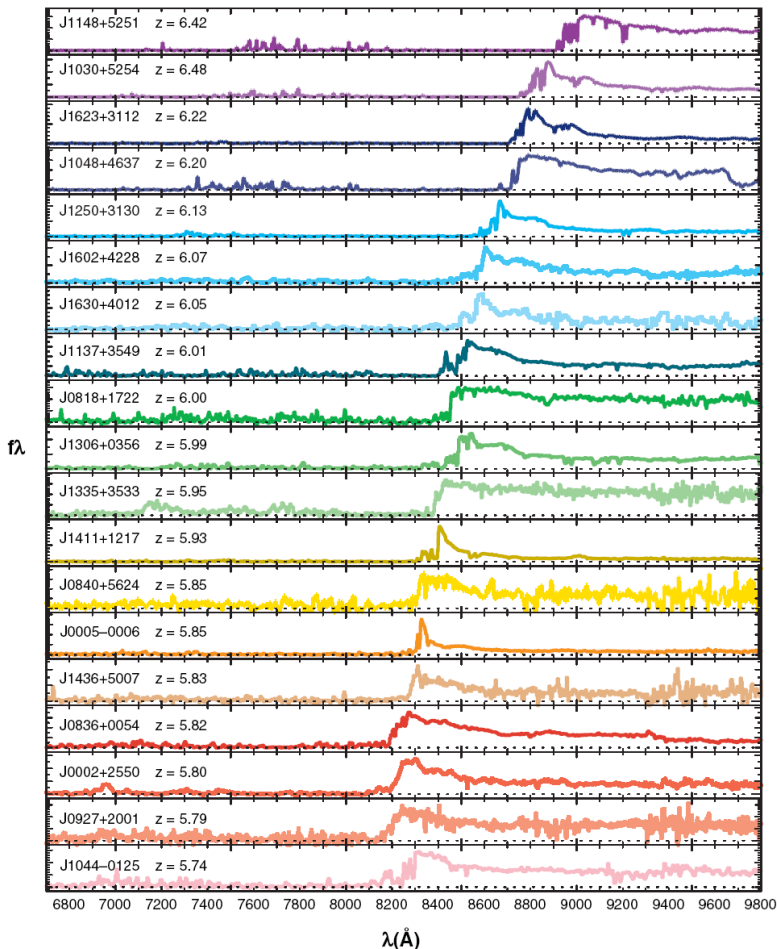


Figure 1.3: Moderate resolution spectra of SDSS quasars at $5.74 < z < 6.42$ (From Fan et al 2006b)

However, this is a lower limit because the Ly α absorption is very quickly saturated with only a small amount of neutral hydrogen. For the same neutral density, the optical depth of Ly β and Ly γ are 6.2 and 17.9 times smaller, thus Ly β can offer more stringent constraints when Ly α absorption is saturated.

1.2.2 CMB polarization and temperature anisotropy

The Cosmic Microwave background (CMB) radiation emitted at the epoch of recombination reveals the initial conditions for structure formation, in the form of small fluctuations in the density, velocity and gravitational potential. These observed anisotropic data provide important informations on the matter content of the universe and on cosmological parameters. The CMB anisotropy can also be used to constrain the details of the EoR. Indeed reionization affects the CMB, both on the temperature anisotropy and polarization by erasing some of the primary anisotropy

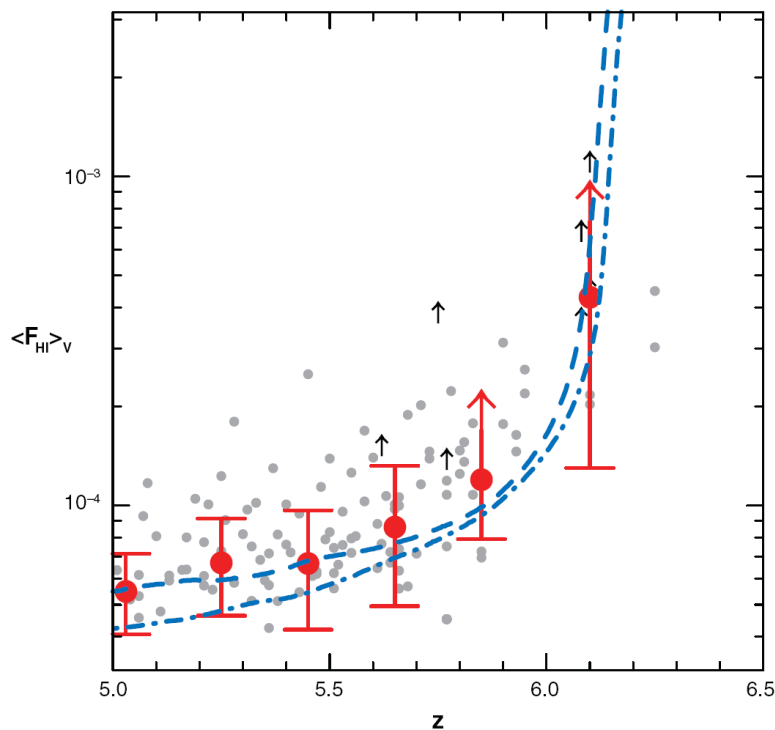


Figure 1.4: Evolution of the volume-averaged neutral hydrogen fraction of the IGM. The solid points with error bars are from 19 quasar observations. Lines are from the A4 and A8 simulations of Gnedin (2004) (From Fan et al. 2006b).

and by generating a secondary anisotropy.

CMB polarization

The Wilkinson Microwave Anisotropy Probe (WMAP) measurements produced a large scale temperature and polarization map of the CMB. The CMB is polarized by scattering off by free electrons, also called the Thomson scattering process that has a quadrupole anisotropy. At the time of recombination, the primary polarization is generated. The E-mode polarization anisotropy peaks at $\simeq 10'$ angular scale (multipole $l \sim 1000$). Since the polarization is a strictly causal process, it does not allow a polarization signal on a scale larger than the horizon at that time ($\sim 1^\circ$). After last scattering surface at recombination, there are no free electrons to scatter the CMB. Then reionization produces free electrons and the CMB radiation undergoes a secondary polarization. Since this process occurs well after recombination, the effects are at comparatively lower values of l , and are separable from the signature of recombination. Measurement of the large angular scale E-mode polarization for angular scale greater than $1^\circ \Leftrightarrow l < 200$ is the result of the secondary polarization

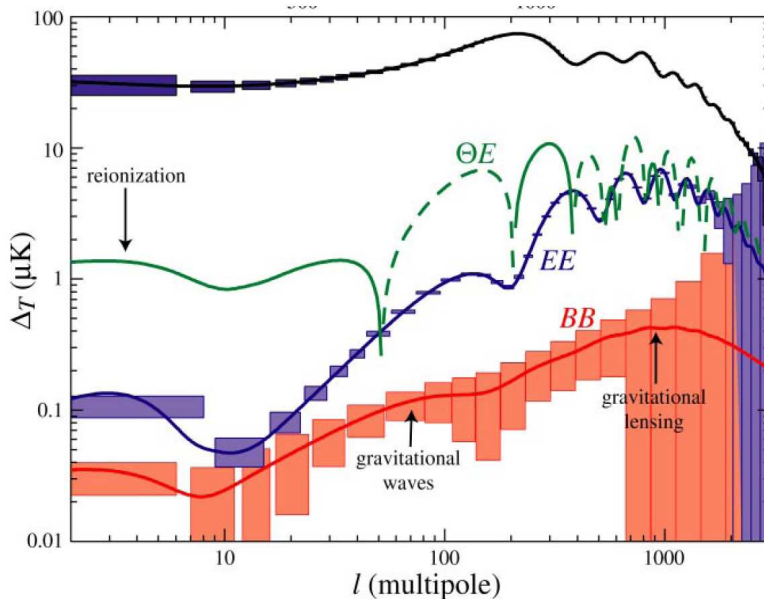


Figure 1.5: Temperature and polarization spectra for $\Omega_{tot} = 1$, $\Omega_{\Lambda} = 2/3$, $\Omega_b h^2 = 0.02$, $\Omega_m h^2 = 0.16$, $n=1$, $z_{reion} = 7$. Dashed lines represent negative cross correlation and boxes represent the statistical errors of the Planck satellite. From Hu & Dodelson (2002)

developed at reionization (see Fig. 1.5). This secondary polarization is helpful to break the degeneracy between certain parameter combinations.

If reionization was instantaneous, only the intrinsic CMB quadrupole from “last scattering surface” ($z \simeq 1000$) projected to the redshift of reionization would contribute to the CMB polarization at $> 10^\circ$ scales. This secondary polarization during the EoR has been detected by WMAP and is interpreted as the integrated Thomson optical depth $\tau \sim 0.069^{+0.026}_{-0.029}$, together with a series of other cosmological parameters (Page et al., 2007).

Temperature anisotropy

Since the large scale polarization of the CMB radiation is sensitive to the redshift of the last scattering surface, it cannot tell us details about the reionization. However, in small scale temperature anisotropies ($< 0.1^\circ$) other interesting astrophysical aspects of reionization are encoded. Several effects can produce secondary fluctuations on the CMB temperature anisotropy. They come from modulated Doppler Effects. However, if the electron density is homogeneous, the Doppler effect cancels out (Sunyaev, 1978; Kaiser, 1984). Both the cluster (the kSZ effect) and linear density fluctuations (the Ostriker-Vishniac effect, Ostriker & Vishniac (1986)) induced by the large scale structure modulate the optical depth and give rise to a Doppler effect. The patchiness of

ionization fraction also give a modulated Doppler effect and make the secondary CMB anisotropy.

The shape of power spectra for these effects depends on the reionization model (Knox, 2003; Santos et al., 2003) although the amplitude depends weakly on the reionization. On the other hand these effects strongly depend on the patchiness and duration of reionization (McQuinn et al., 2005).

1.2.3 Other probes of reionization

Gamma-Ray Bursts

Gamma-ray bursts (GRBs) are powerful explosions occurring during the death of massive stars. They are expected to appear at high redshift ($z > 10$) and their afterglow emission spectra can be used to probe the IGM. Recently, a GRB afterglow has been detected at $z \sim 6.2$ (SWIFT GRB 050904; Kawai et al. (2006)) and at $z \sim 8.2$ (GRB 090423 (2009)). As IGM probes, the absorption spectra of GRBs have an advantage over the GP damping wing test, they are not affected by the proximity effect¹. However, most GRB are embedded in star forming regions, thus GRB spectra contain damped-Ly α absorbers. Such internal absorption or gas infall in the host galaxy environment (Barkana & Loeb 2004) complicates the interpretation of GRB.

Luminosity function of Ly α galaxies

Because the galaxies at high redshift host significant star-forming regions, Ly α narrow-band imaging is a very useful survey technique. A large number of Ly α emitting galaxies have been found at high redshift, using LALA (Dawson et al., 2007), SDF (Shimasaku et al., 2006), Subaru (Taniguchi et al., 2005) etc. The luminosity function of these Ly α emitting galaxies can also constrain reionization. As the IGM becomes neutral at high redshift, the Ly α emission must be suppressed by a GP-like effect. However, obtaining a quantitative constraint on the neutral fraction is difficult because of uncertainties in the intrinsic Ly α line and galaxy population. In addition, Santos (2004) also noticed that the presence of galactic winds may modify significantly the observed Ly α flux.

1.3 21 cm line and reionization

The 21 cm line is the spectral line created by the hyperfine transition of fundamental state of hydrogen atom. The transition is strictly forbidden with a very small

¹Decrease in Ly- α forest absorption due to large ionizing flux near a quasar

probability of $2.9 \times 10^{-15} \text{s}^{-1}$. However, a large total number of hydrogen atom in the interstellar medium makes the line easily observable by radio telescope.

Since it is optically very thin to the intergalactic and interstellar medium, it propagates through dust clouds and it is useful to mapping the interstellar medium.

The 21 cm line was first detected in 1951 by Ewen and Purcell. In 1952, the Milky Way structure of neutral hydrogen is revealed by 21 cm line for the first time.

1.3.1 The HI 21-cm probe

As we discussed in the above section, each currently used technique has some drawbacks, and cannot fully probe the evolution of the neutral IGM. The 21-cm line from the hyperfine transition of the fundamental state of neutral hydrogen provides a direct probe on reionization. Furlanetto et al. (2004) emphasize two advantages of the HI 21-cm probe, *i*) it does not saturate like $\text{Ly}\alpha$, *ii*) it provides a full 3D information unlike CMB polarization studies. Although the 21-cm line has many advantages over the other probes which have been recognized long before (Field, 1959; Hogan & Rees, 1979), it has not been measured at $z > 6$ yet because of the observational challenges. Several meter-wavelength radio telescopes are now programmed to detect highly redshifted 21-cm line, $21(1+z)\text{cm}$, such as LOFAR (Low Frequency Array) and the Square Kilometer Array (SKA). LOFAR started operating in 2007, and SKA will start operating in several year (2014-2020) and will probe the reionization epoch at $z \leq 20(12)$. Numerical simulations of the cosmic reionization will be very helpful not only to design properly these next generation telescopes but also to analyse the data.

1.3.2 Brief review of numerical simulations of the EoR

Simulating the 21 cm line during the epoch of reionization is a very challenging computational task. Simulations of the EoR must simultaneously satisfy two conditions, a large simulation box size and a high resolution. High resolution is necessary to resolve high redshift halos down to $10^7 - 10^8 M_\odot$, where the photoionizing sources are thought to reside. It is also essential to correctly account for clumping and recombination rates. A large simulation volume of $\sim (100\text{Mpc}/h)^3$ is required to correctly sample highly biased sources (Barkana & Loeb, 2004) and the characteristic size of HII regions which are in the $\sim 10 - 50\text{Mpc}/h$ range (Furlanetto & Briggs, 2004).

In addition, three dimensional radiative transfer is imperative to model the EoR but radiative transfer on cosmological scales is computationally very expensive. Now the computational cost has come within reach of the currently available computational power, but still efficient algorithms and numerical techniques are necessary.

Since there exist few constraints on reionization, the properties of the sources, including the initial mass function (IMF), the star formation rate (SFR), and the escape fraction at this epoch remain quite uncertain. The clumpiness of the IGM and its effect on the evolution of structures are also unknown. Thus, they are usually treated as free parameters depending on the model in most simulations. Therefore, it is worth reviewing simulation works to compare the effectiveness of the methods and the results.

Ciardi et al. (2001, 2003a,b)

Ciardi et al. (2001) present high resolution numerical cosmological simulations and Monte Carlo radiative transfer method. The initial conditions are produced with the COSMICS code and the structures are evolved with GADGET (Springel et al., 2001), in a box of 4 comoving Mpc on a 256^3 grid. The details of their Monte Carlo radiative transfer scheme is described in Maselli et al. (2003). They show that an ionizing front(I-front) propagates first in the low density regions then in the high density regions, because of the short recombination time and shadowing effect of the dense region. They find also that the Larson initial mass function (IMF) produces 5 times more ionizing photons than the Salpeter IMF, so the IMF might play an important role for the history of reionization. The mass of a particle is about $1.5 \times 10^5 M_\odot$, which is small enough to correctly account for the clumping and the recombination. However the size of simulation box, $L_{box} = 4$ Mpc (comoving) is too small to fully sample the large-scale structure. In the next work (Ciardi et al., 2003a,b), they enlarge simulation boxes to $20h^{-1}$ Mpc, but it has been argued that a size of $\sim 100 h^{-1}$ Mpc is necessary to correctly sample the rare sources (Barkana & Loeb, 2004) and the characteristic size of the large HII regions is $\sim 10 - 50$ Mpc/h (Furlanetto & Briggs, 2004). Ciardi et al. (2003b) include structure evolution by using a semi-analytical model of galaxy formation to track the evolution of the sources of ionizing radiation. Ciardi et al. (2003a) study the effect of various IMF on reionization. They showed that the Thompson optical depth of their simulations can fit the first-year WMAP polarization data by taking a large escape fraction or a top-heavy IMF. However the third-year data ($\tau_{3rd} \sim 0.07$) is much smaller than the first-year data ($\tau_{1st} \sim 0.17$), so smaller escape fraction or a Salpeter IMF might be adequate to describe the source of reionization.

Furlanetto & Briggs (2004)

They discuss the observability of the 21 cm signal using high-resolution cosmological simulations. They use the Q5 cosmological simulation of Springel & Hernquist (2003), produced with the GADGET code. Stellar formation and the feedback effect are

included. The simulation contains 324^3 ($\sim 3 \times 10^7$) dark matter particles and 324^3 baryon particles in a box of 10 Mpc/h. Radiative transfer is post-processed using an adaptive ray-tracing scheme, which is fully described in Sokasian et al. (2001). Using the assumption that $T_s \sim T_k \gg T_{CMB}$, they find a mean excess brightness temperature $\delta T_b \sim 20 - 30$ mK with rms fluctuations $\langle T_b^2 \rangle^{1/2} \sim 5 - 10$ mK before the Epoch of Reionization. At overlap, both mean signal and fluctuations drop rapidly to zero. They concluded that the 21 cm observations will reveal whether the IGM reionization followed a single or double reionization scenario.

They consider the signal only in emission with the assumption, $T_s \sim T_k \gg T_{CMB}$. However, as they argued in a later paper (Furlanetto, 2006), the signal has the potential to be seen stronger in absorption than in emission. Especially during the early epoch of reionization, heating may not be sufficient to increase T_s above T_{CMB} .

Iliev et al. (2006b); Mellema et al. (2006b); Iliev et al. (2007); Doré et al. (2007); Iliev et al. (2008)

Two series of papers (Iliev et al., 2006a; Mellema et al., 2006b) present the first large-scale radiative transfer simulations in a volume of $(100\text{Mpc}/h)^3$. Their models and methods are described in the first paper, as well as initial results characterizing the global reionization process. N-body simulations have been run with the PMFAST code (Merz et al., 2005) using 4.28 billion dark matter particles. Then, they performed radiative transfer using the C^2 -RAY (Mellema et al., 2006a) code. The minimum resolved halo's mass is $2.5 \times 10^9 M_\odot$. They assume a constant mass-to-light ratio to compute the ionizing flux. The ionizing flux thus depends on the baryon fraction, star formation efficiency and escape fraction. They used two initial mass function models, Salpeter and top-heavy IMF, to compute the ionizing flux. They assume a fixed kinetic temperature of 10^4K everywhere. The overlap occurs by $z \sim 11$, giving a Thomson optical depth within $1 - \sigma$ of the first-year WMAP polarization data. They find that the ionization history of smaller-size (5-10 comoving Mpc) regions show a large scatter so that it does not describe well the global history. Such small-box simulations of reionization have little predictive power for the evolution of the mean ionized fraction. The minimum reliable volume for such predictions is $\sim (30 \text{ Mpc})^3$. They also find that the statistical distributions of the ionized fraction and ionized gas density are clearly non-Gaussian.

The second paper by Mellema et al. (2006) presents the 21-cm emission features and their statistics. Several scenarios for the reionization history, both early and extended reionization, are added. They find that the different scenarios produce quite similar observational signatures, showing gradual transition in the global signature of the mean signal and rms fluctuations. The power spectra analysis shows the

strongest signal around 50% reionization and displays a maximum at an angular scale of $l \sim 3000 - 5000$ (or $\theta \sim 3' - 5'$, ~ 12 comoving Mpc at $z \sim 13$).

For the speed and manageability of simulations, they used transmissive boundary conditions for radiative transfer, and assumed a fixed temperature of 10^4 K everywhere. The effect of a varying temperature would not change very much the morphology of ionization, but it can affect the brightness temperature of the IGM in the early EoR.

The following series of papers is also based on the numerical method presented in the above paragraphs. Improvements and new features are introduced. Iliev et al. (2007) discuss the self-regulating character of reionization due to Jeans-mass filtering of low-mass galaxies. Iliev et al.(2007b) study the small-scale temperature anisotropies of the CMB created by reionization through the kinetic Sunyaev-Zeldovich effect which is due to Compton scattering of the Cosmic Microwave Background photons by moving free electrons. Iliev et al. (2008) discuss the dependence of the redshifted 21-cm emission and kSZ on the basic cosmological parameters and various observational issues. Doré et al. (2007) derive the CMB polarization anisotropy due to reionization and Iliev et al.(2008) discuss the effect of the intergalactic environment on the observability of Ly- α emitters during reionization.

Trac & Cen (2007); Shin et al. (2008); Santos et al. (2008); Trac et al. (2008)

They present a new hybrid code for large volumes, high resolution simulations of the cosmic reionization. They use a particle-multi-mesh (PMM; Trac & Pen (2006)) N-body algorithm for dark matter, and assume the baryons are unbiased tracers of the dark matter with constant density ratio, Ω_b/Ω_m . Star formation is computed considering the cooling and dynamic time scales, and star formation efficiency depends on the generation (PopII, PopIII) and initial mass function (Salpeter, top-heavy). The radiative transfer uses an adaptive ray tracing algorithm and each ray contains three bins of frequencies. They performed simultaneously the radiative transfer and dynamical evolution, which is unique up to now among the other simulations of reionization in a large volume. They find that the global history of the universe depends on the source model, the PopIII stars with a top-heavy IMF producing an order of magnitude more ionizing photons at $z \gtrsim 10$.

Running very high resolution DM simulations and driving the baryonic density field with a constant bias is a common strategy, but it fails on the scale of clusters where hydrodynamics and heating/cooling processes play an important role.

Shin et al. (2007) present the general properties of ionized hydrogen bubbles and their growth in these simulations. Lee et al. (2008) study the topology of cosmological

reionization. They find an inside-out behaviour for the ionization process, and they distinguish four distinct topological phases, pre-reionization, preoverlap, overlap and postoverlap phases. Santos et al. (2008) compare the 21-cm signal between an analytic model and the simulation. The brightness temperature of the 21-cm signal is derived by post-processing the simulation with a semi-analytical prescription accounting for both inhomogeneous X-rays and Ly- α effects to compute the spin temperature. They find that the analytical model provides a reasonable description on the 21-cm power spectrum at $z < 10$, but non-negligible differences arise at $z > 10$ due to the inhomogeneous X-rays and Ly α heating. Trac et al. (2008) study the impact of inhomogeneous hydrogen reionization on the thermal evolution of the intergalactic medium.

Zahn et al. (2007); Furlanetto et al. (2004)

They present results from a large volume simulation of cosmic reionization. The dynamics of dark matter is computed with the N-body code, GADGET-2 (Springel, 2005), and halos are identified using the friend-of-friend algorithm. Then they post-process the simulation with radiative transfer using an adaptive ray-tracing scheme. They use 1024^3 ($\sim 10^9$) dark matter particles (constant ratio for baryons) in a cubic box of comoving size $L_{\text{box}} = 65.6\text{Mpc}/h$. Their numerical technique is essentially a Monte-Carlo implementation of the analytic model developed by Furlanetto et al. (2004). They compare the HII bubble growth in the simulation with analytic calculations based on the excursion set method. They find that the analytic calculation reproduces the size distribution and the power spectrum of the ionization field and the 21 cm very well. The ionization field from the radiative transfer simulation has more small scale structure than the analytic calculation, owing to Poisson noise.

The radiative transfer scheme used in this work has the advantage of being extremely fast, while maintaining accuracy. However, several assumptions of the technique could under-estimate the power of the ionization field and the 21 cm signal on small scales. They assumed optically thin conditions within the ionization front and computed ionization fractions using ionization equilibrium at a uniform temperature $T = 10^4$ K. The remarkable agreement of the results between analytic calculations and simulations could fail without these assumptions.

McQuinn et al. (2007a); Lidz et al. (2007)

McQuinn et al. (2007) study the morphology of HII regions during reionization from simulations. Radiative transfer is treated in a post-processing stage, it uses the adaptive ray-tracing scheme of Abel & Wandelt (2002). The dynamics of dark matter (1024^3 particles) is computed with an N-body algorithm using the GADGET-

2 code. They showed that the morphology of HII regions is dependent on the global ionization fraction, the properties of ionizing sources, and the abundance of minihaloes or of Lyman-limit systems. The effect of patchy reionization on the statistics of Ly α emitting galaxies is also discussed.

Lidz et al. (2007) discuss the contribution of 3rd and 4th order terms to the power spectrum of 21 cm brightness temperature fluctuations based on the results of simulation in Zahn et al. (2007) and McQuinn et al. (2007).

Thomas et al. (2009)

This paper presents an efficient method to generate large scale simulations of the EoR without 3D radiative transfer. Large dark matter only simulations are post-processed to produce the 21 cm line. They assume spherical symmetry around the sources, using results from 1D radiative transfer (BEARS code) and compare the result with the 3D CRASH code and find an agreement for the redshifts and the spatial scales of interest. However, the 1D approach using spherical symmetry has limitations to predict the morphology of ionized region at small scale, and the discrepancy with respect to the 3D radiative transfer grows towards low redshift. Both stellar and quasar type of sources are considered and the signal at low frequency is discussed for the observational strategies for LOFAR.

1.4 Observing the 21 cm line

Observations at low frequency with radio telescopes allow us to detect the highly redshifted 21-cm line. The observed frequency is $\nu = 1420/(1+z)$ MHz. The Low Frequency Array (LOFAR, 115-240 MHz) already started operating. It is possible that they will detect the global signal (Fig. 1.8) or find the redshift when the global IGM neutral fraction is 0.5 using the power spectrum. Then, the Square Kilometer Array (SKA, 70-10⁴ MHz), the next-generation multi-purpose radio-telescope, will deliver a tomography of the signal at 1 comoving Mpc resolution.

1.4.1 Tomography

One of the main advantages of the 21-cm probe over other observations of the EoR is that we can get a three-dimensional information about the neutral IGM. We can construct the 3D data cube as shown Fig. 1.6, since the line is optically thin, the signal emitted at different distances (redshifts) arrives on earth with different frequencies.

The expected mean fluctuation of the 21 cm signal derived from various simulations (e.g. Furlanetto 2006b, Mellema et al 2006, Baek et al. 2008) is about 10 – 100

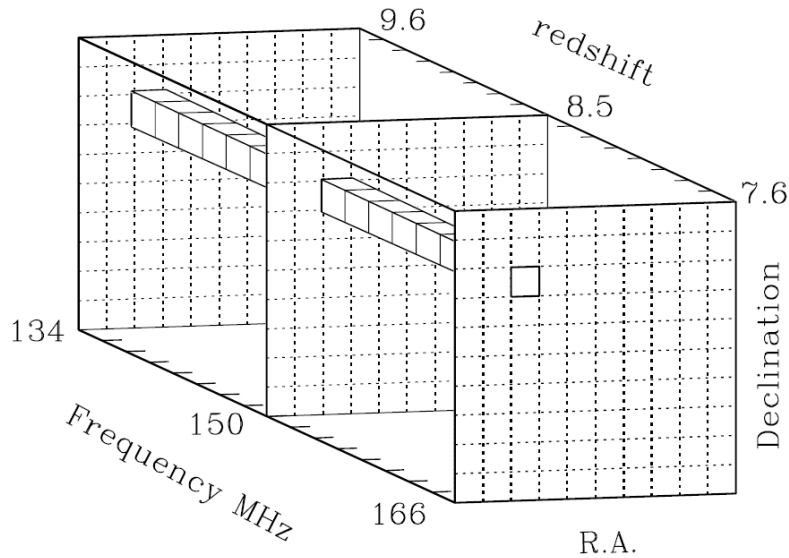


Figure 1.6: Spectral line data cube. The spectral information for one R.A.-Declination coordinate has been drawn for emphasis (Furlanetto & Briggs, 2004).

mK. We can estimate the noise fluctuations by the radiometer equation:

$$\Delta T^N = \kappa_c \frac{T_{sys}}{\sqrt{\Delta\nu t_{int}}} \approx \frac{T_{sys}}{\sqrt{\Delta\nu t_{int}}} \quad (1.3)$$

where $\kappa_c \geq 1$ is a loss factor for the details of the signal detection scheme, $\Delta\nu$ is the observed bandwidth, t_{int} is integration time and t_{sys} is the system temperature.

At the low radio frequencies, the galaxy is so bright that the system temperature is equivalent to the sky temperature, T_{sky} . The sky brightness temperature is dominated by the synchrotron radiation from fast electrons in the Milky Way. In this frequency range, a rule of thumb for the brightness temperature for typical high-latitudes (coldest regions in the sky) is $T_{sky} \sim 180 \left(\frac{\nu}{180\text{MHz}}\right)^{-2.6}$ K. The *rms* noise of antenna temperature, ΔT^N rises proportionally to the sky temperature, so the integration time must increase to achieve a low noise level. The foregrounds are four or five orders of magnitude larger than the expected signal, and their removal is the most challenging problem to observe the EoR 21-cm line.

The SKA has an effective collecting area of one square kilometer at 140 MHz, distributed over 4km, $T_{sys} = 300$ K, and an optimal channel width of 0.3 MHz. More detailed expressions of Eq.(1.3) contains the effective collecting area of the array and the *rms* sensitivity of SKA is then 5.2 mK with a beam FWHM $\sim 2'$ when integrating for one month. This will be acceptable to perform 3D imaging of the IGM during reionization.

The near term low frequency path-finders arrays (LOFAR etc) have less than

Array	N_{ant}	$A_{tot} [10^3 m^2]$	FoV (deg^2)	$D_{min}(m)$	$D_{max}(km)$
ASKAP	500	7.0	$\pi 16^2$	4	1.5
LOFAR	64	42	$4 \times \pi 2^2$	100	100
SKA	5000	600	$\pi 5.6^2$	10	3000

Table 1.1: Existing and planned low-frequency radio telescopes and their parameters

10% of the collecting area of the SKA, so direct 3D imaging may not be available. However, these near term experiments will be capable of probing the IGM in other ways, focusing primarily on large quasar HII regions.

The effective collecting area depends on the distribution of baselines in the array. SKA has a large collecting area to image all modes up to $k = 0.3 - 0.5 \text{ Mpc}^{-1}$ shown in Fig. 1.7 for some realistic configurations as specified in Tab. 1.1. It corresponds to a scale of ~ 3 comoving Mpc at $z = 8$ so it remains difficult to detect small HII regions. Both a longer observation and a larger bandwidth will increase the sensitivity and allow shorter modes to be observed. ASKAP has all its antenna in the core, it does not have any baselines that probe $k_{\perp} > 0.5 \text{ Mpc}^{-1}$ at $z = 8$. LOFAR has only a quarter of antennae in its core region, so a smaller fraction of its baseline can serve for the mode $k_{\perp} < 0.5 \text{ Mpc}^{-1}$. The minimum baseline of 100 m of LOFAR does not allow to detect modes with $k_{\perp} < 0.03 \text{ Mpc}^{-1}$.

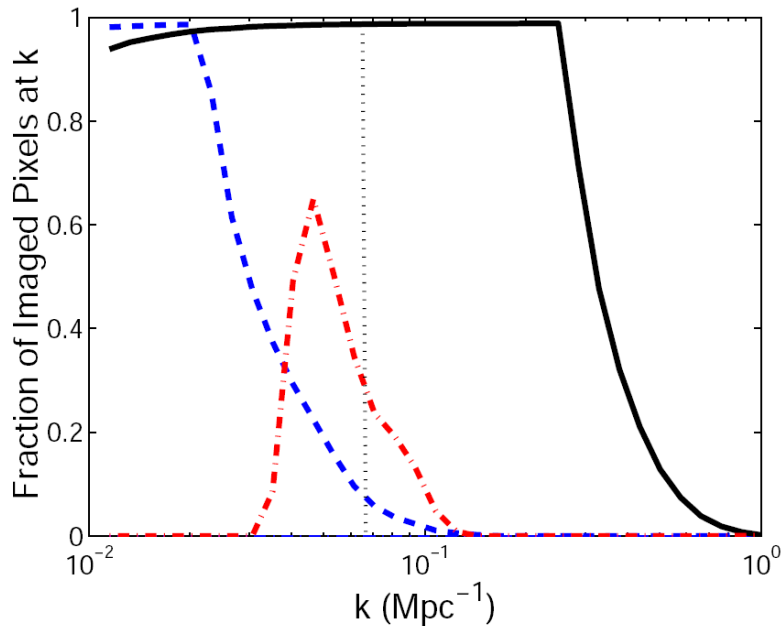


Figure 1.7: Fraction of Fourier pixels for ASKAP (dashed curve), LOFAR (dot-dashed curve), and SKA (solid curve) for which the rms signal exceeds the rms noise in a 1000 hour observation at $z = 8$. The vertical dotted line marks the scale corresponding to 6 MHz. (*from* McQuinn et al. 2006)

1.4.2 Global signal

The evolution of the sky-averaged 21-cm signal can constrain the properties of the first generations of stars and quasars (Furlanetto et al., 2006). If Population II stars dominate, the effective Ly- α coupling renders the 21-cm signal visible in strong absorption before it is heated by X-rays. If Population III stars dominate, the harder photons of massive stars compress this stage into a shorter time interval and decrease the signal amplitude.

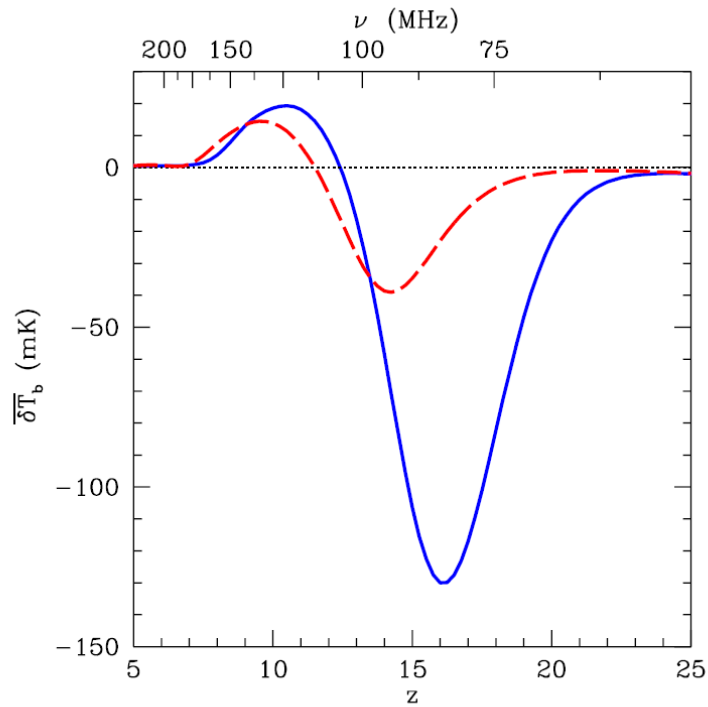


Figure 1.8: Fiducial histories of the sky-averaged 21 cm brightness temperature, The solid blue curve uses a typical Population II star formation history, while the dashed red curve uses only very massive Population III stars. Both fix reionization to end at redshift $z \approx 7$ (From Furlanetto 2006).

For this kind of observation, the sensitivity of the experiment is independent of telescope collecting area and it can be done using small-area telescopes at low frequency. However the line signal is still $10^{-4} - 10^{-3}$ times smaller than that of the mean foreground continuum emission.

1.4.3 Power spectrum

The three dimensional power spectrum of the 21-cm line allows us to measure a large number of independent modes than the 2D angular power spectrum. Particularly we can have a better sensitivity than in the case of direct imaging since the universe is isotropic and we can explore redshift space distortions and derive cosmological information (Barkana & Loeb, 2005).

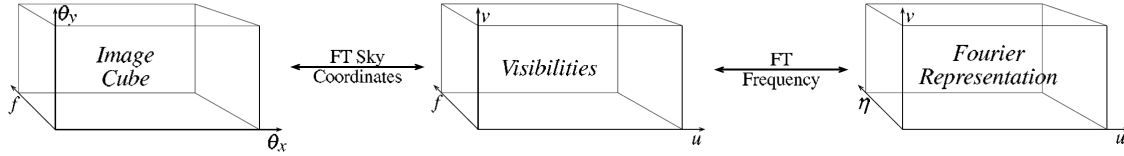


Figure 1.9: The Fourier transform relationships between image cube, the measured visibilities, and the Fourier representation. The fundamental observable is the visibility-frequency cube, which can be transformed into either an image cube or the Fourier representation (From Morales 2005).

The observable quantity for an interferometric array is a single visibility $V(\text{Jy})$. Fig. 1.9 shows the relationship between the image cube, the measured visibility cube, and the three-dimensional Fourier representation. We follow calculations by Morales (2005). We transform the visibilities coordinate from (u, v, ν) to Fourier space (u, v, η) , where η has dimension of time, since it is more convenient for a comparison with theoretical models. The Fourier representation can be expressed as

$$\delta T_b(\mathbf{u}) = \int_B \mathbf{V}(u, v, \nu) e^{2\pi i \eta \nu}, \quad (1.4)$$

where the integration range B means the bandwidth of the observation, and $\mathbf{u} \equiv u\hat{\mathbf{i}} + v\hat{\mathbf{j}} + \eta\hat{\mathbf{z}}$. In this representation, the *rms* of noise fluctuation can be expressed as (Morales, 2005),

$$\Delta T^N(\mathbf{u}) = \frac{\lambda^2 T_{sys} \sqrt{B}}{\delta A \sqrt{t_{\mathbf{u}}}} \approx \frac{T_{sys}}{\sqrt{B t_{\mathbf{u}}}} \times \frac{\lambda^2}{\delta A \delta \eta}. \quad (1.5)$$

where $\delta \eta$ (Hz^{-1}) is the inverse of the bandwidth range, dA (m^2) is the physical size of the antenna and $t_{\mathbf{u}}$ is the integration time of the particular baseline.

The detector noise covariance matrix to observe a mode \mathbf{k} for an interferometer is then,

$$C^N(\mathbf{k}_i, \mathbf{k}_j) \equiv \langle \Delta T^N(\mathbf{u}_i)^* \Delta T^N(\mathbf{u}_j) \rangle = \left(\frac{\lambda^2 B T_{sys}}{\delta A} \right)^2 \frac{\delta_{ij}}{B t_{\mathbf{k}_i}}. \quad (1.6)$$

There exists an isomorphism $\mathbf{u} \leftrightarrow \mathbf{k}$ and $2\pi \mathbf{u}_{\perp} / x = \mathbf{k}_{\perp}$, where x is the comoving distance to the observed 21-cm screen. i and j indicate labels of the observed baselines.

On the other hand, we have to add errors from sample variance,

$$\begin{aligned} C^{SV}(\mathbf{k}_i, \mathbf{k}_j) &= \langle \delta T_b^*(\mathbf{k}_i) \delta T_b(\mathbf{k}_j) \rangle \\ &\approx \delta_{ij} |\delta T_b|^2 \int d^3\mathbf{u} |W(\mathbf{u}_i - \mathbf{u})|^2 P_{21}(\mathbf{u}), \end{aligned} \quad (1.7)$$

where W is the Fourier-transform of the primary beam response function, including the finite bandwidth and P_{21} is the power of the 21-cm signal.

Finally, the errors on a power spectrum from the total covariance matrix $\mathbf{C} = \mathbf{C}^N + \mathbf{C}^{SV}$ is,

$$\delta P_{21}(\mathbf{k}_i) \approx \frac{1}{\sqrt{N_c(\mathbf{k}_i)}} \frac{\delta A x^2 y}{\lambda^2 B^2} [C^V(\mathbf{k}_i, \mathbf{k}_i) + C^{SN}(\mathbf{k}_i, \mathbf{k}_i)], \quad (1.8)$$

where N_c is the number of independent cells in the same Fourier annulus of constant (k, θ) , and y is the comoving width of observation.

$$N_c(k, \theta) = 2\pi k^2 \sin(\theta) \Delta k \Delta \theta \times \frac{\text{Vol}}{(2\pi)^3} \quad (1.9)$$

Substituting N_c in Eq.(1.8) and assuming $C^N \gg C^{SV}$, we can get (Furlanetto et al.2006)

$$\delta P_{21} \approx \delta A^{-3/2} B^{-1/2} \left[\frac{1}{k^{3/2} n(k, \theta)} \right] \left(\frac{T_{sys}^2}{t_{int}} \right). \quad (1.10)$$

Let us consider the scaling relations in order to increase the sensitivity of the power spectrum. If we add more antennae of the same size, we can decrease the errors but it can also increase the number of correlations by the same factor. We can make each antenna larger keeping the same number, but we lose the gain sensitivity which is only proportional to $\delta A^{-3/2}$. It decreases the total field of view. Increasing the bandwidth can also be a solution to increase the sensitivity. However too much bandwidth can increase systematic errors because of strong foregrounds. Increasing the integration time also decreases the uncertainty of the measurement.

The distribution of baselines in an array can affect the sensitivity to the EoR, since the effective collecting area at a given angular resolution depends on that. We are interested in short baseline array to observe the redshift 21 cm signal. We can approximate the collecting area for SKA scales as λ^2 , which is equal to $6 \times 10^5 \text{ m}^2$ within the inner 6 km of the array for $\lambda = 21(1 + 8) \text{ cm}$ (McQuinn et al., 2006).

Fig. 1.10 in McQuinn et al. (2006) compares the expected power spectrum errors of various instruments and signals. SKA has reasonable sensitivity for three redshifts 6, 8, and 12 between $0.01 \text{ Mpc}^{-1} \lesssim k \lesssim 5 \text{ Mpc}^{-1}$ while ASKAP and LOFAR show acceptable sensitivity at $z \lesssim 10$ and $k \lesssim 1 \text{ Mpc}^{-1}$ (all distances in comoving

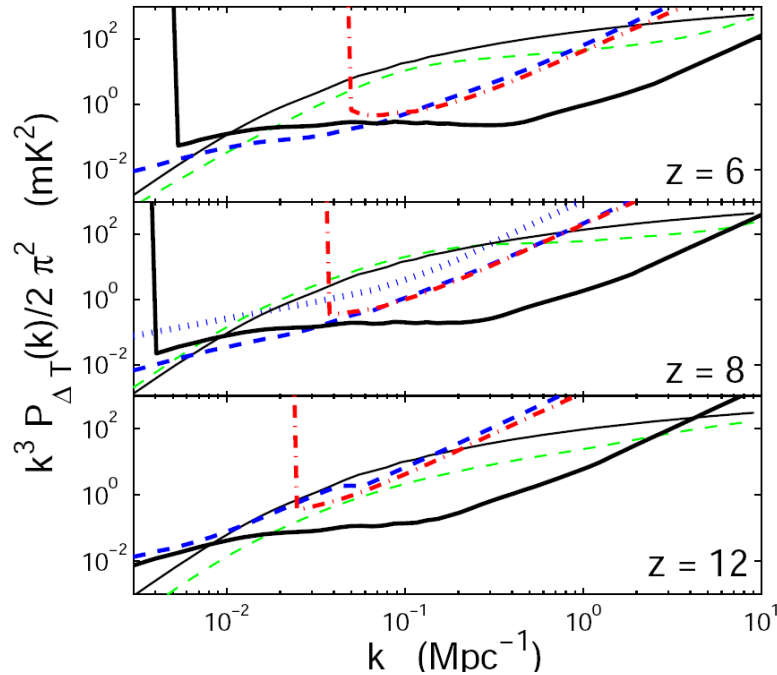


Figure 1.10: Isotropic power spectrum sensitivity. The expected error for the ASKAP (thick dashed curves), LOFAR (thick dot-dashed curves), and the SKA (thick solid curves) and estimated signal (with and without reionization) are shown by the thin dashed and solid line. Each assumes perfect foreground removal (from McQuinn et al. (2006))

coordinates).

1.4.4 Foreground Contamination

The foreground problem is the most challenging difficulty for the 21-cm line measurement. Both the discrete extragalactic radio sources and the large-scale emission of our Galaxy strongly contaminate the signal. The primary foreground from our Galaxy is 3 to 4 orders of magnitude larger than the expected 21-cm signal. However, it will be removable since all the foreground contaminations from our Galaxy are spectrally smooth and we can extract them.

The other foregrounds from discrete radio galaxies, and terrestrial radio frequency interference are not spectrally smooth. Particularly, Di Matteo et al. (2002) shows that the extragalactic point sources may be the hardest to remove. A number of works have been done to develop foreground cleaning techniques, (e.g. Morales (2005); Bowman et al. (2006); Gnedin (2004)) and concluded that spectral decomposition

should be adequate to separate synchrotron foregrounds from the HI-cm signal at mK level. Santos et al. (2005) study the foregrounds and their influence on the 21-cm signal and show that foreground cleaning is aided by the large-scale angular correlation, especially of the extragalactic point sources.

Jelić et al. (2008) present simulated astrophysical foregrounds data cubes and show that the expected LOFAR-EoR noise level is ≈ 52 mK at 150 MHz after 400h of total observing time.

Chapter 2

Numerical code - LICORICE

LICORICE is developed in the Paris Observatory to simulate radiative (UV + Ly- α) hydrodynamics using the TreeSPH algorithm and a Monte Carlo ray-tracing algorithm on an adaptive grid. The LICORICE code integrates three main parts, a TreeSPH dynamical part (see section 2.1), radiative transfer for the ionizing continuum (see section 2.2) and radiative transfer for the Lyman- α line (see section 2.3). LICORICE shows good agreement with the results of other codes used in Iliev et al. 2006, the Cosmological Radiative Transfer Code Comparison Project I (Iliev et al., 2006a) (see section 2.4). We are also participating in the Comparison Project II (Iliev et al., 2009), a set of radiative hydrodynamics tests. The general performance of LICORICE is discussed in section 2.5.

2.1 Tree SPH algorithm for dynamics

The first part of LICORICE is the dynamical part. The gravity and fluid dynamics are followed using a TreeSPH method. More details on different aspects of the implementation are described in Semelin & Combes (2002) and Semelin & Combes (2005).

2.1.1 Tree algorithm for gravitation

Gravity is the driving force of the structure evolution. LICORICE uses the tree algorithm (Barnes & Hut 1986) to compute gravity.

Construction of the Tree

The tree structure is essential for the LICORICE code. All three main parts of LICORICE are based on this oct-tree structure. We construct an adaptive grid using the tree structure level by level. The entire simulation box is the root cell or “0-level

cell”. The n -level cells are split into 8 (4 in 2D) children $(n + 1)$ -level cells if they contain more than 1 particle. The left thin grid of Fig. 2.1 shows the tree structure with 5 levels.

Dynamic equation

Once the tree is constructed, the computational cost for gravitation can be reduced from $\mathcal{O}(N^2)$ to $\mathcal{O}(N \log N)$ where N is the number of particles. This is due to the multipole approximation for gravity computation at large distance. From the low to high level cell, we examine if the angular size of the cell, seen from distant particles, is smaller than a criterion θ . If so, we compute the gravitational force on distant particles using the multipole moments of the particle distribution in the cell. Otherwise we do the same test with the subcells, and so on. Typically we use a value of $\theta = 0.8$ rad and the typical error on the gravitational force is smaller than 1% (Hernquist, 1987).

2.1.2 The SPH algorithm for hydrodynamics

Hydrodynamic forces are also important for structure formation. In hydrodynamic codes, galaxy formation can be modeled self-consistently including cooling and accretion mechanisms. LICORICE treats the hydrodynamic through the SPH method (Gingold & Monaghan, 1977).

In the SPH method, fluid elements constituting the system are sampled and represented by particles. All particles represent the local pressure, density and energy of the fluid, which depend on the properties of neighbor particles. Identifying the neighbor particles is a very important step to compute the equation of motion, and the number of neighbor particles determines the spatial resolution in this algorithm. We compute an individual smoothing length, h , for each particle so that all particles have a similar number of neighbor particles. We use again the tree data structure to find rapidly the neighbor particles and the smoothing length h . Once the list of neighbor particles and the smoothing length is computed for each particle, we compute the local density of the particle (called also “particle density”) ρ_i , through a kernel w (a spherically symmetric spline function) from Monaghan & Lattanzio (1985).

$$\begin{aligned}
 i) \quad w(x, h) &= \frac{1}{\pi h^3} [1 - (3/2)(r/h)^2 + (3/4)(r/h)^3], \quad 0 \leq r/h \leq 1, \\
 ii) \quad w(x, h) &= \frac{1}{\pi h^3} (1/4)[2 - (r/h)]^3, \quad 1 \leq r/h \leq 2, \\
 iii) \quad w(x, h) &= 0, \quad r/h \geq 2.
 \end{aligned} \tag{2.1}$$

where x is the one dimensional distance from the position of the particle and m is

the particle mass. From the equation of state,

$$p(\rho, u) = (\gamma - 1)\rho u \left(\gamma = \frac{5}{3} \right), \quad (2.2)$$

we compute the pressure $p_i = p(\rho_i, u_i)$ where u is the specific energy. Then we integrate the equation of motion as follows (gravity forces excluded) :

$$\begin{aligned} \frac{d\mathbf{r}_i}{dt} &= \mathbf{v}_i \\ \frac{d\mathbf{v}_i}{dt} &= -\frac{1}{\rho_i} \nabla p_i + \mathbf{a}_i^{visc} \end{aligned} \quad (2.3)$$

where \mathbf{a}_i^{visc} is an artificial viscosity term to deal with the presence of shock waves to spread the shock over the spatial resolution. We use the viscosity described in Monaghan (1992). We use the arithmetic average $h_{ij} = \frac{h_i + h_j}{2}$ to compute the interaction between two particles. This is important for a good momentum and energy conservation.

2.1.3 Additional physics

A number of additional physical processes have been implemented in the LICORICE code.

Star formation

Star formation is considered by transforming gas particles into star particles. First we have to choose under which condition stars can be formed. Katz (1992) proposed a criteria that stars form only in Jeans unstable regions and within a convergent flow of gas. Navarro & White (1993) added the condition that the star forming regions undergo rapid cooling. They both reduced the cooling time criterion and the Jeans instability criterion to a density threshold. We agree with these considerations and use a density threshold (where $\rho > \rho_{\text{critical}}$) to select star forming regions. This is coherent with results deduced from the observations (Martin & Kennicutt, 2001). For the gas particles over this density threshold condition, we compute a star formation rate following the Schmidt law,

$$\frac{d\rho_{\text{star}}}{dt} = C\rho_{\text{gas}}^n, \quad (2.4)$$

where C is a constant combining a star formation efficiency and characteristic time and the index n is fixed at 1.5 or 1.

Cooling and heating

The thermal evolution of particles depends on the adiabatic expansion, shocks, external (Γ_{UV}) photo heating and radiative cooling (Λ). Although radiative heating and cooling can be computed in the continuum radiative transfer part of LICORICE, the dynamic part has its own module for simulations without radiative transfer. It uses the tabulated values of Λ in Sutherland & Dopita (1993). In some cases, a constant uniform heating Γ_{UV} is applied to the gas to model the background UV radiation field.

Supernova feedback

Supernova explosion releases an energy amount of $\sim 10^{48}$ erg per unit solar mass of a Salpeter IMF. We include both thermal and kinetic feedback on the neighbor particles to avoid instantaneous dissipation by radiative cooling (Katz et al., 1996). Thermal feedback increases the temperature of neighbor particles up to $10^4 - 10^5$ K and the kinetic feedback kicks away the neighbors in radial directions around the forming star (Mihos & Hernquist, 1994).

2.2 Monte Carlo on an adaptive grid - continuum

The second part of LICORICE is the radiative transfer of the ionizing continuum. We use a 3D Monte Carlo ray-tracing scheme. The radiation field is discretized into photon packets which propagate individually on an adaptive grid and interact with matter. The numerical methods implemented in LICORICE are similar to the ones employed in the CRASH code (Maselli et al., 2003). There are, however, a number of differences which are described in the following sections.

2.2.1 Adaptive grid

Both the continuum and Lyman line radiative transfer (RT) parts of LICORICE use an adaptive grid based on the oct-tree. The oct-tree keeps splitting a mother cell into 8 children cells (4 children cells for 2D) if it contains more than 1 particle as shown in left panel of Fig. 2.1. There is a difference between the usual oct-tree and our adaptive grid. The grid for RT stops splitting a mother cell if it contains less than a tunable parameter N_{max} particles. Therefore, the RT cells can contain from 0 to N_{max} particles while the “leaf-cells” in the oct-tree contain either 0 or 1 particle.

For equivalent spatial resolution, such an adaptive grid requires lower memory and CPU-time than regular grid-based RT codes.

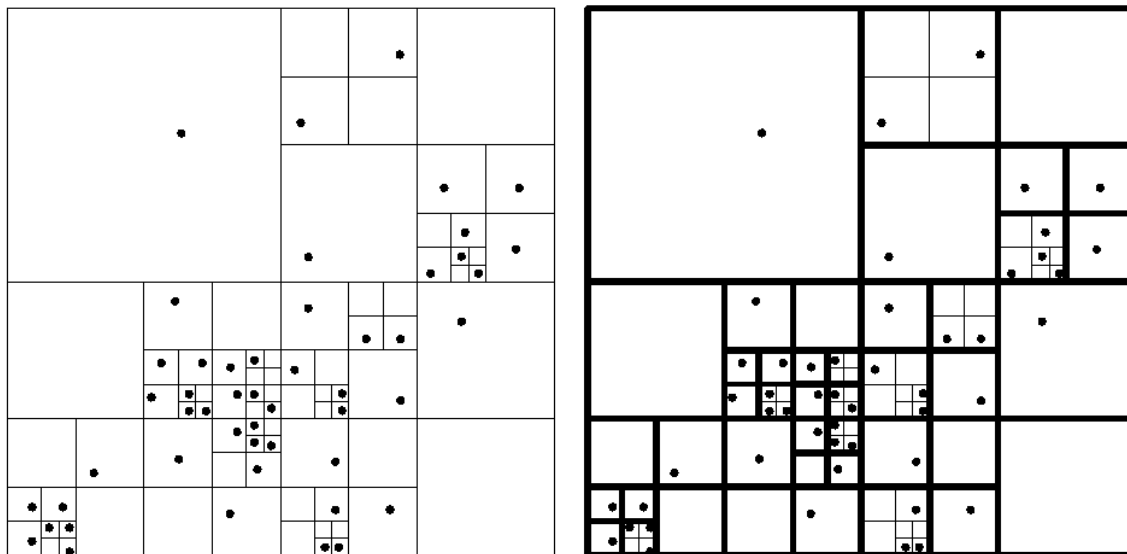


Figure 2.1: The left thin grid is an adaptive grid for TreeSPH dynamical part and the right thick is the one for radiative transfer (continuum and Lyman line). Each RT cell of the thick grid contains less than N_{max} particles, which is a tunable parameter. $N_{max} = 4$ is used for this 2D representation.

We define the RT cell density as the average of the particle densities of an RT cell. We use it to estimate the optical depth of each RT cell. The photon packet travels through RT cells and deposits a fraction of its content in each RT cell crossed depending on this RT cell density. Then we distribute the absorbed photons and energy to each particle in the RT cell proportionally to its HI mass. This scheme is especially relevant if the density field is not static i.e. an RT cell does not always contain the same set of particles.

2.2.2 Ionizing radiation field

The radiation field is discretized into photon packets and they are emitted from the point sources which are located in the simulation box. The number of photons in one photon packet is determined by the photon packet frequency ν , the number of photon packets emitted each time step, and the time dependent luminosity $L(\nu, t)$ of the sources. To each photon packet, a frequency ν is given by sampling the source spectrum. If N_{ph} photon packets are emitted per point source with random direction (θ, ϕ) during the regular time interval Δt_{reg} , each photon packet of frequency ν contains,

$$N_{\gamma}(\nu, t) = \frac{L(\nu, t)\Delta t_{reg}}{N_{ph}h\nu} \quad (2.5)$$

real photons.

2.2.3 Absorption probability of photon packets

Let $O(x_0, y_0, z_0)$ be the position of a point source. The position of a propagating photon, emitted from O with random direction (θ, ϕ) can be described by Eq.(2.6) in spherical coordinate.

$$\begin{aligned} x &= x_0 + r \sin \theta \cos \phi \\ y &= y_0 + r \sin \theta \sin \phi \\ z &= z_0 + r \cos \theta \end{aligned} \tag{2.6}$$

Photon packets propagate through several RT cells and deposit photons and energy in each RT cell depending on the absorption probability. A generic monochromatic packet, initially composed of N_γ photons deposits a fraction of its N_γ ionizing photons into RT cells during the propagation.

At first, let's consider the absorption probability, $\mathcal{P}_{cell}(\tau_{cell})$ for a single photon, passing through an RT cell filled with only the hydrogen absorber. The optical depth of the RT cell, τ_{cell} can be expressed as

$$\tau_{cell} = \sigma l_{cell} n_{\text{H}^0}, \tag{2.7}$$

where σ is the photoionization cross-section and n_{H^0} denotes the number density of the hydrogen in the cell and l_{cell} is the length of the RT cell. From the radiative transfer equation, the absorption probability of this simple case is given by,

$$\mathcal{P}(\tau_{cell}) = 1 - e^{-\tau_{cell}}, \tag{2.8}$$

for arbitrary large values of τ_{cell} . Now let's compute the case for several absorbers ($\text{H}^0, \text{He}^0, \text{H}^+$), how the absorption probability for each absorber is changed with respect to Eq.(2.8)

We divide one RT cell in many small bins as shown in Fig. 2.2. The bins crossed by the photon packet are ordered by the index $i = 1, 2, 3, \dots, (n-1), n$. Let l_{cell} be the length of the RT cell. Then we compute the probability of being absorbed by each absorber in one bin of the RT cell. Since n is very large, each bin is optically thin, then ;

- the probability of being absorbed by H^0 in one bin is¹

$$p_{\text{H}^0} = \sigma_{\text{H}^0} \frac{l_{cell}}{n} n_{\text{H}^0} \equiv \frac{\tau_{cell, \text{H}^0}}{n},$$

¹ H^0 denotes the neutral hydrogen

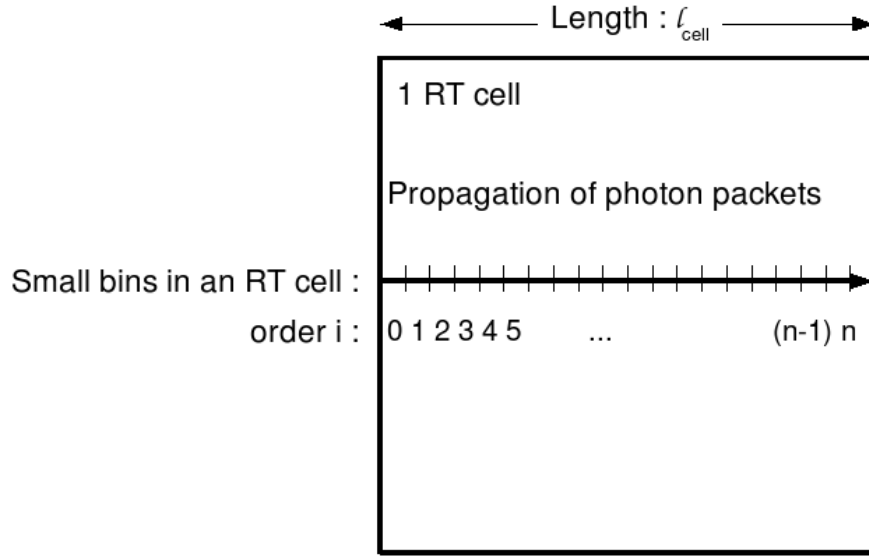


Figure 2.2: The small bins crossed by the photon packet in an RT cell are ordered by the index $i = 1, 2, 3, \dots, (n - 1), n$.

- the probability of being absorbed by He^0 in one bin is²

$$p_{\text{He}^0} = \sigma_{\text{He}^0} \frac{l_{cell}}{n} n_{\text{He}^0} \equiv \frac{\tau_{cell, \text{He}^0}}{n},$$

- the probability of being absorbed by He^+ in one bin is

$$p_{\text{He}^+} = \sigma_{\text{He}^+} \frac{l_{cell}}{n} n_{\text{He}^+} \equiv \frac{\tau_{cell, \text{He}^+}}{n},$$

- the probability of not being absorbed by any absorber in one bin is

$$1 - (p_{cell, \text{H}^0} + p_{cell, \text{He}^0} + p_{cell, \text{He}^+}) = 1 - \left(\frac{\tau_{cell, \text{H}^0} + \tau_{cell, \text{He}^0} + \tau_{cell, \text{He}^+}}{n} \right).$$

The probability of being absorbed in the $i = m$ bin, $\mathcal{P}_{\text{H}^0}^m$, is,

$$\mathcal{P}_{\text{H}^0}^m = (1 - p_{cell, \text{H}^0} - p_{cell, \text{He}^0} - p_{cell, \text{He}^+})^m \times p_{cell, \text{H}^0}. \quad (2.9)$$

e.g. The probability of not being absorbed until m bin multiplied by the probability of being absorbed in m bin.

Therefore, the total probability, \mathcal{P}_{H^0} , of the photon being absorbed by H^0 anywhere in an RT cell is the sum of the probability of being absorbed in each bin.

² He^0 denotes the neutral helium

$$\begin{aligned}
\mathcal{P}_{\text{H}^0} &= \mathcal{P}_{\text{H}^0}^0 + \mathcal{P}_{\text{H}^0}^1 + \mathcal{P}_{\text{H}^0}^2 + \dots + \mathcal{P}_{\text{H}^0}^n \\
&= \frac{\tau_{\text{cell},\text{H}^0}}{n} \sum_{i=0}^{n-1} \left(1 - \frac{\tau_{\text{cell},\text{H}^0} + \tau_{\text{cell},\text{He}^0} + \tau_{\text{cell},\text{He}^+}}{n} \right)^i \\
&= \frac{\tau_{\text{cell},\text{H}^0}}{n} \frac{1 - \left(1 - \frac{\tau_{\text{cell},\text{H}^0} + \tau_{\text{cell},\text{He}^0} + \tau_{\text{cell},\text{He}^+}}{n} \right)^n}{\frac{\tau_{\text{cell},\text{H}^0} + \tau_{\text{cell},\text{He}^0} + \tau_{\text{cell},\text{He}^+}}{n}} \\
&= \frac{\tau_{\text{cell},\text{H}^0}}{\tau_{\text{cell},\text{H}^0} + \tau_{\text{cell},\text{He}^0} + \tau_{\text{cell},\text{He}^+}} \left\{ 1 - \left(1 - \frac{\tau_{\text{cell},\text{H}^0} + \tau_{\text{cell},\text{He}^0} + \tau_{\text{cell},\text{He}^+}}{n} \right)^n \right\} \\
&\simeq \frac{\tau_{\text{cell},\text{H}^0}}{\tau_{\text{cell},\text{H}^0} + \tau_{\text{cell},\text{He}^0} + \tau_{\text{cell},\text{He}^+}} \left(1 - e^{-\tau_{\text{cell},\text{H}^0} + \tau_{\text{cell},\text{He}^0} + \tau_{\text{cell},\text{He}^+}} \right), \tag{2.10}
\end{aligned}$$

since n is very large.

In the same way,

$$\mathcal{P}_{\text{He}^0} = \frac{\tau_{\text{cell},\text{He}^0}}{\tau_{\text{cell},\text{H}^0} + \tau_{\text{cell},\text{He}^0} + \tau_{\text{cell},\text{He}^+}} \left(1 - e^{-\tau_{\text{cell},\text{H}^0} + \tau_{\text{cell},\text{He}^0} + \tau_{\text{cell},\text{He}^+}} \right), \tag{2.11}$$

$$\mathcal{P}_{\text{He}^+} = \frac{\tau_{\text{cell},\text{He}^+}}{\tau_{\text{cell},\text{H}^0} + \tau_{\text{cell},\text{He}^0} + \tau_{\text{cell},\text{He}^+}} \left(1 - e^{-\tau_{\text{cell},\text{H}^0} + \tau_{\text{cell},\text{He}^0} + \tau_{\text{cell},\text{He}^+}} \right). \tag{2.12}$$

Eq.(2.10)-(2.12) are also valid for arbitrary large values of τ_{cell} , while the absorption probabilities used in Eq.(15) of Maselli et al. (2003) are approximately valid for optically thin cases.

The total absorption probability, $\mathcal{P}_{\text{total}}$, for a single photon arriving in an RT cell of optical depth $\tau_{\text{cell}} \equiv \tau_{\text{H}^0} + \tau_{\text{He}^0} + \tau_{\text{He}^+}$ is given by

$$\mathcal{P}_{\text{total}}(\tau_{\text{cell}}) = \mathcal{P}_{\text{H}^0} + \mathcal{P}_{\text{He}^0} + \mathcal{P}_{\text{He}^+} = 1 - e^{-\tau_{\text{cell}}}. \tag{2.13}$$

Photon packets propagates through several RT cells. The RT cells crossed by the photon packets are ordered by the index $l = 1, 2, 3, \dots, (N - 1), N$ and N is the last RT cell where we stop the propagation. For each l -th RT cell crossed, we increment the optical depth by $\Delta\tau^l$,

$$\begin{aligned}
\Delta\tau^l &= \tau_{\text{cell}} = \Delta\tau_{\text{H}^0}^l + \Delta\tau_{\text{He}^0}^l + \Delta\tau_{\text{He}^+}^l \\
&= [\sigma_{\text{H}^0}(\nu)n_{\text{H}^0}^l + \sigma_{\text{He}^0}(\nu)n_{\text{He}^0}^l + \sigma_{\text{He}^+}(\nu)n_{\text{He}^+}^l] l_{\text{cell}} \tag{2.14}
\end{aligned}$$

where σ_A is the photoionization cross-section for absorber $A \in \{\text{H}^0, \text{He}^0, \text{He}^+\}$,

n_{Abs}^l is number density in the l -th RT cell.

Then we can compute the number of photons absorbed in the l -th RT cell. If N_γ^l is the number of photons in a photon packet arriving in the l -th RT cell,

$$N_{Abs}^l = N_\gamma^l \mathcal{P}_{total} = N_\gamma^l (1 - e^{-\Delta\tau^l}) \quad (2.15)$$

is the number of absorbed photon in l -th RT cell, and

$$N_\gamma^l - N_{Abs}^l = N_\gamma^l - N_\gamma^l (1 - e^{-\Delta\tau^l}) = N_\gamma^l e^{-\Delta\tau^l} \quad (2.16)$$

is the number of photon passing through the l -th RT cell. It is also the same as the number of photons arriving in the next $(l + 1)$ -th RT cell. Therefore,

$$N_\gamma^{l+1} = (N_\gamma^l - N_{Abs}^l) = N_\gamma^l e^{-\Delta\tau^l} \leq N_\gamma, \quad (2.17)$$

where N_γ is the initial photon content in a photon packet.

Each photon packet keeps propagating until it exits the simulation box (if we use free boundary condition) or until the remaining photon content is much smaller than the initial photon content, $N_\gamma^l < 10^{-P} N_\gamma$. We typically adopt $p = 4$ for the UV continuum and $p = 2$ for the X-ray continuum. We use $p = 2$ for X-rays for two reasons. X-ray photons have very small photoionizing cross section, and they propagate through the periodic simulation box several times before the remaining photon contents reaches $10^{-4} N_\gamma$. Therefore we use $p = 2$ for X-ray photons in order to reduce the computational cost. In addition, the total energy of the X-ray continuum is much smaller than that of UV continuum (e.g. $L_X = 10^{-3} L_{UV}$) in our chosen models, so taking $p = 2$ for the X-ray continuum is also acceptable for good energy conservation.

2.2.4 Updating physical quantities

From the absorbed photons in the RT cells, we update the ionization fraction using the following coupled equations (Maselli et al., 2003);

$$\begin{aligned}
n_{\text{H}} \frac{dx_{\text{H}^+}}{dt} &= \gamma_{\text{H}^0}(T)n_{\text{H}^0}n_e - \alpha_{\text{H}^+}(T)n_{\text{H}^+}n_e + \Gamma_{\text{H}^0}n_{\text{H}^0}, \\
n_{\text{He}} \frac{dx_{\text{He}^+}}{dt} &= \gamma_{\text{He}^0}(T)n_{\text{He}^0}n_e - \gamma_{\text{He}^+}(T)n_{\text{He}^+}n_e \\
&\quad - \alpha_{\text{He}^+}(T)n_{\text{He}^+}n_e + \alpha_{\text{He}^{++}}(T)n_{\text{He}^{++}}n_e + \Gamma_{\text{He}^0}n_{\text{He}^0}, \\
n_{\text{He}} \frac{dx_{\text{He}^{++}}}{dt} &= \gamma_{\text{He}^+}(T)n_{\text{He}^+}n_e - \alpha_{\text{He}^{++}}(T)n_{\text{He}^{++}}n_e + \Gamma_{\text{He}^+}n_{\text{He}^+}. \tag{2.18}
\end{aligned}$$

where $n = n_{\text{H}} + n_{\text{He}} + n_e$ is the number of free particles per unit volume in the gas; \mathcal{H} and Λ are the heating and cooling functions which account for the energy gained and lost in a unit volume per unit time. α_{I} and γ_{A} indicate the recombination and collisional ionization coefficient and $\text{I} \in \{\text{H}^+, \text{He}^+, \text{H}^{++}\}$; Γ_{A} is the time-dependent photoionization rate.

The last equation is the energy conservation used to update the gas temperature. E is the internal energy of the gas, $E = \frac{3}{2}nk_{\text{B}}T$. Since n and T depend on time,

$$\frac{dE}{dt} = \frac{d}{dt} \left(\frac{3}{2}nk_{\text{B}}T \right) = \frac{3}{2} \frac{dn}{dt} k_{\text{B}}T + \frac{3}{2} nk_{\text{B}} \frac{dT}{dt} = \mathcal{H} - \Lambda. \tag{2.19}$$

From the equation of energy conservation Eq.(2.19), we update the gas temperature,

$$\frac{dT}{dt} = \frac{2}{3k_{\text{B}}n} \left[-\frac{3}{2}k_{\text{B}}T \frac{dn}{dt} + \mathcal{H}(T, x_{\text{I}}) - \Lambda(T, x_{\text{I}}) \right]. \tag{2.20}$$

We update the ionization fraction and temperature of the gas using Eq.(2.18) with the integration time step Δt_{update} . We integrate Eq.(2.21)-(2.24) implicitly (with hydrogen species only) or explicitly (with helium species). Δt_{update} can be equal or less than the Δt_{reg} described in the previous section. The photoionization rate (Γ_{A}) and photoheating rate are considered as constant during the integration time step Δt_{update} . Their contributions are given by :

$$\begin{aligned}
\Delta x_{\text{H}^+} &= \frac{n_{\text{H}}^0}{n_{\text{H}}} \Gamma_{\text{H}^0} \Delta t_{\text{update}} \\
&\equiv \frac{\text{The number of photons absorbed by H}^0 \text{ in } l\text{-th RT cell}}{\text{The total number of hydrogen in the } l\text{-th RT cell}} \\
&= \frac{N_{\text{Abs}}^l \mathcal{P}_{\text{H}^0}}{N_{\text{H}}^l} = \frac{N_{\text{Abs}}^l}{n_{\text{H}}^l l_{\text{cell}}^3} \left(\frac{\Delta \tau_{\text{H}^0}^l (1 - e^{-\Delta \tau^l})}{\Delta \tau_{\text{H}^0}^l + \Delta \tau_{\text{He}^0}^l + \Delta \tau_{\text{He}^+}^l} \right), \tag{2.21}
\end{aligned}$$

$$\begin{aligned}
\Delta x_{\text{He}^+} &= \frac{n_{\text{He}}^0}{n_{\text{H}}} \Gamma_{\text{He}^0} \Delta t_{\text{update}} \\
&\equiv \frac{\text{The number of photons absorbed by He}^0 \text{ in } l\text{-th RT cell}}{\text{The total number of helium in the } l\text{-th RT cell}} \\
&= \frac{N_{\text{Abs}}^l \mathcal{P}_{\text{He}^0}}{N_{\text{He}}^l} = \frac{N_{\text{Abs}}^l}{n_{\text{He}}^l l_{\text{cell}}^3} \left(\frac{\Delta \tau_{\text{He}^0}^l (1 - e^{-\Delta \tau^l})}{\Delta \tau_{\text{H}^0}^l + \Delta \tau_{\text{He}^0}^l + \Delta \tau_{\text{He}^+}^l} \right), \tag{2.22}
\end{aligned}$$

$$\begin{aligned}
\Delta x_{\text{He}^+} &= \frac{n_{\text{He}}^0}{n_{\text{He}}} \Gamma_{\text{He}^0} \Delta t_{\text{update}} \\
&\equiv \frac{\text{The number of photons absorbed by He}^+ \text{ in } l\text{-th RT cell}}{\text{The total number of helium in the } l\text{-th RT cell}} \\
&= \frac{N_{\text{Abs}}^l \mathcal{P}_{\text{He}^+}}{N_{\text{He}}^l} = \frac{N_{\text{Abs}}^l}{n_{\text{He}}^l l_{\text{cell}}^3} \left(\frac{\Delta \tau_{\text{He}^+}^l (1 - e^{-\Delta \tau^l})}{\Delta \tau_{\text{H}^0}^l + \Delta \tau_{\text{He}^0}^l + \Delta \tau_{\text{He}^+}^l} \right), \tag{2.23}
\end{aligned}$$

$$\begin{aligned}
\Delta T &= \frac{2}{3k_B n} \left\{ -\frac{3}{2} k_B T \Delta n + N_{\text{Abs}}^l \mathcal{P}_{\text{H}^0} (h\nu - h\nu_{\text{th},\text{H}^0}) \right. \\
&\quad \left. + N_{\text{Abs}}^l \mathcal{P}_{\text{He}^0} (h\nu - h\nu_{\text{th},\text{He}^0}) + N_{\text{Abs}}^l \mathcal{P}_{\text{He}^+} (h\nu - h\nu_{\text{th},\text{He}^+}) \right\} \tag{2.24}
\end{aligned}$$

where $h\nu_{\text{th},A}$ are the ionization potential of the recombined atom and l_{cell}^3 is the volume of the l -RT cell. Recombination, collisional ionization and cooling are treated as continuous process, with integration time step Δt_{cool} much smaller than Δt_{update}

(50-100 times). All rates for recombination, collisional ionization and cooling are given in Appendix A.

2.2.5 Adaptive time integration

The integration time step for updating the photoionization and photoheating rates, Δt_{update} , is adaptative. We use a typical Δt_{update} smaller than the dynamical time step Δt_{dyn} . Furthermore, recombination, collisional ionization and cooling are treated with an integration time step Δt_{cool} which is much smaller than Δt_{update} .

The ionizing continuum radiative transfer is the repetition of two steps. i) The emission and propagation of N_{ph} photon packets during the time interval Δt_{reg} and then ii) the update of physical quantities.

- i) All the sources emit N_{ph} photon packets along random directions. Each RT cell records the number of absorbed photons and the absorbed energy during this period.
- ii) The physical quantities of the gas are updated with the integration time step Δt_{reg} . This update is applied even to the RT cells that absorbed no photon during Δt_{reg} . This is necessary in order to consider the effect of collisional ionization, recombination, adiabatic expansion, etc.

However, this regular update is not appropriate where the flux of photons is too high, especially close to the sources. In this case, the number of photons absorbed during Δt_{reg} is so high that it can exceed the total number of atoms available in the RT cell. To avoid this excess, we update the physical quantities and optical depth of the RT cell whenever the number of absorbed photons reaches a pre-set limit, for example 30% of the total number of neutral atoms in the RT cell. We update this RT cell with $\Delta t_{update} (< \Delta t_{reg})$ which is equal to the time elapsed since the last update. The hierarchical scale of the different time steps are specified in Fig. 2.3

2.2.6 X-ray radiative transfer

LICORICE can deal with the ray tracing of soft X-ray continuum ($E \leq 2 \text{ keV}$) as well as UV continuum. The main effect of X-rays on the gas is heating rather than ionization. We included only soft X-rays because X-ray heating is dominated by soft X-rays, as harder X-rays have a mean free path comparable to the Hubble scale (Pritchard & Furlanetto, 2007). Here are some differences of the X-ray radiative transfer compared to the UV continuum.

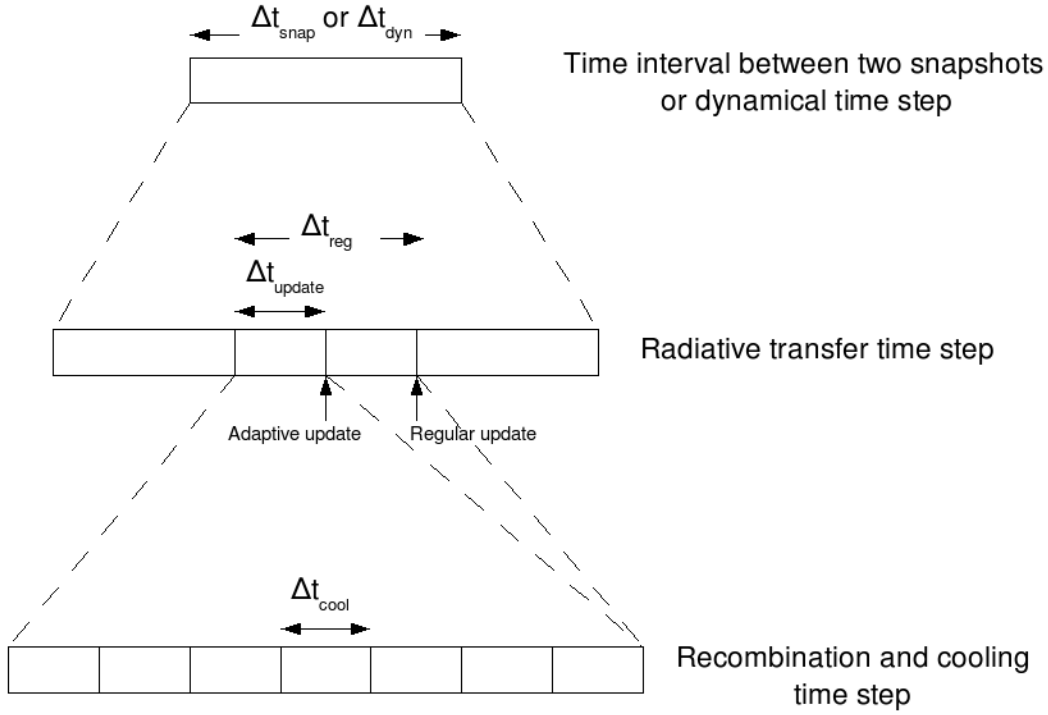


Figure 2.3: Schematic representation of the different time steps of LICORICE.

Finite velocity of light

For the UV continuum transfer, an infinite velocity of light is assumed because the photon mean free path is usually much shorter than the typical simulation box size (10-100 comoving Mpc/h) and the photon content in a photon packet attenuates quickly down to the limit ($N_\gamma^l < 10^{-4} N_\gamma$) within a regular time step of radiative transfer Δt_{reg} .

On the other hand, X-rays have a mean free path comparable with the simulation box size so they can travel several times the simulation box (under periodic boundary conditions) until the number of photons is attenuated below the limit. The comoving mean free path of an X-ray with energy E is (Furlanetto et al 2006),

$$\lambda_X \approx 4.9 x_{\text{HI}}^{-1/3} \left(\frac{1+z}{15} \right)^{-2} \left(\frac{E}{300 \text{ eV}} \right)^3 \text{ Mpc}. \quad (2.25)$$

Therefore, applying the same assumption of infinite velocity to X-ray photons causes incorrect results. We used the real velocity of light for X-rays, so they travel a distance $c\Delta t_{reg}$ for each time step of the radiative transfer, Δt_{reg} . We save these photons for the next time step of radiative transfer. When the photon packet loses $\sim 95\%$ of its initial number of photons, we stop the propagation. The 95% limit is higher than the

limit of the UV continuum ($N_\gamma^l < 10^{-4} N_\gamma$) for the sake of computational cost due to the long mean free path of X-rays.

Redshifting frequency

Since the X-ray photons can propagate over several box sizes during several tens of Myr, the X-ray frequency can redshift considerably between emission and absorption. The cross-section of photoionization has a strong frequency dependence, so we have to redshift the frequency of the photons. At each radiative transfer time step Δt_{reg} , we update the frequency of all the X-ray photon packets,

$$\nu(t + \Delta t_{reg}) = \frac{a(t)}{a(t + \Delta t_{reg})} \nu(t), \quad (2.26)$$

where $a(t)$ is the expansion factor of the Universe.

Secondary heating and ionization

Since X-ray photons have much more energy than the ionization potential, a fraction of a primary electron's energy is deposited as heat, secondary ionization, and H/He excitation depending on the local ionization fraction. The corresponding generic interactions are Coulomb collisions with thermal electrons, collisional ionization of H^0, He^0 or He^+ , and collisional excitation of H^0, He^0 or He^+ . Therefore secondary heating becomes larger with increasing ionization fraction of the background. We used the fitting formulae of Shull & van Steenberg (1985) to account for this effect. For example, according to their numerical work, a primary electron of $2keV$ creates over 24 secondary electrons (17% of its initial energy), deposits 64% of its energy as heat, and leaves the remainder as H I excitation (15%), and He I excitation or ionization (4%) for a local ionization fraction $x = 0.1$.

2.3 Lyman line transfer

The last part of LICORICE, which deals with the Ly- α line radiative transfer, shares its main features with the second part, the Monte Carlo approach and the adaptive grid. The methods for resonant line scattering were presented in Semelin et al. (2007). The implementation is similar to those of other existing codes. (e.g. Zheng & Miralda-Escudé (2002); Cantalupo et al. (2005); Dijkstra et al. (2006); Verhamme et al. (2006); Tasitsiomi (2006)). Necessary improvements have been implemented in our code.

2.3.1 The optical depth

The neutral hydrogen atoms absorb Lyman series photons as well as the ionizing photons, but absorbed Lyman series photons are re-emitted immediately by the spontaneous emission, also considered as scattering. The current version of LICORICE has only the Ly- α line; upper Lyman series lines will be included in a future work.

Similar to the ionizing photon case, a Ly- α photon traveling through the intergalactic medium has a probability $P_\alpha(\tau_\alpha) = 1 - e^{-\tau_\alpha}$ of being scattered after traveling through an optical depth τ_α from its emission point. The optical depth of Ly- α scattering can be expressed as;

$$\tau_\alpha = \int_0^l \int_{-\infty}^{+\infty} ds du_{\parallel} n_{\text{H}^0} p(u_{\parallel}) \sigma_\alpha \left(\nu \left(1 - \frac{v_{\parallel}^{\text{macro}} + u_{\parallel}}{c} \right) \right), \quad (2.27)$$

where ν is the photon frequency in the global rest frame and n_{H^0} is the local number density of neutral hydrogen. u_{\parallel} is the scattering atom thermal velocity along the incoming photons's direction in the moving reference frame of the fluid, $p(u_{\parallel})$ is the normalized probability distribution for u_{\parallel} , $v_{\parallel}^{\text{macro}}$ is the gas macroscopic velocity along the incoming photons's direction in the global rest frame, and c is the speed of light. $\sigma_\alpha(\nu')$ is the Ly- α scattering cross section of a photon with frequency ν' in the atom rest frame. An approximate expression of the Ly- α scattering cross section is given in Peebles (1993) :

$$\sigma_\alpha = f_{12} \frac{\pi e^2}{m_e c} \frac{\Delta\nu_L/2\pi}{(\nu - \nu_0)^2 + (\Delta\nu_L/2)^2} \quad (2.28)$$

where $f_{12} = 0.4162$ is the Ly- α oscillator strength, $\nu_0 = 2.466 \times 10^{15}$ Hz is the line center frequency and $\Delta\nu_L = 9.936 \times 10^7$ Hz is the natural line width. The function $p(u_{\parallel})$ usually results from the thermal distribution of the atoms velocity:

$$p(u_{\parallel}) = \frac{1}{\sqrt{\pi} v_{th}} \exp\left(-\frac{u_{\parallel}^2}{v_{th}^2}\right) \quad \text{with} \quad v_{th} = \sqrt{\frac{2k_B T}{m_p}}. \quad (2.29)$$

With the help of the dimensionless parameter x , the relative frequency shift, and b , the natural to Doppler line width ratio:

$$\begin{aligned} x &= \frac{\nu - \nu_0}{\Delta\nu_D} \quad \text{with} \quad \Delta\nu_D = \frac{v_{th}}{c} \nu_0, \\ b &= \frac{\Delta\nu_L}{2\Delta\nu_D}, \end{aligned} \quad (2.30)$$

we can express the optical depth increment in the fluid rest frame in a compact way :

$$d\tau = ds n_{\text{HI}} \frac{f_{12} \sqrt{\pi} e^2}{m_e c \Delta_D} H(b, x), \quad (2.31)$$

where H is the Voigt function defined as :

$$H(b, x) = \frac{b}{\pi} \int_{-\infty}^{+\infty} \frac{e^{-y^2}}{(x - y)^2 + b^2} dy. \quad (2.32)$$

2.3.2 Hubble Expansion

The Ly- α thermal line width is equivalent to the Hubble flow redshift over only a few 10 comoving kpc during the epoch of reionization. This scale is usually much smaller than the size of the cells in simulations, so we have to consider the full effect of expansion when computing the optical depth within a cell. We use the frequency in the local comoving frame as the reference frequency and include only peculiar velocities in Doppler shifts. Within a cell, the outgoing local comoving frequency ν_{out} at time t_{out} is given by the general formula :

$$\nu_{out} = \frac{a(\nu_{in})}{a(\nu_{out})} \nu_{in}, \quad (2.33)$$

where $a(t)$ is the expansion factor of the universe, ν_{in} is the incoming local frequency at time t_{in} . Between the incoming and outgoing comoving frequency in the cell, we interpolate linearly along the path in a cell. This formulation naturally account for the retarded time.

2.3.3 Scattering off atoms

The recoil effect has been shown to be negligible in most astrophysical situation by several authors Zheng & Miralda-Escudé (2002); Tasitsiomi (2006), etc. When the photon scatters off an atom, the frequency ν of the photon will change due to the various contributions to the atom velocity,

$$\nu_{atom} = \nu \left(1 - \frac{\mathbf{v}_{macro} + \mathbf{u}}{c} \cdot \mathbf{k}_i \right), \quad (2.34)$$

where \mathbf{u} is the thermal velocity of the atom, \mathbf{v}_m is the macroscopic velocity of the gas and \mathbf{k}_i is the direction of the incoming photon. Then we compute the direction of the photon after scattering. The change of the frequency due to the Hubble flow is already included through the Eq.(2.33).

2.3.4 Propagation

The grid for the propagation of photons is built in the same way as shown in Fig. 2.1. The density (RT cell density) and velocity (\mathbf{v}_m) fields are then interpolated from

the particle distribution to the RT cell.

We send individual photon packets from the source along a direction chosen at random. Then we follow them from scattering to scattering and from RT cell to RT cell, until they exit the simulation box or the frequency is redshifted to the red side of Ly- α . The photon emitted or scattered undergoes the following processes:

- Step 1 : Draw randomly the new photon direction.
- Step 2 : Compute the photon comoving frame frequency, either from the scattering atom rest frame frequency, or from the source spectrum.
- Step 3 : Draw a variable p from a uniform distribution between $[0,1]$. The photon will travel an optical depth $\tau = -\ln(p)$ to the next scattering event.
- Step 4 : Increment optical depth with the current cell contribution. Determine if scattering occurs in this cell. If yes go to step 5, if no, pass on to next cell and repeat step 4
- Step 5 : Draw scattering atom thermal velocity, and compute frequency in the scattering atom rest frame. Go back to step 1.

2.3.5 Acceleration scheme

A Ly- α photon which travels through the Universe average density at $z \sim 10$ faces an optical depth of $\tau \sim 10^6$ (Gunn & Peterson, 1965; Loeb & Rybicki, 1999). To compute $\sim 10^6$ scatterings for each photon is impossible because up to $\sim 10^9$ photon packets are used for a simulation. The usual method is the core-skipping scheme (Avery & House, 1968; Ahn et al., 2002). A photon entering the core of the line is systematically shifted out when it next scatters off a thermal atom. This scheme reduces the number of scatterings and CPU cost by several orders of magnitude while preserving the shape of the emerging spectrum.

However, when we do not need to compute the emerging spectrum but we need to know only where the scatterings occur, the acceleration scheme can be more drastic. For example, we are interested in P_α , the average number of scatterings per atom per second, for computing the 21cm emission. The photon propagates until the local comoving frequency is shifted within 10 thermal line widths of the line center, in the blue wing, at a location \mathbf{x}_0 . Then we consider that the $\sim 10^6$ scatterings that this photon is bound to undergo all occur at \mathbf{x}_0 . At 10 thermal linewidths off the center, the mean free path of the photons is less than 1 kpc and much shorter than 1 pc in the core of the line. We can neglect the spatial diffusion while the photon remains within the 10 linewidth frequency range.

2.3.6 Further improvements for future

Colored photon packet

Current version of LICORICE uses monochromatic photon packets, but this approach has several drawbacks due to the nature of Monte Carlo sampling. Photon packets with high frequency have long mean free paths so they propagate beyond the ionizing front. It results unphysical spikes and anisotropic ionization front. Using colored photon packets is a solution to overcome this effect.

If we consider only the photoionization of hydrogen, the method described in Susa & Umemura (2000) is very effective to deal with colored photon packet. The optical depth is rewritten in terms of the optical depth at Lyman limit, τ_{ν_L} ,

$$\tau_\nu = \tau_{\nu_L}(\nu_L/\nu)^3, \quad (2.35)$$

because the photoionization cross-section is $\sigma_\nu \simeq \sigma_{\nu_L}(\nu_L/\nu)^3$. The specific intensity, I_ν is expressed as,

$$I_\nu = I_\nu^{in} \exp[-\tau_\nu], \quad (2.36)$$

where I_ν^{in} is the initial value. We can write the photoionization rate, k_{HI}^{abs} , and the UV heating rate, Γ_{HI} in terms of an integration as,

$$\begin{aligned} k_{HI}^{abs} &= \int_{\nu_L}^{\infty} \frac{I_\nu}{h\nu} \sigma_\nu d\nu \\ \Gamma_{HI}^{abs} &= \int_{\nu_L}^{\infty} \frac{I_\nu}{h\nu} (h\sigma_\nu - h\sigma_{\nu_L}) d\nu. \end{aligned} \quad (2.37)$$

Therefore, if we tabulate two integrations in Eq. 2.37 as a function of the total value of the optical depth τ and use it during the photon packet propagation, we can easily compute k_{HI}^{abs} and Γ_{HI} without introducing a vector on photon packets.

However, this method can not be used to helium reionization, since the photoionization cross-section is more complicated, and we have to introduce a vector on photon packets as Maselli et al. (2009). In any case, Monte Carlo ray-tracing needs sufficient sampling of angle as well as frequency, so adapting the HEALPix algorithm (Górski et al., 2002) will be also helpful for further improvement of LICORICE.

Recombination radiation

The recombination radiation is important for the reionization scenario since it is related to the clumping factor and the effect of minihalos. LICORICE does not have recombination radiation yet to speed up the code and we use case B recombination rate to be consistent with this approximation. However, recombination rate can be

implemented straightforwardly in the Monte Carlo ray-tracing. It will be included to the code with other increasing efficiency and performance.

Higher Lyman series radiation

A photon redshifting into a higher Lyman series are absorbed immediately and re-emitted. Typically, a Lyn photon is rapidly cascaded down to the lower energy state. Thus coupling from the direct scattering of Lyn photons is unimportant relative to $Ly-\alpha$ photons (Pritchard & Furlanetto, 2006). However, the cascade process from Lyn photons can make $Ly-\alpha$ photons. (Pritchard & Furlanetto, 2006) found that the 1/3 of Lyn photons are cascade through $Ly-\alpha$.

Including radiative transfer of higher Lyn series to LICORICE is not complicated. We can adjust them without losing much computing time and efficiency. Higher Lyman series radiation will be included in near future to LICORICE.

2.4 Radiative Transfer Comparison Test

With increasing computational power, we now are able to deal with many astrophysical and cosmological radiative transfer problems. A cosmological radiative transfer code comparison project is proposed by Iliev et al. (2006). The aim of this project is to understand which algorithms (including various flavours of ray-tracing and moment schemes) are suitable for a given non-trivial problem as well as to validate each code by comparing the results with other codes. Currently 13 independent RT codes are participating in this project and 8 test problems have been done. The first 5 tests are for radiative transfer in a static density field, and results are published in Iliev et al. (2006). 3 additional tests are for the coupled gas dynamical and radiative transfer evolution, (Iliev et al., submitted). LICORICE shows good agreement with the results of several tests appearing in the comparison project I, and we are also participating in the second project.

2.4.1 Static density field cases

A. Isothermal HII region expansion

This test is the classical problem of an H II region expansion in a uniform gas around a single ionizing source (Strömberg, 1939; Spitzer, 1978). A steady, monochromatic ($h\nu = 13.6$ eV) source emits \dot{N}_γ ionizing photons per unit time which propagate through an initially neutral gas, with uniform density and hydrogen number density n_H .

For this test, the temperature is fixed at $T = 10^4$ K. Under this condition, if we assume that the ionization front is sharp, there is a well-known analytical solution for the evolution of the I-front radius, r_I , given by

$$r_I(t) = r_s [1 - \exp(-t/t_{rec})]^{1/3}, \quad (2.38)$$

where

$$r_s = \left[\frac{3\dot{N}_\gamma}{4\pi\alpha_B(T)^2} \right]^{1/3}, \quad (2.39)$$

where α_B is the case B recombination coefficient (see Appendix) and

$$t_{rec} = [\alpha_B(T)n_H]^{-1}, \quad (2.40)$$

is the definition of the recombination time. The H II region initially expands quickly and then slows considerably as the evolution time approaches the recombination time $t \sim t_{rec}$. After a few recombination times, the I-front stops at a radius $r_I = r_s$ and in absence of gas motions remains static thereafter.

Initial conditions : The numerical parameters used in the test are:

- Box dimension : $L = 6.6$ kpc
- Gas number density : $n_H = 10^{-3} \text{ cm}^{-3}$
- Initial ionization fraction (given by collisional equilibrium) : $x = 1.2 \times 10^{-3}$
- Ionizing photon production rates: $\dot{N}_\gamma = 5 \times 10^{48} \text{ photons } s^{-1}$
- Monochromatic frequency : $h\nu = 13.6 \text{ eV}$
- Position of the source : center of the box
- Recombination time $t_{rec} = 3.86 \times 10^{15} s = 122.4 \text{ Myr}$
- Temperature : $T = 10^4 \text{ K}$
- Analytic radius Strömgen : $r_s = 5.4 \text{ kpc}$
- Simulation time : $t_{sim} = 500 \text{ Myr} \approx 4t_{rec}$
- I-front position is defined by a 50 % neutral fraction .

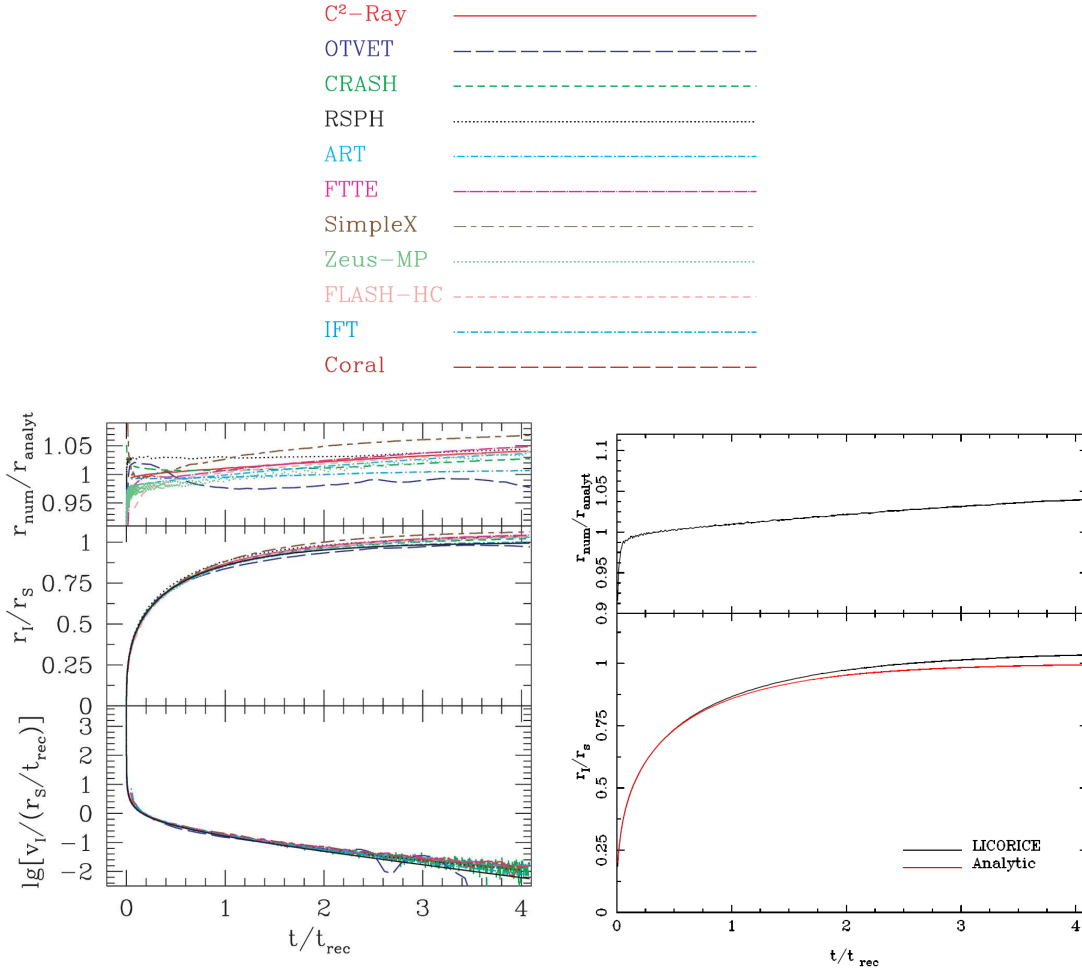


Figure 2.4: The line plots used in Iliev et al. (2006a) (top). [HII expansion in a uniform gas at fixed temperature] The evolution of the position and velocity of the I-front (left). The evolution of the I-front position for LICORICE (right).

Results In Fig. 2.4, we show the evolution of the I-front position with respect to the analytical solution. The maximum excess rate of r_{num}/r_{analyt} is less than 5% throughout the simulation time. All other codes compared in Iliev et al. (2006a) in Fig. 2.4 never varied by more than 5% from the analytical solution. Considering that the 11 other codes in Iliev et al. (2006a) have 128^3 grid resolution, LICORICE used 128^3 particles, uniformly distributed in the simulation box. We placed the source at the center of the box size $2L = 13.3$ kpc and we set the $N_{max} = 8$ (8 particles in a RT cell) which results in the effective RT grid resolution of 64^3 for one quadrant. LICORICE shows very satisfactory results with only 1/4 at the linear spatial resolution of other codes.

B. H II region expansion with evolving temperature

This test solves essentially the same problem as the previous one, but the ionizing source is now assumed to have a 10^5 K black-body spectrum and the gas temperature varies due to heating and cooling processes. Contrary to the previous test, disagreements appear among the different codes compared in Iliev et al. (2006a) in this multi-frequency approach and an analytic solution does not exist.

Initial condition and result

The test geometry and gas density are the same as in the previous test. The ionizing source has a 10^5 K black-body spectrum and the gas is initially fully neutral and has a temperature of $T = 100$ K. The global evolution of the I-front is presented in Fig. 2.5. Even if there exists no analytical solution, we compared the I-front position with the analytical solution of the previous test. LICORICE shows good agreement with other codes. The numerical I-front is slower than analytic solution of the homogeneous temperature case until $t \approx t_{rec}$. This is to be expected due to the initial temperature of $T = 100$ K and the inverse temperature dependence of the recombination coefficient. The gas at $T = 100$ K consumes more photons than at $T = 10^4$ K. However, the numerical I-front starts to catch up with the analytical solution around $t \approx t_{rec}$ and then the difference becomes ever larger. This is also due to the temperature of the ionized bubble being higher than $T = 10^4$ K, which consumes less photons because of a lower recombination rate.

In Fig. 2.6 we show the spherically-averaged radial profiles of the neutral ($1 - x$) and ionized fraction (x) during the slowing-down phase at $t = 100$ Myr. All codes do not show perfect agreement, but LICORICE gives results similar to CRASH, RSPH, ART and C^2 -Ray, which are based on a ray-tracing method.

The corresponding spherically-averaged radial temperature profiles at $t \approx t_{rec}$ is shown in Fig. 2.7. LICORICE agrees well with CRASH, ART and RSPH in the spectral hardening region ahead of I-front, where the gas is preheated due to hard photons.

C. I-front trapping

This test examines the propagation of a plane-parallel I-front and its trapping by a dense, uniform, and spherical clump. Clumping is known to have a significant effect on the penetration and escape of radiation from an inhomogeneous medium (Boisse, 1990). The inclusion of clumpiness introduces several parameters into the calculation, such as the overdensity of the clumps, and the spatial correlation between the clumps and the ionizing sources. Therefore succeeding at this clumping test is required for all codes which will simulate the epoch of reionization.

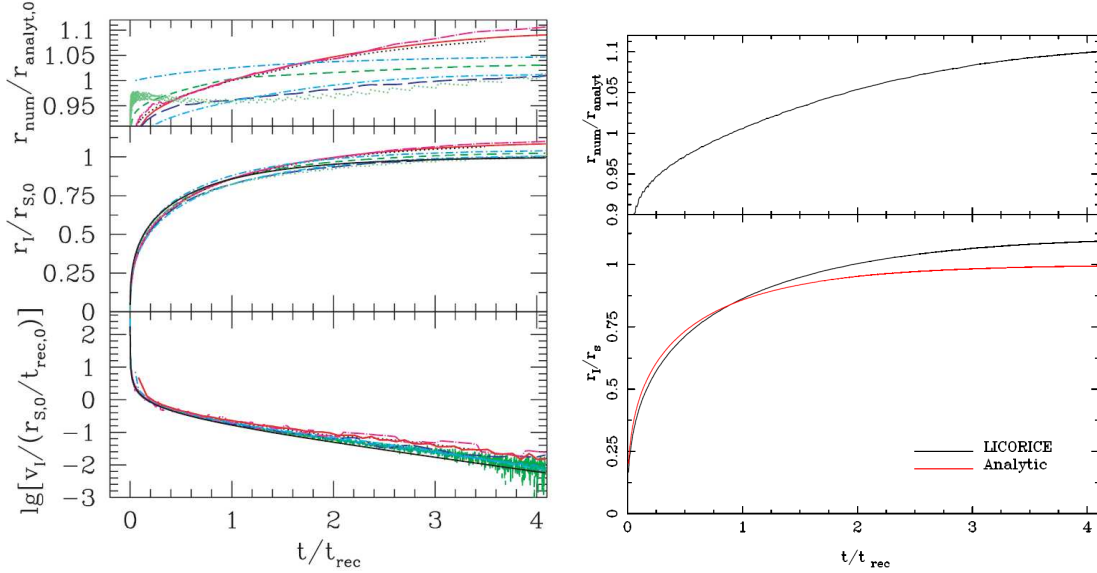


Figure 2.5: [H II region expansion in a uniform gas with varying temperature] The evolution of position and velocity of I-front(left). The evolution of the I-front position of LICORICE(right).

From the numerical point of view, we are especially interested in this test because it deals with an over-dense region which puts the adaptive grid to the rest. We distribute more particles inside the clump instead of attributing more massive particles to this region. Therefore we construct more RT cells and can have a high resolution with only 40% of the number of particles used in Iliev et al. (2006a).

Initial conditions A constant ionizing photon flux hits the $y = 0$ side of the simulation box and the center of the clump is located at $(x_c, y_c, z_c) = (5, 3.3, 3.3)$ kpc of the $(6.6\text{kpc})^3$ box as shown in Fig 2.8. The density and temperature of the clump and background are chosen so that they are in pressure equilibrium. Knowing that the Strömgen radius r_s is obtained from

$$F = \int_0^{r_s} dl n_e n_H \alpha_\beta(T) , \quad (2.41)$$

for a uniform-density clump the above equation reduces to

$$l_s = \frac{F}{\alpha_H n_H^2} , \quad (2.42)$$

where F is the flux of ionizing photons. Let us define the Strömgen length $l_s(r)$ at impact parameter (Strömgen radius) r from the clump center using Eq.(2.41). We then can define the Strömgen number for the clump as $L \equiv 2r_{clump}/l_s$, where r_{clump}

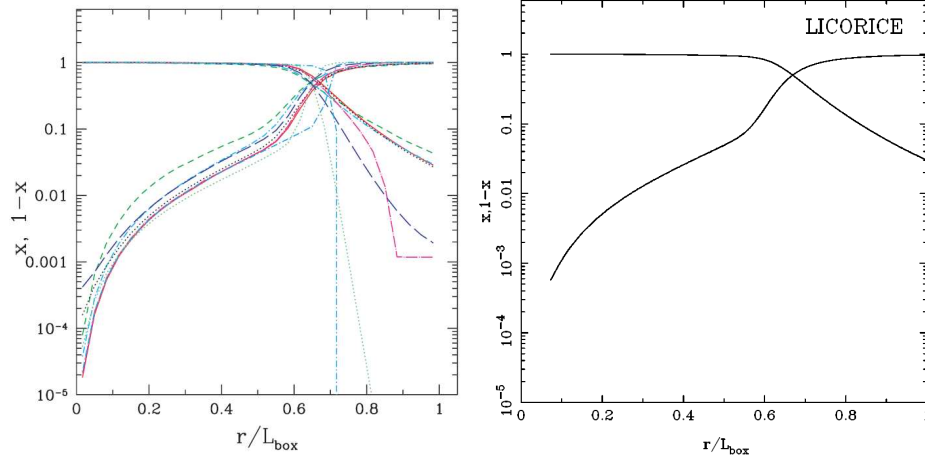


Figure 2.6: [H II region expansion in an uniform gas with varying temperature] : Spherically-averaged ionized fraction x and neutral fraction $1 - x$ profiles at time $t = 100$ Myr.

is the clump radius and $l(0)$ is the Stromgren length at zero impact parameter r . If $L_s > 1$ the clump is able to trap the I-front, while if $L_s < 1$, the clump is unable to trap. We obtain $l_s \approx 0.78(T/10^4)^{3/4}$ kpc, and $L_s \approx 2.05(T/10^4)^{3/4}$; thus along the axis of symmetry the I-front should be trapped approximately at the center of the clump for $T = 10^4$ K.

The numerical parameters for this test are :

- Spectrum : black-body radiation with effective temperature $T_{eff} = 10^5$ K
- Constant ionizing photon flux : $F = 10^6 \text{ s}^{-1} \text{ cm}^{-2}$
- Hydrogen number density of the background: $n_{out} = 2 \times 10^{-4} \text{ cm}^{-3}$
- Initial temperature of the background : $T_{out,init} = 8000$ K
- Initial temperature of inside the clump : $T_{in,init} = 40$ K
- n_{H} inside the clump : $n_{clump} = 200 n_{out} = 0.04 \text{ cm}^{-3}$
- Box size : $L = 6.6$ kpc
- Radius of the clump : $r_{clump} = 0.8$ kpc
- Center of the clump : $(x_c, y_c, z_c) = (5, 3.3, 3.3)$ kpc
- Evolution time : 15 Myr

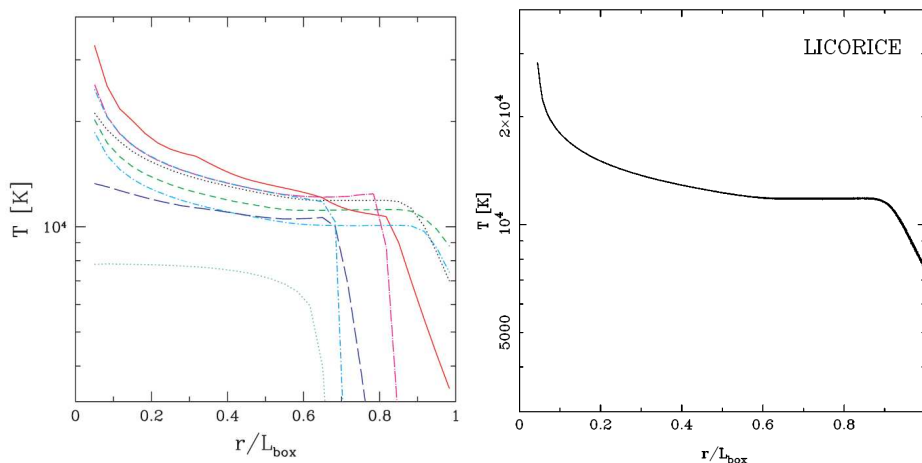


Figure 2.7: [H II region expansion in an uniform gas with varying temperature] : Spherically-averaged ionized temperature profiles at time $t = 100$ Myr.

Results In Fig. 2.9 we show the ionized and neutral fraction profiles along the axis of symmetry during the slow-down due to recombination at $t = 3$ Myr, about one recombination time in the clump. Only the region inside and around the clump is plotted in order to show details. There are some differences in the position of the I-front and the neutral fraction profiles behind the I-front among the codes, but LICORICE shows results close to CRASH, C^2 -Ray and Coral. In the pre-ionization region, LICORICE has a little bit higher ionization fraction, similar to RSPH. The reason for this can be seen in the corresponding temperature profiles (Fig. 2.10). LICORICE obtains a slightly higher temperature in pre-ionization region, resulting in a lower recombination rate. The temperatures in the post-front region of the clump otherwise agree quite well.

As we expect from the $L_s > 1$ value in Eq.(2.42), the clump traps the I-front at the end of simulation ($t = 15$ Myr). (see Fig. 2.11) The I-front position and ionization fraction in pre-ionized region are quite similar to the results of the other codes.

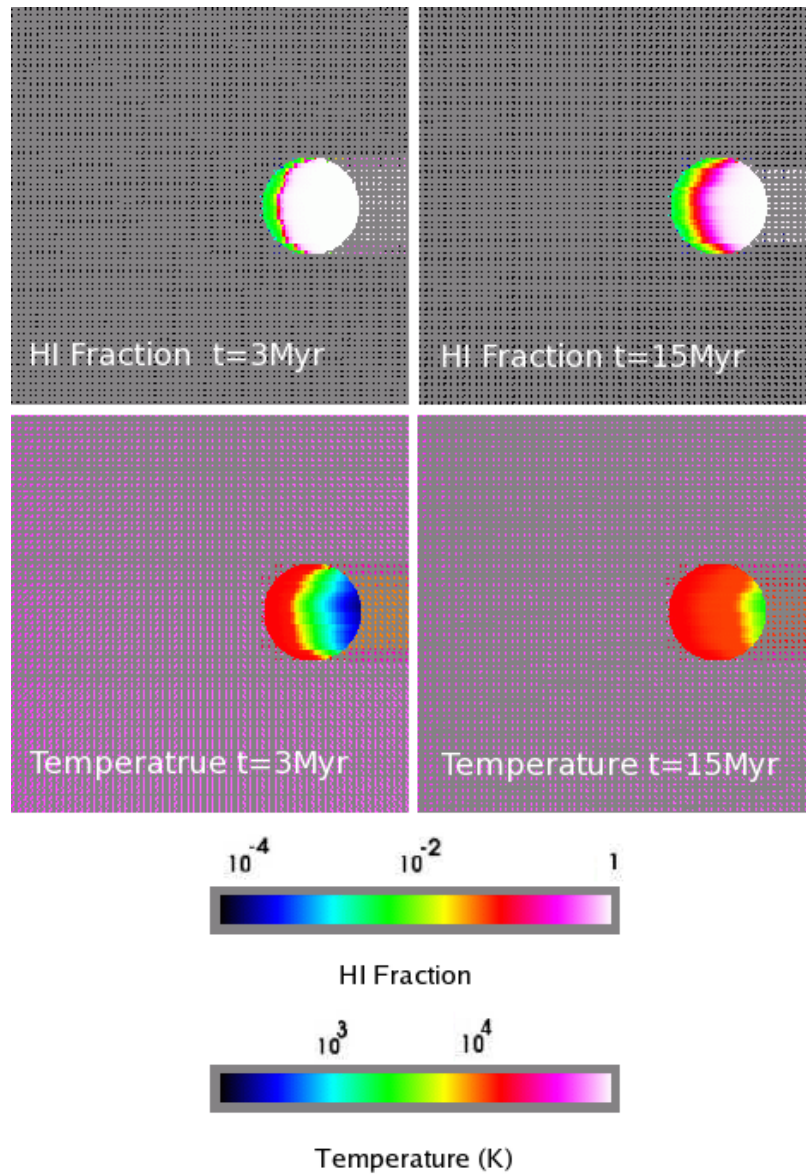


Figure 2.8: Image of HI fraction and temperature cut through the simulation volume at midplane at time $t = 1 \text{ Myr}$ and $t = 15 \text{ Myr}$.

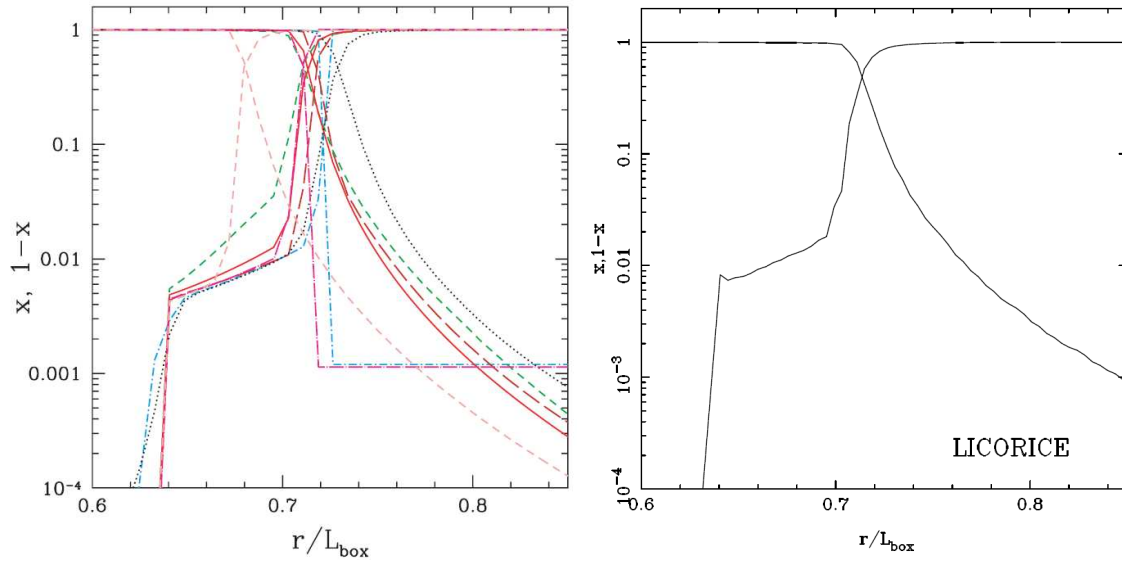


Figure 2.9: [I-front trapping in dense clump] : Line cuts of the ionized and neutral fraction along the axis of symmetry through the center of the clump at times $t = 3$ Myr.

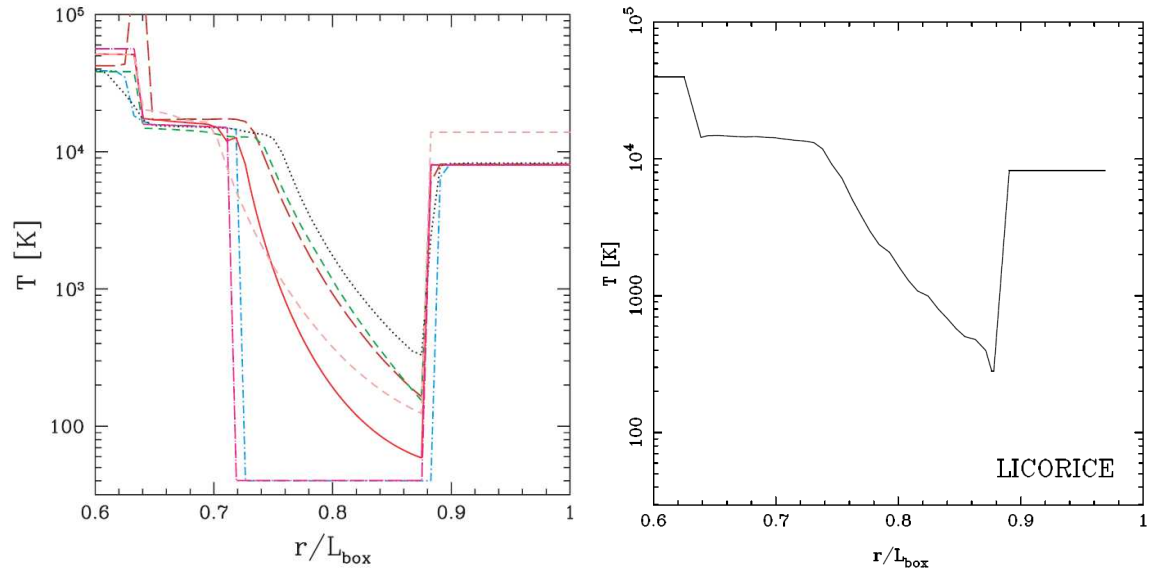


Figure 2.10: [I-front trapping in dense clump] : Line cuts of the temperature along the axis of symmetry through the center of the clump at times $t = 3$ Myr.

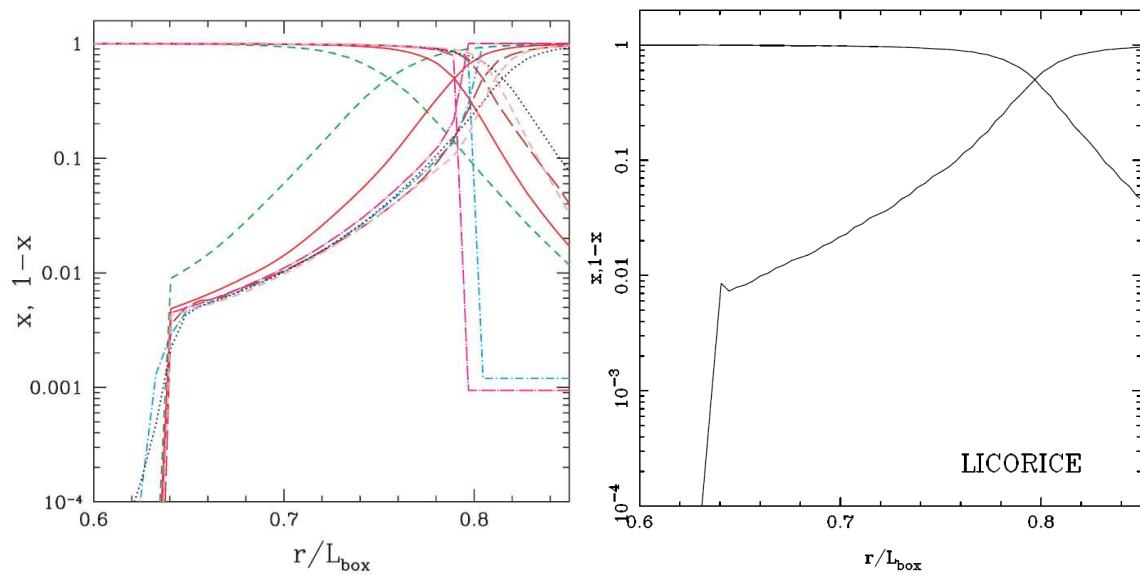


Figure 2.11: [I-front trapping in dense clump] : Line cuts of the ionized and neutral fraction along the axis of symmetry through the center of the clump at times $t = 15$ Myr.

2.4.2 Radiative-hydrodynamics cases

The next three tests deal with the radiative transfer coupled with hydrodynamics. Such dynamics with radiative feedback is very complex and there is no approximate analytic solution to validate the codes. An alternative validation procedure is to compare different numerical methods on common problems. The Cosmological Radiative Transfer Code Comparison Project II compares 10 independent RT codes on these problems. LICORICE participates in this project. We present a brief result of this comparison test here.

The first radiative-hydrodynamic test (**Test 5**) is the classical problem of expansion of HII region in an initially-uniform gas. 8 different codes (Capreole+ C^2 -ray, HART, RSPH, ZEUS-MP, RH1D, LICORICE, Flash-HC and Enzo) are used in this test, and all the codes show good agreement. The main differences originate from the different handling of the energy equation and the hard photons with long mean free paths. LICORICE, using frequency sampling, finds a larger pre-heated region than several other codes. An effective pre-heating makes a weaker shock leading the I-front, and a lower number density which results in faster moving I-front. The codes using multifrequency show a double-peaked feature in the radially averaged profile of the density and Mach number. This is due to the preheating of the dense shocked neutral gas by hard photons. It shows that multifrequency photon transport is necessary to capture the correct structure of I-front and shocks.

The second radiative-hydrodynamic test (**Test 6**) is the propagation of an I-front created by a point source at the center of a spherically-symmetric, steeply-decreasing power law density profile($1/r^2$) with a small flat central core. The $1/r^2$ density profile approximates those of galactic molecular cloud cores or cosmological minihalos at high redshift. 8 codes (Capreole+ C^2 -ray, TVD+ C^2 -ray, HART, RSPH, ZEUS-MP, RH1D, LICORICE, Flash-HC) participate in this test, and show agreement in terms of the position of the I-front and the shock, the HII size, density and temperature. However, some instabilities occur for several codes. LICORICE shows visible instabilities in the ionized fractions, temperatures, densities, and Mach numbers. It seems that these instabilities are numerical, due to both the SPH method and the corner effects of the Cartesian grid. LICORICE's irregular morphology of the shell is due to spurious fluctuations in the density field, where the local particle number changes sharply. This is a well-known feature of SPH. A grainy structure of the Mach number shown in Test 5 also originate from the properties of the SPH method, because of the low resolution in the evacuated interior of the H II regions.

The third radiative-hydrodynamic test (**Test 7**) is for the photoevaporating dense clump. A plane-parallel I-front encounters a uniform spherical clump in a constant background density field. As the heated and ionized gas is evaporated and expands to-

wards the gas, the trapped I-front slowly consumes the clump until it photoevaporates completely. 6 codes (Capreole+ C^2 -ray, RSPH, ZEUS-MP, LICORICE, Flach-HC and Coral) participate in this test and show good agreement both on the I-front position and its profile. The treatment of the energy equation and the hard photons create differences between the codes, but the differences remain small. The temperature profiles agree well but the amplitude varies by up to 50%. This large variation does not affect later-time evolution however. Mach numbers show similar trends, with growing differences during the evolution, but does not affect largely the later-time evolution.

Cosmological Radiative Transfer Codes Comparison Project II: The Radiation-Hydrodynamic Tests

Ilian T. Iliev^{1,2,3*}, Daniel Whalen⁴, Kyungjin Ahn^{5,6}, Sunghye Baek⁷, Nickolay Y. Gnedin⁸, Andrey V. Kravtsov⁹, Garrelt Mellema¹⁰, Michael Norman¹¹, Milan Raicevic¹², Daniel R. Reynolds¹³, Daisuke Sato¹⁴, Paul R. Shapiro⁶, Benoit Semelin⁷, Joseph Smidt¹⁵, Hajime Susa¹⁶, Tom Theuns^{12,17}, Masayuki Umemura¹⁴

¹ Astronomy Centre, Department of Physics & Astronomy, Pevensey II Building, University of Sussex, Falmer, Brighton BN1 9QH, United Kingdom

² Universität Zürich, Institut für Theoretische Physik, Winterthurerstrasse 190, CH-8057 Zürich, Switzerland

³ Canadian Institute for Theoretical Astrophysics, University of Toronto, 60 St. George Street, Toronto, ON M5S 3H8, Canada

⁴ T-2 Nuclear and Particle Physics, Astrophysics, and Cosmology, Los Alamos National Laboratory, Los Alamos, NM 87545, U.S.A.

⁵ Department of Earth Science Education, Chosun University, Gwangju 501-759, Korea

⁶ Department of Astronomy, University of Texas, Austin, TX 78712-1083, U.S.A.

⁷ LERMA, Observatoire de Paris, 77 av Denfert Rochereau, 75014 Paris, France

⁸ Fermilab, MS209, P.O. 500, Batavia, IL 60510, U.S.A.

⁹ Dept. of Astronomy and Astrophysics, Center for Cosmological Physics, The University of Chicago, Chicago, IL 60637, U.S.A.

¹⁰ Stockholm Observatory, AlbaNova University Center, Stockholm University, SE-106 91 Stockholm, Sweden

¹¹ Center for Astrophysics and Space Sciences, University of California, San Diego, 9500 Gilman Drive, La Jolla, CA 92093-0424, U.S.A.

¹² Institute for Computational Cosmology, Durham University, Durham, United Kingdom

¹³ Department of Mathematics, 208 Clements Hall, Southern Methodist University, Dallas, TX 75275, USA

¹⁴ Center for Computational Sciences, University of Tsukuba, Tsukuba, Ibaraki 305-8577, Japan

¹⁵ Department of Physics and Astronomy, 4129 Frederick Reines Hall, UC Irvine, Irvine, CA 84602, U.S.A.

¹⁶ Department of Physics, Konan University, Kobe, Japan

¹⁷ Department of Physics, University of Antwerp, Campus Groenenborger, Groenenborgerlaan B-171, B2020 Antwerp, Belgium

6 May 2009

ABSTRACT

The development of radiation hydrodynamical methods that are able to follow gas dynamics and radiative transfer self-consistently is key to the solution of many problems in numerical astrophysics. Such fluid flows are highly complex, rarely allowing even for approximate analytical solutions against which numerical codes can be tested. An alternative validation procedure is to compare different methods against each other on common problems, in order to assess the robustness of the results and establish a range of validity for the methods. Previously, we presented such a comparison for a set of pure radiative transfer tests (i.e. for fixed, non-evolving density fields). This is the second paper of the Cosmological Radiative Transfer (RT) Code Comparison Project, in which we compare 9 independent RT codes directly coupled to gasdynamics on 3 relatively simple astrophysical hydrodynamics problems: (5) the expansion of an H II region in a uniform medium; (6) an ionization front (I-front) in a $1/r^2$ density profile with a flat core, and (7), the photoevaporation of a uniform dense clump. Results show a broad agreement between the different methods and no big failures, indicating that the participating codes has reached a certain level of maturity and reliability. However, many details still do differ virtually every code has showed some shortcomings and has disagreed, in one respect or another, with the majority of the results. This underscores the fact that no method is universal and all require careful testing of the particular features which are most relevant to the specific problem at hand.

Key words: H II regions—ISM: bubbles—ISM: galaxies: halos—galaxies: high-redshift—galaxies: formation—intergalactic medium—cosmology: theory—radiative transfer— methods: numerical

1 INTRODUCTION

The transfer of ionizing radiation through optically-thick media is a key process in many astrophysical phenomena. Some examples in-

* e-mail: I.T.Iliev@sussex.ac.uk

2 *I. T. Iliev, et al.*

clude cosmological reionization (*e.g.* Gnedin 2000; Nakamoto et al. 2001; Razoumov et al. 2002; Sokasian et al. 2003; Ciardi et al. 2003; Iliev et al. 2006b; Kohler et al. 2007), star formation (*e.g.* Hosokawa & Inutsuka 2005; Iliev et al. 2006a; Razoumov et al. 2006; Susa & Umemura 2006; Ahn & Shapiro 2007; Whalen & Norman 2008b), radiative feedback in molecular clouds (Mellema et al. 2006a; Mac Low et al. 2007; Krumholz et al. 2007), and planetary nebulae (*e.g.* Mellema et al. 1998; Lim & Mellema 2003). In some of these problems, fast, R-type I-fronts predominate. Those fronts propagate faster than the hydrodynamic response of the gas, so gas motions do not affect the I-front evolution. In these cases the radiative transfer could be done on a fixed density field (or a succession of such fields), and dynamic coupling to the gas dynamics is generally not required. However, the majority of astrophysical and cosmological applications involve slow, D-type I-fronts (or a combination of R-type and D-type, as we describe in detail in section 3.1), so the radiative transfer and gasdynamics should be directly coupled and evolved simultaneously. Until recently self-consistent radiation hydrodynamical codes for radiative transport have been rare, but this unsatisfactory situation is now rapidly changing due to the development of a number of such codes using a variety of numerical approaches.

A number of radiative transfer methods have been developed in recent years, both stand-alone and coupled to hydrodynamics. High computational costs necessitate the usage of various approximations. Thus, it is of prime importance to validate the numerical methods developed and to evaluate their reliability and accuracy. However, there are relatively few simple tests with either exact or good approximate analytical solutions, which would be the first choice for code testing. An alternative approach is a comparison of the different methods on a set of well-defined problems in more realistic settings. This is the approach we have taken in this project.

Our aim is to determine the type of problems the codes are (un)able to solve, to understand the origin of any differences inevitably found in the results, to stimulate improvements and further developments of the existing codes and, finally, to serve as a benchmark for testing future algorithms. All test descriptions, parameters, and results can be found at the project website:

<http://www.cita.utoronto.ca/~iliev/rtwiki/doku.php>.

The first paper of this comparison project discussed the results from fixed density field tests (Iliev & et al. 2006, hereafter Paper I), *i.e.* without any gas evolution. We found that all participating codes are able to track I-fronts quite well, within $\sim 10\%$ of each other. Some important differences also emerged, especially in the derived temperatures and spectral hardening. We found that some of these differences were due to variations in microphysics (chemical reaction rates, heating/cooling rates and photoionization cross-sections), while others were due to the method itself, *e.g.* how the energy equation is solved, how many frequency bins are used for the spectral evolution, etc. We concluded that the tested radiative transfer methods are producing reliable results overall, but that not all methods are equally appropriate for any given problem, especially in cases when obtaining precise temperatures and spectral features is important.

We now extend our previous work by considering a set of radiation hydrodynamical tests. In the spirit of Paper I, we have chosen a set of test problems which are relatively simple, so as to be most inclusive given the current limitations of the available codes (*e.g.* 1-D or 2-D vs. 3-D codes). At the same time, our tests consider problems of astrophysical importance, and cover a sufficiently wide variety of situations to sufficiently thoroughly test the attributes of

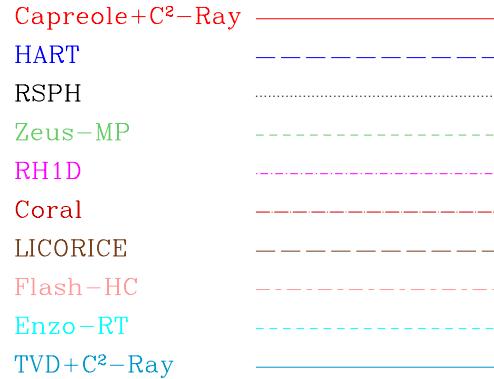


Figure 1. Legend for the line plots.

each method, including its radiative and hydrodynamic components and their coupling.

The efficiency, optimization and performance of the codes are very important, especially for the most complex and computationally-intensive problems. However, there are a number of complications, which we discussed in Paper I, preventing us from doing such testing in a meaningful way at present. We therefore leave it for future work.

All test results in this paper are required on a regular grid of 128^3 computational cells. This relatively modest resolution was chosen in the interests of inclusivity, so that even codes which are not yet fully optimized in terms of either computations or memory can participate in the comparison. We note that production runs at present are typically run at 256^3 or better resolution. Codes which utilize AMR grids or particles have been requested to run the problem at resolution which approximates as closely as possible the fixed-grid one for fair comparison. Their results have then been interpolated on a regular grid for submission.

2 THE CODES

In this section we briefly describe the nine radiative transfer codes participating in this stage of the comparison project, with references to more detailed method papers if available. Details of the codes and their basic features and methods are summarized in Table 1. Figure 1 provides a legend allowing the reader to identify which line corresponds to which code in the figures throughout the paper. The images we present are identified in the corresponding figure caption.

2.1 Capreole+C²-Ray (G. Mellema, I. Iliev, P. Shapiro, M. Alvarez)

C²-Ray Mellema et al. (2006b) is a grid-based short characteristics (*e.g.* Raga et al. 1999) ray-tracing code which is photon-conserving and causally traces the rays away from the ionizing sources up to each cell. Explicit photon-conservation is assured by taking a finite-volume approach when calculating the photoionization rates, and by using time-averaged optical depths. The latter property allows for integration time steps much larger than the ionization time scale, which results in a considerable speed-up of the calculation

Cosmological Radiative Transfer Codes Comparison II 3

Table 1. Participating codes and their current features.

Code	Grid	Parallelization	hydro method	rad. transfer method
Capreole+C ² -Ray	fixed	shared/distributed	Eulerian, Riemann solver	short-characteristics ray-tracing
TVD+C ² -Ray	fixed	shared/distributed	Eulerian, TVD solver	short-characteristics ray-tracing
HART	AMR	shared/distributed	Eulerian, Riemann solver	Eddington tensor moment
RSPH	particle-based	distributed	SPH	long-characteristics ray-tracing
ZEUS-MP	fixed	distributed	Eulerian	3-D ray-tracing
RHID	sph. Lagrangian	no	Lagrangian	1-D ray-tracing
Coral	AMR	no	Eulerian, flux-vector splitting	short-characteristics ray tracing
LICORICE	AMR	shared	SPH	Monte-Carlo ray-tracing
Flash-HC	AMR	distributed	Eulerian, PPM	Hybrid characteristics ray-tracing
Enzo-RHD	fixed	distributed	Eulerian, PPM	Flux-limited diffusion

and facilitates the coupling of the code to gasdynamic evolution. The code and the various tests performed during its development are described in detail in Mellema et al. (2006b).

The frequency dependence of the photoionization rates and photoionization heating rates are dealt with by using frequency-integrated rates, stored as functions of the optical depth at the ionization threshold. In its current version the code includes only hydrogen and does not include the effects of helium, although they could be added in a relatively straightforward way.

The transfer calculation is done using short characteristics, where the optical depth is calculated by interpolating values of grid cells lying along the line-of-sight towards the source. Because of the causal nature of the ray-tracing, the calculation cannot easily be parallelized through domain decomposition. However, using OpenMP and MPI the code is efficiently parallelized over the sources and grid octants (Iliev et al. 2008b). The code has been applied for large-scale simulations of cosmic reionization and its observability (Iliev et al. 2006b; Mellema et al. 2006c; Iliev et al. 2007a,b; Holder et al. 2007; Doré et al. 2007; Iliev et al. 2008a) on grid sizes up to 406^3 and up to $\sim 10^6$ ionizing sources, running on up to 10,240 computing cores.

There are 1D, 2D and 3D versions of the code available. It was developed to be directly coupled with hydrodynamics calculations. The large time steps allowed for the radiative transfer enable the use of the hydrodynamic time step for evolving the combined system. The C²-Ray radiative transfer and nonequilibrium chemistry code has been coupled to several different gasdynamics codes, utilizing both fixed and adaptive grids. The tests in this project were mostly performed with the version coupled to the Riemann solver based hydrodynamics code Capreole developed by Garrelt Mellema. The first gasdynamic application of our code is presented in Mellema et al. (2006a). Additionally, one of the tests has also been run with C²-Ray coupled to a different hydro solver, namely the TVD method of Trac and Pen (Trac & Pen 2004) (see Test 6 below).

2.2 Hydrodynamic Adaptive Refinement Tree (HART) (N. Gnedin, A. Kravtsov)

The Hydrodynamic Adaptive Refinement Tree (HART) code is an implementation of the Adaptive Mesh Refinement (AMR) technique and uses a combination of multi-level particle-mesh and shock-capturing Eulerian methods for simulating the evolution of the dark matter particles and gas, respectively. High dynamic range

is achieved by applying adaptive mesh refinement to both gas dynamics and gravity calculations.

The code performs refinements locally on individual cells, and cells are organized in refinement trees (Khokhlov 1998). The data structure is designed both to reduce the memory overhead for maintaining a tree and to fully eliminate the neighbor search required for finite-difference operations. All operations, including tree modifications and adaptive mesh refinement, can be performed in parallel. The advantage of the tree-based AMR is its ability to control the computational mesh on the level of individual cells. This results in a very efficient and flexible (and thus highly adaptive) refinement mesh which can be easily built and modified and, therefore, effectively match the complex geometry of cosmologically interesting regions: filaments, sheets, and clumps. Several refinement criteria can be combined with different weights allowing for a flexible refinement strategy that can be tuned to the needs of each particular simulation. The adaptive refinement in space is accompanied by a temporal refinement (smaller time steps on meshes of higher resolutions).

The ART code was initially developed by A. Kravtsov in collaboration with A. A. Klypin and A. M. Khokhlov (Kravtsov et al. 1997; Kravtsov 1999; Kravtsov et al. 2002). N. Gnedin joined the HART code development team in the spring of 2003 and has adopted the OTVET algorithm for modeling 3D radiative transfer for the ART mesh structure and implemented a non-equilibrium chemical network and cooling (e.g. Gnedin et al. 2008).

2.3 RSPH (H. Susa, M. Umemura, D. Sato)

The Radiation-SPH (RSPH) scheme is specifically designed to investigate the formation and evolution of first-generation objects at $z \gtrsim 10$, where the radiative feedback from various sources plays important roles. The code can compute the fraction of chemical species e^- , H^+ , H , H^- , H_2 , and H_2^+ by fully implicit time integration. It also can deal with multiple sources of ionizing radiation, as well as with Lyman-Werner band photons.

Hydrodynamics is calculated by the smoothed particle hydrodynamics (SPH) method. It uses the version of SPH by Umemura (1993) with the modification according to Steinmetz & Mueller (1993), and adopts the particle resizing formalism by Thacker et al. (2000). In the present version, it does not use the so-called entropy formalism (Springel & Hernquist 2002). The non-equilibrium chemistry and radiative cooling for primordial gas are calculated using the code developed by Susa & Kitayama (2000), where H_2

4 *I. T. Iliev, et al.*

cooling and reaction rates are mostly taken from Galli & Palla (1998a).

As for the photoionization process, the on-the-spot approximation is employed (Spitzer 1978), meaning that the transfer of ionizing photons directly from the source is solved, but diffuse photons are not transported. Instead, it is assumed that recombination photons are absorbed in the same zone from which they are emitted. Due to the absence of the source term in this approximation, the radiation transfer equation becomes very simple. Solving the transfer equation reduces to the easier problem of assessing the optical depth from the source to every SPH particle.

The optical depth is integrated utilizing the neighbour lists of SPH particles. It is similar to the code described in Susa & Umemura (2004), but can now also deal with multiple point sources. In the new scheme fewer grid points are created on the light ray than in its predecessor. Instead, just one grid point per SPH particle is created in particle's neighborhood. The 'upstream' particle for each SPH particle on its line of sight to the source is then found. Then the optical depth from the source to the SPH particle is obtained by summing up the optical depth at the 'upstream' particle and the differential optical depth between the two particles.

The code is parallelized with the MPI library. The computational domain is divided by the Orthogonal Recursive Bisection method. The parallelization method for radiation transfer is similar to the Multiple Wave Front method developed by Nakamoto et al. (2001) and Heinemann et al. (2006), but it is adapted to fit the SPH code. The details are described in Susa (2006).

The code computes self-gravity using Barnes-Hut tree, which is parallelized as well. A Tree-GRAPe version of the code has also been developed. This code has been applied to radiative feedback in primordial star formation (Susa & Umemura 2006; Susa 2007; Hasegawa et al. 2009), as well as the regulation of star formation in forming galaxies by ultraviolet background (Susa 2008).

2.4 ZEUS-MP (D. Whalen, J. Smidt, M. Norman)

The ZEUS-MP code applied to this suite of radiation hydrodynamical benchmarks solves explicit finite-difference approximations to Euler's equations of fluid dynamics along with a 9-species reaction network with H, H⁺, He, He⁺, He⁺⁺, H⁻, H₂, H₂⁺ and e) and photoionization rate coefficients obtained from ray-tracing radiative transfer. The algorithm has been described elsewhere (Whalen & Norman 2006; Iliev & et al. 2006); here only the multifrequency upgrades to the radiative transfer and the three dimensional parallelization scheme for implementing these tests are detailed (Whalen & Norman 2008a).

The ZEUS-MPRT module evaluates radiative rate coefficients by solving the static equation of transfer in flux form. The number of absorptions in a zone per second is calculated in a photon-conserving manner to be the number of photons entering the zone minus the number exiting the zone per second. The number of photons absorbed per second in a zone by all processes at a particular frequency ν is proportional to

$$N_{abs} \propto \dot{n}_\nu (1 - e^{-\tau}), \quad (1)$$

where

$$\tau = \sum_{i=1}^n \sigma_i n_i \Delta r, \quad (2)$$

the total optical depth of the cell and \dot{n}_ν is the emission rate of photons at frequency ν determined from a total source emission

rate \dot{n} and a spectrum from, e.g., equation 6 of Whalen & Norman (2008b). In equation 2, n_i is the number density of the species absorbing the photon in the reaction, σ_i is the interaction cross section of the reaction, Δr is the zone length in the direction of propagation, and the summation is over all absorption processes that can occur at frequency ν .

On the other hand, the number of absorptions N_i per second due to a particular reaction is proportional to

$$N_i \propto \dot{n}_\nu (1 - e^{-\tau_i}), \quad (3)$$

where $\tau_i = n_i \sigma_i \Delta r$ is that associated with the reaction. As such, the sum of the N_i is inconsistent with N_{abs} , but the two can be reconciled by requiring that

$$N_i = \frac{1 - e^{-\tau_i}}{\sum_{i=1}^n 1 - e^{-\tau_i}} N_{abs}. \quad (4)$$

This formulation guarantees that the N_i sum to N_{abs} (thus preserving photon conservation) while properly binning individual reactions according to their numbers. The radiative rate coefficients used in the reaction network are then easily derived from the N_i :

$$k_{i,\nu} = \frac{N_i}{n_i V_{cell}}. \quad (5)$$

To obtain the total rate coefficient k_i for a zone the $k_{i,\nu}$ are summed over all energies by looping the solution to the transfer equation over them; in tests spanning 40 to 2000 logarithmically-spaced energy bins, a good convergence is obtained with 80 bins.

Previously applied to one-dimensional problems only, the code is now fully parallelized for three-dimensional applications. Parallelism is achieved by domain decomposing the simulation volume into subunits, or tiles, and assigning each to a single processor. Global solution concurrency is maintained by MPI message calls between processors. At present, domain decomposition is performed only along the 2- and 3-axes and the RT is confined to the 1-axis, so photon transport is limited to point sources centered in a spherical coordinate system or plane waves in Cartesian and cylindrical coordinates. These two restrictions eliminate the need to pass photon fluxes between tiles and ensure that the I-front is present in all tiles. The latter is essential to effective load balancing, as decomposition along the 1-axis would confine the front to a subset of the tiles, which would shoulder the bulk of the subcycling in the reaction network while the others remain relatively quiescent.

The H and He recombination and cooling rates responsible for some minor departures between ZEUS-MP and the other codes in Paper I in the temperature structure of H II regions have now been updated and now use the most recent data from Hummer (1994) and Hummer & Storey (1998). ZEUS-MP has been validated with stringent tests of R-type and D-type I-fronts in a variety of stratified media (Whalen & Norman 2006) and applied to both cosmological and astrophysical problems, such as the breakout of UV radiation from primordial star-forming clouds (Whalen et al. 2004), the formation of dynamical instabilities in galactic H II regions (Whalen & Norman 2008b), the circumstellar environments of gamma-ray bursts (Whalen et al. 2008b), the photoevaporation of cosmological minihalos by nearby primordial stars (Whalen et al. 2008a), and Pop III supernovae explosions in cosmological H II regions (Whalen et al. 2008c).

2.5 RH1D (K. Ahn, P. Shapiro)

RH1D is a 1D, Lagrangian, spherically-symmetric, radiation-hydrodynamics code for a two-component gas of baryons and col-

Cosmological Radiative Transfer Codes Comparison II 5

collisionless dark matter coupled by gravity (Ahn & Shapiro 2007). For the baryonic component, the Euler equations and the equation of state are solved, together with multi-frequency, multi-species radiative transfer equations and a reaction network with nine primordial species (H, H⁺, He, He⁺, He⁺⁺, H⁻, H₂, H₂⁺ and e). Dark matter dynamics, governed by the collisionless Boltzmann equations, takes a simplified form in spherical symmetry. The code solves an effective set of Euler equations for a dark matter fluid, based upon the “fluid approximation” of dark matter dynamics for a spherically symmetric system with an isotropic velocity dispersion, derived and justified elsewhere (Ahn & Shapiro 2005). These effective Euler equations are identical to those for an inviscid, ideal gas with a ratio of specific heats $\gamma = 5/3$.

The Euler equations are solved using the so-called “leap-frog” method, where the Lagrangian position (radius) and velocity (radial velocity) are staggered in time to achieve a second-order accuracy in time steps, both for baryonic and dark matter fluid. The usual artificial viscosity scheme is used to capture shocks. We typically adopt a few thousand uniformly spaced bins in radius.

Non-equilibrium rate equations for the nine primordial species are solved using the backward differencing scheme suggested by Anninos et al. (1997). For H⁻ and H₂⁺, due to their relatively fast reaction rates, the equilibrium values may be used.

Radiative transfer is performed by ray-tracing, taking account of the optical depth to bound-free opacity of H I, He I, He II, H⁻, and H₂, as well as bound-free and dissociation opacity of H₂⁺. The optical depth to the Lyman-Werner band photons of H₂, which are capable of dissociating H₂, is treated using a pre-calculated self-shielding function by Draine & Bertoldi (1996), which is determined by the H₂ column density and gas temperature. Diffuse flux is not explicitly calculated, but is accounted for implicitly by adopting case B recombination rates. The radiative reaction rates are calculated using a photon-conserving scheme, which enables the code to treat optically-thick shells (e.g. Razoumov & Scott 1999; Abel et al. 1999a). A wide range of radiation frequency (energy), $h\nu \sim [0.7 - 7000]$ eV, is covered by a few hundred, logarithmically spaced bins, together with additive, linearly spaced bins where radiative cross sections change rapidly as frequency changes. For each frequency and species, the corresponding radiative reaction rate is calculated, then summed over frequency to obtain the net radiative reaction rate.

The radiative transfer scheme is able to treat 1) an internal point source, 2) an external, radially-directed source, and 3) an external, isotropic background. The transfer for (1) and (2) is 1D, performed along the radial direction only. For (3), the transfer is 2D in nature, and at each point the mean intensity is required to calculate the radiative rates, which involves an angle integration. The radiative transfer calculation is performed for each pre-selected angle (θ , measured from the radial direction), and then the angle integral is calculated using the Gaussian quadrature method.

The code adopts a very stringent time step criterion for accuracy. The minimum of dynamical, sound-crossing, cooling/heating, and species change time scales, which is multiplied by a coefficient smaller than unity (~ 0.1), is chosen as the time step. All the Euler equations and rate equations are solved with this time step, which makes the whole calculation self-consistent. This code has been tested extensively and used to study the radiative feedback effects by the first stars on their nearby minihalos (Ahn & Shapiro 2007).

2.6 Coral (I. Iliev, A. Raga, G. Mellema, P. Shapiro)

CORAL is a 2-D, axisymmetric Eulerian fluid dynamics adaptive mesh refinement (AMR) code (see Mellema et al. 1998; Shapiro et al. 2004, and references therein for detailed description). It solves the Euler equations in their conservative finite-volume form using the second-order method of van Leer flux-splitting, which allows for correct and precise treatment of shocks. The grid refinement and de-refinement criteria are based on the gradients of all code variables. When the gradient of any variable is larger than a pre-defined value the cell is refined, and when the criterion for refinement is not met the cell is de-refined.

The code follows, by a semi-implicit method, the non-equilibrium chemistry of multiple species (H, He, C II-VI, N I-VI, O I-VI, Ne I-VI, and S II-VI) and the corresponding cooling (Raga et al. 1997; Mellema et al. 1998), as well as Compton cooling. The photoheating rate is the sum of the photoionization heating rates for H I, He I and He II. For computational efficiency all heating and cooling rates are pre-computed and stored in tables. The microphysical processes – chemical reactions, radiative processes, transfer of radiation, heating and cooling – are implemented though the standard approach of operator-splitting (i.e. solved at each time-step, side-by-side with the hydrodynamics and coupled to it through the energy equation). The latest versions of the code also include the effects of an external gravity force.

Currently the code uses a black-body or power-law ionizing source spectrum, although any other spectrum can be accommodated. Radiative transfer of the ionizing photons is treated explicitly by taking into account the bound-free opacity of H and He in the photoionization and photoheating rates. The photoionization and photoheating rates of H I, He I and He II are pre-computed for the given spectrum and stored in tables vs. the optical depths at the ionizing thresholds of these species, which are then used to obtain the total optical depths. The code correctly tracks both fast (by evolving on an ionization timestep, $\Delta t \sim \dot{n}_{\text{H}}/n_{\text{H}}$) and slow I-fronts.

The code has been tested extensively and has been applied to many astrophysical problems, e.g. photoevaporation of clumps in planetary nebulae (Mellema et al. 1998), cosmological minihalo photoevaporation during reionization (Shapiro et al. 2004; Iliev et al. 2005), and studies of the radiative feedback from propagating ionization fronts on dense clumps in Damped Lyman- α systems (Iliev et al. 2006a).

2.7 LICORICE: Line Continuum Radiative transfer Integrated Computing Engine (S. Baek, B. Semelin, F. Combes)

The LICORICE code has three main components: TreeSPH to compute gravity and hydrodynamics, continuum radiative transfer with hydrogen ionization physics, and Lyman-alpha line transfer. The latter is not relevant to this comparison and will be described elsewhere. The current version of LICORICE does not include H₂ formation, He ionization, or diffuse radiation from recombinations, but they will be incorporated in the future. LICORICE uses SPH particles for the gas dynamics and an adaptive grid for the radiative transfer. Physical quantities are interpolated from one to the other as required.

The fluid dynamics are followed using a TreeSPH method. The implementation is described in detail in Semelin & Combes (2002) and Semelin & Combes (2005). Since there are many varieties of SPH, we summarize the main features of our algorithm here. We use a spherically-symmetric spline-smoothing kernel and

6 *I. T. Iliev, et al.*

50 neighbours to compute the SPH quantities using an arithmetic average between the neighbours, a smoothing length h and the simple viscosity scheme by Monaghan (1992).

For the tests in this paper we implemented mirror boundary conditions. This was achieved as follows: for each SPH particle within a distance of the simulation box boundary smaller than its smoothing length h , we create a symmetrical *ghost* particle on the other side of the boundary. These ghost particles are used as neighbours to compute the SPH quantities of real particles. The ghost particles are erased and recreated at each time step.

The continuum radiative transfer is solved using a Monte Carlo approach similar to the one employed in the CRASH code (Maselli et al. 2003). Here we summarize only the differences between LICORICE and CRASH. We compute the gas density at each particle's position with the SPH smoothing kernel, and physical quantities such as ionization fraction and temperature are updated according to these particle densities. The density field is generally smooth, but may sometimes show spurious fluctuations if the local particle number changes sharply. This is a well known but unavoidable problem with SPH.

The radiation field is discretized into photon packets and propagated through cells along directions chosen at random. The cells form an adaptive grid which is derived from the tree structure of the particle distribution. Our adaptive grid is built to keep the number of particles in each cell within a given range (1 to 8 and 1 to 1 ranges have been used). This yields greater resolution in the denser regions. The adaptive grid also requires fewer cells than a fixed grid to best sample a given inhomogeneous particle distribution, thus saving both memory and CPU time.

The time step for updating physical quantities within a cell is also adaptive. We update the physical quantities for all cells and particles after the propagation of the number of photon packets corresponding to an integration time dt . However, if the number of accumulated photons in a cell during this integration time is greater than a pre-set limit (e.g. 10% of the total number of neutral hydrogen atoms in the cell), we update the physical quantities in this cell with a time step $dt' < dt$ corresponding to the time elapsed since the last update.

The data required for the tests are interpolated from the particle distribution onto the 128^3 grids required by the tests. Currently, the dynamical part of the code is parallelized for both shared and distributed memory architectures using OpenMP and MPI, while the radiative transfer is parallelized with OpenMP only. The code can now handle 128^3 particles, to be increased to 256^3 in the near future. We note that compared to a uniform grid with the same number of cells, the SPH Lagrangean approach results in higher resolution in the dense regions, and lower resolution in more diffuse regions.

2.8 Flash-HC: Hybrid Characteristics (T. Theuns, M. Raicevic, E.-J. Rijkhorst)

The Hybrid Characteristics (HC) method (Rijkhorst 2005; Rijkhorst et al. 2006) is a three-dimensional ray-tracing scheme for parallel AMR codes. It combines elements of long and short characteristics, using the precision and parallelizability of the former with efficient execution through interpolation of the latter. It has been implemented into the Flash-HC AMR code (Fryxell et al. 2000), enabling simulations of radiation hydrodynamics problems with point sources of radiation.

The block-structured AMR grid used in Flash-HC is distributed over processors using a space-filling curve. Parallel ray

tracing requires each ray to be split in the independent sections where the ray traverses the blocks held by a given processor. First, every processor traces rays on its local blocks in directions which start from the source, and end in the corners of each cell on the faces of the (cubic) block. Since rays cross several blocks, interpolation is used to assemble a ray from local block contributions. However, because some of these blocks will be held by other processors, local column densities need to be exchanged in one global communication. Note that only face values are exchanged. Finally, local and imported column densities are combined using interpolation to assemble the complete ray. At the end of this parallel operation, each cell has the total column density to the source along a ray that traverses all intervening cells at the full resolution of the AMR grid. Interpolation coefficients are chosen such that the exact solution for the column density is obtained for a uniform density distribution. Even in a non-uniform density distribution, for example $1/r^2$, the differences between the value of the correct column density and that obtained using HC is typically less than half a percent.

Recent improvements introduced since Paper I include the implementation of a fully photon conserving chemistry solver, taking into account the effects of both spatial and temporal discretization (Abel et al. 1999b; Mellema et al. 2006b). This implementation employs the Livermore Solver for Ordinary Differential Equations (LSODE Hindmarsh 1980), which, although more computationally intensive than the original solver used in DORIC (Frank & Mellema 1994), eliminates the need for an independent radiative transfer time step irrespective of the ionization front type and guarantees correct front positions and ionization heating. Details of the scheme will be presented elsewhere. Additional functionality allows for a radiation source outside of the computational volume, a feature used in Test 7 to approximate a parallel ionization front.

The parallel scaling of HC was examined in Rijkhorst (2005) and Iliev & et al. (2006): the algorithm scales well for ~ 100 processors on a SGI Altix, and ~ 1000 processors on a IBM Blue Gene/L systems. The algorithm scales linearly with the number of sources. The photon-conserving RT and chemistry upgrades should not affect HC's scaling.

2.9 ENZO-RHD (D.R. Reynolds, M.L. Norman, J.C. Hayes, P. Paschos)

The ENZO-RHD code is an extension to the freely-available ENZO code¹ that self-consistently incorporates coupled radiation transport and chemical ionization kinetics within ENZO's formulation for cosmological hydrodynamics on AMR meshes Norman et al. (2007). In the current code we approximate the radiation transport processes using a single integrated radiation energy density in each spatial cell that is propagated with flux-limited diffusion on a finite-volume mesh. The radiation field is implicitly coupled in time to a multi-species chemical reaction network. This implicit radiation chemistry system is then coupled in an operator-split fashion with ENZO's cosmological hydrodynamics solver, which utilizes the Piecewise Parabolic Method for the advection of matter and gas energy Colella & Woodward (1984). The coupled algorithm, along with a suite of verification tests, is fully described in Reynolds et al. (2009).

The frequency dependence of the photoionization rates is treated by integrating a prescribed radiation frequency spectrum, typically chosen to be either monochromatic, blackbody, or a

¹ <http://lca.ucsd.edu/portal/software/enzo>

Cosmological Radiative Transfer Codes Comparison II 7

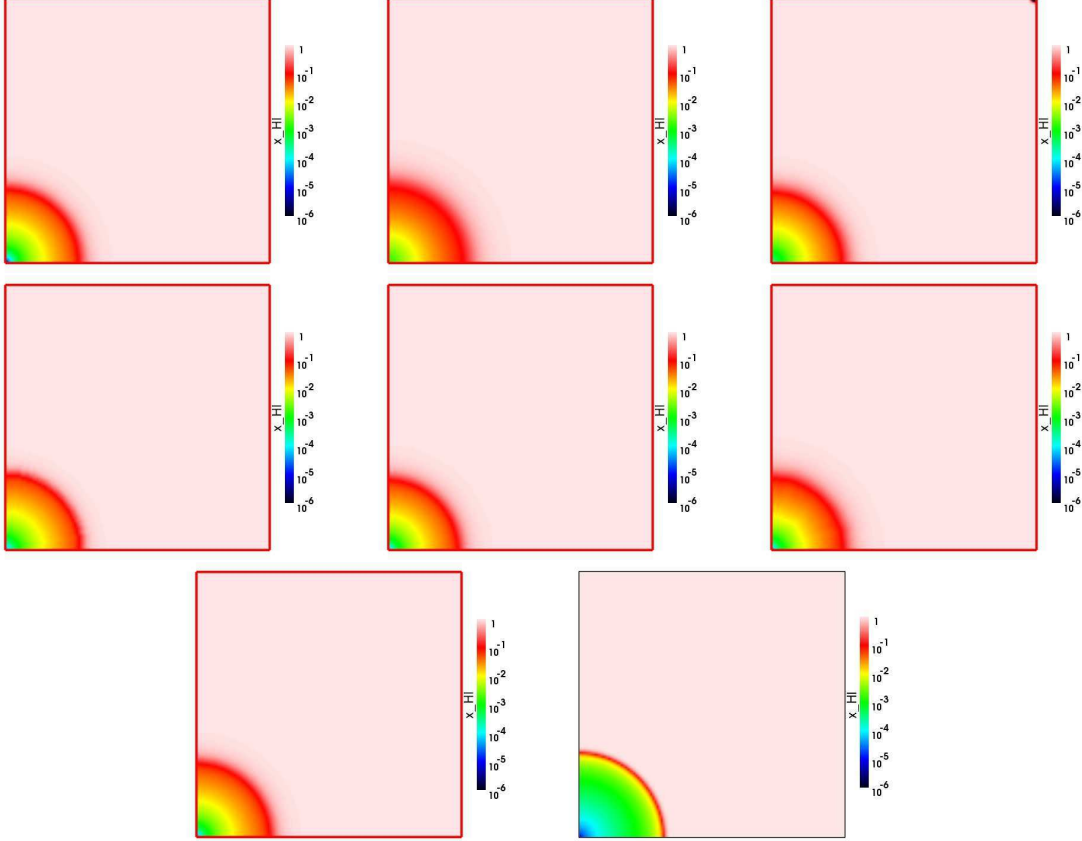


Figure 2. Test 5 (H II region expansion in an initially-uniform gas): Images of the H I fraction, cut through the simulation volume at coordinate $z = 0$ at time $t = 100$ Myr for (left to right and top to bottom) Capreole+C²-Ray, HART, RSPH, ZEUS-MP, RH1D, LICORICE, Flash-HC and Enzo.

$(\frac{\nu}{\nu_0})^{-\beta}$ power law. This integration is performed upon initialization of the solver and the integrated rates are re-used throughout the simulation. In the current version of the code, only a single radiation profile is allowed, although this formulation may be easily extended to allow for multifrequency calculations.

The solver for propagating radiation throughout the domain follows a standard flux-limited diffusion model, in which the radiation flux \mathbf{F} is approximated by

$$\mathbf{F} = -\frac{1}{a} D \nabla E. \quad (6)$$

Here E is the radiation energy density, and the flux-limiter D smoothly connects the limiting cases of (nearly) isotropic and free-streaming radiation:

$$D(E) = \text{diag}(D_1(E), D_2(E), D_3(E)), \quad (7)$$

where

$$D_i(E) = \frac{c(2\kappa_T + R_i)}{6\kappa_T^2 + 3\kappa_T R_i + R_i^2}, \quad i = 1, \dots, 3, \quad (8)$$

and $R_i = |\partial_i E|/E$, c is the speed of light, and κ_T is the opacity.

The coupled implicit radiation-chemistry system further includes a gas energy feedback field, which allows us to self-consistently heat and cool the gas in an operator-split manner,

capturing all of the stiff components involved in radiation transport, primordial chemistry and thermal heating/cooling in a tightly-coupled implicit system. ENZO's explicit Eulerian hydrodynamics solver and its parallel implementation have been exhaustively described elsewhere Norman et al. (2007). Parallelism of the coupled implicit system follows a standard domain-decomposition approach and is solved using state-of-the-art Newton-Krylov-Multigrid solvers Knoll & Keyes (2004), potentially allowing scalability of the algorithm to up to tens of thousands of processors.

While ENZO allows for spatial adaptivity through structured adaptive mesh refinement (SAMR), our initial implementation of ENZO-RHD is currently limited to uniform grids in 1-, 2- or 3-dimensions, although their upgrade to AMR is under development. Extensions of this approach to variable Eddington tensors, multi-group flux-limited diffusion, or multigroup variable Eddington tensors are easily accommodated within our implicit formulation and are planned as future extensions. The implicit coupling between radiation, ionization, and gas energy is fundamentally new, and eliminates costly subcycling or unphysical speed-of-light reduction techniques. One benefit of implicit coupling is that accurate solutions to I-front problems can be achieved with surprisingly low resolution. Another benefit is that the timestep is independent of grid resolution, at least for the radiation solve. A third advantage of our

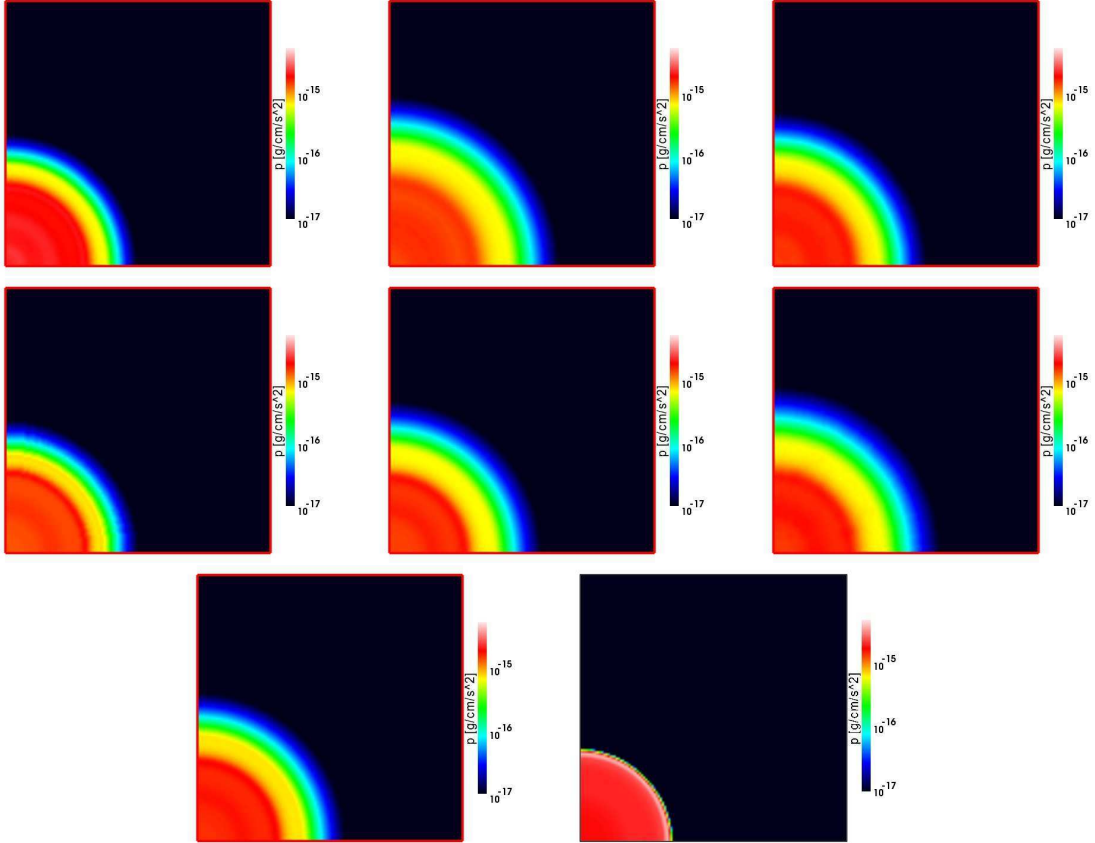
8 *I. T. Iliev, et al.*

Figure 3. Test 5 (H II region expansion in an initially-uniform gas): Images of the pressure, cut through the simulation volume at coordinate $z = 0$ at time $t = 100$ Myr for (left to right and top to bottom) Capreole+C²-Ray, HART, RSPH, ZEUS-MP, RH1D, LICORICE, Flash-HC and Enzo.

approach is that by defining radiation as a field variable, scalability with respect to the number of point sources ceases to be an issue. Instead, scalability is dictated by the underlying linear system solver, which for the case of multigrid is optimal.

3 RADIATION HYDRODYNAMICS TESTS: DESCRIPTION

For simplicity and inclusivity (since currently not all codes have implemented Helium or metals chemistry and cooling) all tests assume the gas to be composed of pure Hydrogen.

3.1 Test 5: Classical H II Region Expansion

Test 5 is the classical problem of expansion of an I-front due to a point source in an initially uniform-density medium. In general, I-fronts are classified according to their speed with respect to the gas and the change in gas density through the I-front (c.f. Kahn & Dyson 1965; Spitzer 1978). There are two critical speeds: R-critical, defined as $v_R = 2c_{s,I,2}$, and D-critical, given by $v_D = c_{s,I,2} - (c_{s,I,2}^2 - c_{s,I,1}^2)^{1/2} \approx c_{s,I,1}^2 / (2c_{s,I,2})$, where $c_{s,I,1} = (p_1/\rho_1)^{1/2}$ and $c_{s,I,2} = (p_2/\rho_2)^{1/2}$ are the *isothermal*

sound speeds in the gas ahead of and behind the I-front, respectively. We note that the gas is *not* assumed isothermal. The velocity of the I-front is given by the jump condition $v_I = F/n$ (which guarantees photon conservation), where n is the number density of the neutral gas entering the front and F is the flux of ionizing photons at the I-front transition (which is attenuated due to absorptions in the gas on the source side). We note that this jump condition is modified significantly for I-fronts moving with relativistic speeds with respect to the gas (Shapiro et al. 2006). This can occur in a number of astrophysical and cosmological environments. However, we do not consider such cases here since currently few radiative transfer codes (and no radiation hydrodynamics codes, to our knowledge) are able to handle such relativistic I-fronts.

When $v_I \geq v_R$ (e.g. close to the source, where the flux F is large) the I-front is R-type (R-critical when $v_I = v_R$). R-type I-fronts always move supersonically with respect to the neutral gas ahead, while with respect to the ionized gas the front can move either subsonically (strong R-type, highly compressive, but generally irrelevant to H II regions since it means that the isothermal sound speed behind the front is lower than the one ahead of it), or supersonically (weak R-type, resulting in only slight compression of the gas moving through the front). When $v_I \leq v_D$, the I-front is D-type (D-critical in the case that $v_I = v_D$). The gas passing through this

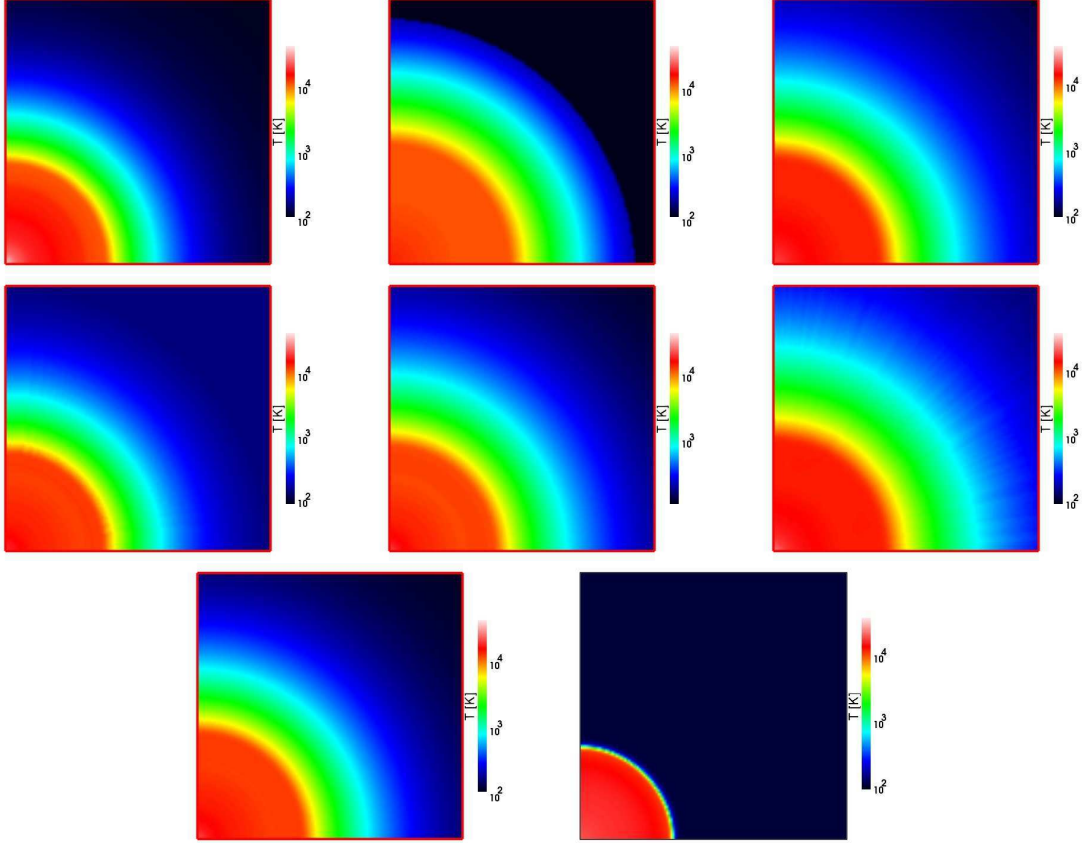


Figure 4. Test 5 (H II region expansion in an initially-uniform gas): Images of the temperature, cut through the simulation volume at coordinate $z = 0$ at time $t = 100$ Myr for (left to right and top to bottom) Capreole+C²-Ray, HART, RSPH, ZEUS-MP, RH1D, LICORICE, Flash-HC and Enzo.

type of I-front always expands, and the front is subsonic with respect to the gas beyond. With respect to the ionized gas, the I-front can again be either supersonic (strong D-type), or subsonic (weak D-type). When $v_D < v_I < v_R$ (sometimes referred to as M-type I-front) the I-front is necessarily led by a shock which compresses the gas entering the I-front sufficiently to slow it down and guarantee that $v_I \leq v_D$.

In a static medium with number density n_{H} and constant ionized gas temperature T , the evolution of the I-front radius r_I and velocity v_I for a point source emitting \dot{N}_γ ionizing photons per second are given by

$$r_I = r_S^0 [1 - \exp(-t/t_{\text{rec}})]^{1/3} \quad (9)$$

$$v_I = \frac{r_S}{3t_{\text{rec}}} \frac{\exp(-t/t_{\text{rec}})}{[1 - \exp(-t/t_{\text{rec}})]^{2/3}}, \quad (10)$$

where

$$r_S^0 = \left[\frac{3\dot{N}_\gamma}{4\pi\alpha_B(T)n_{\text{H}}^2} \right]^{1/3}, \quad (11)$$

the Strömgren radius (assuming full ionization), which is reached when the number of recombinations in the ionized volume per unit time exactly balances the number of ionizing photons emitted by

the source per unit time. This final static stage is commonly referred to as Strömgren sphere. The recombination time is given by

$$t_{\text{rec}} = [\alpha_B(T)n_{\text{H}}]^{-1}. \quad (12)$$

Here $\alpha_B(T)$ is the case B recombination coefficient of hydrogen at temperature T in the ionized region.

In reality, the gas is not static and evolves beyond the Strömgren sphere. The high gas pressure of the ionized and heated gas inside the H II region creates strong forces pushing the gas outwards, and the I-front continues to expand. Analytical models predict that in this phase the I-front radius evolves approximately according to (c.f. Spitzer 1978)

$$r_I = r_S^0 \left(1 + \frac{7c_s t}{4r_S^0} \right)^{4/7}, \quad (13)$$

where r_S^0 is the Strömgren radius and c_s is the sound speed in the ionized gas. The expansion finally stalls when a pressure equilibrium is reached. The predicted final H II region radius is

$$r_f = \left(\frac{2T}{T_e} \right)^{2/3} r_S^0, \quad (14)$$

where T is the temperature inside the H II region and T_e is the external temperature. In reality, the evolution is more complicated,

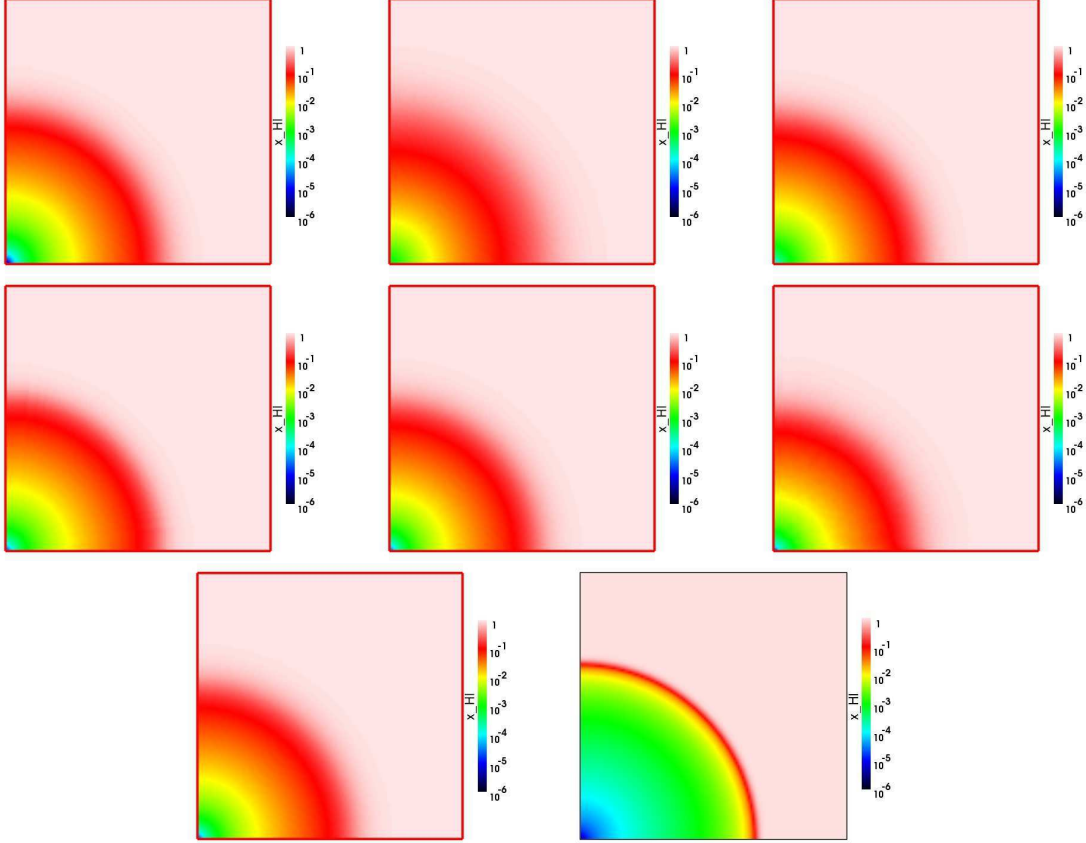
10 *I. T. Iliev, et al.*

Figure 5. Test 5 (H II region expansion in an initially-uniform gas): Images of the HI fraction, cut through the simulation volume at coordinate $z = 0$ at time $t = 500$ Myr for (left to right and top to bottom) Capreole+C²-Ray, HART, RSPH, ZEUS-MP, RH1D, LICORICE, Flash-HC and Enzo.

with non-uniform temperatures inside the H II region, broadened I-fronts due to pre-heating by energetic photons, etc. Furthermore, equation 13 describes correctly only in the purely pressure-driven, late-time evolution, but not the transition from fast, R-type to D-type I-front. These analytical solutions should therefore only be considered guidelines for the expected behaviour, not as exact analytical solutions of this problem.

The numerical parameters for Test 5 are as follows: computational box size $L = 15$ kpc, initial gas number density $n_H = 10^{-3}$ cm⁻³, initial ionization fraction $x = 0$, constant ionizing photon emission rate $\dot{N}_\gamma = 5 \times 10^{48}$ s⁻¹, initial gas velocity zero and initial gas temperature $T_e = 100$ K. The radiation source is at the $(x_s, y_s, z_s) = (0, 0, 0)$ corner of the computational box. For reference, if we assume that the temperature of the ionized gas is $T = 10^4$ K, and that the recombination rate is given by $\alpha_B(T) = 2.59 \times 10^{-13}$ cm³s⁻¹, we find $t_{\text{rec}} = 3.86 \times 10^{15}$ s = 122.4 Myr, $r_S = 5.4$ kpc, and $r_f \approx 185$ kpc. This rough final pressure-equilibrium radius is thus well outside of our computational volume, which was instead chosen to resolve the more physically-interesting transition from R-type to D-type, which occurs around r_S^0 . The ionizing spectrum is that of a 10^5 K black body, as expected for a massive, metal-free Pop. III star. Hydrogen line cooling, recombinational cooling, and bremsstrahlung cooling are all

included, but not Compton cooling. The simulation running time is $t_{\text{sim}} = 500$ Myr $\approx 4 t_{\text{rec}}$. The required outputs are the neutral fraction of hydrogen, gas pressure, temperature and Mach number on the entire grid at $t = 10, 30, 100, 200,$ and 500 Myr, and the I-front position (defined as the position where the neutral fraction is 50%) and I-front velocity vs. time along the x -axis.

3.2 Test 6: H II region expansion in $1/r^2$ density profile

Test 6 is the propagation of an I-front created by a point source at the center of a spherically-symmetric, steeply-decreasing power-law density profile with a small flat central core of gas number density n_0 and radius r_0 :

$$n_H(r) = \begin{cases} n_0 & \text{if } r \leq r_0 \\ n_0(r/r_0)^{-2} & \text{if } r \geq r_0 \end{cases}$$

For a static-density medium the evolution of the I-front within the flat-density core is described by equations 9 and 10. In this case, if the Strömgren radius associated with the core density n_0 , $r_{S,0} = [3\dot{N}_\gamma / (4\pi\alpha_B(T)n_0^2)]^{1/3}$, is smaller than r_0 , the front will come to a halt within the core. If, instead, $r_{S,0} > r_0$, the front escapes the core and propagates into the stratified envelope. Thereafter, the I-front position and velocity as a function of time have

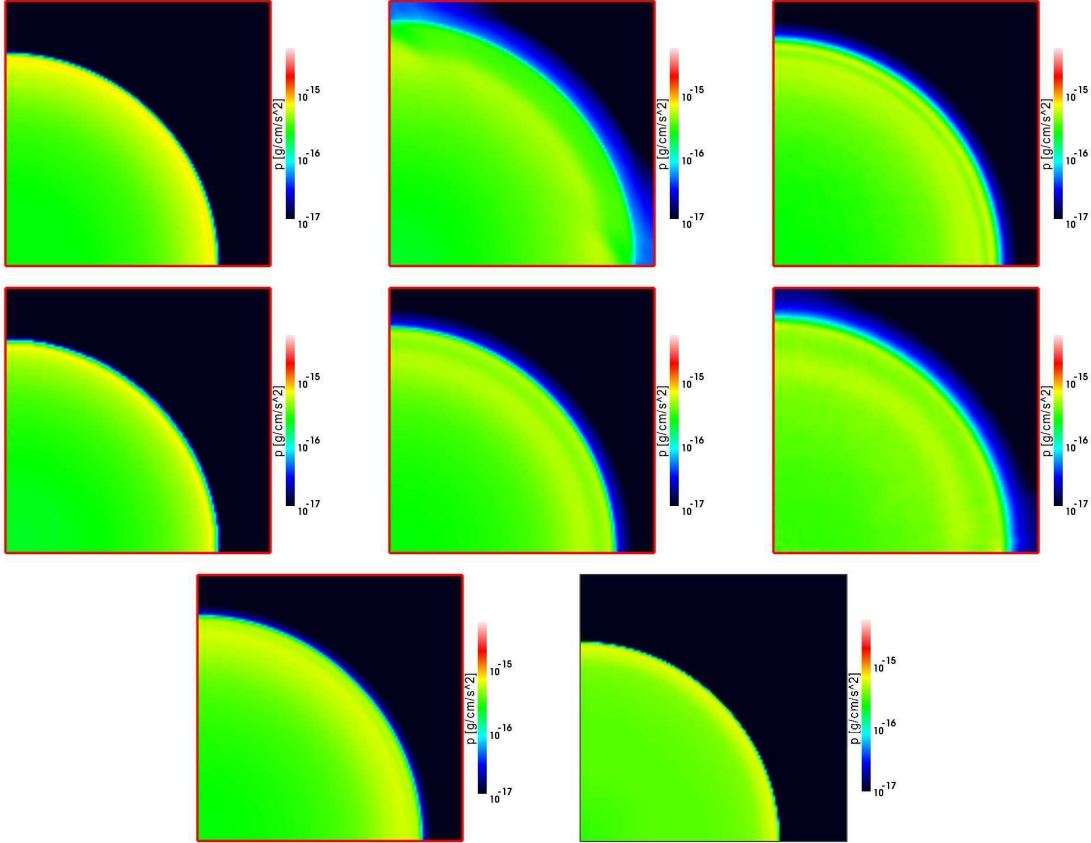


Figure 6. Test 5 (H II region expansion in an initially-uniform gas): Images of the pressure, cut through the simulation volume at coordinate $z = 0$ at time $t = 500$ Myr for (left to right and top to bottom) Capreole+ C^2 -Ray, HART, RSPH, ZEUS-MP, RH1D, LICORICE, Flash-HC and Enzo.

complex analytical forms for an arbitrary source fluxes and densities (Mellema et al. 2006b). A simple solution exists for the special case of the central ionizing source rate of photon emission $\dot{N}_\gamma = 16\pi r_0^3 n_0^2 \alpha_B / 3$, in which case the I-front radius upon leaving the core is

$$r_I = r_0(1 + 2t/t_{\text{rec,core}})^{1/2}, \quad (15)$$

where $t_{\text{rec,core}}$ is the recombination time in the core (Mellema et al. 2006b). Similar solutions exist also when the I-front is moving relativistically (Shapiro et al. 2006).

The propagation of an I-front in r^{-2} density profiles with full gas dynamics does not have an exact analytical solution, but has been well studied with both semianalytical and numerical methods (Franco et al. 1990). If $r_{S,0} < r_0$ then the I-front converts to D-type within the core, but starts to re-accelerate upon entering the steep density gradient. Numerical simulations indicate that in density profiles approximating those of galactic molecular cloud cores or cosmological minihalos at high redshift, the I-front remains D-type for the lifetime of typical UV sources (Whalen & Norman 2008a). If $r_{S,0}$ is instead equal to or greater than r_0 , the I-front may briefly convert to D-type, but then rapidly reverts to R-type and flash-ionizes the cloud on timescales shorter than the dynamical time of the gas. Now completely ionized and nearly isothermal,

strong pressure gradients form wherever there are steep density gradients, the sharpest of which are found at the edge of what was once the edge of the core. These pressure gradients drive the gas outward into the ionized cloud forming a shock that moves with a roughly constant velocity in r^{-2} density profiles (Franco et al. 1990).

In Test 6 we examine the former case, in which the initial Strömgren radius is smaller than the core radius. The aim of this test is to study the initial transition of the I-front from R-type to D-type and back to R-type over a fairly restricted range of radii, rather than its long-term behavior thereafter. Accordingly, we adopt the following numerical parameters: computational box length $L = 0.8$ kpc, $n_0 = 3.2 \text{ cm}^{-3}$, $r_0 = 91.5$ pc, zero initial ionization fraction, ionizing photon emission rate $\dot{N}_\gamma = 10^{50} \text{ photons s}^{-1}$ and initial temperature $T = 100$ K. The source position is at the corner of the computational volume $(x_s, y_s, z_s) = (0, 0, 0)$. For these parameters the I-front changes from R-type to D-type inside the core. Once the front reaches the core edge it will accelerate as it propagates down the steep density slope. The initial recombination time inside the core (assuming ionized gas temperature $T = 10^4$ K) is $t_{\text{rec,core}} = 0.04$ Myr. The ionizing spectrum is again that of a 10^5 K black body, as expected for a massive, metal-free Pop. III star. Hydrogen line cooling, recombinational cooling, and bremsstrahlung cooling are all included, but again not Comp-

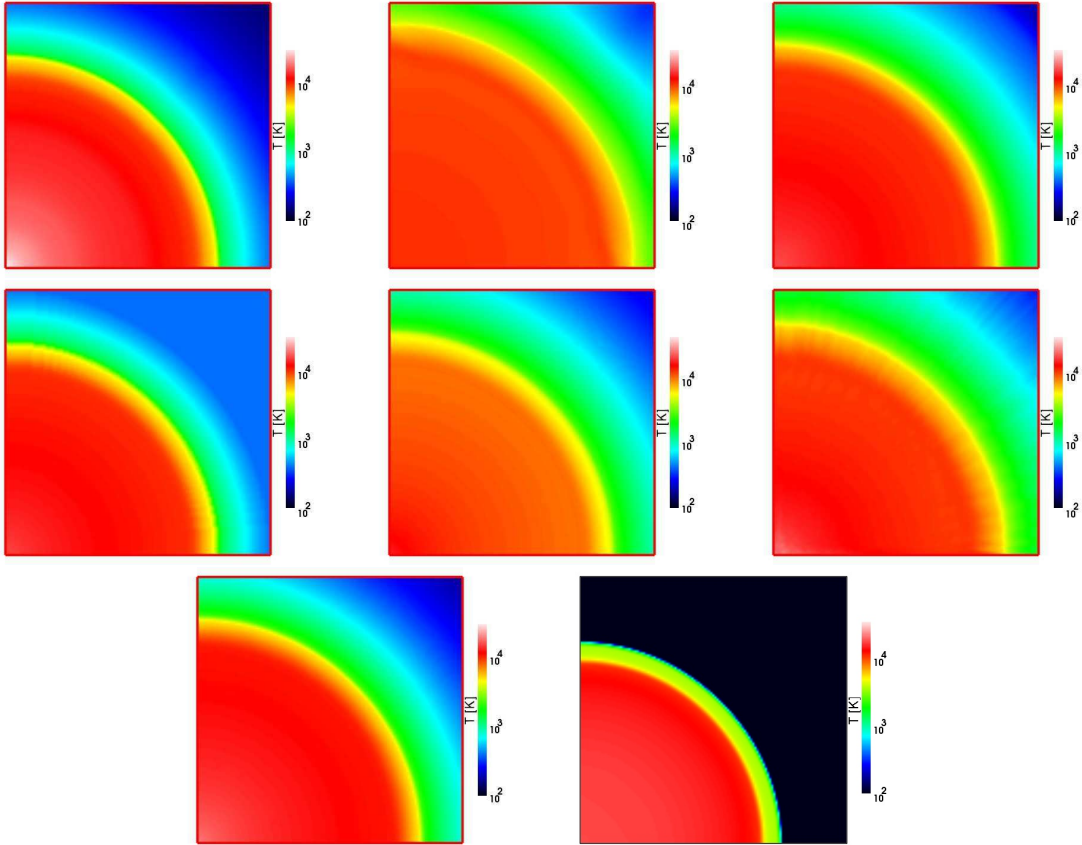
12 *I. T. Iliev, et al.*

Figure 7. Test 5 (H II region expansion in an initially-uniform gas): Images of the temperature, cut through the simulation volume at coordinate $z = 0$ at time $t = 500$ Myr for (left to right and top to bottom) Capreole+C²-Ray, HART, RSPH, ZEUS-MP, RH1D, LICORICE, Flash-HC and Enzo.

ton cooling. For simplicity gravitational forces are ignored and no hydrostatic equilibrium is imposed on the cloud. Unlike in Test 5, left on their own the pressure forces will accelerate gas outward in this density-stratified cloud, albeit those forces are much inferior than the stronger ones due to pressure from the photoheated gas. The running time is $t_{\text{sim}} = 75$ Myr. The required outputs are neutral fraction of hydrogen, gas number density, temperature and Mach number on the grid at times $t = 1, 3, 10, 25$ and 75 Myr, and the I-front position (as defined in Test 5) and velocity vs. time along the x -axis.

3.3 Test 7: Photoevaporation of a dense clump

In Test 7, a plane-parallel I-front encounters a uniform spherical clump in a constant background density field. This problem has been studied in many contexts, *e.g.* in relation to the photoevaporation of dense clumps in planetary nebulae (Mellema et al. 1998). Depending on the assumed parameters the clump may either initially trap the I-front, or be ‘zapped’, or flash-ionized, without ever trapping the I-front (c.f. Bertoldi 1989). The condition for an I-front to be trapped by a dense clump with number density n_H can be derived by defining a ‘‘Strömgren length’’, $\ell_S(r)$, at a given impact parameter r using equations (9) and (10), and solving them for

each impact parameter (Shapiro et al. 2004). We can then define the ‘‘Strömgren number’’ for the clump as $L_S \equiv 2r_{\text{clump}}/\ell_S(0)$, where r_{clump} is the clump radius and $\ell_S(0)$ is the Strömgren length for zero impact parameter. If $L_S > 1$, then the clump is able to trap the I-front, while if $L_S < 1$, the I-front quickly ionizes the clump and is never trapped (the so-called ‘cloud-zapping’ regime in Bertoldi 1989). For a uniform clump equation (11) reduces to

$$\ell_S = \frac{F}{\alpha_H^{(2)} n_H^2}, \quad (16)$$

and L_S becomes

$$L_S = \frac{2r_{\text{clump}} \alpha_H^{(2)} n_H^2}{F}. \quad (17)$$

The numerical parameters for Test 7 are the same as for Test 3 in Paper I: a constant ionizing photon flux of $F = 10^6 \text{ s}^{-1} \text{ cm}^{-2}$ is incident at $y = 0$, the ambient hydrogen gas number density and temperature are $n_{\text{out}} = 2 \times 10^{-4} \text{ cm}^{-3}$ and $T_{\text{out}} = 8,000$ K, respectively, while the initial clump density and temperature are $n_{\text{clump}} = 200 n_{\text{out}} = 0.04 \text{ cm}^{-3}$ and $T_{\text{clump}} = 40$ K. These parameters ensure that outward pressures in the clump balance those from the hot gas so that the clump is initially in pressure equilibrium with the surrounding medium. The column density of the

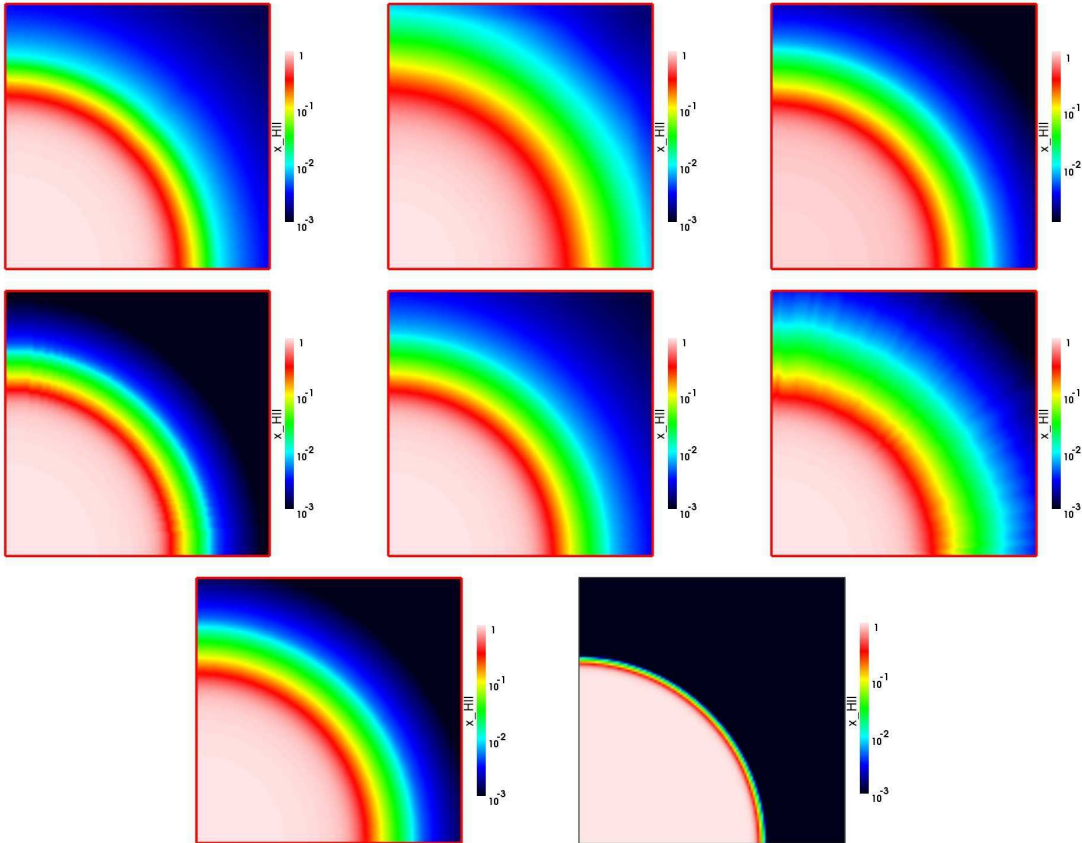


Figure 8. Test 5 (H II region expansion in an initially-uniform gas): Images of the H II fraction, cut through the simulation volume at coordinate $z = 0$ at time $t = 500$ Myr for (left to right and top to bottom) Capreole+ C^2 -Ray, HART, RSPH, ZEUS-MP, RH1D, LICORICE, Flash-HC and Enzo.

clump is sufficient to trap the I-front and compel its transition to D-type, in contrast to the less interesting for us “cloud-zapping” regime in which the front flash-ionizes the cloud and remains R-type throughout. The computational box size is $x_{\text{box}} = 6.6$ kpc, the radius of the clump is $r_{\text{clump}} = 0.8$ kpc, and its center is at $(x_c, y_c, z_c) = (5, 3.3, 3.3)$ kpc = (97, 64, 64) cells. Hydrogen line cooling, recombinational cooling, and bremsstrahlung cooling are included, but not Compton cooling.

With hydrodynamics the evolution beyond the trapping phase proceeds very differently from the static Test 3 in Paper I. As the heated and ionized gas is evaporated and expands towards the source, its recombination rate falls and it attenuates the ionizing flux less. As a consequence, the I-front slowly consumes the clump until it photoevaporates completely. The required outputs are H I fraction, gas pressure, temperature, and Mach number at times $t = 1, 5, 10, 25$ and 50 Myr and the position and velocity of the I-front along the axis of symmetry.

4 RESULTS

4.1 Test 5

We start by comparing the fluid flow and ionization structure at two characteristic stages of the evolution, at $t = 100$ Myr, of order of one recombination time, which is the start of the I-front conversion from R- to D-type, shortly before the initial Strömgren radius is reached, and at $t = 500$ Myr, corresponding to a few recombination times, when the I-front is D-type preceded by a shock. In Figures 2 - 4 and 5 - 7 we show image cuts at coordinate $z = 0$ of the neutral hydrogen fraction, pressure, and temperature at 100 Myr and at 500 Myr, respectively, while in Figures 8 and 9 we show the ionized fraction and number density at 500 Myr.

With a few exceptions, discussed below, all results exhibit reasonably good agreement throughout the flow evolution. As we found also for the static tests in Paper I, the majority of the differences are consequence of the different handling of the energy equation and the hard photons with long mean free paths. These differences yield different spatial structures in temperature (Figures 4, 7 and 13) and different ionized fraction distributions ahead of the I-front (which is dictated by the hard photons and non-equilibrium chemistry, Figures 8 and 11), but very similar ionization distribu-

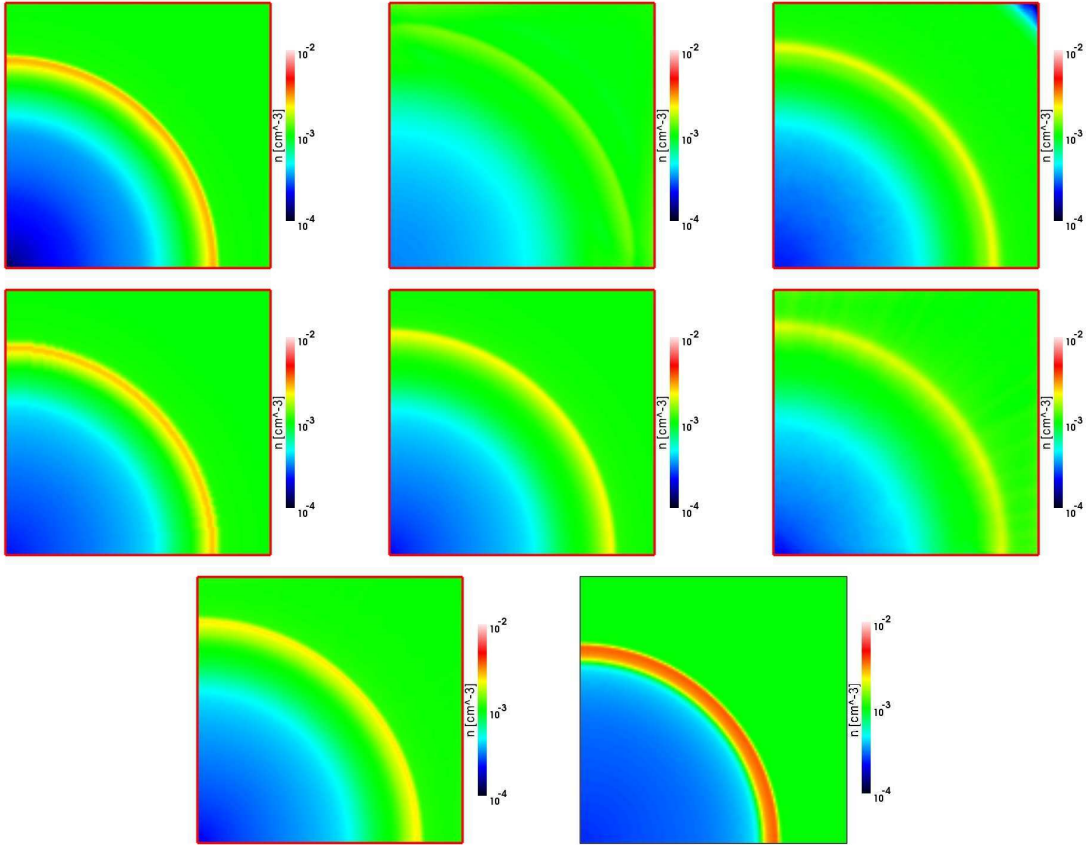
14 *I. T. Iliev, et al.*

Figure 9. Test 5 (H II region expansion in an initially-uniform gas): Images of the gas number density, cut through the simulation volume at coordinate $z = 0$ at time $t = 500$ Myr for (left to right and top to bottom) Capreole+C²-Ray, HART, RSPH, ZEUS-MP, RH1D, LICORICE, Flash-HC and Enzo.

tions inside the H II region (which sees the whole spectrum of photons and is mostly chemically equilibrated, Figures 2, 5 and 11).

However, in contrast with Paper I’s results, where the lack of dynamics meant that the I-front motion itself was generally little affected by these differences, the fluid flow can be significantly affected. In particular, a more effective pre-heating by hard photons leaking ahead of the I-front in those two cases, makes for a weaker shock (evidenced by a smaller pressure jump and lower Mach number) leading the I-front, corresponding lower density compression and thus a bit faster propagation of both the I-front and shock (Figures 9 and 11-15). Stronger preheating invariably results in weaker shock, which yields lower gas compression and results in faster-moving I-front, and vice versa. More specifically, the HART and LICORICE methods give faster-moving I-fronts, while ZEUS-MP, C²-Ray, and especially Enzo (due to its utilization of monochromatic ionizing spectrum, more about which below) - slower moving ones. The overall differences in the I-front position and velocity are nonetheless very modest, of order only a few percent, with the exception of Enzo and, to a lesser extent HART. In contrast, the differences in the temperature structure inside the H II region has no appreciable effect on the I-front propagation.

The hydrodynamical profiles cluster fairly closely together. The codes agree fairly well on the temperature structure of the

evolving H II region except for HART, which predicts flat, lower temperatures at later times, and C²-Ray, which yields higher ionized gas temperatures due to its simplified method for handling the energy, and again Enzo because of its monochromatic spectrum. The reason for the sharp drop in pressure at $0.6 L_{\text{box}}$ at 10 Myr in the HART results is unclear.

Apart from the differences discussed above, there are several features of the HART, LICORICE and Enzo methods worth noting. The OTVET moment radiative transfer method used in HART is somewhat diffusive, as was already noted in Paper I, which results in thicker I-front and less sharp flow features overall. There are some radial striations visible in the LICORICE results, especially in the temperature images that are reminiscent of those observed in the CRASH code results in Test 2 of Paper I. Since LICORICE adopts the Monte Carlo radiative transfer found in the original version of CRASH, the radial artifacts in its temperatures are similarly due to the noise in that version’s energy sampling scheme, which has been corrected in the latest release of the CRASH code (Maselli et al. 2009). Some wall effects in the upper left and lower right corners of the box in the HART pressure and Mach number images reflecting the fact that mirror rather than outflow boundary conditions were utilized. This is due to the natively-periodic nature of the OTVET method, which demands special handling in

Cosmological Radiative Transfer Codes Comparison II 15

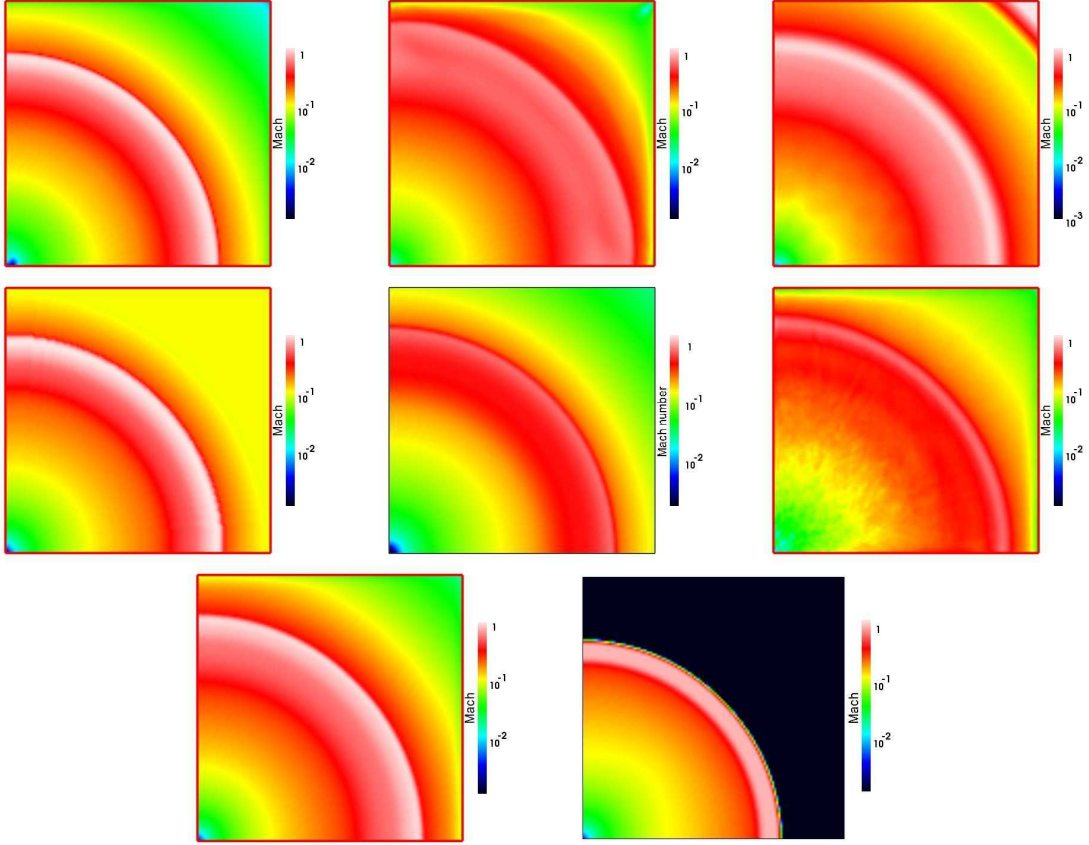


Figure 10. Test 5 (H II region expansion in an initially-uniform gas): Images of the Mach number, cut through the simulation volume at coordinate $z = 0$ at time $t = 500$ Myr for (left to right and top to bottom) Capreole+C²-Ray, HART, RSPH, ZEUS-MP, RHID, LICORICE, Flash-HC and Enzo.

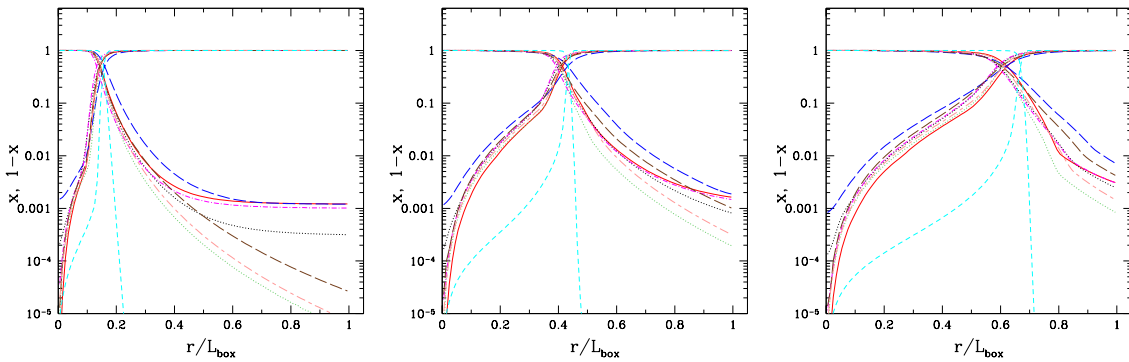


Figure 11. Test 5 (H II region expansion in an initially-uniform gas): Spherically-averaged profiles for ionized fractions x and neutral fractions $x_{\text{HI}} = 1 - x$ at times $t = 10$ Myr, 200 Myr and 500 Myr vs. dimensionless radius (in units of the box size).

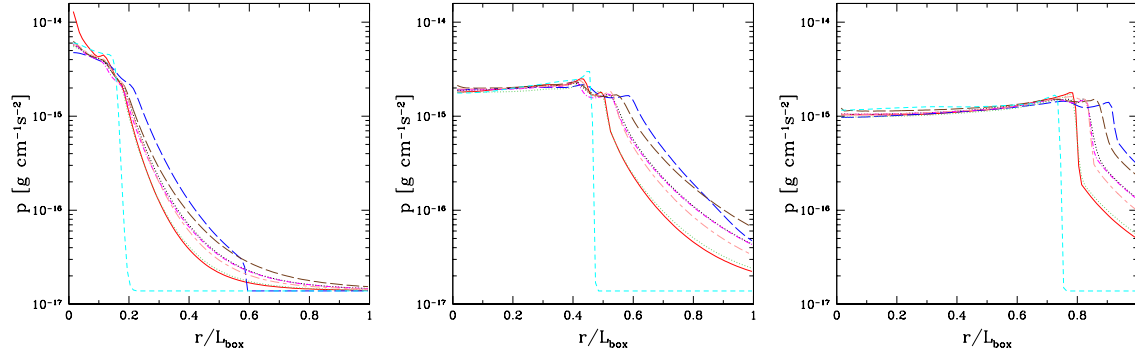
16 *I. T. Iliev, et al.*

Figure 12. Test 5 (H II region expansion in an initially-uniform gas): Spherically-averaged profiles for pressure, p , at times $t = 10$ Myr, 200 Myr and 500 Myr vs. dimensionless radius (in units of the box size).

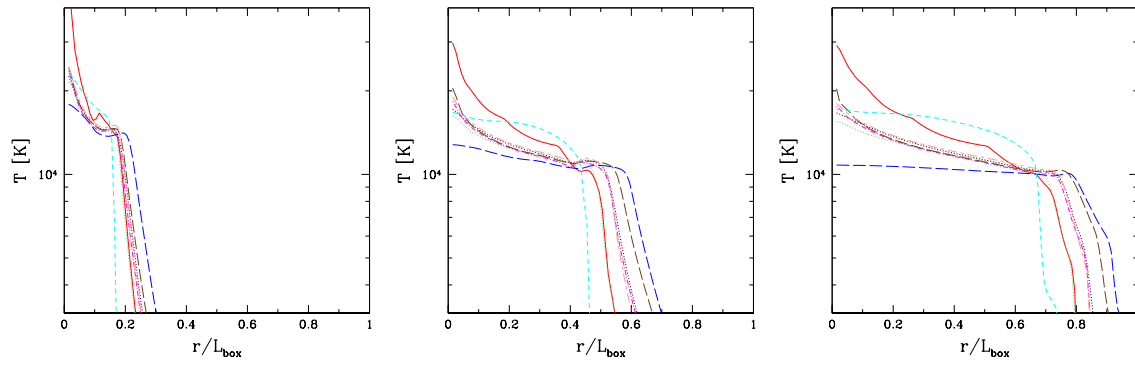


Figure 13. Test 5 (H II region expansion in an initially-uniform gas): Spherically-averaged profiles for temperature at times $t = 10$ Myr, 200 Myr and 500 Myr vs. dimensionless radius (in units of the box size).

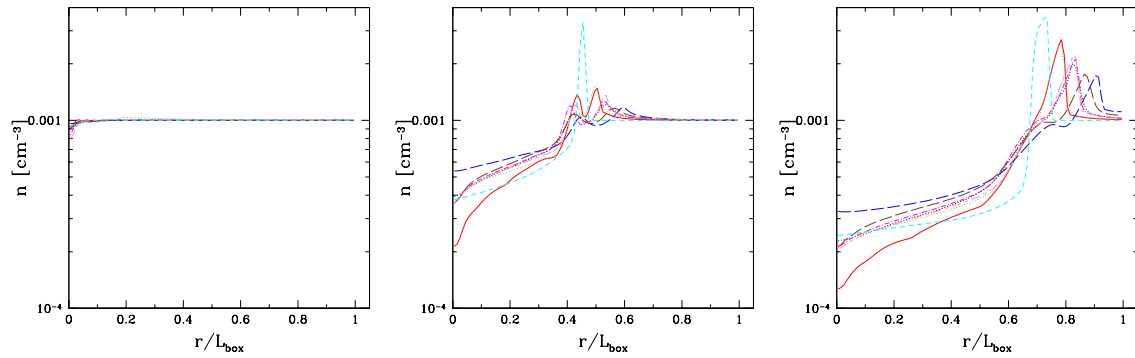


Figure 14. Test 5 (H II region expansion in an initially-uniform gas): Spherically-averaged profiles for the hydrogen number density, n , at times $t = 10$ Myr, 200 Myr and 500 Myr vs. dimensionless radius (in units of the box size).

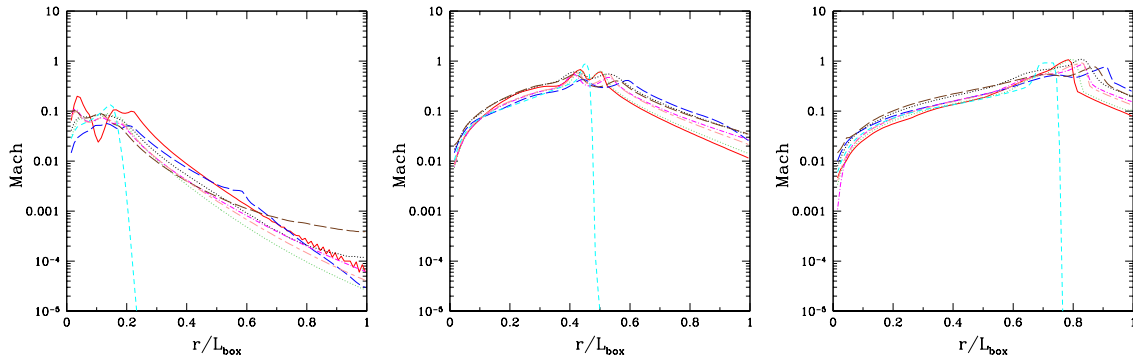


Figure 15. Test 5 (H II region expansion in an initially-uniform gas): Spherically-averaged profiles for the flow Mach number, M , at times $t = 10$ Myr, 200 Myr and 500 Myr vs. dimensionless radius (in units of the box size).

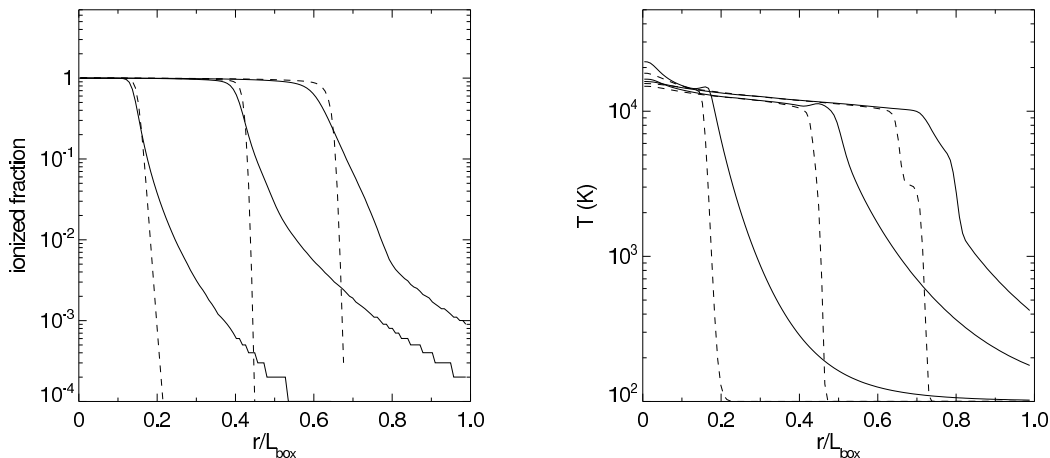


Figure 16. ZEUS-MP Test 5 ionized fraction (left) and temperature (right) profiles with monoenergetic photons (dashed) and a 10^5 K blackbody spectrum (solid) at times $t = 10$ Myr (left pairs), 200 Myr (central pairs) and 500 Myr (right pairs) vs. dimensionless radius (in units of the box size).

order to run the non-periodic test problems in this comparison. The LICORICE, and to a lesser extent the RSPH Mach number results exhibit a somewhat grainy structure deep inside the H II region not visible in the other quantities. The origin of these features is likely due to the low SPH resolution in the evacuated interior of the H II region, which is nearly an order of magnitude lower in density than its surroundings. The difference in the degree of graininess between the two SPH codes may in part be due to how each code's particle data was mapped onto the Cartesian grid. The origin of the third outermost band in the RSPH Mach numbers, which is not present in those of the other codes, is likely due to the utilization of a larger box in that calculation compared to the other cases, which changes the flow boundary conditions.

The only code whose results are markedly different from the rest is Enzo. This is primarily due to the fact that this code in its current form severely suppresses the propagation of hard photons

ahead of the I-front. The probable reasons for this are the use of a single radiation energy field (i.e. essentially a gray approximation for the photoionization cross-section) that does not allow transport of higher-frequency radiation through the neutral hydrogen region, and the flux-limited diffusion approximation for the radiation that retains a sharp radiation front for causal propagation. The lack of the hard photons yields no pre-heating running ahead of the front and therefore much sharper transition at the front itself. This lack of pre-heating in turn means that the shock which forms is stronger, as evidenced by the somewhat higher Mach number, density compression and pressure jump as compared to the other results, although the shock still remains a weak one. As a consequence, the shock also propagates slower compared to the rest. Interestingly, in the case of Enzo the I-front is in fact faster than the others, almost coincidental in space with the shock, in marked contrast with the other results where the I-front lags well behind the corresponding

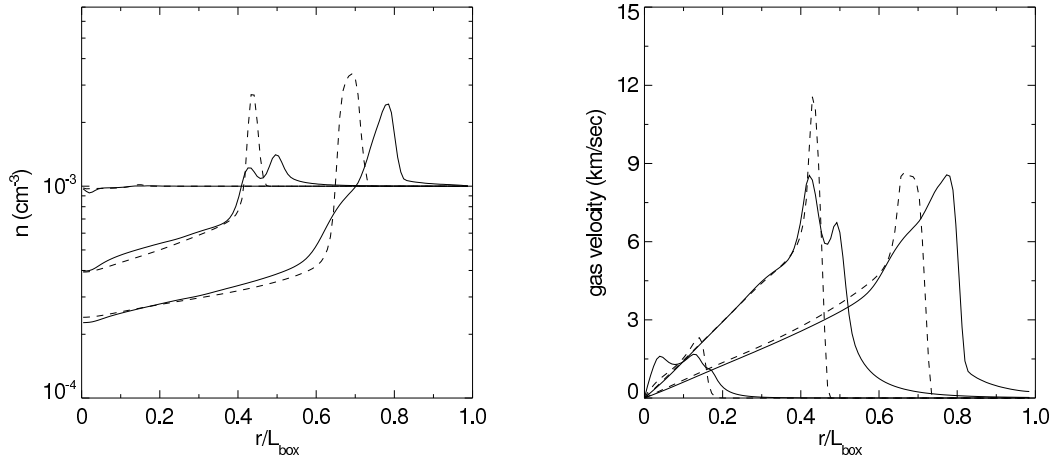
18 *I. T. Iliev, et al.*

Figure 17. ZEUS-MP Test 5 density (left) and gas velocity (right) profiles with monoenergetic photons (dashed) and a 10^5 K blackbody spectrum (solid) at times $t = 10$ Myr (left pairs), 200 Myr (central pairs) and 500 Myr (right pairs) vs. dimensionless radius (in units of the box size).

shock. The faster I-front propagation is due to the higher on average temperature inside the H II region found by Enzo, which results in lower recombination rate and less absorption inside the H II region. The temperature is also more uniform and has no peak near the ionizing source. This temperature profile is similar to the flat profile found by HART (but at a higher value), and is similarly due to the more diffusive nature of the flux-limited diffusion radiative transfer employed compared to the ray-tracing methods.

An interesting double-peaked feature is seen in the radially-averaged profiles at $t = 200$ Myr (Figures 14 and 15). This feature is transient and disappears by $t = 500$ Myr. Its lead cause appears to be the preheating of the dense shocked neutral gas swept up by the I-front by the hard UV photons in the high-energy tail of the 100,000 K blackbody spectrum, combined with some compression heating. To illustrate this, we show ionized fractions, temperatures, velocities, and densities in Figures 16 and 17 for two ZEUS-MP runs at times $t = 10$, 200, and 500 Myr. The first run is Test 5 with all its parameters intact, except for using ionizing flux of monoenergetic photons at 17.0 eV rather than a 10^5 K blackbody energy distribution. The second run is the original ZEUS-MP multifrequency calculation for Test 5. The use of 17.0 eV photons yields post-front gas temperatures that are slightly lower than those of the full blackbody spectrum, which causes the I-front to lag increasingly behind its multifrequency counterpart over time. At 200 Myr, there is a prominent layer of partially ionized gas in the outer layers of the multifrequency front that is absent in the monoenergetic front: ionized fractions of 10% or more extend out to $0.5 L_{\text{box}}$. The high frequency tail of the spectrum cannot maintain large ionized fractions in this region, but does effectively deposit heat there, as evidenced by the rise in temperature at $0.45 L_{\text{box}}$. This energy ablates the lower layer of the dense shocked shell being driven by the I-front, driving both inward and outward photoevaporative flows in the frame of the shock that divide the density peak into two smaller ones. The forward flow accelerates the gas in the outer peak to 7 km s^{-1} by 200 Myr. However, pressure gradients from the ionized

[h]

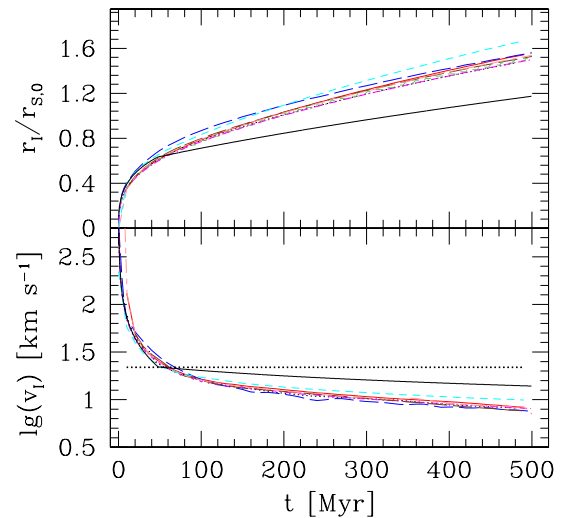


Figure 18. Test 5 (H II region) gasdynamic expansion in an initially-uniform gas): The evolution of the position and velocity of the I-front. Solid lines show the approximate analytical solution as described in the text. Dotted horizontal line indicates the approximate value of v_R .

interior of the H II region drive the inner peak to higher velocities that overtake the forward peak by 500 Myr. At this distance from the central source, high energy photons continue to heat the base of the shocked shell but not to sufficient temperatures to generate

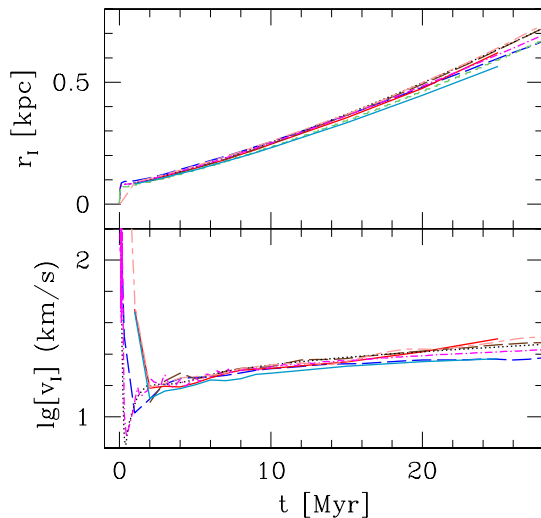


Figure 19. Test 6 (H II region gasdynamic expansion down a power-law initial density profile): The evolution of the position and velocity of the I-front.

backflow, as seen in the disappearance of the temperature bump that was present at 200 Myr.

In contrast, the temperature and velocity profiles of the monoenergetic front exhibit a much simpler structure. At 500 Myr, 15,000 K ionized gas drives a clearly defined 3000 K shocked shell. In contrast, energy deposition by high energy photons smears out the density and ionization profiles of the multifrequency front, even at 500 Myr. The reverse ablation flow in the frame of the shock is conspicuously absent from the velocity profiles of the monoenergetic I-front. The absence of backflows allow peak gas velocities to reach higher values at intermediate times than in the hard spectrum case. We note that the Enzo results, similarly ran with monoenergetic photons, also lack this double-peaked feature. It is clear from this comparison that multifrequency photon transport, or the use of optical depth lookup tables as a proxy, is necessary to capture the correct structure of I-fronts and shocks driven by high temperature UV sources.

Except for the variations noted above, the codes agree well on I-front position and velocity but are at variance with the analytical solution, leading it by roughly 30%. This is in part because the solution plotted in Figure 17 is for fixed temperatures of 15,000 K behind and 1000 K ahead of the I-front (allowing for some pre-heating by hard photons), while in reality the solution exhibits complex temperature structure. Furthermore, as we discussed above the analytical solution describes well the early and late evolution, but not the intermediate one. The H II region radial evolution at late times does not exactly match the asymptotic $t^{4/7}$ slope predicted for self-similar flows but approaches it at larger radii. This is to be expected since the box size was chosen to enclose only the transition of the I-front from R-type to D-type, during which the assumption of self-similarity is not satisfied. The codes asymptotically approach the expected solution as the fronts grow in radius.

Finally, we note that the I-fronts in this test are dynamically stable. If H₂ cooling, LW photodissociation, and self-shielding to

LW photons had been included, violent hydrodynamical instabilities mediated by H₂ cooling might have erupted in the fronts after becoming D-type, as explained in greater detail in Test 6 below. Line cooling in H alone appears unable to incite such instabilities (Whalen & Norman 2008b).

4.2 Test 6

We start our analysis with head-to-head comparison of the evolution of the position and velocity of the I-front, plotted in Figure 19. In the velocity plot we clearly see the evolution stages outlined in the discussion of Test 6 above. Initially, while it is still within the density core the I-front moves very fast (is of R-type), but precipitously slows down as it approaches its Strömgen radius (whose precise value is temperature-dependent, but is slightly smaller than the core radius chosen here). The fast R-type phase is over within a fraction of a Myr, after which the expansion becomes pressure-driven, and the front itself converts to a D-type led by a shock. The I-front speed reaches a minimum of just a few kilometers per second, well below v_R - the critical velocity defined in § 3.1. We note that although some of the results appear to never show I-front velocities below ~ 10 km/s, this is in fact due to insufficient number of early-time snapshots being saved in the I-front evolution data. This results in this early, short evolution stage not showing in the plotted results. However, this does not necessarily indicate any problem with those codes. The later-time evolution is not affected, as long as the actual time-stepping in the code is sufficiently fine to properly follow the early evolution. Once out of the core, the I-front re-accelerates as it descends the steep r^{-2} density gradient, eventually reaching speeds of 25 – 28 km/s. These speeds never surpass v_R and therefore the front remains D-type until leaving the computational volume at $t \sim 30$ Myr.

All codes agree on the later-time, pressure-driven expansion, both qualitatively (a slow, D-type I-front, preceded by a relatively weak, as we shall see below, shock), and quantitatively. There are some modest differences in the I-front speed, $\sim 10\%$ or less between cases, which results in I-front positions whose departure grows with time, but never exceeds $\sim 5 - 7\%$.

Next we turn our attention to the overall structure of the fluid flow and ionization, shown in Figures 20 - 24, which show 2-D cuts along the x-y plain of the H I and H II fractions, density, temperature and Mach number at time $t = 25$ Myr. There is a significant level of agreement between the results, in terms of the positions of the I-front and the shock, the size of the forming H II region and its ionization, density and temperature structures. There are some differences in the level of hard photon penetration ahead of the I-front and the temperature distribution, similar to the ones we observed in Test 5 and Paper I.

However, in this test also a new kind of difference shows up, namely the appearance of instabilities near the I-front. Such instabilities occur for several of the codes, and their nature varies between codes. In the cases of C²-Ray+Capreole and LICORICE, the instabilities are clearly visible in the ionized fractions, temperatures, densities, and Mach numbers, while in Flash-HC they are mostly visible in the temperatures and ionized fractions. RSPH exhibits a minor anomaly in only the temperature at 25 Myr. The RHID data cannot exhibit such instabilities because they are 1D spherical polar coordinate profiles mapped onto the 3D Cartesian grid mandated for this test. The ZEUS-MP profiles, which were computed on a 3D spherical polar coordinate grid and then mapped onto 3D Cartesian coordinates, manifest no instabilities in any of

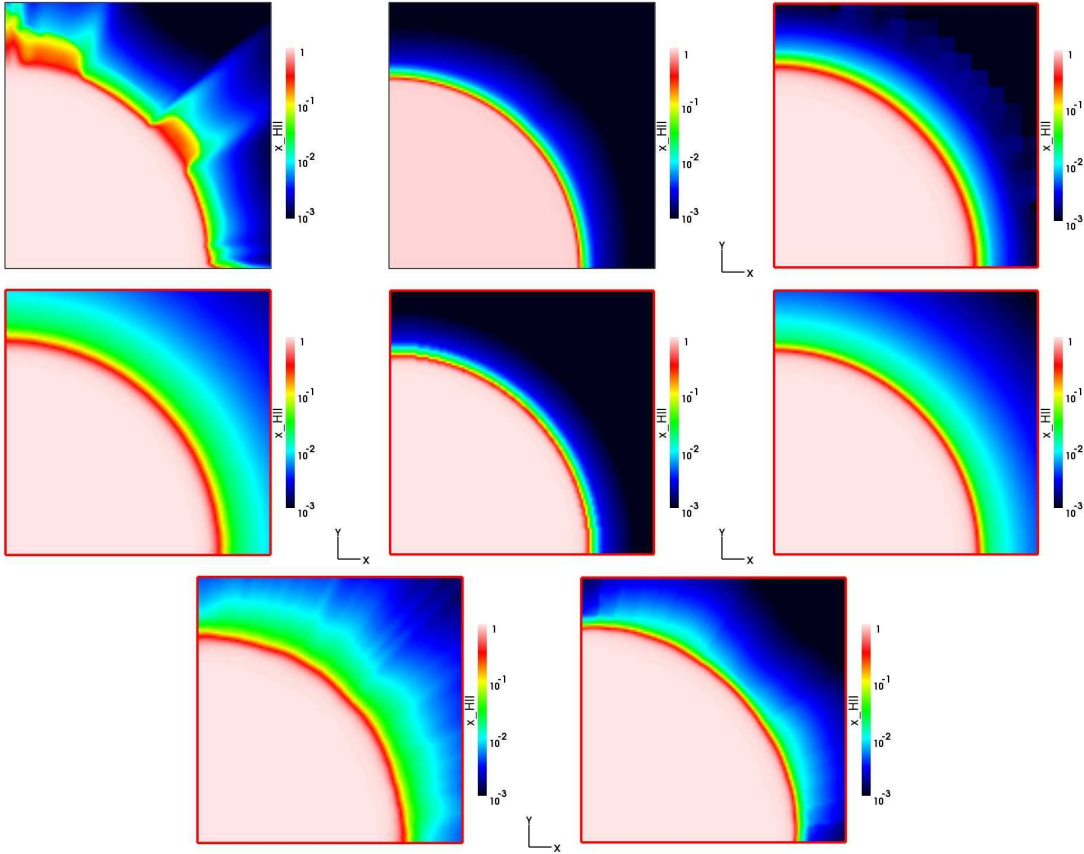


Figure 21. Test 6 (H II region gasdynamic expansion down a power-law initial density profile): Images of the H II fraction, cut through the simulation volume at coordinate $z = 0$ at time $t = 25$ Myr for (left to right) and top to bottom) Capreole+C²-Ray, TVD+C²-Ray, HART, RSPH, ZEUS-MP, RH1D, LICORICE, and Flash-HC.

at early times reveal that they are the infamous ‘carbuncle’ phenomenon or ‘odd-even decoupling’ (Quirk 1994). Low-diffusion solvers, such as the Roe Riemann solver employed in Capreole used with C²-Ray in this test, sometimes suffer from these numerical instabilities. They occur when shocks travel parallel to one of the coordinate axes, in this case beginning near the symmetry axes of the expanding shell. These instabilities are well-known and mostly understood, although their occurrence is not always predictable. Although by 25 Myr most of the shell has been disrupted, we find that the perturbations begin near the axis and exhibit the characteristic morphology of the carbuncle instability. While the usual solution is to artificially introduce more diffusion only where it is needed, this approach did not suppress the phenomenon in C²-Ray. If the test is instead run with C²-Ray coupled to the TVD solver of Trac and Pen (Trac & Pen 2004), which is more diffusive and not known to suffer from the carbuncle instability, the shell indeed remains well behaved. We also note that this carbuncle instability, while fairly violent does not in fact affect the fluid flow and I-front propagation significantly, and the I-front position and velocity evolution discussed above and the spherically-averaged profiles discussed below are still in good agreement with the other results.

Another possibility is that there is a hitherto unknown break-

out instability associated with the transition of the D-type I-front back to R-type as it descends the density gradient. However, such an instability would not have the opportunity to propagate throughout and disrupt the entire shell during breakout as in the C²-Ray results because the transition from D-type to R-type is too abrupt, and, as discussed above the I-front remains D-type within the computational volume. Such an instability would instead be manifest as a premature supersonic runaway of radiation from the surface of the shell along certain lines of sight with little disruption of the shell itself, as observed in the Flash-HC results. However, this does not happen in the ZEUS-MP profiles, which are computed on a 3D spherical coordinate grid that is naturally suited to spherically-symmetric density fields and on which the ‘corner’ effects inherent in Cartesian grids are absent. Furthermore, as the spherically averaged profiles show, the I-front in this test is not on the verge of breaking past the shock and becoming R-type at late times. We therefore conclude that the instability in the Flash-HC results is not physical and that the early breakout of radiation there is at least partly the result of gridding a spherical density on a Cartesian grid. The effect of this is fairly modest, however, and does not disturb the overall dynamics significantly.

The irregular morphology of the shell in the LICORICE re-

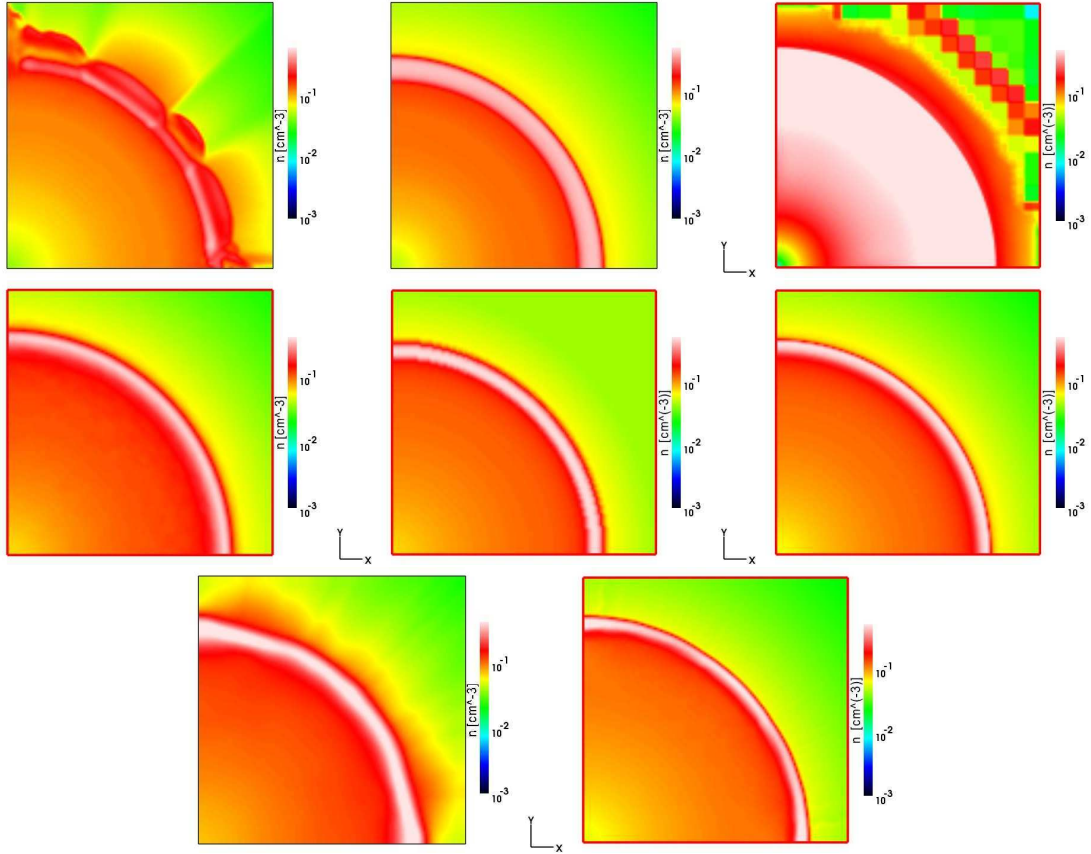
22 *I. T. Iliev, et al.*

Figure 22. Test 6 (H II region gasdynamic expansion down a power-law initial density profile): Images of the density, cut through the simulation volume at coordinate $z = 0$ at time $t = 25$ Myr for (left to right and top to bottom) Capreole+C²-Ray, TVD+C²-Ray, HART, RSPH, ZEUS-MP, RH1D, LICORICE, and Flash-HC.

sults and to a small extent in the RSPH profile at 25 Myr is likely due to spurious fluctuations in the density field where the local particle number changes sharply, in this case in the vicinity of the dense shell. This well-known feature of SPH, as discussed in section 2.7, is what probably allows radiation to preferentially advance along lines of sight through low-density fluctuations in the two profiles. The larger effects for LICORICE compared to RSPH are probably due to the usage in the former of a grid to perform the radiative transfer. Once again, none of these effects appears to affect the overall evolution significantly, but they might matter in certain astrophysical situations.

The HART results exhibit banding in all the profiles except for HI fraction at 25 Myr. The origin of these features is unclear, but is possibly related to the much coarser AMR gridding used around the outer edges. They may also be related to the greater diffusivity of the OTVET algorithm, although no such features were observed in the other tests performed with OTVET. However, the density profile found by HART is much flatter, with no clear dense shell swept by the shock, in clear contrast to all other results. It is possible that the time step applied to the gas energy updates in HART is too coarse for I-fronts in r^{-2} density gradients, which has been found to lead

to banding in temperatures and densities in H II regions in stratified media (Tenorio-Tagle et al. 1986; Whalen & Norman 2006).

We finally note that had H₂ cooling been included in either this test or in Test 5, violent physical instabilities might have arisen in the I-front when it became D-type (Whalen & Norman 2008a). Hard UV spectra significantly broaden ionization fronts, forming regions of a few thousand K and ionized fractions of 10% in their outer layers. These are prime conditions for the catalysis of H₂ via the H⁻ channel, which forms between the I-front and the dense shocked shell when the front becomes D-type (Ricotti et al. 2002). H₂ - H, H₂ - e⁻, and H₂ - H⁺ collision channels emit ro-vibrational lines (Lepp & Shull 1983; Galli & Palla 1998b; Glover & Abel 2008) that can radiatively cool the base of the shocked layer and incite dynamical instabilities there just as metal ions do in galactic I-fronts. These instabilities may have been common in the early universe, such as in UV breakout from the first star-forming clouds. They appear if there is enough H₂ in the cloud to self-shield from the Lyman-Werner (LW) flux (11.18-13.6 eV) also being emitted by the source, which photodissociates molecular hydrogen (Draine & Bertoldi 1996). Thus, while the instabilities manifested by some of the codes in Test 6 are numerical, physical ones are possible when H₂ cooling, LW photons, and self-shielding to LW radiation

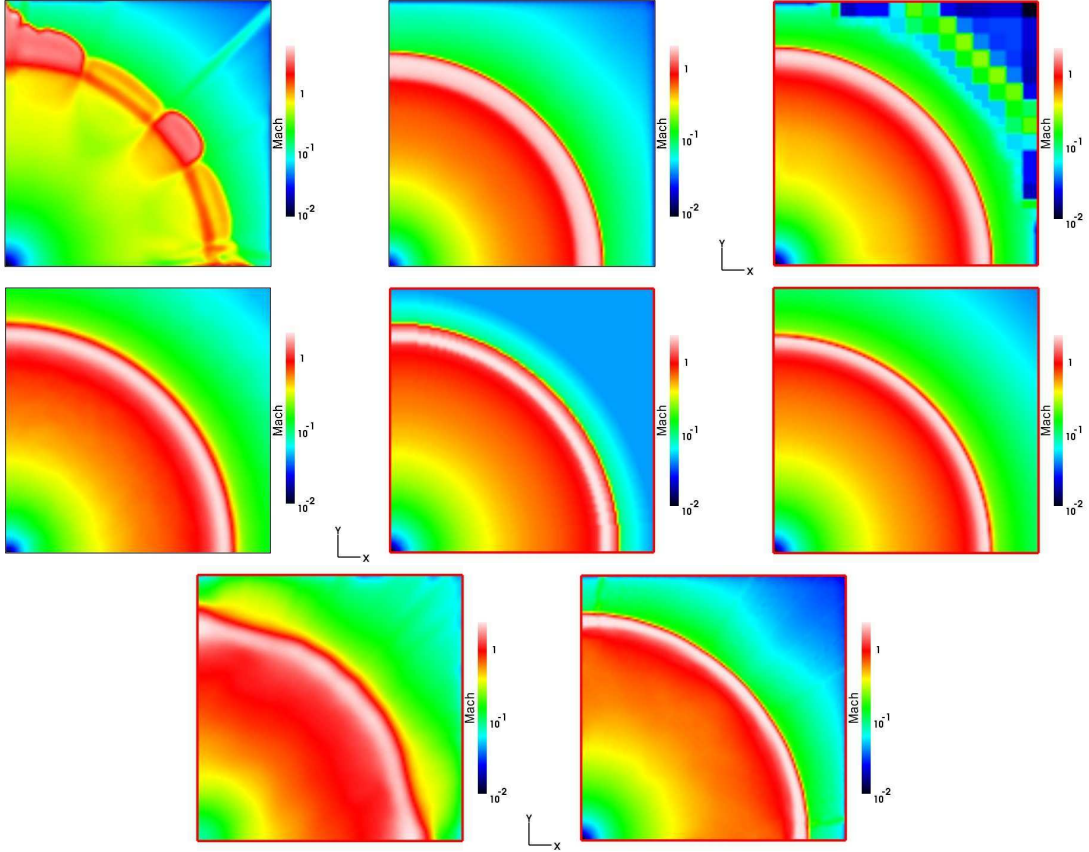


Figure 23. Test 6 (H II region gasdynamic expansion down a power-law initial density profile): Images of the Mach number, cut through the simulation volume at coordinate $z = 0$ at time $t = 25$ Myr for (left to right) and top to bottom) Capreole+ C^2 -Ray, TVD+ C^2 -Ray, HART, RSPH, ZEUS-MP, RH1D, LICORICE, and Flash-HC.

are properly included. Since not all the codes contain these physical processes, it was not included in any of the current tests, but will be a target for future stages of this comparison project.

In spite of the prominence of the numerical instabilities in some of the codes, we re-iterate that they were not catastrophic to the overall dynamics, as shown by the spherically averaged hydrodynamical profiles. In Figs 25 - 29 we show ionization fractions, number densities, pressures, temperatures and Mach numbers at 3, 10, and 25 Myr. Comparison of ionization fractions and densities at 3 Myr indicates that the I-front is D-type at $r \sim 120$ pc, somewhat beyond the flat central core of the initial density profile. A thin layer of shocked neutral gas that is not yet fully detached from the I-front is visible at $r \sim 140$ pc in the Mach number profile. Acoustic waves are evident at $r < 100$ pc within the H II region in both the density and Mach number plots and are consistently reproduced by all the codes.

At this early stage, the I-front widths (customarily defined by the difference between the positions at which 0.1 and 0.9 ionization fractions are reached) vary from ~ 20 pc to 40 pc. At the relatively high inner-profile density of $n \sim 1 \text{ cm}^{-3}$, the mean free paths (mfp) of 13.6 eV and 60 eV photons, which roughly bracket the available energies in the 10^5 K black-body spectrum used for this test,

are ~ 0.05 pc and 4 pc, respectively. The intrinsic width of the I-front is approximately 20 mean-free paths, or between 1 and 80 pc. Therefore, all the codes give widths roughly consistent with the expected values, but somewhat on the wider side, primarily due to the diffusivity of some of the algorithms. In particular, LICORICE and HART have wider fronts, while ZEUS-MP has the narrowest one and the rest are spread between those two extremes. As explained above, the details of the structure of the I-front are interesting since they relate to the formation of molecular hydrogen in its outer layers (e.g. Ricotti et al, 2002) where hard, deeply penetrating photons could yield a positive feedback mechanism during early structure formation. The post-front (ionized) gas temperatures of the codes at these early times differ by at most 10%. The low Mach numbers outside the H II region at early times, ranging from 0.001 to 0.01 arise because hydrostatic equilibrium was not imposed on the original density profile in any of the codes except for ZEUS-MP. Pressure forces gently accelerate the gas outward, but this has little effect on the late-time evolution of the H II region. For the purposes of this comparison the lack of initial pressure equilibrium is of course irrelevant, as long as all codes start from the same initial conditions.

By 10 Myr the H II region has grown to 240 pc, with all results

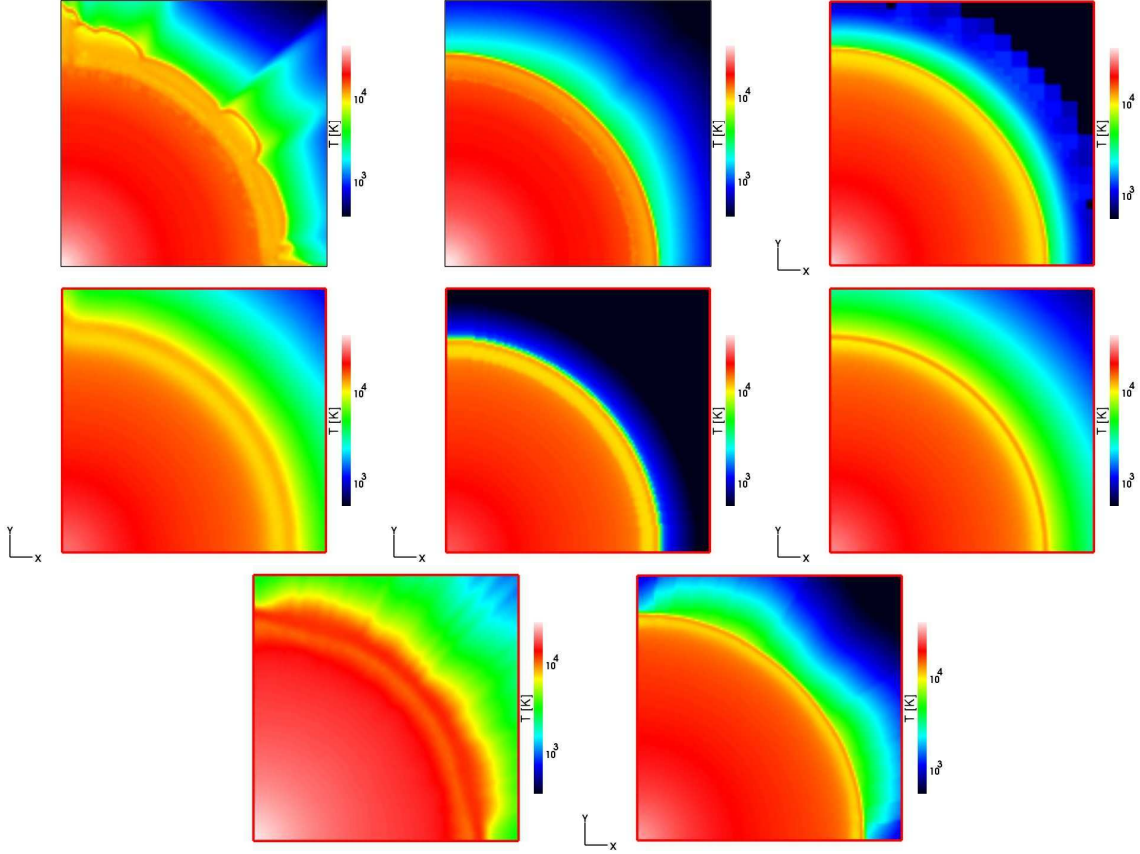
24 *I. T. Iliev, et al.*

Figure 24. Test 6 (H II region gasdynamic expansion down a power-law initial density profile): Images of the temperature, cut through the simulation volume at coordinate $z = 0$ at time $t = 25$ Myr for (left to right and top to bottom) Capreole+C²-Ray, TVD+C²-Ray, HART, RSPH, ZEUS-MP, RH1D, LICORICE, and Flash-HC.

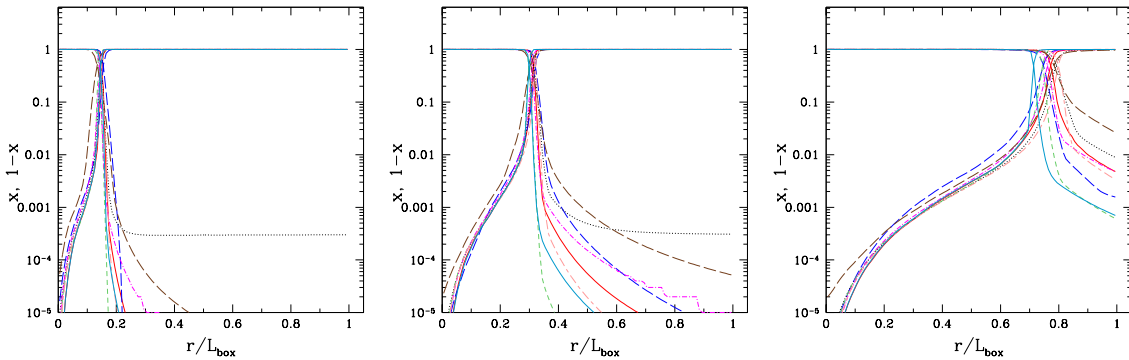


Figure 25. Test 6 (H II region gasdynamic expansion down a power-law initial density profile): Spherically-averaged profiles for ionized fractions x_i and neutral fractions $x_{\text{HI}} = 1 - x_i$ at times $t = 3$ Myr, 10 Myr and 25 Myr vs. dimensionless radius (in units of the box size).

Cosmological Radiative Transfer Codes Comparison II 25

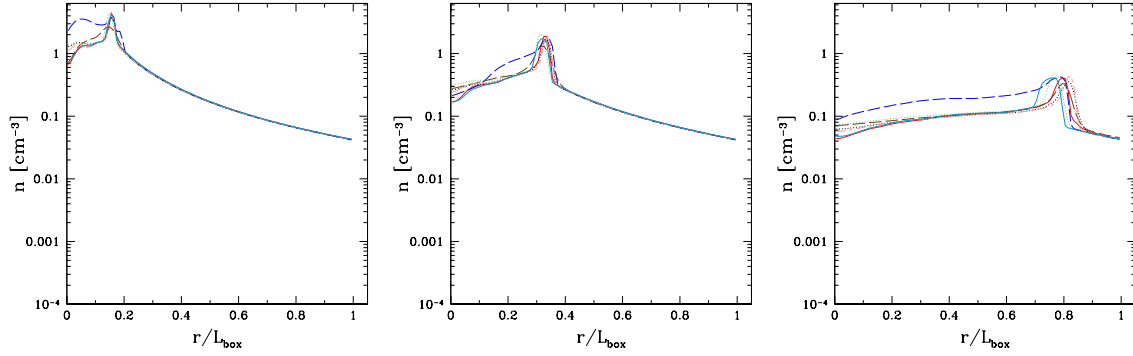


Figure 26. Test 6 (H II region gasdynamic expansion down a power-law initial density profile): Spherically-averaged profiles for the gas number density, n , at times $t = 3$ Myr, 10 Myr and 25 Myr vs. dimensionless radius (in units of the box size).

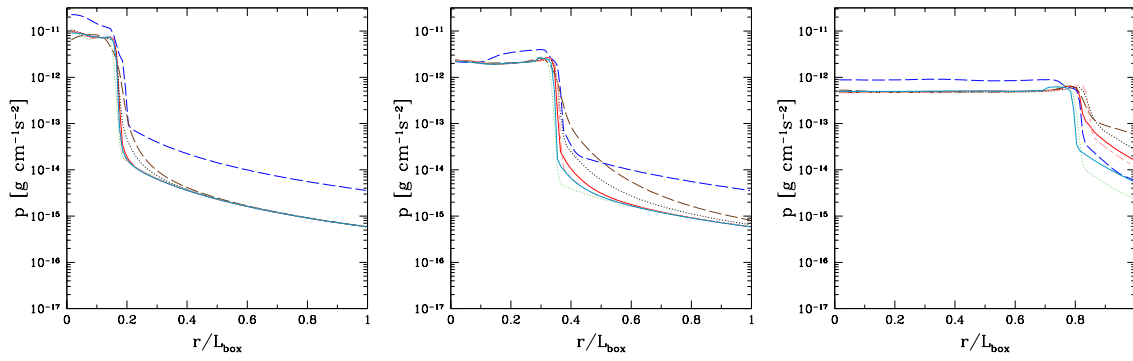


Figure 27. Test 6 (H II region gasdynamic expansion down a power-law initial density profile): Spherically-averaged profiles for pressure, p , at times $t = 3$ Myr, 10 Myr and 25 Myr vs. dimensionless radius (in units of the box size).

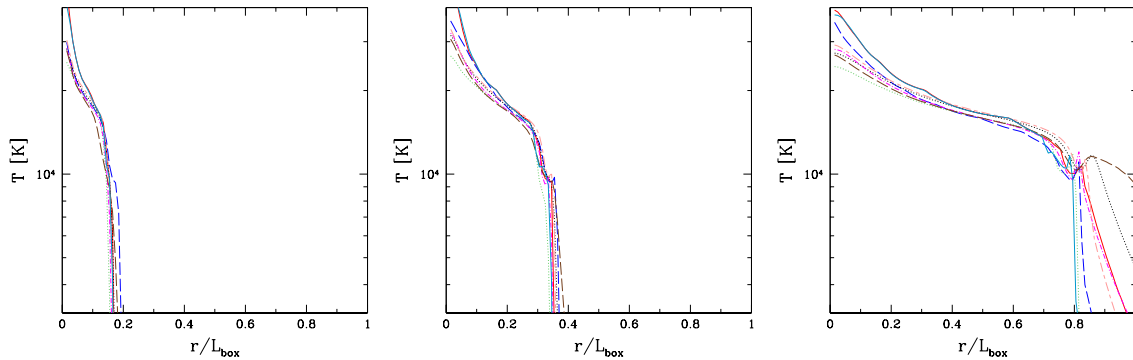


Figure 28. Test 6 (H II region gasdynamic expansion down a power-law initial density profile): Spherically-averaged profiles for temperature at times $t = 3$ Myr, 10 Myr and 25 Myr vs. dimensionless radius (in units of the box size).

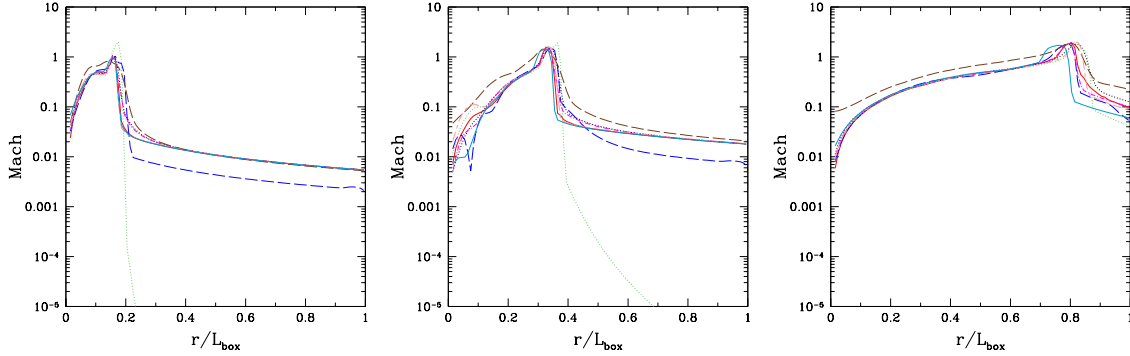
26 *I. T. Iliev, et al.*

Figure 29. Test 6 (H II region gasdynamic expansion down a power-law initial density profile): Spherically-averaged profiles of the Mach number at times $t = 3$ Myr, 10 Myr and 25 Myr vs. dimensionless radius (in units of the box size).

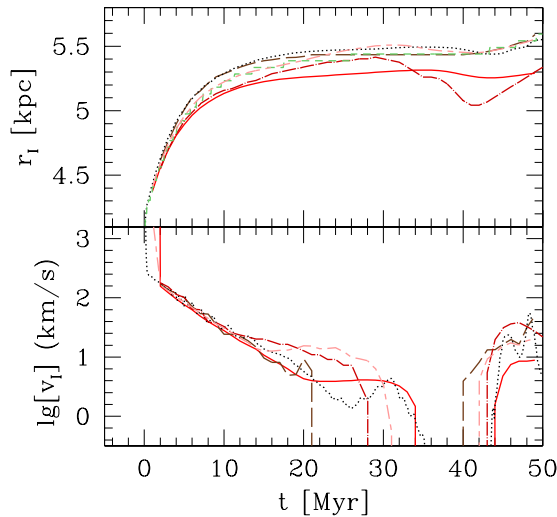


Figure 30. Test 7 (Photoevaporation of a dense clump): The evolution of the position and velocity of the I-front.

agreeing well on the I-front position. There is very little variation in the ionization structure inside the H II region, with only LICORICE finding a slightly lower level of ionization. The differences in the pre-front ionization structures are much more pronounced, underlying again the variety in the treatments of multi-frequency photons. All the codes still find postfront gas temperatures within 10% of one another at most radii. The temperature profiles drop sharply just beyond the I-front as before, but then briefly plateau at 10^4 K for ~ 16 pc before falling further. This is the dense ambient neutral gas shell-swept up by the shock, clearly seen in the density profiles (Figure 26), which is now fully detached from the front and is sufficiently hot and dense to become collisionally ionized to a small degree. However, the minute residual ionized fractions (10^{-4} - 10^{-3}) in and beyond the shell in most of the plots occur because the I-front broadens over time. As more neutral gas accumulates on

the shell with the expansion of the H II region, its density decreases because its area grows, and its optical depth to photons in the high-energy tail of the spectrum decreases. ZEUS-MP still finds the sharpest I-front and LICORICE the thickest, with the rest dispersed between. No single cause can be ascribed to the moderate variation in I-front structure amongst the codes; for example, both ZEUS-MP and RHID perform multifrequency ray-tracing radiative transfer with similar integration schemes and frequency binning, but RHID has a noticeably wider I-front. Tabulating pre-computed frequency-dependent ionization rate integrals as a function of optical depth as an alternative to full multifrequency RT in Capreole+ C^2 -Ray leads to a somewhat different structure for the front. There is an unmistakable trend toward greater diffusivity with the SPH-coupled radiative transfer codes RSPH and LICORICE that likely related to the inherent difficulty in representing low-density regions with SPH particles and the tendency of SPH to broaden shocks. Nonetheless, the grid-based codes and RSPH agree to within a few percent on the density structure of the shocked shell at 10 Myr. LICORICE does not resolve the shell as well, but this would likely be remedied by using more particles to resolve the flow, or by using a more adaptive smoothing kernel. Overall, all codes agree reasonably well on the shock position and the corresponding density and pressure jumps (although, as was discussed above, HART yields higher and more uniform density and pressure distributions behind the shock than the other the methods, which agree on that quite well among themselves).

At 25 Myr the I-front is at 640 pc, approaching the boundary of our computational volume. At this stage the subsonic expansion of the front with respect to the sound speed in the ionized gas is evident: acoustic waves have erased density fluctuations up to the shocked shell in the pressure and density plots. The acceleration of the shock down the density gradient can be seen in the heating by the shock: the temperature of the dense shell is 25% greater than at 10 Myr. The velocities beyond the shock are now 20% of the sound speed of the neutral gas, and the peak density of the shell has fallen to 0.4 cm^{-3} . There is a 10% variation in the position of the I-front among the codes that is not attributable to differences in chemistry or radiative transfer because of the uniformity in ionized gas temperatures (and therefore sound speeds). More likely, it is due to the variety of hydrodynamics schemes (both grid and particle based) applied to the models. Apart from the diffusivity of some of the algorithms as manifest in I-front structure, we find good agreement

on the evolution of the H II region in this stratified medium between all the codes. Direct multifrequency RT and approximations to full multifrequency transfer with precomputed ionization integrals both yield extended I-front structures, but it is difficult to assess which is more accurate since even the two direct methods disagree with each other to some degree. The disagreement between the multifrequency codes on the width of the I-front is probably due to their discretization of the blackbody curve and resultant binning of ionizing photon rates according to energy, since they otherwise employ the same ionization cross sections and photon-conserving ray tracing. The number of bins per decade in energy and their distribution in frequency can lead to different thicknesses for the front. They have a much smaller effect on the temperature of the ionized gas, and therefore the position of the front, because the temperature is more strongly governed by the cooling rates than by minor discrepancies in spectral profile.

4.3 Test 7

The main phases of the evolution could be seen in Figure 30. The I-front starts off very fast, R-type in the low-density medium surrounding the dense clump, but slows down quickly once it enters the high-density gas, which occurs within less than a Myr. Thereafter the slowing down continues more gradually, as intervening column density on the source side gradually increases, decreasing through recombinations the ionizing flux which reaches the I-front. This initial trapping phase is largely over by $t = 1$ Myr, yielding a thin ionized layer in the dense clump on the source side and a clear shadow behind, as illustrated in Figure 31. Due to the short evolution time, by this point the gas is still essentially static and Test 6 reproduces the analogous stage in Test 3 in Paper I. There are only a few modest differences between the neutral gas distributions. The boundary of shadowed region "flares" especially for RSPH result, primary because their particle neighbour list based ray-tracing scheme inevitably introduces some "diffusion of optical depth". Flaring of boundary is also in part due to the interpolation procedures to set up the initial conditions which, with their sharp boundaries, are unnatural for SPH and thus difficult to represent well. In fact even grid-based codes encounter similar problems, since the at low resolution imposed introduces some grid artefacts when a dense spherical clump is laid, unless some interpolation procedure is introduced. (such procedures were used to set up the initial conditions for e.g. ZEUS-MP and C^2 -Ray in the current test). There is also slight striping of the neutral fraction in the low-density region for the case of Licorice, probably due to insufficient Monte-Carlo sampling, as was discussed earlier. However, this does not have any apparent effect on the evolution.

Once the front speed drops below v_R a shock starts to form ahead of it, converting it to D-type front. The photoheated material on the source side starts photoevaporating, by blowing supersonic wind towards the ionizing source. The I-front slowly eats its way into the dense clump, as shell after shell of gas boils off and joins the wind. The I-front velocity gradually drops to a few km/s and its position remains roughly constant. Some differences between the derived I-front evolution in position and velocity are observed, but they remain small throughout the evolution, never exceeding 10% in terms of position. In Figure 32 we show images of the neutral hydrogen fraction at $t = 10$ Myr. Overall results agree fairly well, with the expanding wind and shadow at very similar stages of evolution. There are also a few, relatively minor, differences which should be noted. The RSPH result remains somewhat more diffuse and asymmetric than the rest, as noted above, but the as the evolu-

tion proceeds the differences are somewhat less notable. However, the evolution in this case does proceed somewhat faster due to the inevitably more diffuse initial conditions. There is some leakage of light at the edges of the LICORICE shadow which is not seen in the other results and should therefore be related to the radiative transfer method employed, rather than to other factors, e.g. to the limb column density of the clump being small and allowing some light to go through. Finally, there are some uneven features at the edge of the shadow on the source side in the case of Flash-HC, whose origin is currently unclear.

The pressure distribution images at the same time $t = -10$ Myr (shown in Figure 33) essentially agree, with only minor morphological differences between the results. The shadow is somewhat thicker and less squeezed at the edges for C^2 -Ray, ZEUS-MP and Flash-HC, compared to RSPH and LICORICE, with Coral results intermediate between the two groups. The reason for this difference becomes apparent from the corresponding temperature images (Figure 34). In the cases of C^2 -Ray, ZEUS-MP and Flash-HC there is clear temperature gradient from the edges of the shadow going inward, while for RSPH and LICORICE this temperature gradient is largely absent. There are also noticeable temperature variations within the clump for C^2 -Ray, ZEUS-MP and Flash-HC which are less pronounced for RSPH and LICORICE. The reason for these differences appears to be the different levels of penetration by hard photons through the high column density material in the clump, and the corresponding varying levels of energy deposit by those photons. The evolution variations this introduces seem minor in our particular test problem, but such differences might matter more in problems in which the precise level of the number of free electrons and the local temperature within dense clumps is of importance. An example of such problem may be the study of the production of molecular hydrogen within dense regions irradiated by UV radiation, which can regulate (stimulate or suppress) local star formation (Iliev et al. 2006a). Finally, the Mach number images at $t = 10$ Myr are shown in Figure 35. The supersonic wind which starts to blow towards the ionizing source is clearly visible, with only small differences in terms of the thickness of this layer and the Mach number values between the different runs. The only peculiarity visible here is that in the case of ZEUS-MP this supersonic layer is almost spherical, surrounding the clump from all sides, which is not seen in any of the other results. This appears to be a consequence of the very cold ($T < 1000$ K) region remaining at the back of the clump, which is not present in any of the other results (see also Figure 43). The reason for this region remaining so cold in the Zeus simulation is unclear at present, considering that (as we discussed above) the spectrum hardening and penetration of hard photons through the clump and into the shadow are similar to C^2 -Ray, Flash-HC and Coral and stronger than RSPH and LICORICE.

By $t = 50$ Myr (Figures 36-39) the photoevaporation process is well advanced. The region swept by the expanding supersonic wind has grown quite large and takes significant fraction of the simulation volume. There are only modest differences in its size between the different codes. In the case of Flash-HC and, to a lesser extent Coral, the edge of the expanding wind region is uneven, as a consequence of the grid effects in the initial conditions, as discussed above, when representing a spherical object on a relatively coarse rectangular grid with no interpolation used. These grid effects could be seen at earlier times as well, but at a lower level. The overall size of the wind region is the same, however, thus this problem does not affect the evolution significantly.

A small core region from the initial clump remains neutral and

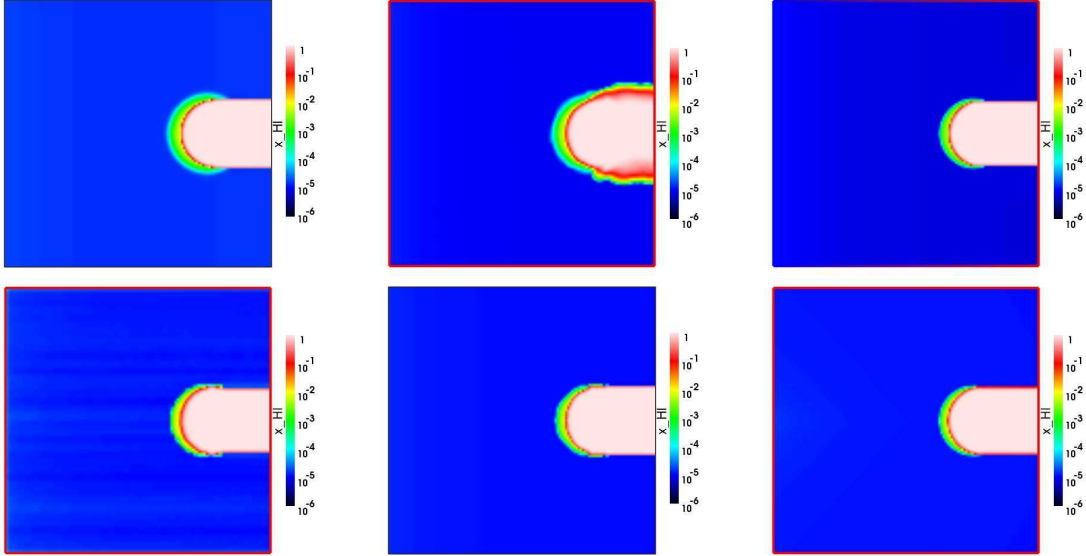
28 *I. T. Iliev, et al.*

Figure 31. Test 7 (Photoevaporation of a dense clump.): Images of the H I fraction, cut through the simulation volume at coordinate $z = 0$ at time $t = 1$ Myr for (left to right and top to bottom) Capreole+C²-Ray, RSPH, ZEUS-MP, LICORICE, Flash-HC and Coral.

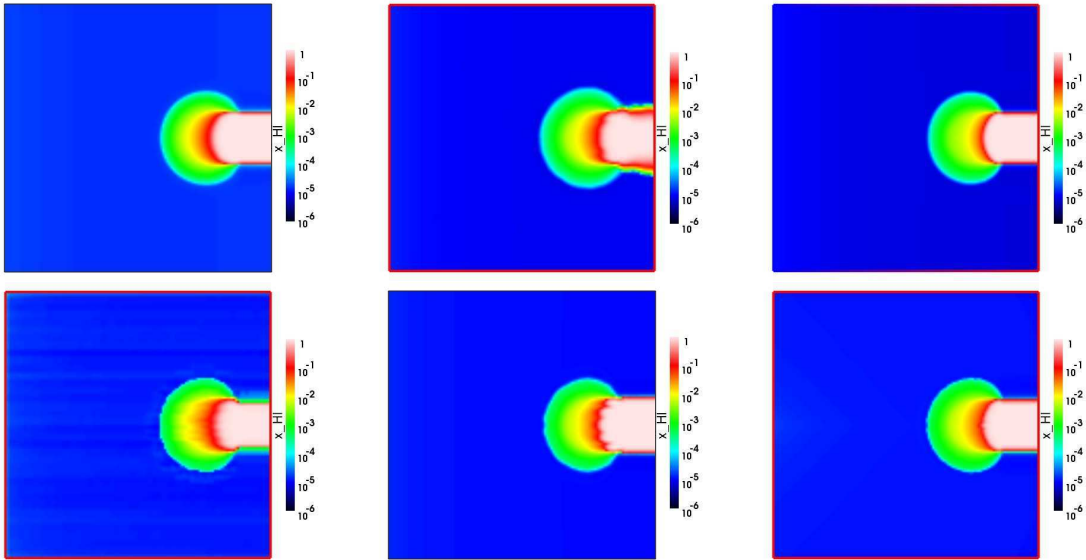


Figure 32. Test 7 (Photoevaporation of a dense clump.): Images of the H I fraction, cut through the simulation volume at coordinate $z = 0$ at time $t = 10$ Myr for (left to right and top to bottom) Capreole+C²-Ray, RSPH, ZEUS-MP, LICORICE, Flash-HC and Coral.

still casts a clear shadow which also remains neutral in all cases. This neutral region is moderately compressed by the higher external pressure of the ionized and heated gas surrounding it. The size of this neutral dense core and its shadow varies between the runs, being somewhat larger for Capreole+C²-Ray, Flash-HC and Coral than for RSPH, ZEUS-MP and LICORICE. There is also some ‘flaring’ (i.e. widening) of the shadow for Flash-HC and Coral,

probably due to the specific interpolation weighting used in the short characteristics methods they both employ (for discussion and testing of this see Mellema et al. 2006b, Appendix A).

In the pressure and temperature images shown in Figures 37 and 38 we clearly see the shocked shell of gas swept by the supersonic wind of evaporating clump material. The inner zone around towards the clump is being evacuated and is accordingly colder due

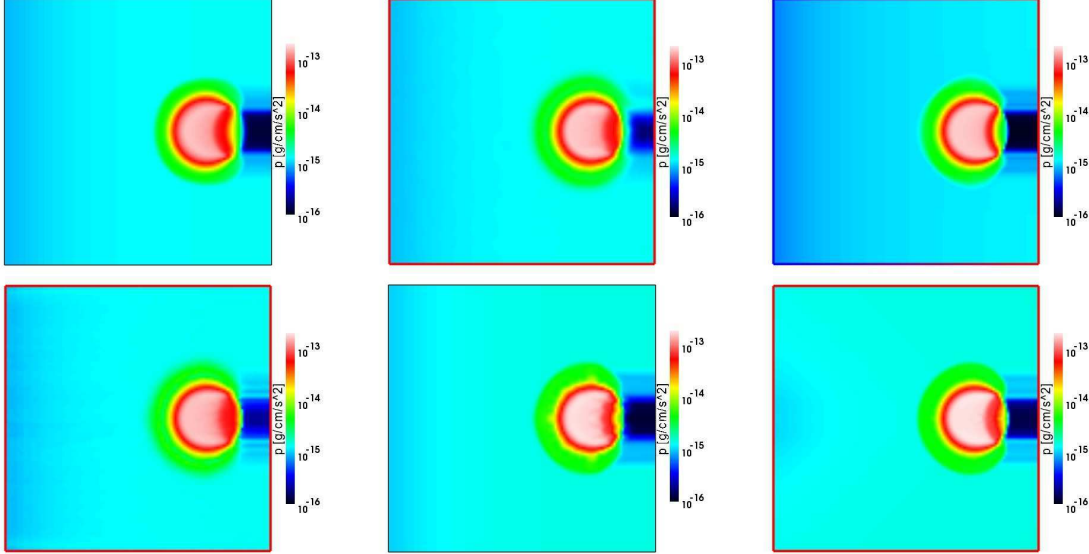


Figure 33. Test 7 (Photoevaporation of a dense clump): Images of the gas pressure, cut through the simulation volume at coordinate $z = 0$ at time $t = 10$ Myr for (left to right and top to bottom) Capreole+C²-Ray, RSPH, ZEUS-MP, LICORICE, Flash-HC and Coral.

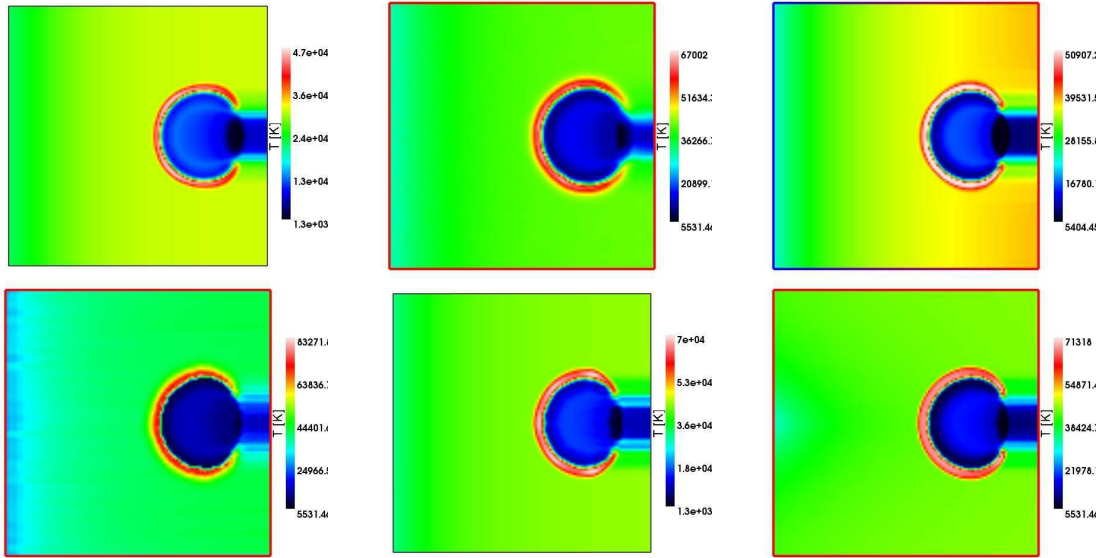


Figure 34. Test 7 (Photoevaporation of a dense clump): Images of the gas temperature, cut through the simulation volume at coordinate $z = 0$ at time $t = 10$ Myr for (left to right and top to bottom) Capreole+C²-Ray, RSPH, ZEUS-MP, LICORICE, Flash-HC and Coral.

to adiabatic cooling, while the outer shocked shell is much hotter, with temperatures reaching 40,000-70,000 K (note the different upper limits for the temperature images). Some quantitative and morphological differences are easily noticed. The evacuated region yields a shell of low pressure whose depth varies between the runs by about an order of magnitude, from the very low pressure $\sim 10^{-16}$ g/cm/s² found by Flash-HC, through the interme-

diated cases of RSPH and ZEUS-MP, to the relatively higher pressure $\sim 10^{-15}$ g/cm/s² found by Capreole+C²-Ray, LICORICE and Coral. The dense, high-pressure central region which remains neutral and the shadow behind it show quite different morphologies between the runs, clearly seen in the pressure images (less so in the temperature ones, due to the lack of color dynamic range). This morphology arises as a consequence of successive reflecting

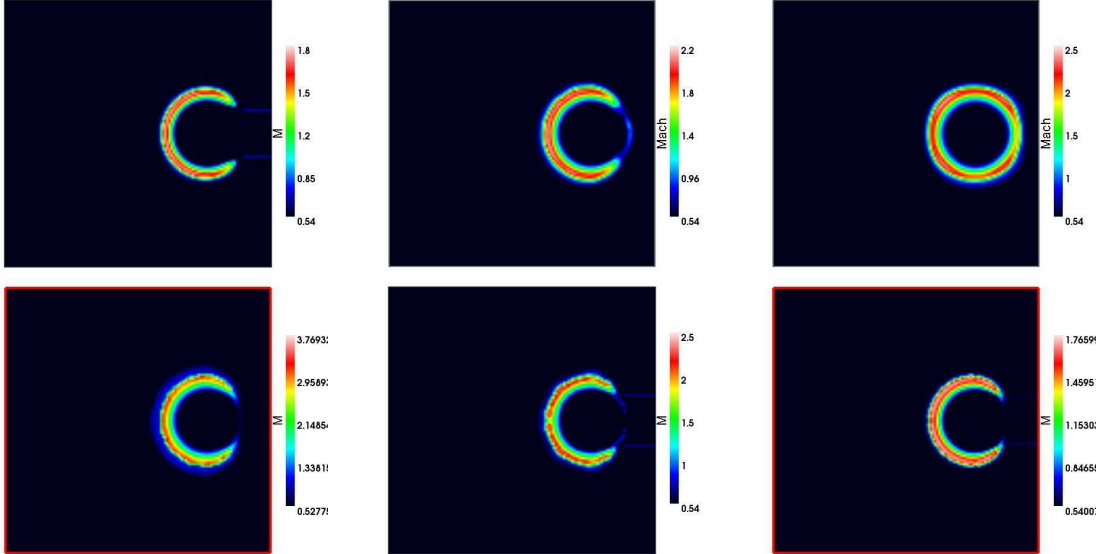
30 *I. T. Iliev, et al.*

Figure 35. Test 7 (Photoevaporation of a dense clump): Images of the flow Mach number, cut through the simulation volume at coordinate $z = 0$ at time $t = 10$ Myr for (left to right and top to bottom) Capreole+C²-Ray, RSPH, ZEUS-MP, LICORICE, Flash-HC and Coral.

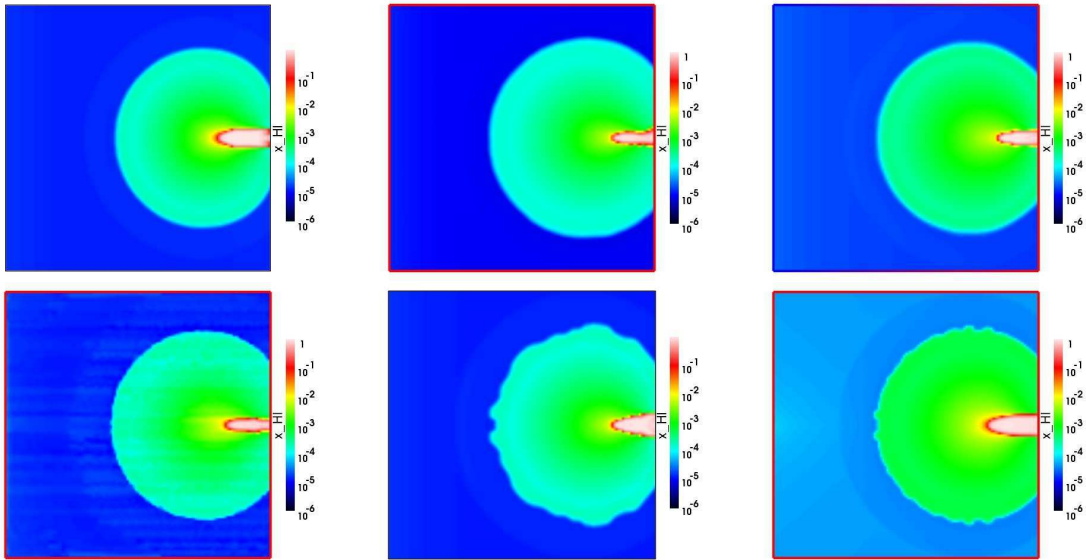


Figure 36. Test 7 (Photoevaporation of a dense clump): Images of the H I fraction, cut through the simulation volume at coordinate $z = 0$ at time $t = 50$ Myr for (left to right and top to bottom) Capreole+C²-Ray, RSPH, ZEUS-MP, LICORICE, Flash-HC and Coral.

oblique shocks which form behind the evaporating clump by the interaction between the evaporative wind and the squeeze of the shadow by the high external pressure of the ionized region. The reason for the morphological differences between the cases is most probably a slight difference in the timing of these shocks for each run, but ascertaining this will require more detailed analysis of the evolution.

Finally, the Mach number images at $t = 50$ Myr shown in Figure 39 show that while the wind is clearly supersonic, with Mach numbers of a few, the shocked swept material moves subsonically. The peak Mach numbers vary from 2 to 3.7, with typical peak values around 3. The shock is clearly somewhat weaker for Coral, consequence of this code's more diffusive hydrodynamic solver (based on van Leer flux splitting). All other methods, both Eulerian grid-

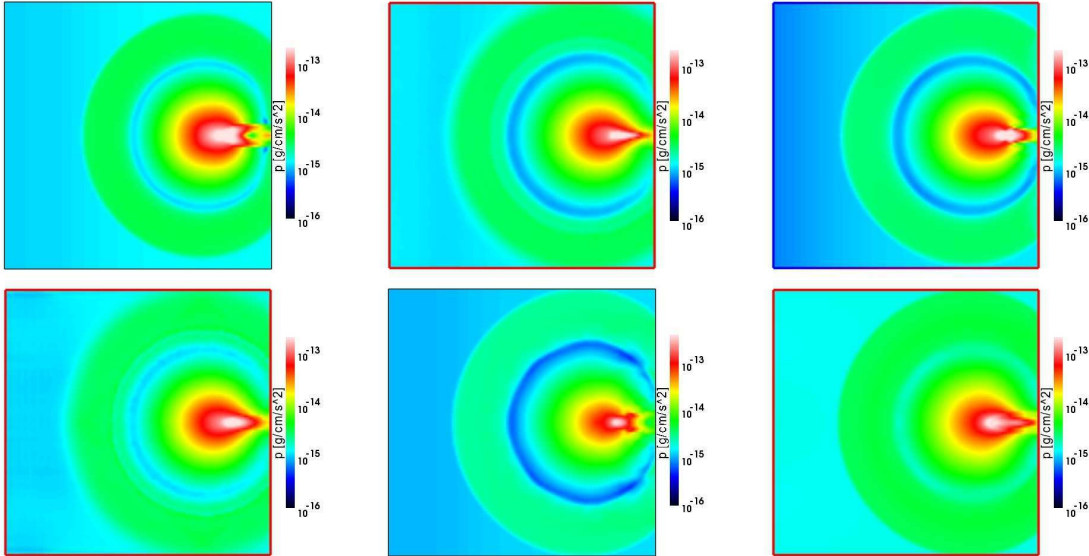


Figure 37. Test 7 (Photoevaporation of a dense clump.): Images of the pressure, cut through the simulation volume at coordinate $z = 0$ at time $t = 50$ Myr for (left to right and top to bottom) Capreole+ C^2 -Ray, RSPH, ZEUS-MP, LICORICE, Flash-HC and Coral.

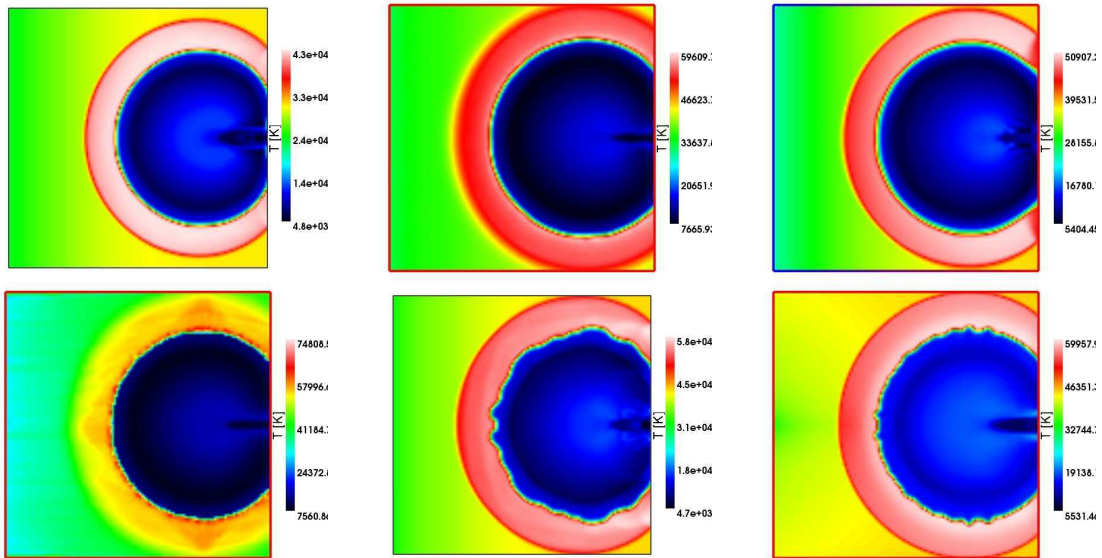


Figure 38. Test 7 (Photoevaporation of a dense clump.): Images of the temperature, cut through the simulation volume at coordinate $z = 0$ at time $t = 50$ Myr for (left to right and top to bottom) Capreole+ C^2 -Ray, RSPH, ZEUS-MP, LICORICE, Flash-HC and Coral.

based (Capreole+ C^2 -Ray, ZEUS-MP and Flash-HC) or particle-based (RSPH, LICORICE) yield very similar results in terms of Mach number values. The only significant difference between the results is again the more spherical high Mach number shell found by ZEUS-MP.

Next we turn our attention to the statistical distributions of the temperature (shown in Figure 40) and the Mach number (in

Figure 41). We notice that three distinct temperature phases (represented by the three peaks of the histograms) exist throughout the evolution - hot, photoionized gas with temperatures $T \sim 25,000 - 45,000$ K, very hot, $T > 50,000$ K, shock-heated gas and a cold phase, consisting in part of self-shielded gas and in part of adiabatically cooled gas behind the expanding supersonic wind. These three phases are observed in all cases and the histograms are very similar.

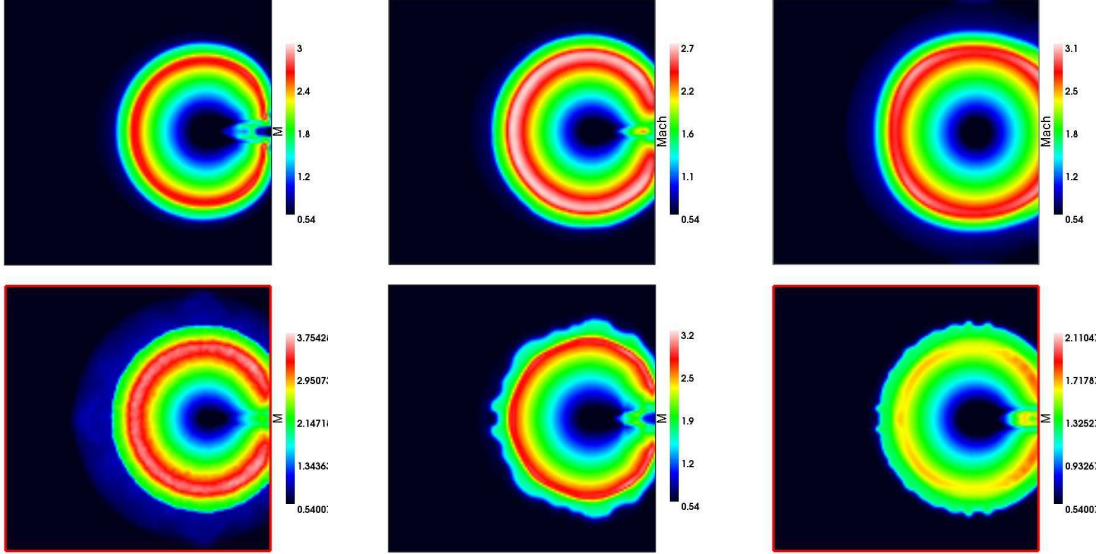
32 *I. T. Iliev, et al.*

Figure 39. Test 7 (Photoevaporation of a dense clump): Images of the flow Mach number, cut through the simulation volume at coordinate $z = 0$ at time $t = 50$ Myr for (left to right and top to bottom) Capreole+C²-Ray, RSPH, ZEUS-MP, LICORICE, Flash-HC and Coral.

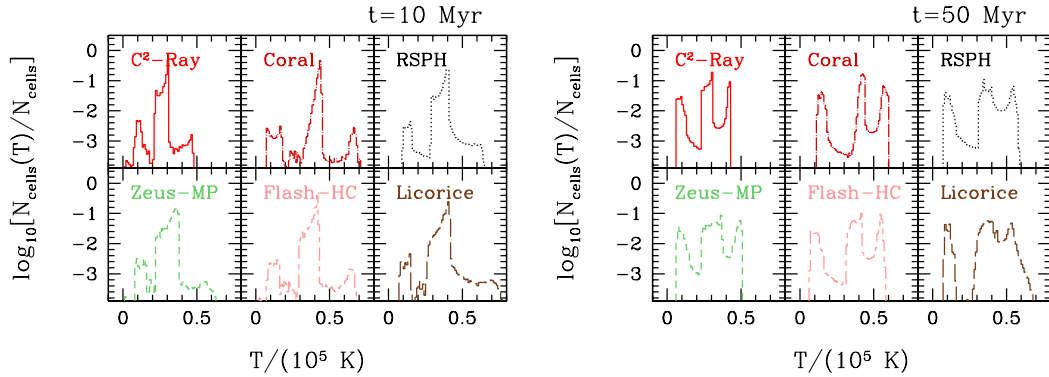


Figure 40. Test 7 (Photoevaporation of a dense clump): Histograms of the gas temperature at times $t = 10$ and 50 Myrs.

The Mach number histograms are in good agreement as well. For RSPH and LICORICE the hot, shocked phase is less distinct from the photoionized phase. The shocked gas temperature is a bit higher for LICORICE, due to the stronger shock (evidenced by the higher peak Mach number) observed in this case. On the other hand, the temperatures found by Capreole+C²-Ray are somewhat lower than the rest, which is related to the more approximate treatment of the energy equation in that case.

Finally, in Figures 42-44 we present cuts along the x -axis of the neutral fraction, x_{HI} , temperature, T , pressure, p , and Mach number M at selected times, as indicated. These cuts present information already shown in the corresponding images above, but allow for easier direct comparison between the results and for more precise reading of the specific values of each variable. At early times ($t = 1 - 10$ Myr) all codes agree very well on both the ionization

front position and its profile. The only modest differences are found in the semi-shielded part of the dense gas ($x_{\text{HI}} = 0.01 - 1$), due to variations of the treatment of hard photons, and in the low-density gas between the clump and the source, where the neutral fractions are affected by the slightly different temperatures found by the different methods. This is confirming the conclusions reached in Paper I that with no (or little) gas motions any differences are due to the treatment of the energy equation and the hard photons. The hydrodynamic evolution introduces some differences, particularly in the I-front position, but the scatter remains small.

The temperature profiles generally agree in shape and in the position of the flow features, the expanding wind and its leading shock. The main differences are in the amplitude, which varies by up to 50%, except for the cold, shielded gas at the back of the remaining dense clump at $t = 10$ Myr (at position $x/L_{\text{box}} \sim 0.8$),

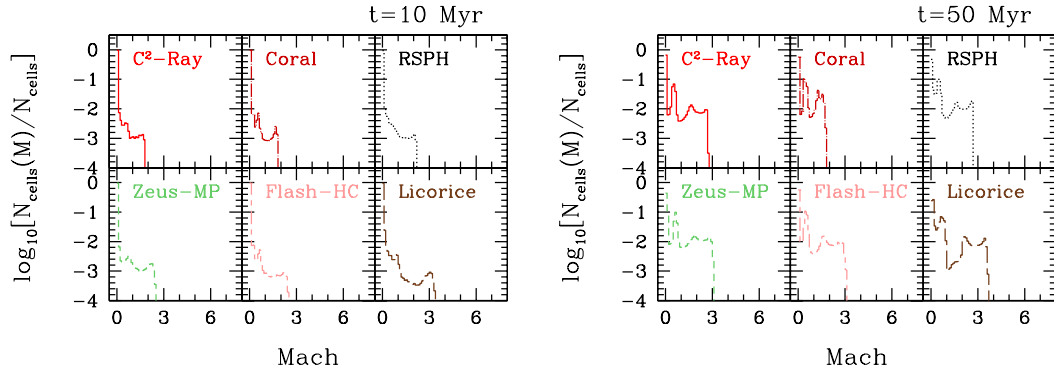


Figure 41. Test 7 (Photoevaporation of a dense clump): Histograms of the flow Mach number at times $t = 10$, and 50 Myrs.

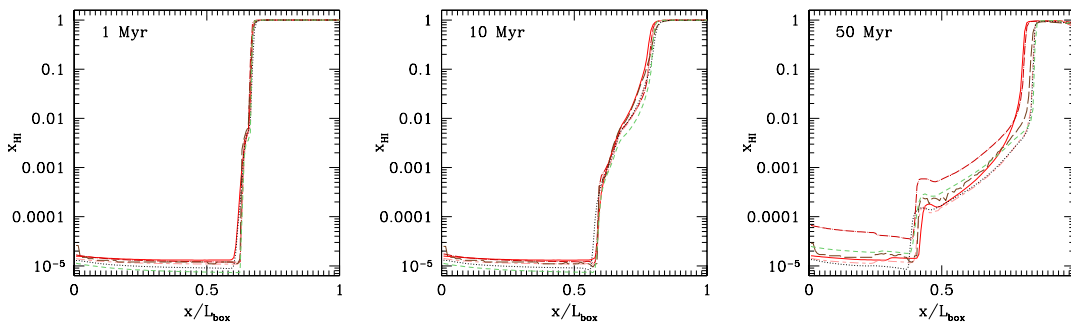


Figure 42. Test 7 (Photoevaporation of a dense clump): Line cuts of the neutral fraction along the axis of symmetry through the centre of the clump at times $t = 1$ Myr, 10 Myr and 50 Myr (left to right).

where the variation between results reached an order of magnitude. This large variation does not affect the later-time evolution considerably, however. The pressure and Mach number profiles (Figure 44) show similar trends, with very small differences during the early evolution, growing to somewhat larger ones at later times, but with all prominent flow features agreeing in both nature and position.

4.4 Summary and Conclusions

In this work we compared the results from 10 directly coupled hydrodynamics and radiative transfer codes on three test problems of astrophysical interest - H II region expansion in initially uniform gas, as well as internal and external photoevaporation of dense clumps of galactic-like size and density. Our aims are to validate our codes and test their reliability. Our test problems, while chosen to be relatively simple and clean, nevertheless cover a wide range of regimes applicable to photoionization-driven astrophysical flows, including propagation of fast (R-type) and slow (D-type) I-fronts, shock creation and supersonic photoevaporative wind. All available data is made available through the Radiative Transfer Comparison Project wiki-based website, so future code developers can test their codes against our results.

Overall, the agreement is quite good and all codes are gener-

ally reliable and produce reasonable results. However the results also highlighted some important differences between the methods. All participating algorithms track fast, R-type I-fronts well, in agreement with the results we obtained in Paper I. We note that this is not the trivial statement that we simply reproduce our previous static density field results, since in this second Comparison Project phase there are several codes which are newly developed (RHID, LICORICE, Enzo-RT) and therefore did not participate in Paper I, and furthermore even the ones which were present then have been further developed over the intervening period and are thus not identical to the versions used in Paper I.

Again similarly to what we found in Paper I, the treatment of multi-frequency radiative transfer and particularly of the hard tail of the photon spectrum varies significantly among the methods and yields correspondingly large range of temperature and ionization structures beyond the edge of the H II region, ahead of the I-front proper. We showed with a specific example that the spectral energy distribution of the ionizing source changes the I-front structure and fluid flow features considerably. Monochromatic light yields much sharper I-fronts and shocks and certain flow features like the double-peaked profile found in Test 5 disappear altogether.

For static density distributions the variations in the multi-frequency radiative transfer treatment had little effect on the I-front positions and propagation speeds since those are largely deter-

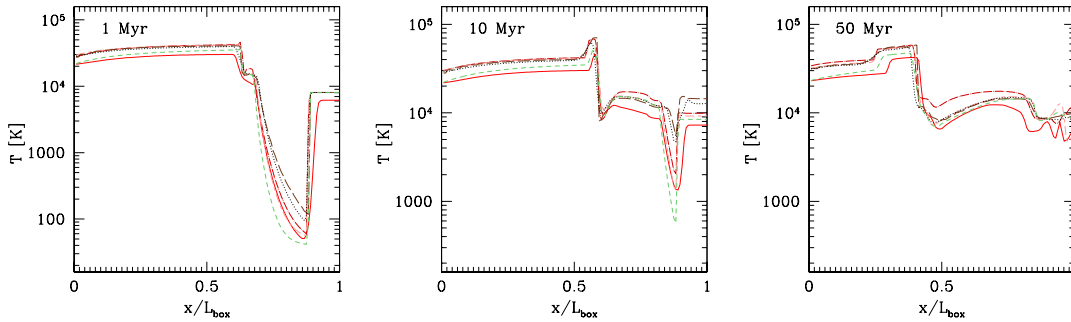
34 *I. T. Iliev, et al.*

Figure 43. Test 7 (Photoevaporation of a dense clump): Line cuts of the temperature along the axis of symmetry through the centre of the clump at times $t = 1$ Myr, 10 Myr and 50 Myr (left to right),

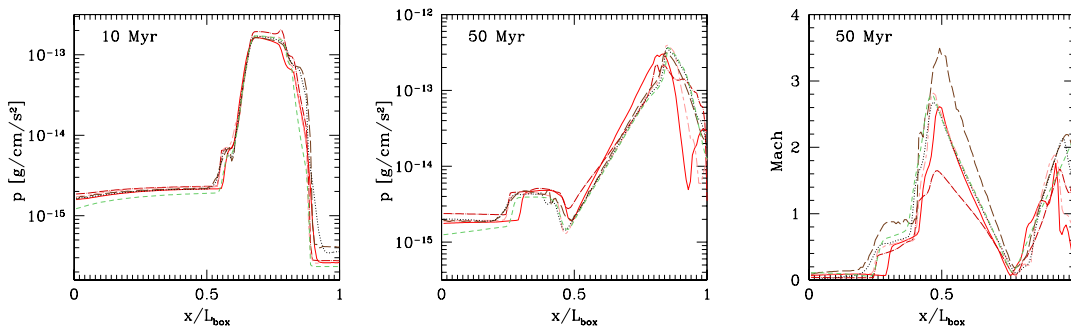


Figure 44. Test 7 (Photoevaporation of a dense clump): Line cuts of the pressure at times $t = 10$ Myr (left), and 50 Myr (centre) and of the Mach number at time $t = 50$ Myr (right) along the axis of symmetry through the centre of the clump.

mined (apart from recombinations-related effects) by simple photon counting and balancing this number against the number of atoms entering the front. For dynamically-coupled evolution, this changes and there are significant feedback effects, with the radiative transfer effects affecting the gas dynamics and vice versa. For example, pre-heating by hard photons, or lack of it, can affect the dynamics significantly. More specifically, higher pre-heating results in shocks, e.g. ones typically leading D-type I-fronts, which are weaker and faster-propagating, and vice-versa. The internal structure of such a front and the relative spacing between the shock and the I-front can also change considerably. Shocks created by photoheating effects tend to be relatively weak, with Mach numbers of a few or less. The density compression resulting from them is strongly dependent of the pre-heating by hard photons, but generally did not exceed factors of 1.5-2. The profiles of the fluid quantities in supersonically expanding regions (e.g. the photoevaporative wind in Test 7) show good agreement among the different methods.

Significant differences were noted in the numerical diffusivity properties of different methods. Numerical diffusion could be due to either the radiative transfer method employed (e.g. the moment method OTVET used in HART), or the hydrodynamics (SPH in LICORICE). Higher diffusion could have notable effects on some properties of the flow (features become smoother, high contrasts are diminished), but seems to have modest effects on the overall gross

features and the basic dynamics remains largely unaffected. However, care should be taken when using such methods for problems in which the sharp features might matter, e.g. enhanced molecule formation due to shocks.

The propagation of an accelerating I-front down a steep $(1/r^2)$ density profile (Test 6) proved to be a quite difficult problem and several codes developed significant instabilities, while the rest did not. While there are a number of possible instabilities which can develop in similar situations, as we discussed in some detail, in this particular case the instabilities we observed prove to be numerical in nature. The most severe one was the known carbuncle instability or odd-even decoupling, which in some cases affect low-diffusion hydrodynamic solvers (here a Roe Riemann solver). This problem can be eliminated by either adding some artificial diffusion or using a more diffusive hydrodynamic solver.

In summary, we have found a considerable level of agreement between the wide variety of radiative transfer and hydrodynamics coupled methods participating in this project. The basic flow features and their evolution are reproduced well by all methods. There are some variations whose origins we did our best to understand. The recurring differences were mostly due to the different treatment of the energy equation and the transfer of multi-frequency radiation. There were also some problems specific to certain methods which we discussed in detail. While none of the codes gave any ob-

viously unphysical or incorrect results and all largely agreed with each other, some of the methods were clearly less suited for certain problems. No method is universally applicable to all astrophysical situations and every one of the participating codes showed some behaviour discrepant with the majority in one respect or another. Care should therefore be taken in applying any given algorithm to a new type of problem and detailed testing is always advised.

ACKNOWLEDGMENTS

This study was supported in part by Swiss National Science Foundation grant 200021-116696/1, U.S. Department of Energy at Los Alamos National Laboratory under Contract No. DE-AC52-06NA25396, research funds from Chosun University, NSF grant AST 0708176, NASA grants NNX07AH09G and NNG04G177G, Chandra grant SAO T8-9009X, and Swedish Research Council grant 60336701. The work with RSPH was supported in part by the *FIRST* project based on Grants-in-Aid for Specially Promoted Research by MEXT (16002003), JSPS Grant-in-Aid for Scientific Research (S) (20224002) and Inamori foundation. The Flash code was developed by the DOE-supported ASC / Alliance Center for Astrophysical Thermonuclear Flashes at the University of Chicago. MLN and DRR acknowledge partial support from NSF Grant AST-0808184.

REFERENCES

- Abel T., Norman M. L., Madau P., 1999a, *ApJ*, 523, 66
 —, 1999b, *ApJ*, 523, 66
 Ahn K., Shapiro P. R., 2005, *MNRAS*, 363, 1092
 —, 2007, *MNRAS*, 375, 881
 Anninos P., Zhang Y., Abel T., Norman M. L., 1997, *New Astronomy*, 2, 209
 Bertoldi F., 1989, *ApJ*, 346, 735
 Ciardi B., Stoehr F., White S. D. M., 2003, *MNRAS*, 343, 1101
 Colella P., Woodward P. R., 1984, *Journal of Computational Physics*, 54, 174
 Doré O., Holder G., Alvarez M. A., Iliev I. T., Mellema G., Pen U.-L., Shapiro P. R., 2007, *Phys Rev D*, 76, 043002
 Draine B. T., Bertoldi F., 1996, *ApJ*, 468, 269
 Franco J., Tenorio-Tagle G., Bodenheimer P., 1990, *ApJ*, 349, 126
 Frank A., Mellema G., 1994, *A.&A*, 289, 937
 Fryxell B., Olson K., Ricker P., Timmes F. X., Zingale M., Lamb D. Q., MacNeice P., Rosner R., Truran J. W., Tufo H., 2000, *ApJS*, 131, 273
 Galli D., Palla F., 1998a, *A.&A*, 335, 403
 —, 1998b, *A.&A*, 335, 403
 Garcia-Segura G., Franco J., 1996, *ApJ*, 469, 171
 Giuliani Jr. J. L., 1979, *ApJ*, 233, 280
 Glover S. C. O., Abel T., 2008, *MNRAS*, 388, 1627
 Gnedin N. Y., 2000, *ApJ*, 535, 530
 Gnedin N. Y., Tassis K., Kravtsov A. V., 2008, *ArXiv e-prints*
 Hasegawa K., Umemura M., Susa H., 2009, *MNRAS*, 445
 Heinemann T., Dobler W., Nordlund Å., Brandenburg A., 2006, *A.&A*, 448, 731
 Hindmarsh A. C., 1980, *SIGNUM Newsl.*, 15, 10
 Holder G. P., Iliev I. T., Mellema G., 2007, *ApJL*, 663, L1
 Hosokawa T., Inutsuka S., 2005, *ApJ*, 623, 917
 Hummer D. G., 1994, *MNRAS*, 268, 109
 Hummer D. G., Storey P. J., 1998, *MNRAS*, 297, 1073
 Iliev I. T., et al., 2006, *MNRAS*, 371, 1057
 Iliev I. T., Hirashita H., Ferrara A., 2006a, *MNRAS*, 368, 1885
 Iliev I. T., Mellema G., Pen U.-L., Bond J. R., Shapiro P. R., 2008a, *MNRAS*, 77
 Iliev I. T., Mellema G., Pen U.-L., Merz H., Shapiro P. R., Alvarez M. A., 2006b, *MNRAS*, 369, 1625
 Iliev I. T., Mellema G., Shapiro P. R., Pen U.-L., 2007a, *MNRAS*, 376, 534
 Iliev I. T., Pen U.-L., Bond J. R., Mellema G., Shapiro P. R., 2007b, *ApJ*, 660, 933
 Iliev I. T., Shapiro P. R., Mellema G., Merz H., Pen U.-L., 2008b, in refereed proceedings of TeraGrid08, *ArXiv e-prints* (0806.2887)
 Iliev I. T., Shapiro P. R., Raga A. C., 2005, *MNRAS*, 361, 405
 Kahn F. D., Dyson J. E., 1965, *Ann. Rev. Astron. & Astrophys.*, 3, 47
 Khokhlov A. M., 1998, *JCP*, 143, 519
 Knoll D. A., Keyes D. E., 2004, *Journal of Computational Physics*, 193, 357
 Kohler K., Gnedin N. Y., Hamilton A. J. S., 2007, *ApJ*, 657, 15
 Kravtsov A. V., 1999, PhD thesis, New Mexico State University
 Kravtsov A. V., Klypin A., Hoffman Y., 2002, *ApJ*, 571, 563
 Kravtsov A. V., Klypin A. A., Khokhlov A. M., 1997, *ApJS*, 111, 73
 Krumholz M. R., Stone J. M., Gardiner T. A., 2007, *ApJ*, 671, 518
 Lepp S., Shull J. M., 1983, *ApJ*, 270, 578
 Lim A. J., Mellema G., 2003, *A.&A*, 405, 189
 Mac Low M.-M., Toraskar J., Oishi J. S., Abel T., 2007, *ApJ*, 668, 980
 Maselli A., Ciardi B., Kanekar A., 2009, *MNRAS*, 393, 171
 Maselli A., Ferrara A., Ciardi B., 2003, *MNRAS*, 345, 379
 Mellema G., Arthur S. J., Henney W. J., Iliev I. T., Shapiro P. R., 2006a, *ApJ*, 647, 397
 Mellema G., Iliev I. T., Alvarez M. A., Shapiro P. R., 2006b, *New Astronomy*, 11, 374
 Mellema G., Iliev I. T., Pen U.-L., Shapiro P. R., 2006c, *MNRAS*, 372, 679
 Mellema G., Raga A. C., Canto J., Lundqvist P., Balick B., Steffen W., Noriega-Crespo A., 1998, *A.&A*, 331, 335
 Monaghan J. J., 1992, *Ann. Rev. Astron. & Astrophys.*, 30, 543
 Nakamoto T., Umemura M., Susa H., 2001, *MNRAS*, 321, 593
 Norman M. L., Bryan G. L., Harkness R., Bordner J., Reynolds D., O'Shea B., Wagner R., 2007, *ArXiv e-prints*
 Quirk J. J., 1994, *International Journal for Numerical Methods in Fluids*, 18, 555
 Raga A. C., Mellema G., Arthur S. J., Binette L., Ferruit P., Steffen W., 1999, *Revista Mexicana de Astronomia y Astrofisica*, 35, 123
 Raga A. C., Mellema G., Lundqvist P., 1997, *ApJS*, 109, 517
 Razoumov A. O., Norman M. L., Abel T., Scott D., 2002, *ApJ*, 572, 695
 Razoumov A. O., Norman M. L., Prochaska J. X., Wolfe A. M., 2006, *ApJ*, 645, 55
 Razoumov A. O., Scott D., 1999, *MNRAS*, 309, 287
 Reynolds D. R., Hayes J. C., Paschos P., Norman M. L., 2009, *ArXiv e-prints*
 Ricotti M., Gnedin N. Y., Shull J. M., 2002, *ApJ*, 575, 49
 Rijkhorst E.-J., 2005, PhD thesis, Leiden Observatory, Leiden University, P.O. Box 9513, 2300 RA Leiden, The Netherlands
 Rijkhorst E.-J., Plewa T., Dubey A., Mellema G., 2006, *A.&A*, 452, 907
 Semelin B., Combes F., 2002, *A.&A*, 388, 826

36 *I. T. Iliev, et al.*

- , 2005, *A.&A.*, 441, 55
- Shapiro P. R., Iliev I. T., Alvarez M. A., Scannapieco E., 2006, *ApJ*, 648, 922
- Shapiro P. R., Iliev I. T., Raga A. C., 2004, *MNRAS*, 348, 753
- Sokasian A., Abel T., Hemquist L., Springel V., 2003, *MNRAS*, 344, 607
- Spitzer L., 1978, *Physical processes in the interstellar medium.* New York Wiley-Interscience, 1978
- Springel V., Hemquist L., 2002, *MNRAS*, 333, 649
- Steinmetz M., Mueller E., 1993, *A.&A.*, 268, 391
- Susa H., 2006, *PASJ*, 58, 445
- , 2007, *ApJ*, 659, 908
- , 2008, *ApJ*, 684, 226
- Susa H., Kitayama T., 2000, *MNRAS*, 317, 175
- Susa H., Umemura M., 2004, *ApJ*, 600, 1
- , 2006, *ApJL*, 645, L93
- Tenorio-Tagle G., Bodenheimer P., Lin D. N. C., Noriega-Crespo A., 1986, *MNRAS*, 221, 635
- Thacker R. J., Tittley E. R., Pearce F. R., Couchman H. M. P., Thomas P. A., 2000, *MNRAS*, 319, 619
- Trac H., Pen U.-L., 2004, *New Astronomy*, 9, 443
- Umemura M., 1993, *ApJ*, 406, 361
- Vishniac E. T., 1983, *ApJ*, 274, 152
- Whalen D., Abel T., Norman M. L., 2004, *ApJ*, 610, 14
- Whalen D., Norman M. L., 2006, *ApJS*, 162, 281
- , 2008a, *ApJ*, 673, 664
- Whalen D., O’Shea B. W., Smidt J., Norman M. L., 2008a, *ApJ*, 679, 925
- Whalen D., Prochaska J. X., Heger A., Tumlinson J., 2008b, *ApJ*, 682, 1114
- Whalen D., van Veelen B., O’Shea B. W., Norman M. L., 2008c, *ApJ*, 682, 49
- Whalen D. J., Norman M. L., 2008b, *ApJ*, 672, 287
- Williams R. J. R., 1999, *MNRAS*, 310, 789
- , 2002, *MNRAS*, 331, 693

2.5 Performance

Currently the dynamical part of the code is parallelized for both shared and distributed memory architectures using OpenMP and MPI. The two radiative transfer parts (continuum and Lyman line) are Parallelized with OpenMP only. The continuum part needs about 250 CPU hours and 10 Go of shared memory for a typical run for reionization (~ 100 snapshots, 2×256^3 particles). The Lyman line part consumes about ~ 500 CPU hours and 10 Go shared memory for the same typical run. Now using the Vargas machine at IDRIS (Institut du Développement et des Ressource en Informatique Scientifique , the CNRS computing center) which possesses 256 Go of shared memory on a single node, simulations with 2×512^3 particles are possible.

Chapter 3

The simulated 21 cm signal I

3.1 Physics of the 21 cm signal

3.1.1 Basic equations

Radiative transfer equation

In the Rayleigh-Jeans limit ($h\nu \ll kT$), the equation of radiative transfer of the 21-cm line along a line of sight through a cloud in the local thermodynamic equilibrium (LTE) can be expressed as,

$$I_\nu(\tau_\nu) = I_\nu(0)e^{-\tau_\nu} + \frac{2kT\nu^2}{c^2} (1 - e^{-\tau_\nu}) . \quad (3.1)$$

The first term of Eq.(3.1) describes the attenuating specific intensity from emitter to observer, and the second term is related to the emissivity which is assumed to be constant along the line of sight. If we define the brightness temperature as $T_B \equiv \frac{c^2}{2k\nu^2} I_\nu$, the equation becomes,

$$T_B(\tau_\nu) = T_B(0)e^{-\tau_\nu} + (1 - e^{-\tau_\nu})T , \quad (3.2)$$

where $T_B(0)$ is the temperature of the background source. The received signal is given by,

$$T_B(\tau_\nu) - T_B(0) = (T - T_B(0))(1 - e^{-\tau_\nu}). \quad (3.3)$$

For the 21cm transition, the excitation temperature T is the spin temperature T_s , and $T_B(0)$ is the Cosmic Microwave Background Temperature. The spin temperature is determined by the population of hyperfine levels,

$$\frac{n_1}{n_0} = \frac{g_1}{g_0} \exp\left(-\frac{E_{10}}{kT_s}\right) , \quad (3.4)$$

where g_1 and g_0 are the statistical weights of each level and E_{10} is the energy gap between the two hyperfine levels corresponding to $F = 1 \rightarrow F = 0$.

Optical depth

The 21 cm emission is related to the hyperfine transition in the ground state of neutral hydrogen. The optical depth is

$$\begin{aligned}\tau_\nu &= \int ds \frac{3c^2 A_{10}}{8\pi\nu^2} (1 - e^{-E_{10}/k_B T_s}) \phi(\nu) n_0 \\ &\approx \frac{3c^2 A_{10}}{8\pi\nu^2} \left(\frac{h\nu}{k_B T_s} \right) \left(\frac{N_{\text{HI}}}{4} \right) \phi(\nu),\end{aligned}\quad (3.5)$$

where N_{HI} is the column density of HI and the factor 1/4 is the fraction of HI atoms in the hyperfine singlet state. A_{10} is the Einstein coefficient for spontaneous emission. $\phi(\nu)$ is the line profile (defined so that $\int d\nu \phi(\nu) = 1$) includes natural, thermal, and pressure broadening, as well as bulk motion. If we call $\Delta\nu$ the full-width at half maximum (FWHM) (or Δv if we express it as the radial velocity), we have $\phi(\nu_0) \approx 1/\Delta\nu = c/(\nu_0 \Delta v)$. The most important application for the velocity broadening is the Hubble flow. In a region of linear dimension s , the velocity broadening is approximately $\Delta v \sim sH(z)$ and $\phi(\nu_0) \sim c/[\nu_0 sH(z)]$. The column density is $N_{\text{HI}} = x_{\text{HI}} n_H(z) s$. Therefore the optical depth at the 21 cm line center can be expressed as,

$$\begin{aligned}\tau_{\nu_0} &= \frac{3}{32\pi} \frac{hc^3 A_{10}}{k_B T_s \nu_0^2} \frac{x_{\text{HI}} n_H}{(1+z)(dv_{\parallel}/dr_{\parallel})} \\ &\approx 0.0092 (1+\delta) (1+z)^{3/2} \frac{x_{\text{HI}}}{T_s} \left[\frac{H(z)/(1+z)}{dv_{\parallel}/dr_{\parallel}} \right],\end{aligned}\quad (3.6)$$

where $(1+\delta)$ is the fractional overdensity of baryons and $dv_{\parallel}/dr_{\parallel}$ is the gradient of the proper velocity along the line of sight, including the Hubble expansion.

The 21 cm line transition

Eq.(3.2) indicates that if the brightness temperature of the medium (T) is hotter than that of the background ($T_B(0)$), the signal ($\propto T_B(\tau_\nu) - T_B(0)$) appears in emission, while in absorption on the contrary. The differential brightness temperature observed

from the Earth will be

$$\begin{aligned}\delta T_b &= \frac{T_s - T_{cmb}}{1+z}(1 - e^{-\tau_{\nu_0}}) \approx \frac{T_s - T_{cmb}}{1+z}\tau_{\nu_0} \\ &\approx 28.1 x_{\text{HI}}(1 + \delta) \left(\frac{1+z}{10}\right)^{1/2} \left[1 - \frac{T_{cmb}}{T_s}\right] \left[\frac{H(z)/(1+z)}{dv_{\parallel}/dr_{\parallel}}\right] \text{ mK}. \quad (3.7)\end{aligned}$$

If $T_s \gg T_{cmb}$, δT_b of Eq.(3.7) saturates to 28.1 mK. If $T_s \ll T_{cmb}$ it can be arbitrarily large and negative.

3.1.2 The spin temperature

The spin temperature (or excitation temperature) of the 21 cm transition is affected by *i*) the absorption of CMB photons, *ii*) collisions (with other hydrogen atoms, free electrons, and protons) and *iii*) scattering of Lyman- α photons. The equilibrium spin temperature is then determined by

$$n_1(C_{10} + P_{10} + A_{10} + B_{10}I_{CMB}) = n_0(C_{01} + P_{01} + B_{01}I_{CMB}), \quad (3.8)$$

where C_{10} and P_{10} is the de-excitation rates from collisions and Ly- α scattering and C_{01} and P_{01} are the corresponding excitation rates. A_{10} , B_{10} and B_{01} are the usual Einstein coefficients and I_{CMB} is the energy flux of CMB photons. In the Rayleigh-Jeans approximation, the equilibrium spin temperature can be written as (Field, 1959)

$$T_s^{-1} = \frac{T_{cmb}^{-1} + x_c T_K^{-1} + x_\alpha T_e^{-1}}{1 + x_c + x_\alpha} \quad (3.9)$$

where x_c and x_α are coupling coefficient for collisions and Lyman- α scattering and T_K is the gas kinetic temperature.

Normally the interaction with CMB photons couples the spin temperature to the CMB temperature in a very short time scale $T_*/(T_{cmb}A_{10}) \approx 5 \times 10^4$ yr, and $T_s \approx T_{cmb}$ makes the signal δT_b invisible. Two other processes, collisions and UV photon scattering, makes the 21 cm transition detectable.

Collisional coupling

Large values of the coupling coefficient x_c in Eq.(3.9) can decouple the spin temperature from the CMB temperature. A more detailed expression for x_c is

$$x_c \equiv \frac{T_*}{A_{10}T_{cmb}}(C_H + C_p + C_e), \quad (3.10)$$

where $T_* = \frac{h\nu_0}{k_B} = 0.068$ K and C_H , C_p and C_e are the de-excitation rates due to collisions with neutral atoms, protons and electrons. We need $x_c \sim 1$ in order to decouple the spin temperature from CMB temperature which means baryon over density $\delta_b > 5[(1+z)/20]^{-2}$ in the absence of Ly- α scattering. This condition is fulfilled in the early universe beyond a redshift of 20 or in the virialized mini halos or filamentary structures.

The Wouthuysen-Field Effect

The coupling process by UV photons scattering is known as the Wouthuysen-Field effect (WFE). An atom initially in the $n = 1$ ${}_0S_{1/2}$ singlet state moves to the $n = 2$ ${}_1P_{1/2}$ $n = 1$ ${}_1S_{1/2}$ state by spontaneous decay. Similarly, a triplet atom can de-excite indirectly to a singlet atom via $n = 2$ ${}_1P_{1/2}$ or ${}_1P_{3/2}$ state. The efficiency of the effect is determined by the shape of the radiation spectrum near Lyman- α . Thus we define the color temperature T_c of the radiation field,

$$\frac{1}{k_B T_c} = -\frac{d \ln n_\nu}{d h\nu}, \quad (3.11)$$

where n_ν is the photon occupation number at frequency ν . Since the medium at the redshift of interest is extremely optically thick, a large number of ($\sim 10^6$) Ly α scattering brings the Ly α profile close to a blackbody spectrum of temperature T_K near the line center, so $T_c \rightarrow T_K$.

In Eq.(3.9) x_α indicates how T_s is coupled to T_K .

$$x_\alpha = \frac{P_{10}}{A_{10}} \frac{T_*}{T_{cmb}}, \quad (3.12)$$

where P_{10} is the $1 \rightarrow 0$ transition rate via Ly α and $T_* = E_{10}/k_B$. P_{10} can be replaced by the total rate P_α ,

$$P_\alpha = \int d\Omega \int \frac{I_\nu}{h\nu} \sigma_\nu d\nu, \quad (3.13)$$

at which Ly α photons are scattered by an H atom, $P_{10} = 4P_\alpha/27$ (Field, 1959).

3.2 Lyman-alpha radiative transfer during the EoR

Summary

The effect of fluctuations in the Lyman- α flux on the spin temperature during the early epoch of reionization has not been fully considered yet. Barkana & Loeb (2005) or Furlanetto et al. (2006) remark that Lyman- α fluctuations can produce additional fluctuations on the 21-cm signal and the intensity of the absorption phase has the

potential to be stronger than the emission since the absorption phase has no saturation limit. To fully account for these Lyman- α fluctuations, in other words the inhomogeneous Wouthuysen-Field effect, we need to know the local number of Ly α scatterings. In the following paper we introduce the numerical method implemented in LICORICE for the Lyman- α line radiative transfer. All cosmological aspects are included, redshifting photons, retarded time etc. Three validation tests show good agreement with analytic solutions in simple cases. The Ly α cross section is so large that photons can be scattered $\sim 10^6$ times in the hydrogen medium at $z \sim 10$, therefore computing all these scatterings is almost impossible. Fortunately, the fact that we do not need to know the emerging spectrum but only the position where the scattering occurs permits a large acceleration factor. We found that Lyman α flux does not follow an $\sim 1/r^2$ profile around a single source because of wing scattering, and an even stronger effect is obtained when we introduce fluctuations in the density of gas surrounding the source.

A&A 474, 365–374 (2007)
 DOI: 10.1051/0004-6361:20077965
 © ESO 2007

**Astronomy
&
Astrophysics**

Lyman-alpha radiative transfer during the epoch of reionization: contribution to 21-cm signal fluctuations

B. Semelin, F. Combes, and S. Baek

LERMA, Observatoire de Paris, UPMC, CNRS, 61 Av. de l'Observatoire, 75014 Paris, France
 e-mail: benoit.semelin@obspm.fr

Received 29 May 2007 / Accepted 31 July 2007

ABSTRACT

During the epoch of reionization, Ly- α photons emitted by the first stars can couple the neutral hydrogen spin temperature to the kinetic gas temperature, providing an opportunity to observe the gas in emission or absorption in the 21-cm line. Given the bright foregrounds, it is particularly important to determine the fluctuation signature of the signal precisely, so as to be able to extract it by its correlation power. LICORICE is a Monte-Carlo radiative transfer code, coupled to the dynamics via an adaptive Tree-SPH code. We present here the Ly- α part of the implementation and validate it through three classical tests. Unlike previous works, we do not assume that P_α , the number of scatterings of Ly- α photons per atom per second, is proportional to the Ly- α background flux, but take the scatterings in the Ly- α line wings into account. The latter have the effect of steepening the radial profile of P_α around each source, and re-inforce the contrast of the fluctuations. In the particular geometry of cosmic filaments of baryonic matter, Ly- α photons are scattered out of the filament, and the large-scale structure of P_α is significantly anisotropic. This could have strong implications for the possible detection of the 21-cm signal.

Key words. methods: N-body simulations – radiative transfer – method: numerical – galaxies: intergalactic medium – cosmology: large-scale structure of Universe

1. Introduction

The epoch of reionization (EoR) extends from the time when the first sources form as a result of the nonlinear growth of primordial density fluctuations in a fully neutral universe ($z \sim 20$) to the moment when the intergalactic medium is fully reionized under the effect of UV radiations emitted by the sources ($z \sim 6$). This simple picture, however, hides a number of uncertainties. At this time, there are only two observational constraints on the EoR. The first comes from the Gunn-Peterson effect in the absorption spectrum of high redshift quasars. Indeed the transmitted flux drops sharply as a small neutral fraction appears toward high redshifts, which implies an ionization fraction $x_{\text{HI}} < 10^{-4}$ at $z < 5.5$ (Fan et al. 2006). The second constraint is set by the Thomson scattering of CMB photons by the free electrons produced during the EoR. The corresponding optical depth, $\tau = 0.09 \pm 0.03$ (Spergel et al. 2007) implies that the intergalactic medium is already significantly reionized at $z = 11$. In the next decade, we will learn a lot more by direct observation of the redshifted 21-cm emission from the neutral IGM during the EoR. Such instruments as LOFAR, PAST, or MWA will be able to probe the statistical properties of the 21-cm signal, while SKA will be able to make a full tomography of the IGM up to $z \sim 11$. See Carilli et al. (2004) and Carilli (2006) for detailed prospects.

In the last decade, a lot of work has been done, both theoretical and numerical, to predict the properties of the 21-cm emission and better optimize the design of the future instruments. Madau et al. (1997) and Tozzi et al. (2000) have presented the first theoretical models of 21-cm emission. The signal can be seen either in emission or in absorption against the CMB, depending on the spin temperature of the neutral hydrogen.

Interaction with CMB photons couples the spin temperature to the CMB temperature in less than 10^5 years during the EoR, which would make the signal undetectable. Fortunately, two other processes tend to couple the spin temperature to the gas kinetic temperature instead. The first is the excitation of the hyperfine transition through collisions with electrons or other hydrogen atoms (see Nusser 2005; Kuhlen et al. 2006, for numerical simulations), which is, however, only efficient in overdense regions (baryonic $\delta\rho/\rho > 5/[1+(1+z)/20]^2$). The second is the pumping of the 21-cm transition by Ly- α photons (Wouthuysen-Field effect, Wouthuysen 1952; Field 1959), which requires a threshold value for the local Ly- α flux to be effective. Consequently, the value of the kinetic temperature of the gas relative to the CMB temperature is crucial for determining the 21-cm emission brightness temperature.

During the EoR, the gas is cooling down due to the expansion of the universe faster than the CMB, but is heated by hydrodynamical shocks from structure formation, by X-ray from pop-III star or quasars and, to a much lesser extent, by Ly- α photons (see e.g., Furlanetto et al. 2006). Simple analytical models are now available that take various source types and formation history into account (Furlanetto 2006). They usually predict that the signal can be seen in absorption early on, then later on in emission. The prediction of the typical amplitude for the differential brightness temperature is a few 10 mK. Analytical models cannot, however, take the full complexity of the 3D inhomogeneous IGM into account. Indeed, both numerical simulations including the dynamics of structure formation and, usually as a post-treatment, a full 3D radiative transfer are required.

Dynamical simulations of structure formation have a long history, but cosmological radiative transfer simulations are a more recent field of investigation. Simulations showed that the

ionized bubbles around the first sources are not spherical: indeed the ionization fronts propagate fast in the void and more slowly in the high-density filaments (see Abel et al. 1999, for the first simulation). The geometry of reionization is now studied in large simulation boxes (~ 100 Mpc) to get a statistical sample of ionized bubbles of various sizes (Iliev et al. 2006a; McQuinn et al. 2007). However, in such large boxes, even with very high resolution simulations, small-scale density structures, also called minihaloes, are not resolved and are often included through a simple clumping factor. The global effect of minihaloes is to slow down reionization by consuming photons during their photoevaporation. But a simple, uniform clumping factor may be insufficient for modeling the role of minihaloes, and more detailed studies have been performed (Ciardi et al. 2006; Iliev et al. 2005; and Shapiro et al. 2006 for the impact on the 21-cm signal). Using the density field from the dynamical simulations and the ionization fraction and gas temperature from the radiative transfer simulations, it is possible to produce 21-cm emission maps.

A number of authors provide predictions for different aspects of the 21-cm signal: the emission map at a given redshift, the average signal as a function of redshift, or the signal power as a function of the angular scale. These quantities were first predicted from rather small simulation boxes (~ 10 Mpc) limiting the angular information to $\theta < 10$ arcmin (Ciardi & Madau 2003; Gnedin & Shaver 2004; Furlanetto et al. 2004; Valdes et al. 2006). Recently, predictions from larger simulation boxes (~ 100 Mpc) became available (Mellema et al. 2006; Iliev et al. 2007). It is a fact that the predictions, in particular the duration and intensity of the absorption phase, crucially depend on the modeling of the sources. But other factors have the potential to alter these predictions. Indeed, all predictions from simulations, at this time, assume a uniform efficiency for the Wouthuysen-Field effect. However, Barkana & Loeb (2005) or Furlanetto et al. (2006a) recognize that fluctuations in the local Ly- α flux can produce additional fluctuations in the brightness temperature. An accurate quantitative modeling of these fluctuations is important. Indeed, the 21 cm signal will be difficult to detect due to brighter foregrounds: but the unique signature of its brightness fluctuations will make the extraction possible. Barkana & Loeb used simplified analytic models (neglecting radiative transfer effects on the local Ly- α flux) to compute this contribution. Our goal in this paper is to investigate how computing the full radiative transfer in the Ly- α line in a cosmological, inhomogeneous medium can modify the picture presented by these authors. The 21 cm signal will be difficult to detect, due to brighter foregrounds, and the unique character of its brightness fluctuations is a signature that will make its extraction possible. It is therefore crucial to predict those fluctuations in more details.

Although Monte-Carlo simulations of Ly- α transfer have a long history, starting with Avery & House (1968), only recently has the computing power become sufficient for tackling the case of a 3D inhomogeneous medium with kinematics, without restrictions on the optical thickness regime (Ahn et al. 2001). Several authors have now developed similar codes to simulate the Ly- α emission from high-redshift galaxies (Zheng & Miralda-Escudé 2002; Cantalupo et al. 2005; Dijkstra et al. 2006; Verhamme et al. 2006; Tasitsiomi 2006).

In this paper, we present the implementation and validation of the Ly- α radiative transfer in LICORICE, a dynamics-radiative transfer code, with special emphasis on the treatment of large Hubble flows, which is specific to the EoR applications. This work is part of the SKADS¹ effort (DS2-T1 task) to produce

simulated emission maps that can be used to optimize the design of the future SKA telescope.

In Sect. 2, we present which physics of the Ly- α transfer is included in LICORICE and justify why some aspects of the physics do not need to be included. In Sect. 3 we explain some aspects of the algorithms and acceleration schemes implemented in the code. Three validation tests are presented in Sect. 4, comparing the outputs of LICORICE to either analytic solutions or standard numerical results. Finally, in Sect. 5, we apply the code to some typical EoR situation to investigate possible fluctuations in the Wouthuysen-Field effect.

2. The code: LICORICE

LICORICE consists of three parts. A TreeSPH code with multiphase modeling of the gas computes the dynamics of structure formation (Semelin & Combes 2002). A continuum radiative transfer part is added to compute reionization. This part uses a Monte-Carlo approach and is similar to CRASH (Maselli et al. 2003). It has the advantage over CRASH of using an adaptative grid. LICORICE is currently participating in the second part of the Cosmological Radiative Transfer Comparison Project (see Iliev et al. 2006b, for the first part of the project). The third part is the Ly- α radiative transfer, which is described in this paper.

2.1. Physics of the Ly- α radiative transfer

LICORICE implements a Monte-Carlo approach to radiative transfer by propagating photons on an adaptative grid. Consequently, we describe the physics of Ly- α radiative transfer from the point of view of a photon traveling through the simulation box.

2.1.1. Computing the optical depth

A photon propagating through neutral hydrogen has a probability $P(\tau) = e^{-\tau}$ of not being scattered after traveling through an optical depth τ from its emission point. We only consider Ly- α scattering, so the optical depth can be computed as:

$$\tau = \int_0^l \int_{-\infty}^{+\infty} ds du_{\parallel} n_{\text{HI}} p(u_{\parallel}) \sigma \left(\nu \left(1 - \frac{v_{\parallel}^{\text{macro}} + u_{\parallel}}{c} \right) \right), \quad (1)$$

where ν is the photon frequency in the global rest frame and n_{HI} the local number density of neutral hydrogen. Also, u_{\parallel} is the scattering atom velocity along the incoming photon's direction in the moving reference frame of the fluid, $p(u_{\parallel})$ the normalized probability distribution for u_{\parallel} , $v_{\parallel}^{\text{macro}}$ the gas macroscopic velocity along the incoming photon's direction in the global rest frame, and c the speed of light. Finally, $\sigma(\nu')$ is the Ly- α scattering cross section of a photon with frequency ν' in the atom rest frame.

The function $p(u_{\parallel})$ usually results from the thermal distribution of the atoms velocity:

$$p(u_{\parallel}) = \frac{1}{\sqrt{\pi} v_{\text{th}}} \exp \left(-\frac{u_{\parallel}^2}{v_{\text{th}}^2} \right) \quad \text{with} \quad v_{\text{th}} = \sqrt{\frac{2k_{\text{B}}T}{m_{\text{p}}}}. \quad (2)$$

Some astrophysical systems have significant velocity gradients on scales below the best possible resolution of the simulations. In these cases it may be relevant to model the small-scale velocity contribution by adding a turbulent component to the thermal velocity dispersion. We did not include any turbulent contribution in this paper.

¹ <http://www.skads-eu.org>

The exact expression of the Ly- α scattering cross section is given in Peebles (1993). It is well-approximated by the usual Lorentzian profile:

$$\sigma(\nu) = f_{12} \frac{\pi e^2}{m_e c} \frac{\Delta\nu_L/2\pi}{(\nu - \nu_0)^2 + (\Delta\nu_L/2)^2}, \quad (3)$$

where $f_{12} = 0.4162$ is the Ly- α oscillator strength, $\nu_0 = 2.466 \times 10^{15}$ Hz is the line center frequency, and $\Delta\nu_L = 9.936 \times 10^7$ Hz is the natural line width.

We introduce the dimensionless parameters x , the relative frequency shift, and b , the natural to Doppler line width ratio:

$$x = \frac{\nu - \nu_0}{\Delta\nu_D} \quad \text{with} \quad \Delta\nu_D = \frac{v_{\text{th}}}{c} \nu_0, \quad (4)$$

$$b = \frac{\Delta\nu_L}{2\Delta\nu_D}. \quad (5)$$

Using these notations, we can write the optical depth increment in the local rest frame of the gas ($v_{\parallel}^{\text{macro}} = 0$) as

$$d\tau = ds n_{\text{HI}} \frac{f_{12} \sqrt{\pi} e^2}{m_e c \Delta\nu_D} H(b, x), \quad (6)$$

or in cgs units

$$d\tau = ds n_{\text{HI}} 6.87 \times 10^{-14} \left(\frac{T}{10^4}\right)^{-\frac{1}{2}} H(b, x), \quad (7)$$

where H is the Voigt function defined as

$$H(b, x) = \frac{b}{\pi} \int_{-\infty}^{+\infty} \frac{e^{-y^2}}{(x-y)^2 + b^2} dy. \quad (8)$$

To compute the Voigt function, we either use the analytic fit given by Tasitsiomi (2006) or, in cosmological situations where the Hubble flow on a scale of the order of the simulation spatial resolution produces a frequency shift larger than the Ly- α line width (see Sect. 2.1.3), we use the simple approximation

$$H(x, b) \simeq \max\left(e^{-x^2}, \frac{b}{\sqrt{\pi}x^2}\right). \quad (9)$$

2.1.2. Effect of the $n=2$ state splitting, dust, and deuterium.

A Ly- α photon can excite a hydrogen atom from the $1S_{1/2}$ ground state to either the $2P_{1/2}$ or the $2P_{3/2}$ state. As discussed by Tasitsiomi (2006), the splitting between these two $n=2$ states is small: only 10 GHz or 1 km s^{-1} . If the thermal velocity dispersion is much larger than $\sim 1 \text{ km s}^{-1}$ (i.e. $T > 100 \text{ K}$), the level splitting is washed out from the radiation spectrum after just one scattering. In the case of the Ly- α background radiation during the EoR, the gas temperature drops to $\sim 30 \text{ K}$. However the optical depth as the photon redshifts from one side to the other of the Ly- α line is very high: $\sim 8 \times 10^5$ for the average gas density of the universe ($\Omega_b = 0.045$) at $z = 9.5$ in a standard cosmological model. Thus the photon will scatter off thermal atoms many times and still the splitting will be washed out. Consequently, we did not distinguish between the two $2P$ states in this paper.

Another issue is the possible reshuffling from $2P$ to $2S$ through collisions with free protons or electrons. An atom cannot be excited directly to the $2S$ state because of the dipole selection rule. But if the $2P \rightarrow 2S$ transition is induced by a collision, then the atom will de-excite through the emission of 2 continuum

photons losing the Ly- α photon. Tasitsiomi (2006, see Eq. (26)) computed the probability that an atom in the $2P$ state will reshuffle to $2S$ before it de-excites normally by emitting a Ly- α photon, $p \sim 8.5 \times 10^{-13} n_p \left(\frac{T}{10^4}\right)^{-0.17}$, where n_p is the proton number density. What can we expect during the EoR? First, we are interested in the Ly- α background in the cold, *neutral* region of the universe, thus $n_p \ll 1$. Moreover, even if we assume a non negligible ionization fraction, $p \sim 5 \times 10^{-13}$ at $z \sim 10$ for $T = 50 \text{ K}$ and for the critical density of the universe with $\Omega_b = 0.045$. This probability must be compared with the average number of scatterings a photon undergoes as it redshifts through the Ly- α line, which is similar to the optical depth: $\sim 10^6$. We see that only a fraction of 5×10^{-7} of the Ly- α photons will be degraded into 2 continuum photons before they redshift out of the line, so we conclude that this process is not relevant during the EoR.

Dust is usually a factor in Ly- α transfer simulations since it absorbs Ly- α photons. Hansen & Oh (2006) study the effect of dust absorption in a multiphase medium and show that photons can escape such a medium, while they would be absorbed in a more homogeneous single-phase medium, for the same total HI column density. In the cosmological context we are working in ($z > 6$), there are no observations to help us constrain the dust abundance and distribution. We can assume that, during the EoR, dust may be found only around the sources and that the IGM is completely dust free. Under this assumption, the effect of dust on the Ly- α flux can be modeled with a simple escape-fraction coefficient. Furthermore, if this coefficient is assumed to be independent of the source, dust will not have any effect on the Ly- α flux *fluctuations* that are the focus of this paper. Therefore, we did not include the effect of dust.

Dijkstra et al. (2006) show that the presence of deuterium with an abundance $[D/H] = 3 \times 10^{-5}$ leaves a clear imprint on the spectrum emerging from a uniform sphere of gas with a central source and a total optical depth $\tau = 7.3 \times 10^5$. Is deuterium relevant to the Ly- α flux during the EoR? The deuterium line center is 82 km s^{-1} blueward of the hydrogen line. This is equivalent to the redshift of a photon traveling ~ 0.5 comoving Mpc at $z = 9.5$, so the first answer is that deuterium may have an effect on the Ly- α flux fluctuations only on small scales ($< 1 \text{ Mpc}$ comoving). However, the total optical depth for deuterium through the Ly- α line is $\tau \sim 20$ for an abundance $[D/H] = 2 \times 10^{-5}$, and the optical depth in the wing of the Hydrogen Ly- α line, as the photon redshifts from far in the blue to the center of the deuterium line happens to also be $\tau \sim 20$. This means that, while the photon will indeed scatter a few times in the deuterium line, it will also have been scattered in the hydrogen line wing several times before it reaches the frequency range where deuterium scattering dominates (a few 10 km s^{-1} around the line center). We conclude that the presence of deuterium is unlikely to affect the Ly- α flux fluctuations noticeably. This does not mean that the effect of deuterium on Ly- α radiation cannot be observed during the EoR. Indeed, in the case of an ionizing bubble around a source with a sharp ionization front, the continuum spectrum of the source will show a Gunn-Peterson trough with a step at the bubble redshift. Deuterium should create a secondary small step.

2.1.3. Dealing with large Hubble flows

In $z \sim 10$ cosmological simulations, the Ly- α thermal line width is equivalent to the Hubble-flow redshift over only a few 10 comoving kpc. This scale is usually (much) smaller than the size of cells in simulations, so we must be careful when we compute the optical depth: using a single comoving frequency for the photons

throughout a cell would result in photons flowing through the line core without feeling it. We must actually compute an integral along the path of the photon, with a redshifting comoving frequency, to obtain the correct optical depth. If we consider that the expansion velocity between any two points of the same cell is non-relativistic ($\frac{\Delta x}{c} \sim 0.01$ for 20 comoving Mpc at $z \sim 10$), the computation gets easier. Let ν_{in} be the comoving frequency and x_{in} the local rest frame value of x when the photon enters the cell:

$$x_{in} = \frac{\nu_{in}(1 - \frac{\mathbf{v}^{\text{macro}} \cdot \mathbf{k}}{c}) - \nu_0}{\Delta \nu_D}, \quad (10)$$

where $\mathbf{v}^{\text{macro}}$ is the macroscopic velocity of the gas (uniform inside the cell), and \mathbf{k} the direction of the photon. Then, at a given point inside the cell defined by the vector $r\mathbf{k}$ from the entering point of the photon, the comoving frequency is

$$\nu = \frac{a(\nu_{in})}{a(\nu)} \nu_{in} \sim \frac{\nu_{in}}{1 + \frac{Hr}{c}} \sim \nu_{in} \left(1 - \frac{Hr}{c}\right), \quad (11)$$

where H is the Hubble constant at the simulation redshift, and a the expansion factor. We neglect any variation of H during the photon travel and consider non-relativistic expansion velocities. For non-relativistic macroscopic velocities of the gas, the corresponding value of x writes as

$$x = x_{in} - \frac{Hr}{c} \frac{\nu_{in}}{\Delta \nu_D}. \quad (12)$$

As a result, we linearized the relation between r , the current path length inside the cell, and the current local rest-frame value of the x variable. In this approximation, noting x_{out} as the value of x when the photon exits the cell, computing the optical depth reduces to computing the integral Voigt function $H_{int}(x_{out})$, with the following definition for the H_{int} function:

$$H_{int}(x) = \int_{x_{in}}^x H(x', b) dx'. \quad (13)$$

However, in the Monte-Carlo method, to find the location of a scattering event, we need to solve the equation $H_{int}(x) = A$, where A is a constant. This is simplified if we can provide an analytic expression for $H_{int}(x)$, with an explicit inverse function. This is the case if we use the simple approximation of $H(x, a)$ given in Eq. (9). It involves the $\text{erf}(x)$ function for which we are using an approximation that has an explicit inverse function.

Modeling the effects of expansion only by a redshift computed from a radial dilatation is the usual approximation for Ly- α radiative transfer codes. Other effects of the variation in the expansion factor a , such as variation in the average density during the photon flight time, are usually ignored. However, let us emphasize that adding the expansion velocity to the other types of velocities (macro or microscopic) to compute Doppler shifts, either during scattering events or for computing local rest frame values of x , works only if all velocities are non-relativistic. However, we want to study the Ly- α flux during the EoR; and at $z \sim 10$, a photon emitted just below the Ly- β frequency will travel ~ 350 comoving Mpc and be redshifted to Ly- α by a Hubble flow velocity such that $v_H/c \sim \frac{\Delta \nu}{\nu} \sim \frac{\Delta a}{a} \sim 0.15$. In this case, the second-order errors in computing the redshift are not completely negligible. But, what is more important, neglecting the variations in a along the photons' path, in computing gas densities for example, produces first-order errors in $\frac{\Delta a}{a}$. Consequently, we should limit ourselves to ~ 100 comoving Mpc boxes. In this work, we do neglect variations in a , except for

the cosmological redshift, and in most cases we use simulation boxes smaller than ~ 30 comoving Mpc. The full effect of expansion will be introduced in the future to handle larger boxes.

2.2. Scattering off hydrogen atoms

In an expanding universe, the natural variable is the comoving frame frequency of the photon. However, as long as the Hubble flow velocities are non-relativistic, we can use the frequency in the rest frame of the zero-coordinate point of the simulation, hereafter named *global frame*, and treat the expansion as a simple radial dilatation with a $\mathbf{v}_H = Hr$ velocity field to be added to the peculiar velocities.

In the rest frame of the atom, we consider the scattering to be resonant. The effect of the recoil, which would change the frequency of the photon by transferring part of its momentum to the atom, has been shown to be negligible in astrophysical situations by several authors (Zheng & Miralda-Escudé 2002; Tasitsiomi 2006). In the global frame, however, the frequency ν of the photon will change due to the various contributions to the atoms velocity.

There are three main contributions to the atom velocity: the thermal motion, the macroscopic peculiar motion and the Hubble flow. When the photon scatters off an atom, we first compute the frequency in the atom rest frame:

$$\nu_{\text{atom}} = \nu \left(1 - \left(\frac{\mathbf{v}_H + \mathbf{v}^{\text{macro}} + \mathbf{u}}{c}\right) \cdot \mathbf{k}_i\right), \quad (14)$$

where \mathbf{u} is the thermal velocity of the atom, and \mathbf{k}_i the direction of the incoming photon. Let us split \mathbf{u} into \mathbf{u}_{\parallel} , the component parallel to the incoming photon direction, and \mathbf{u}_{\perp} , the perpendicular component. $\frac{\mathbf{u}_{\perp}}{v_{\text{th}}}$ obeys the distribution:

$$P_1(y) = \frac{b}{\pi H(b, x)} \frac{e^{-y^2}}{(x-y)^2 + b^2}, \quad (15)$$

while each of the 2 components of \mathbf{u}_{\perp} obeys

$$P_2(y) = \frac{1}{\sqrt{\pi} v_{\text{th}}} e^{-\frac{y^2}{v_{\text{th}}^2}}. \quad (16)$$

Then we compute the direction of the photon after scattering. As described by Tasitsiomi (2006) the scattering phase function depends on the excitation state and on whether the photon scatters in the wing or in the core of the line. Several authors (see e.g. Cantalupo et al. 2005; Verhamme et al. 2006) have shown that, for high optical depth media, the shape of the phase function does not alter the results of the simulation. In this work, we use isotropic scattering. With the new direction of the photon, we then recompute the frequency in the global frame using a non-relativistic Doppler effect.

3. Ly- α radiative transfer: numerical methods

3.1. Gas density and velocity field

LICORICE is meant to use results from dynamical simulations realized with the TreeSPH part of the code (Semelin & Combes 2002). It uses the same Tree structure as the dynamical code to build an adaptative grid. The grid is built in such a way that each cell contains between 1 and N_{max} gas particles. Values from 1 to 30 are commonly used for N_{max} . The density and velocity fields are then interpolated from the particle distribution. The

cells limit the resolution of the simulation only by having uniform dynamical properties. Ly- α transfer inside one cell is still computed exactly under the assumption that the expansion velocity on the scale of the cell is non-relativistic.

3.2. Monte-Carlo method

Using the Monte-Carlo approach, we send individual photon from the source and follow them from scattering to scattering and from grid cell to grid cell until they exit the simulation box. After one event (emission or scattering), the algorithm is the following:

- Step 1: compute the photon global frame frequency either from the scattering atom rest frame frequency or from the source spectrum.
- Step 2: draw the new photon direction (isotropically in this work).
- Step 3: draw a variable p from a uniform distribution between $[0, 1]$. The photon will travel an optical depth $\tau = -\ln(p)$ to the next scattering event.
- Step 4: increment optical depth with current cell contribution. Determine if scattering occurs in this cell: if yes, go to step 5; if no, pass on to next cell and repeat step 4.
- Step 5: draw scattering atom thermal velocity and compute frequency in the scattering atom rest frame. Go back to step 1.

3.3. Acceleration scheme

To generate random variable following Eq. (15) distribution, we use the method by Zheng & Miralda-Escudé (2002). These authors introduce a parameter u_0 for which an optimal value is needed. We use the following empirical fit:

$$u_0 = 1.85 - \log(b)/6.73 + \ln(\ln(x)) \quad \text{for } x > 3, \quad (17)$$

and $u_0 = 0$ otherwise. This has been determined from a systematic numerical optimization and works well for $10^{-4} < b < 10^{-1}$. For high values of x , quite common in cosmological simulations, drawing a value from P_1 is still slow, even with the Zheng & Miralda-Escudé method. In this case, however, scattering will most likely occur in the wing of the line. Consequently, for $x > 10$, we revert to $u_0 = 0$ but truncate the distribution to the limited range $[-3, 3]$.

We use the core-skipping acceleration scheme; see Avery & House (1968) or Ahn et al. (2002) for the first applications. In this scheme, we choose a core value x_c for the variable x . In the regime $x < x_c$, the medium must be thick. If so, the photon will scatter many times over a very short distance. Only when x gets larger than x_c (scattering in the wing by a fast moving atom) will the medium become transparent and the photon will travel a long distance. The idea is to ignore the insignificant core scatterings: every time the photon enters the core ($x < x_c$), it leaves again immediately by scattering off an atom with a thermal velocity $u_{\text{at}} > x_c u_{\text{th}}$. We use the detailed prescriptions given by Tasitsiomi (2006) on choosing x_c as a function of $b\tau_0$, where b is defined in Eq. (5) and τ_0 is the optical depth at the line center. The core-skipping scheme works well when the expected output of the code is an emerging spectrum. We show that it also works for computing the fluctuations of the local scattering rate.

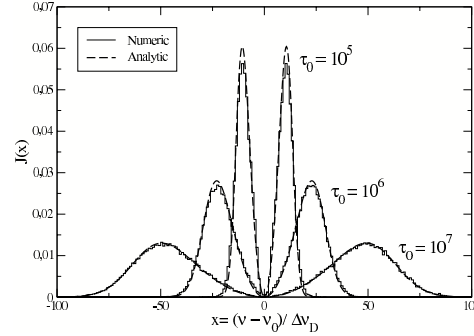


Fig. 1. Emerging spectrum for a uniform and spherical cloud of gas at $T = 10$ K and several values of τ_0 , the total optical depth at line center; Numerical histograms are computed with 10^5 photons. The analytic solution is given in Dijkstra et al. (2006).

4. Validation tests

Since LICORICE is a complex, multipurpose code, we make certain to validate each part separately. We present validation tests for the Ly- α part here, comparing our results to analytical solutions or standard numerical setups.

4.1. Static homogeneous sphere: emerging spectrum

A classical validation test for Ly- α codes is the emerging spectrum for a monochromatic source in the middle plane of a static homogeneous slab of gas. The main reason is that Neufeld (1990) gives an analytic solution for the emerging spectrum in the case of an extremely thick system. However, Dijkstra et al. (2006) provide a new analytic expression in the case of a uniform spherical cloud of gas:

$$J(x) = \frac{\sqrt{\pi}}{\sqrt{24a\tau_0}} \left[\frac{x^2}{1 + \cosh\left(\sqrt{\frac{2\pi^3 |x^3|}{27 a\tau_0}}\right)} \right]. \quad (18)$$

Since this geometry is more relevant in a cosmological context, we present results for this case (we also performed the Neufeld test and found good agreement). Figure 1 shows the comparison between numerical and analytic spectra for a static spherical cloud of gas with temperature $T = 10$ K and optical depths at line center from center to edge equal to 10^5 , 10^6 , and 10^7 . For each run, 10^5 photons were injected at the center of the cloud with frequency ν_0 . The emerging spectrum $J(x)$ was obtained by computing a normalized histogram of the frequencies of the photons as they leave the cloud. The agreement is good in all cases, although it gets better and better as τ_0 increases. Indeed in the case $\tau_0 = 10^5$, we have $a\tau_0 = 1500$, which is close to the lower limit for an extremely thick medium.

4.2. Expanding homogeneous sphere: emerging spectrum

The second test is also becoming a classic. It was first performed by Zheng & Miralda-Escudé (2002), followed by several authors such as Verhamme et al. (2006) who present especially detailed results. The system is a uniform sphere of gas expanding (or contracting) with a Hubble-like velocity field: the radial velocity is proportional to the radius. We used the same physical condition as Zheng & Miralda-Escudé (2002): a temperature of 20 000 K

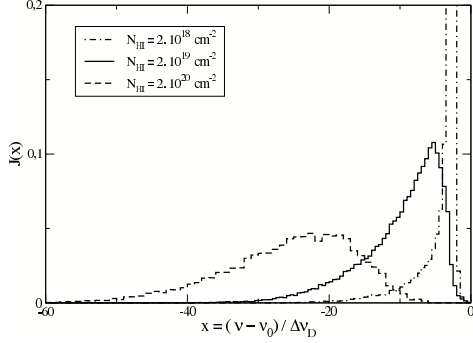


Fig. 2. Emerging spectrum for a spherical, uniform, and expanding cloud of gas at $T = 20000$ K and several values of N_{H} , the column density from the center to the edge of the cloud. The emission is at Ly- α frequency from the central point of the cloud. The radial velocity of the gas is proportional to the radius and equals 200 km s^{-1} at the edge of the cloud. The peak blueward of the Ly- α frequency is completely suppressed by the expansion.

and a radial velocity of 200 km s^{-1} at the edge of the cloud. We used three different column densities from the center to the edge of the cloud: N_{H} equals $2 \times 10^{18} \text{ cm}^{-2}$, $2 \times 10^{19} \text{ cm}^{-2}$ or $2 \times 10^{20} \text{ cm}^{-2}$ (that is $\tau_0 = 8.3 \times 10^4$, 8.3×10^5 , or 8.3×10^7). We did not run the tests for a contracting cloud, and we only considered a central point source emitting at Ly- α frequency, not the case of uniform emissivity. An expanding cloud with a central point source is the most relevant to the EoR. The emerging spectra are shown in Fig. 2. We find very similar results to Zheng & Miralda-Escudé (2002) or Verhamme et al. (2006). The peak blueward of the Ly- α frequency is completely suppressed by the expansion (not shown in Fig. 2). For the case of a contracting cloud, the red peak would be suppressed

4.3. Expanding homogeneous sphere at $T=0$ K: mean intensity field

Our last validation test relies on an analytic solution given by Loeb & Rybicki (1999). The setup is again an expanding uniform hydrogen medium with a central monochromatic source at Ly- α frequency. The velocity field is a Hubble flow again, but this time, the gas temperature is $T = 0$ K. Loeb & Rybicki introduced the dimensionless variable $\tilde{\nu} = \frac{\nu_0 - \nu}{\nu_\star}$, where ν_\star is the comoving frequency shift from Ly- α at which the optical depth to infinity equals 1, and $\tilde{r} = \frac{r}{r_\star}$, where r_\star is the proper radius at which the Doppler shift from the source due to the Hubble expansion equals ν_\star . Loeb & Rybicki give an analytic expression for the corresponding dimensionless mean intensity \tilde{J} , valid in the diffusion regime:

$$\tilde{J}(\tilde{r}, \tilde{\nu}) = \frac{1}{4\pi} \left(\frac{9}{4\pi\tilde{\nu}^3} \right)^{\frac{3}{2}} \exp\left[-\frac{9\tilde{r}^2}{4\tilde{\nu}^3}\right]. \quad (19)$$

Loeb & Rybicki (1999) show the comparison between the analytic solution and the numerical solution given by a dedicated Monte-Carlo code. Tasitsiomi (2006) runs this test with his general purpose code. Our results are presented in Figs. 3 and 4. They are very similar to those of Loeb and Rybicki and Tasitsiomi: the numerical results are close to the analytic solution where the diffusion regime is valid. However, where photons enter the free-streaming regime ($\tilde{\tau}_0 = 1$ in Fig. 3 and $\log \tilde{\nu}_0 = 0.5$

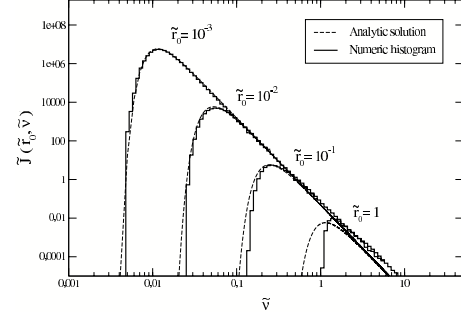


Fig. 3. Mean intensity spectra at various radii for a Ly- α monochromatic source in a uniform expanding medium at $T = 0$ K. The numerical result is compared to the analytic solution given in the diffusion regime by Loeb & Rybicki (1999).

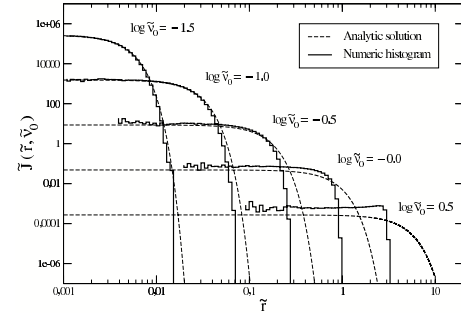


Fig. 4. Mean intensity profile at various frequencies for a Ly- α monochromatic source in a uniform expanding medium at $T = 0$ K. The numerical result is compared to the analytic solution given, in the diffusion regime, by Loeb & Rybicki (1999).

in Fig. 4), the numerical solution diverges from the analytic solution, which becomes invalid.

Here are some details on how we ran this test. We used a temperature $T = 2$ K for computing the optical depth, which is singular for $T = 0$ K, but we used a zero thermal velocity for the atoms in all scattering events. We used a simulation box holding a sphere of gas of radius $10r_\star$. Since the temperature is not zero in all respects, it reintroduces a dimension into the problem. Very close to the source the thermal speed is higher than the expansion velocity and the numerical behavior should diverge from the analytic solution. For reference, we used a proper expansion velocity of 200 km s^{-1} at r_\star . In our setup, the thermal and expansion velocities similar for $r \sim 10^{-3}r_\star$.

The radii range covered by this test is quite wide, from $10^{-3}r_\star$ to $10r_\star$. Using 10^{12} cells for the radiative transfer grid is not really an option. Actually, we used only 16^3 cells, but we took advantage of the integral scheme described in Eqs. (12) and (13) for computing the optical depth exactly between two points in the same cell. This approach is obviously validated by the good agreement shown in Fig. 4 at small radii.

5. Ly- α during the EoR

5.1. The role of Ly- α photons in the 21 cm emission

The 21-cm signal can be seen in emission or absorption against the CMB. The differential brightness temperature observed at redshift $z = 0$ is

$$\delta T_b = \frac{T_S - T_{\text{CMB}}}{1+z} (1 - e^{-\tau_{21}}), \quad (20)$$

where T_S is the neutral hydrogen spin temperature, T_{CMB} the CMB radiation blackbody temperature at redshift z , and τ_{21} the 21-cm line optical depth. The value of τ_{21} is given, among others, by Tozzi et al. (2000) or Furlanetto et al. (2006a). Injecting the formula for $\tau_{21} \ll 1$, the differential brightness temperature can be written as

$$\delta T_b \sim 9 \cdot x_{\text{HI}} (1 + \delta)(1+z)^{\frac{1}{2}} \frac{T_S - T_{\text{CMB}}}{T_S} \text{ mK}, \quad (21)$$

where δ is the local overdensity at redshift z , and x_{HI} the neutral hydrogen fraction. This value of δT_b is for a flat Λ CDM model with $h_0 = 0.7$ and $\Omega_b = 0.044$. It changes by ± 0.5 mK when Ω_m varies from 0.25 to 0.3. The value of the spin temperature T_S is the result of three competing processes. The absorption/reemission of CMB photons tends to bring T_S to T_{CMB} over a time scale under 10^5 years during the EoR (Tozzi et al. 2000). As we have seen in the Introduction, both collisions between hydrogen atoms and the pumping by Ly- α photons, also known as the Wouthuysen-Field effect (Wouthuysen 1952; Field 1958), instead tends to couple T_S to the kinetic temperature of the gas. As a result, the spin temperature can be written (Furlanetto et al. 2006a) as

$$T_S^{-1} = \frac{T_{\text{CMB}}^{-1} + x_c T_K^{-1} + x_\alpha T_C^{-1}}{1 + x_c + x_\alpha} \quad \text{with} \quad T_C \simeq T_K, \quad (22)$$

where x_c and x_α are the coupling coefficients for collisions and Ly- α pumping respectively, and T_C is the effective color temperature of the UV radiation field (see Furlanetto et al. 2006a). The coefficient x_α , which is the focus of this work, can be explicitly written as

$$x_\alpha = \frac{4P_\alpha T_\star}{27A_{10} T_{\text{CMB}}},$$

where $T_\star = 0.068$ K, $A_{10} = 2.85 \times 10^{-15} \text{ s}^{-1}$ is the spontaneous emission factor of the 21-cm transition, and P_α is the number of scatterings of Ly- α photons per atom per second. Now, two approximations usually occur that we do not make in this paper. The first is that P_α is considered proportional to $J(\nu_\alpha)$, the angle averaged specific intensity at the local Ly- α frequency, neglecting the contribution of wing absorptions. We will see that this approximation is valid, provided $J(\nu)$ itself has been computed taking wing absorptions into account. The second, more drastic approximation is to evaluate $J(\nu)$ without performing the full radiative transfer computation. Actually, to our knowledge, all numerical simulations of 21-cm emission consider a uniform value for $J(\nu_\alpha)$. However, Barkana & Loeb (2005) have shown that several factors induce fluctuations in $J(\nu_\alpha)$: the $1/r^2$ scaling of the flux that magnifies the Poisson noise in the source distribution, the clustering of the sources, and the contribution of higher Ly- α series photons (also studied in detail by Pritchard & Furlanetto 2006). They predict the power spectrum of the 21-cm brightness temperature due to the fluctuation in $J(\nu_\alpha)$. Although this is a vast improvement over using a uniform Ly- α flux, they are still neglecting radiative transfer effects in

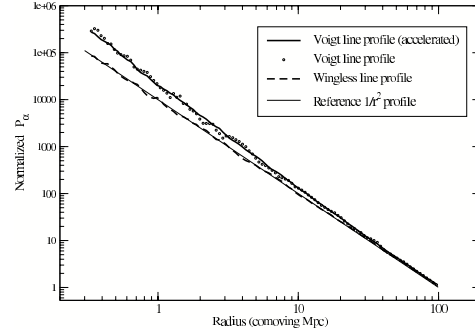


Fig. 5. Profiles of the scattering rate per atom, P_α , in the Ly- α line, around a central source with a continuous flat spectrum in a homogeneous medium of neutral hydrogen at 30 K and the average baryon density of the universe at $z \sim 10$.

assuming that photons are freely streaming until they redshift to the local Ly- α frequency. We show that this assumption breaks down at scales smaller than ~ 10 comoving Mpc.

Potentially, pumping the upper excitation level is not the only way for Ly- α photons to influence the 21-cm emission: they also heat up the gas. This heating mechanism was first thought to be efficient by Madau et al. (1997). However, Chen & Miralda-Escudé (2004), taking the atoms' thermal velocity distribution into account that had been neglected by Madau et al., found a much lower, actually negligible, heating rate. Furlanetto & Pritchard (2006), considering the effect of higher Lyman series photons, confirmed this result and found, for typical EoR conditions, the Ly- α heating rate to be 140 lower than the heating rate from X-rays. Chuzhoy & Shapiro (2007) recently challenged this result, in particular adding the effect of the deuterium Ly- β resonance line, but the strength of this effect is not yet completely probed.

5.2. P_α profiles for spherically symmetric configurations

In the next three cases, we consider a central source in a spherically symmetric medium of neutral hydrogen at $T_K = 30$ K and $z \simeq 10$, which is typical of the EoR. The main difference with the setup of the tests in Sect. 4.3 is that the source emits a flat continuous spectrum. We only deal with photons between Ly- α and Ly- β frequencies.

5.2.1. Homogeneous medium

First, we consider the case where the gas is homogeneous with a density equal to the average density of the universe at $z \sim 10$. We ran the simulation in a 600 comoving Mpc box with the source in the center of the box. We present the results up to a radius of 100 comoving Mpc. At larger radii, the effect of the box boundaries (no retrodiffusion) and the variation in a during the photon flight (see Sect. 2.1.3) alter the validity of the simulation. Figure 5 presents the radial profile of the scattering rate per atom, P_α , in different cases.

Using the real Voigt line profile, we can see a deviation at small radii from the simple $1/r^2$ profile expected if photons stream freely from the source until they redshift to the local Ly- α frequency. Here is why. Let us consider a photon emitted above the Ly- α frequency. As it travels away from the source, it is redshifted toward the local Ly- α frequency. Because of the contribution of the wings of the Voigt profile to the optical depth, it

has a probability of scattering before reaching the local Ly- α frequency. On average, it will scatter for the first time when the optical depth along its path reaches 1. This is achieved when the photon is redshifted to the frequency $\sim\nu_\alpha + \nu_\star$ (see Sect. 4.3), which occurs at a distance r_\star before the location where it would reach the local Ly- α frequency (quantities defined in Loeb & Rybicki 1999). In our setup, typical of the EoR, $r_\star \sim 10$ comoving Mpc. After the photons scatter for the first time, they change direction. Consequently, the location where a photon actually enters the core of the local Ly- α line has a probability of being anywhere within ~ 10 comoving Mpc of the location determined by free streaming alone. This is not crucial on large scales where the expected $1/r^2$ profile is recovered, but it creates a steeper profile on small scales (exponent ~ -2.3 in our setup). To validate our interpretation, we computed the transfer with a modified line profile: the core of the line is unchanged, but the wings are set to zero. As can be seen in Fig. 5, we then recover the $1/r^2$ profile. After this paper was submitted, Chuzhoy & Zheng (2007) posted a paper with a similar result. They considered a very similar setup and computed the transfer with a simple Monte Carlo code that is 1-D (spherical symmetry) and uses a simplified line profile but does include Ly- α photons locally injected by cascades from upper Lyman series lines. They find the same steepening of the scattering rate profile on short scales. However, they show that photons injected from upper Lyman series lines are much less sensitive to radiative transfer effect, and they follow the $1/r^2$ profile more closely. Consequently, the discrepancy between the full radiative transfer computation and the simple $1/r^2$ evaluation is somewhat reduced.

Finally we checked the effect of using the core-skipping acceleration scheme for evaluating the fluctuations of P_α : since all core absorptions are avoided, it could have modified the spatial P_α fluctuation map. As can be seen in Fig. 5, this is not the case. Although the wings modify the location where photons enter the core, the scattering number is still dominated by the close-to-the-core contribution.

5.2.2. Central clump

Until now, the Ly- α scattering rate has been evaluated during the EoR only in a homogeneous medium (Barkana & Loeb 2006; Pritchard & Furlanetto 2006). With a general-purpose 3D code such as LICORICE, we can investigate the impact of density fluctuations in the gas on the Ly- α scattering rate per baryon. First we choose a very simple setup by considering a box of size 64 comoving Mpc, with a central homogeneous spherical clump of gas of radius 1 comoving Mpc. The clump is 64 times denser than the surrounding medium, which has the average baryon density of the universe at the redshift of the simulation ($z \sim 10$). The source is in the center of the clump and has a continuous flat spectrum. The radial profile of the Ly- α scattering rate per atom, P_α , is shown in Fig. 6. The main feature is a depletion of P_α in the low-density medium just outside the clump. Indeed, photons that should redshift to the Ly- α frequency in this region first have to travel through the high-density region where they have an enhanced probability of being scattered in the wing of an atom and redirected to redshift to local Ly- α while still inside the core. In other words, the enhanced wing scatterings in the clump draw core scatterings from surrounding regions to the clump itself. This is somewhat similar to the usual shadowing effect in radiative transfer, although in this case the process occurs in the frequency space, so the *shadowing* can be seen even in a spherical configuration. Obviously, in addition to the $1/r^2$ decline of the flux and the fluctuations in the source distribution,

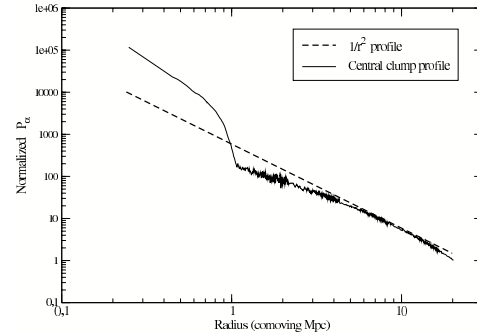


Fig. 6. Profile of the scattering rate per atom, P_α , in the Ly- α line, around a central source with a continuous flat spectrum, inside an over-dense spherical clump of gas (64 times the density of the surrounding medium) of radius 1 comoving Mpc.

we can expect a new source of fluctuations for P_α : the density fluctuations of the intergalactic medium.

5.2.3. Isothermal density profile

Instead of the sharp density transition between the clump and the surrounding medium we now consider an isothermal density profile ($\rho \sim 1/r^2$) around the source. The isothermal profile connects to the surrounding homogeneous medium at a radius of 10 comoving Mpc. All other parameters of the simulation are the same as in the previous setup. The radial profile of the Ly- α scattering rate per atom, P_α , is shown in Fig. 7. Since the average density is higher than in the other setups, photons scatter many times and even with an acceleration method, we used only 2×10^4 photons. To avoid a very high noise level at large radii, we used an adaptive resolution: high in the center, lower in the outer regions. We can see in the figure that, inside the region with an isothermal density profile, P_α matches a $1/r^3$ profile closely. It reverts to $1/r^2$ in the homogeneous medium outside the 10 Mpc radius. This shows that the brightness temperature fluctuations of the 21-cm emission may be stronger than previously estimated on small scales, at least during the early EoR when P_α fluctuations are meaningful.

Is this setup more effective in predicting P_α fluctuations during the EoR than a uniform medium? Yes, in the sense that the medium should obviously be denser closer to the source. However the spherical symmetry and the specific profile used here are oversimplified, since the actual intergalactic medium in the EoR is not in an equilibrium configuration, especially during this early period of sources formation, and the spherical symmetry is broken by the presence of filaments. In the next section we investigate how filaments modify P_α .

5.3. P_α map for an axisymmetric configuration

We now consider an axisymmetric density field for the gas. Inside a cylinder of radius 1 comoving Mpc, the density is 64 times the critical baryon density, while outside it is equal to the critical baryon density. The source is located on the symmetry axis. All other parameters are identical to the previous setup. This new setup is a simplified representation of the real case of source formation during the EoR at the intersection of several filaments, where the filaments have a density profile. The P_α contour map is shown in Fig. 8. The shaded area represents

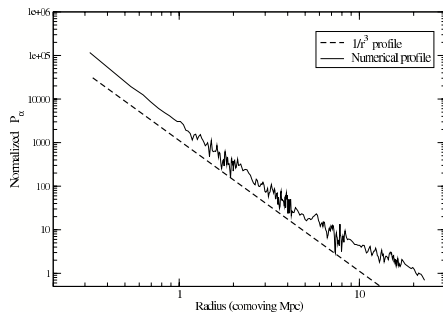


Fig. 7. Profile of the scattering rate per atom P_α in the Ly- α line, around a central source with a continuous flat spectrum. Inside a sphere of radius 10 comoving Mpc, the gas density field is an isothermal sphere, while outside it is homogeneous at the average baryon density of the universe ($z \sim 10$). The two regions connect smoothly. A $1/r^3$ profile is plotted for comparison.

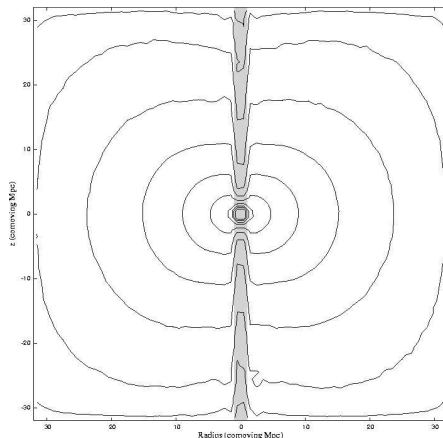


Fig. 8. Contours of the scattering rate per atom P_α in the Ly- α line, around a central source with a continuous flat spectrum. The source is located inside a cylindrical homogeneous filament of gas (shaded zone in the figure) with a density 64 times the density of the surrounding medium, which is at the average baryon density of the universe ($z \sim 10$). The contours are equally spaced on a logarithmic scale with a step of $\sqrt{10}$.

the filament, and the contours are equally spaced on a logarithmic scale (two per decade). The map is integrated over a variation of π in the angular variable. About 5×10^6 photons were used for this simulation. There is some boundary effect due to the finite size of the simulation box: photons that would scatter just outside the simulation box and possibly reenter the box are lost instead. This affects a few Mpc near the boundary. We can see a sharp depletion in the number of scatterings per atom inside the filament. We have checked that a lower density contrast creates a smaller depletion, as expected. Once again, we see that the gas density field fluctuations induce fluctuations in P_α . However, the weaker Wouthuysen-Field effect in denser regions may be balanced by the greater coupling due to collisions (which is proportional to the density). What may be more relevant to the future observations than what occurs on small scales inside the filaments is that the presence of the filaments modifies the shape of the contours in the low-density surrounding medium: they are

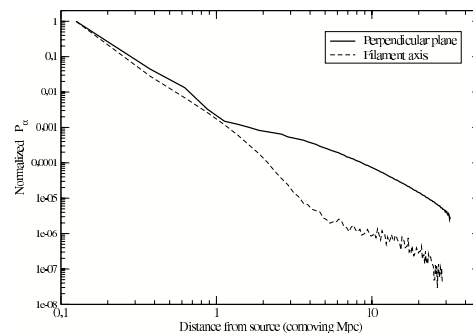


Fig. 9. Scattering rate per atom P_α in the Ly- α line along the axis of a filament and in a perpendicular plane. A central source with a continuous flat spectrum is located at the intersection of the filament and the plane. The filament is cylindrical with radius 1 comoving Mpc and homogeneous with a density 64 times the density of the surrounding medium, which is at the average baryon density of the universe ($z \sim 10$).

not spherical but oblate. With our density contrast, the axis ratio is about 2 in the 5–10 Mpc range and decreases at large distances. Figure 9 shows the normalized P_α profiles along filament axis and in the perpendicular plane containing the source. While inside the filament (distance smaller than 1 comoving Mpc), the profiles match. At larger distances, Fig. 9 quantifies the P_α ratio between the two regions: it reaches a maximum value of ~ 100 at a distance of ~ 5 Mpc.

6. Conclusions

The main goal of this paper was to investigate a source of fluctuations in the brightness temperature of the 21-cm emission during the EoR, which is usually neglected in numerical simulations. The Wouthuysen-Field effect, which couples the hydrogen spin temperature to the kinetic temperature of the gas, is regulated by the crucial parameter P_α , the number of scatterings per atom per second. While all previous simulations of the 21-cm emission used a uniform value for P_α , Loeb & Barkana (2005) have shown, in a simple theoretical framework, that several sources of fluctuations in P_α can modify the power spectrum of the 21-cm emission. We studied how a full 3D radiative transfer treatment of the Ly- α line in a cosmological context modifies the picture given by Loeb and Barkana.

The first step was to implement and validate the Ly- α radiative transfer in LICORICE. We used a Monte-Carlo approach, and implemented an algorithm and acceleration schemes along the same lines as those of other existing codes. We discarded physical processes such as recoil or deuterium contribution, which have negligible effects on the Ly- α transfer during the EoR. On the other hand we accurately computed the optical depth in an expanding cosmological medium without any resolution effects. We presented three validation tests for the code. The first two are classical setups: a monochromatic source in a static uniform sphere of gas and in an expanding sphere of gas. The agreement for the emerging spectrum with analytic solutions and results by other authors is good. The third test, the mean intensity map for a monochromatic source in an expanding sphere of gas at $T = 0$ K, focuses on a quantity that is more closely related to P_α . The comparison with the analytic solution provided by Loeb and Rybicki is good where the analytic solution is valid: in the diffusion regime. This set of tests strongly suggests that LICORICE is valid.

Barkana & Loeb (2005) show that several factors contribute to the fluctuations in the local Ly- α flux: the $1/r^2$ scaling of the flux and the Poisson noise and clustering in the sources distribution. They assume, however that photons redshift freely from the source until they reach the local Ly- α frequency and only then scatter off hydrogen atoms. In other words, they neglect wing scattering. We computed the P_α profile for a source with a flat continuous spectrum in a uniform expanding medium. We showed that the effect of taking the wing scatterings into account in a full radiative transfer code is to steepen the profile on small scales to a $\sim 1/r^{2.3}$ profile (with our choice of parameters). On large scales, or when wings are suppressed, we recover the $1/r^2$ profile. Thus we may expect, on small scales, more power in the 21-cm emission than predicted by Barkana & Loeb. But a still stronger effect was obtained when we introduced fluctuations in the density of the gas surrounding the source. We investigated a central clump setup and an isothermal profile. In both cases, we observed alterations in the P_α profile. In the case of an isothermal density profile, we found a $\sim 1/r^3$ profile for P_α . This also suggests stronger fluctuations than predicted by Barkana & Loeb but, once again, mainly on small scales since the σ_8 at $z = 10$ is only ~ 0.1 . Large scale structures had not grow much yet.

Finally, we tried to create a more realistic situation by placing a flat spectrum source inside a filament of overdense gas. We observed a sharp depletion of P_α inside the filament. The photons scatter out of the filament before they reach the core of the line. This fluctuation inside the filament is once again a small-scale feature, so it may be difficult to catch with LOFAR or SKA. However, the presence of the filament also produced oblate contours for P_α at larger scales (>10 comoving Mpc), in the surrounding medium. This effect may be more within reach of the resolution of these instruments.

The increased fluctuations of P_α due to radiative transfer effects and to the inhomogeneous distribution of the gas translate linearly into fluctuations of the x_α coefficient. On one hand, we expect these fluctuations to be globally significant and produce brightness temperature fluctuations only as long as $x_\alpha \sim 1$, i.e. as long as the coupling does not saturate to $T_s = T_K$. This occurs in the early phase of reionization. It is not possible to be much more specific in terms of redshift because the Ly- α pumping efficiency depends strongly on the model for the source type and formation history. On the other hand, we have shown that density fluctuations in the gas can create fluctuations of P_α of a factor greater than 10. The depleted regions will fill up only when the amount of young sources gets more than 10 times larger. Cosmological simulations suggest that this corresponds to a change in redshift between 1 and 2 around redshift 10. Consequently, we expect that the fluctuations of P_α due to inhomogeneous gas will lead to a longer survival of depleted regions where T_S remains coupled to T_{CMB} . One may argue that the strongest fluctuations of the gas density are located around the sources and are ionized very early. However, numerical simulations have shown that the ionization front is not spherical but that it is trapped in the high density regions such as filaments pointing to the source, where reionization is delayed a lot (see for example, Gnedin 2000). As a result, these filaments should be able to play their role in creating P_α fluctuations.

We have not investigated the effect on P_α of an anisotropic peculiar velocity field around the source. In principle, it would also induce non spherical contours. However, cosmological simulations in a 20 Mpc box suggest peculiar velocities on the order of 100 km s^{-1} during the EoR, when the Hubble constant is $H(z = 10) \sim 1000 \text{ km s}^{-1} \text{ Mpc}^{-1}$. Moreover, only velocity

differences will alter P_α contours, which should be smaller than 100 km s^{-1} on large scales. We estimate that the impact of the velocity field of the gas is smaller than the impact of the density fluctuations. However, LICORICE fully implements the effects of the gas peculiar velocity and it will be taken into account in the future simulations of a cosmological box.

Another process will have to be included in the future: the effect of higher Lyman series lines. Barkana & Loeb (2005) and Pritchard & Furlanetto (2006) have shown that these lines, which have horizons closer to the source than the Ly- α line, add to the power of the P_α fluctuations close to the sources. In a forthcoming paper, we will apply LICORICE to a cosmological field during the EoR, using simulation outputs from the HORIZON project², and compute the resulting 21-cm brightness temperature map. If, as we believe, we find significant modification of the predictions, we will include higher Lyman series lines.

Acknowledgements. This work was realized in the context of the SKADS and HORIZON projects.

References

- Abel, T., Norman, M. L., & Madau, P. 1999, *ApJ*, 523, 66
 Ahn, S.-H., Lee, H.-W., & Lee, H. M. 2001, *ApJ*, 554, 604
 Ahn, S.-H., Lee, H.-W., & Lee, H. M. 2002, *ApJ*, 567, 922
 Avery, L. W., & House, L. L. 1968, *ApJ*, 152, 493
 Barkana, R., & Loeb, A. 2005, *ApJ*, 626, 1
 Carilli, C. L. 2006, *NewAR*, 50, 162
 Carilli, C. L., Gnedin, N., Furlanetto, S., & Owen, F. 2004, *NewAR*, 48, 1053
 Chen, X., & Mivalda-Escudé, J. 2004, *ApJ*, 602, 1
 Chuzhoy, L., & Shapiro, P. R. 2007, *ApJ*, 655, 843
 Chuzhoy, L., & Zheng, Z. 2007 [arXiv:astro-ph/0706.0895]
 Ciardi, B., & Madau, P. 2003, *ApJ*, 596, 1
 Ciardi, B., Scannapieco, E., Stoehr, F., et al. 2006, *MNRAS*, 366, 689
 Cantalupo, S., Porciani, C., Lilly, S., & Miniati, F. 2005, *ApJ*, 628, 61
 Dijkstra, M., Haiman, Z., & Spaans, M. 2006, *ApJ*, 649, 14
 Fan, X., Carilli, C. L., & Keating, B. 2006, *ARA&A*, 44, 415
 Field, G. B. 1958, *Oric. IRE*, 46
 Furlanetto, S. R. 2006, *MNRAS*, 371, 867
 Furlanetto, S. R., & Pritchard, J. R. 2006, *MNRAS*, 372, 1093
 Furlanetto, S. R., Sokasian, A., & Hernquist, L. 2004, *MNRAS*, 347, 187
 Furlanetto, S. R., Oh, S. P., & Briggs, F. H. 2006, *PhR*, 433, 181
 Gnedin, N. Y. 2000, *ApJ*, 535, 530
 Gnedin, N. Y., & Shaver, P. A. 2004, *ApJ*, 608, 611
 Hansen, M., & Oh, P. 2006, *MNRAS*, 367, 979
 Iliev, I. T., Shapiro, P. R., & Raga, A. C. 2005, *MNRAS*, 361, 405
 Iliev, I. T., Mellema, G., Pen, U.-L., et al. 2006a, *MNRAS*, 369, 1625
 Iliev, I. T., Ciardi, B., Alvarez, M., et al. 2006b, *MNRAS*, 371, 1057
 Iliev, I. T., Mellema, G., Pen, U.-L., Bond, J. R., & Shapiro, P. R. 2007 [arXiv:astro-ph/0702099]
 Kuhlen, M., Madau, P., & Montgomery, R. 2006, *ApJ*, 637, L1
 Loeb, A., & Rybicki, G. 1999, *ApJ*, 524, 527
 Maselli, A., Ferrara, A., & Ciardi, B. 2003, *MNRAS*, 345, 379
 McQuinn, M., Lidz, A., Zahn, O., et al. 2007, *MNRAS*, 377, 1043
 Madau, P., Meiksin, A., & Rees, M. J. 1997, *ApJ*, 475, 429
 Mellema, G., Iliev, I. T., Pen, U.-L., & Shapiro, P. R. 2006, *MNRAS*, 372, 679
 Neufeld, D. A. 1990, *ApJ*, 350, 216
 Nusser, A. 2005, *MNRAS*, 359, 183
 Peebles, P. J. E. 1993, *Principles of Physical Cosmology* (Princeton Univ. Press), 573
 Pritchard, J. R., & Furlanetto, S. R. 2006, *MNRAS*, 367, 1057
 Semelin, B., & Combes, F. 2002, *A&A*, 388, 826
 Shapiro, P. R., Ahn, K., Alvarez, M. A., et al. 2006, *ApJ*, 646, 681
 Spergel, D. N., Bean, R., Dore, O., et al. 2007, *ApJS*, 170, 377
 Tasitsiomi, A. 2006, *ApJ*, 645, 792
 Tozzi, P., Madau, P., Meiksin, A., & Rees, M. 2000, *ApJ*, 528, 597
 Verhamme, A., Schaerer, D., & Maselli, A. 2006, *A&A*, 460, 397
 Valdés, M., Ciardi, B., Ferrara, A., Johnston-Hollitt, M., & Röttgering, H. 2006, *MNRAS*, 369, L66
 Wouthuysen, S. A. 1952, *AJ*, 57, 31
 Zheng, Z., & Mivalda-Escudé, J. 2002, *ApJ*, 578, 33

² <http://www.projet-horizon.fr>

3.3 The simulated 21 cm signal during the EoR

Summary

We present the simulated 21 cm signal during the Epoch of reionization including the contribution of Ly- α fluctuations. We post-processed N-body and SPH hydrodynamic cosmological simulations with radiative transfer, and the results are further post-processed with Ly- α radiative transfer. Two simulations, each with 16.7 million dark matter and the same number of baryons particles in a volume of $(20\text{Mpc}/h)^3$ and $(100\text{Mpc}/h)^3$ have been performed. We extracted 130 snapshots from the dynamic simulation done with the GADGET2 code, from the redshift $z \sim 40$ to $z \sim 5.5$. Sources are self-consistently formed among the baryon particles in the SPH hydrodynamic simulation. We considered only stellar sources with a Salpeter IMF (mass range $1-100M_{\odot}$), roughly intermediate between PopII and PopIII stars. The first source appears at redshift $z \sim 12$ and the IGM is almost reionized at redshift around $z \sim 6$, which is consistent with SDSS quasar absorption spectra (Fan et al., 2006). The integrated Thomson optical depths for the two simulations are also within $1-\sigma$ of the WMAP3 value. We computed the differential brightness temperature of the 21 cm signal using several assumptions, *i*) the spin temperature is much higher than the CMB temperature, *ii*) the spin temperature is strongly coupled to kinetic temperature of the gas, *iii*) the spin temperature is computed with an homogeneous Ly- α flux, and *iv*) the spin temperature is computed with the local Ly- α flux. We found that the brightness temperature shows up to 50% difference even between the assumption *iii*) and *iv*), and the Ly- α flux is not always strong enough to couple the spin temperature and kinetic temperature. In addition, we can observe the signal in absorption with high intensity during the early reionization while assumption *i*) always predicts the signal in emission. The inhomogeneous Ly- α fluctuation changes the overall amplitude of the 21-cm signal, and adds its own fluctuations to the power spectrum.

A&A 495, 389–405 (2009)
 DOI: 10.1051/0004-6361:200810757
 © ESO 2009

**Astronomy
&
Astrophysics**

The simulated 21 cm signal during the epoch of reionization: full modeling of the Ly- α pumping

S. Baek¹, P. Di Matteo^{1,2}, B. Semelin¹, F. Combes¹, and Y. Revaz^{1,3}

¹ LERMA, Observatoire de Paris, UPMC, CNRS, 61 Av. de l'Observatoire, 75014 Paris, France
 e-mail: sunghye.baek@obspm.fr

² GEPI, Observatoire de Paris, section de Meudon, CNRS, Place Jules Janssen, 92190 Meudon, France

³ Laboratoire d'Astrophysique, École Polytechnique Fédérale de Lausanne (EPFL), Switzerland

Received 6 August 2008 / Accepted 3 November 2008

ABSTRACT

The 21 cm emission of neutral hydrogen is the most promising probe of the epoch of reionization (EoR). In the next few years, the SKA pathfinders will provide statistical measurements of this signal, such as its power spectrum. Within one decade, SKA should produce a full tomography of the signal. Numerical simulations predicting these observations are necessary to optimize the design of the instruments and help in the interpretation of the data. Simulations are reaching a reasonable level in terms of scale range, but still often rely on simplifications to compute the strength of the signal. The main difficulty is the computation of the spin temperature of neutral hydrogen which depends on the gas kinetic temperature and on the level of the local Lyman- α flux (The Wouthuysen-Field effect). A $T_S \gg T_{\text{CMB}}$ assumption is usual. However, this assumption does not apply early in the reionization history, or even later in the history as long as the sources of X-rays are too weak to heat the intergalactic medium significantly. This work presents the first EoR numerical simulations including, beside dynamics and ionizing continuum radiative transfer, a self-consistent treatment of the Ly- α radiative transfer. This allows us to compute the spin temperature more accurately. We use two different box sizes, $20h^{-1}$ Mpc and $100h^{-1}$ Mpc, and a star source model. Using the redshift dependence of average quantities, maps, and power spectra, we quantify the effect of using different assumptions to compute the spin temperature and the influence of the box size. The first effect comes from allowing for a signal in absorption (i.e. not making the $T_S \gg T_{\text{CMB}}$ approximation). The magnitude of this effect depends on the amount of heating by hydrodynamic shocks and X-rays in the intergalactic medium (IGM). With our source model we have little heating so regions seen in absorption survive almost until the end of reionization. The second effects comes from using the real, local, Lyman- α flux. This effect is important for an average ionization fraction of less than $\sim 10\%$: it changes the overall amplitude of the 21 cm signal, and adds its own fluctuations to the power spectrum.

Key words. radiative transfer – methods: numerical – ISM: HII regions – ISM: bubbles – cosmology: early Universe

1. Introduction

The Epoch of Reionization (EoR) begins with the formation of the first sources of light resulting from the non-linear growth of primordial density fluctuations. When this event occurs, which could be anytime between $z \sim 30$ and $z \sim 15$, the intergalactic medium (IGM) is mostly cold, neutral and optically thick at many wavelengths. Our main probe of baryonic matter during this era is the 21 cm emission of neutral hydrogen, to which the IGM is optically thin (Madau et al. 1997). To observe a 21 cm signal in emission or absorption against the cosmic microwave background (CMB), however, we need either a sufficient local flux of Ly- α photons (Wouthuysen-Field effect, Wouthuysen 1952; Field 1958) or a high enough baryon density (collisions), either of which will decouple the hydrogen spin temperature from the CMB temperature. The first condition requires a sufficient number of sources and the second a sufficient growth of the density fluctuations. During the EoR, the Wouthuysen-Field effect is prevalent as it becomes efficient everywhere with time. Where the 21 cm signal turns on, its intensity is determined, in addition to the spin temperature, by the neutral hydrogen density field which is the combination of the baryon density field and the complex distribution of growing ionized regions. This means that observing the 21 cm signal will teach us a lot about the reionization history. Presently, what is known about this history defines two constraints. The first is the value of τ , the optical

depth of the Thomson scattering of CMB photons by free electrons, which is proportional to the column density of ionized hydrogen from us to the CMB. This value is 0.09 ± 0.03 for *WMAP3* cosmology (Spergel et al. 2007) and 0.087 ± 0.017 in *WMAP5* cosmology (Komatsu et al. 2008). In the over-simplified model of instantaneous reionization, this gives a reionization redshift of $z \sim 11$. In realistic models, τ provides a constraint on a redshift integral of the mean ionization fraction. The second constraint on reionization arises from the spectra of high- z quasars. The Gunn-Peterson trough appears as a sharp feature in the quasar spectra when the neutral fraction in the IGM surrounding the quasar rises above 1%. From observations this happens at z greater than ~ 6 (Fan et al. 2006). The reduced error bar on the value of τ in the *WMAP5* results, together with the quasar constraint, strongly favor an extended reionization history.

Much information is coded in the 21 cm emission. First, the nature of the sources (Pop II, Pop III stars or X-ray sources: QSO, SNe or X-ray binaries) and their formation history determine the evolution of the sky-averaged signal with redshift. It may also be possible to pinpoint specific events in the reionization history like an average ionization fraction of 0.5 using the redshift dependence of the power spectrum (Mellema et al. 2006b; Lidz et al. 2007b). This type of information will be available in the next few years from pathfinders like LOFAR or MWA. Within one decade, the Square Kilometer Array (SKA) will deliver a tomography (maps at many different redshifts) of

the signal at 1 comoving Mpc resolution. If the different physics can be separated in the signal (Barkana & Loeb 2005a; McQuinn et al. 2006), we will be able to extract information about the growth rate of large scale structures directly. If not, it is possible to use them as independent source planes for gravitational lensing by lower z clusters and still deduce information on the structure growth rate (Metcalf & White 2007).

Numerical simulations of the 21 cm signal are useful to explore the different possible source models and derive constraints for the design of the future instruments in terms of frequency range, bandwidth, angular resolution and sensitivity. Comparison with observations will then enable us to discriminate between source models and formation histories. Predicting the 21 cm signal requires the knowledge of three local quantities: the baryonic density field, the ionization fraction of hydrogen and the Ly- α flux (to compute the spin temperature). Moreover, high resolution is critical to obtain realistic, non-spherical ionized regions arising from the high photon consumption in dense small scale structures, and large simulation boxes ($>100 h^{-1}$ Mpc) are necessary to correctly sample the large-scale clustering in the source distribution and the abundance of rare sources (Barkana & Loeb 2004; Iliev et al. 2006). With the development of 3D radiative transfer codes (Gnedin & Ostriker 1997; Gnedin & Abel 2001; Nakamoto et al. 2001; Maselli et al. 2003; Razoumov & Cardall 2005; Mellema et al. 2006a; Rijkhorst et al. 2006; Susa 2006; Whalen & Norman 2006; Trac & Cen 2007; Pawlik & Schaye 2008; Altay et al. 2008) and increases in computational power, it has become possible in the last few years to predict the 21 cm signal. But some compromises still have been necessary. The most common approximation is to assume $T_S \gg T_{\text{CMB}}$, where T_S is the hydrogen spin temperature and T_{CMB} is the CMB temperature. In this regime the 21 cm brightness temperature is independent of the spin temperature: no information about the gas temperature and local Ly- α flux is needed. Obviously, this approximation fails if either the coupling of T_S to T_K , the gas kinetic temperature, by Ly- α is weak (early and/or far from the sources), then $T_S \sim T_{\text{CMB}}$, or if the gas is not significantly heated in the voids by X-rays. In other words, this approximation removes any possible absorption regime. However, the signal seen in absorption has the potential to be stronger than in emission (Furlanetto et al. 2006). Kuhlen et al. (2006), Shapiro et al. (2006), Gnedin & Shaver (2004) and Santos et al. (2007) have probed the absorption regime in numerical simulations. In Kuhlen et al. and Shapiro et al., this is done taking only the role of collisions into account in determining the 21 cm signal, i.e. ignoring the role of Ly- α pumping or prior to the existence of any Ly- α source. Gnedin et al., in turn, add the effect of a Ly- α flux in their analysis, but still use a drastic simplification: a homogeneous Ly- α flux changing with redshift. Considering a simple r^{-2} profile around the sources to compute the Ly- α flux fluctuations, Barkana & Loeb (2005b) have shown that clustering and Poisson noise in the source distribution modify the 21 cm power spectrum. Furthermore, several recent works (Semelin et al. 2007; Chuzhoy & Zheng 2007; Naoz & Barkana 2008) have shown that 3D radiative transfer effects modify the expected r^{-2} dependence of the flux in a homogeneous medium, and even more so in an inhomogeneous density field. The present work includes a full modeling of the Ly- α radiative transfer and examines how the resulting 21 cm signal compares to the one using a homogeneous Ly- α flux.

Often working with the $T_S \gg T_{\text{CMB}}$ approximation, the early simulations used box sizes equal to or smaller than $20 h^{-1}$ Mpc (Ciardi & Madau 2003; Gnedin & Shaver 2004;

Furlanetto et al. 2004; Salvaterra et al. 2005; Valdés et al. 2006). Recent works put the effort on simulating larger boxes, usually $\sim 100 h^{-1}$ Mpc, while trying to preserve a good enough resolution (Mellema et al. 2006b; Zahn et al. 2007; Lidz et al. 2007a; McQuinn et al. 2007; Lidz et al. 2007b; Iliev et al. 2008). For the same resolution, radiative transfer simulations are usually more demanding than dark matter dynamical simulations. Consequently, a common strategy is to run very high resolution DM simulations, derive the baryonic density field with a constant bias, and compute a clumping factor within each larger scale radiative transfer cell. This is a method to include the effect of minihalos (Ciardi et al. 2006) as subgrid physics. In this method, the least robust assumption is the use of a constant baryonic to DM density ratio: while correct on a large scale, it fails on the scale of clusters where hydrodynamics and heating/cooling processes play an important role. In this work, we rely on self-consistent hydrodynamic simulations and do not use a clumping factor.

Section 2 presents the radiative transfer code used, Sect. 3 describes the simulation runs, which are analyzed in Sect. 4. Section 5 summarizes the main results.

2. The radiative transfer code: LICORICE

The LICORICE code integrates three main parts, a TreeSPH dynamical part which is not used for this work (see Sect. 3.1), and two radiative transfer parts for the ionizing continuum and the Lyman- α line. All three parts are parallelized using OpenMP.

2.1. Ionizing continuum radiative transfer

We use a 3D Monte Carlo ray-tracing scheme. The radiation field is discretized into photon packets which are propagated individually on an adaptive grid and interact with matter. The numerical methods implemented in LICORICE are similar to those presented by Maselli et al. (2003) for the code CRASH. There are, however, a number of differences which are described in the following subsections.

The version of LICORICE used in this work does not include H₂ formation, He ionization nor diffuse radiation from recombination.

2.1.1. Adaptive grid

LICORICE uses an adaptive grid based on an oct-tree. There is a difference between the usual oct-tree and our adaptive grid. The oct-tree keeps splitting a mother cell into 8 children cells if it contains more than 1 particle. However, the grid for RT stops splitting a mother cell if it contains less than a tunable parameter, N_{max} particles. Therefore, the RT cells can contain from 0 to N_{max} particles while the cells in the oct-tree contain either 0 or 1 particle.

For equivalent spatial resolution, such an adaptive grid requires lower memory and CPU-time than other grid-based RT codes. In this paper, we adopted $N_{\text{max}} = 30$ for the continuum ionization part, which makes the minimum RT cell size of $1 h^{-1}$ kpc at the end of the S20 simulation ($z = 5.6$) and $200 h^{-1}$ kpc for the S100 simulation ($z = 6.6$).

2.1.2. SPH-particle density and grid-cell density

We compute the gas density at each particle's position using the SPH smoothing kernel (Monaghan 1992). We use on average

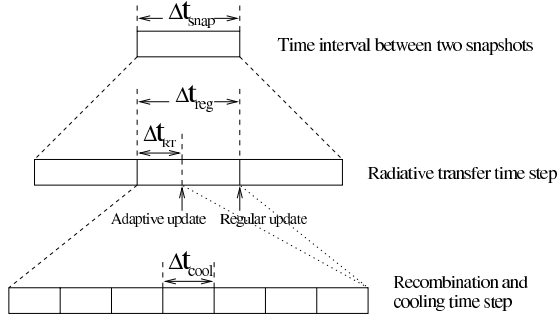


Fig. 1. Schematic representation of the different time steps used in LICORICE.

50 neighbor particles, N_{neighbor} , to compute the SPH smoothing kernel. We call it *particle density* and consider that the particle density is close to the physical density of the fluid (Hernquist & Katz 1989). We define another density: the average density of an RT cell that can contain several particles. We call it *RT cell density* and use it to estimate the optical depth of each RT cell. When a photon packet travels through an RT cell with optical depth $\Delta\tau$, the absorption probability is given by $P(\Delta\tau) = 1 - e^{-\Delta\tau}$. For each RT cell crossed, we deposit a fraction of its initial photon content $\propto P(\Delta\tau)$. Then, we distribute the absorbed photons and energy to each particle in the RT cell proportionally to its HI mass. We do not take into account any form of sub-cell density fluctuations. Indeed, particles in one RT cell have similar particle density because we limited the maximum number of particles in one RT cell at $N_{\text{max}} = 30$ which is smaller than N_{neighbor} , the number of neighbor particles of the SPH smoothing kernel. Choosing a smaller N_{max} requires using more photons, more memory and updating cells more frequently. Updating cells can be especially costly around the sources where cells receive many photons. We use the particle density to update physical quantities such as the ionization fraction and temperature. Therefore, we compute the photo-ionization rate and temperature individually for each particle even if they are in the same RT cell. Recombination and collisional ionization are also computed individually for each particle.

This scheme is especially relevant if the density field is not static i.e. an RT cell does not always contain the same set of particles.

2.1.3. Adaptive time integration

The integration time step for updating the photoionization and photoheating rates, Δt_{RT} , is adaptive. We use a typical Δt_{RT} much smaller than the time interval Δt_{snap} between two snapshots of the dynamical simulation. Furthermore, recombination, collisional ionization and cooling are treated with an integration time step Δt_{cool} which is much smaller than Δt_{RT} . The photoionization and photoheating rates are kept constant over all the Δt_{cool} in one Δt_{RT} . The relation between the different time steps is summarized in Fig. 1.

The ionizing continuum radiative transfer is the repetition of two steps. The emission and propagation of N_{ph} photon packets during the time interval Δt_{reg} (for continuum transfer an infinite velocity of light is assumed) and the update of physical quantities.

- i) Step 1: all the sources emit a number N_{ph} of photon packets along directions chosen at random. A photon packet leaves a

fraction of its content of photon number and energy in each RT cell it passes through. Each RT cell records the number of absorbed photons and energy during the emission of the N_{ph} photon packets

- ii) Step 2: then, the ionization state and the temperature are updated with the integration time step Δt_{reg} for all particles in all RT cells. This update is applied even to the RT cells that absorbed no photon during Δt_{reg} . This is necessary in order to consider the effect of collisional ionization, recombination and adiabatic expansion of the gas (which is interpolated between snapshots). In view of the 21 cm emission, the change of temperature due to the adiabatic expansion of the Universe is especially important in diffuse regions, independently of the photo-heating rate.

However, this regular update is not appropriate where the flux of photons is too high (around sources for example). In this case, the number of absorbed photons can exceed the total number of atoms available for ionization in the RT cell, or, in other words, the fixed update time step Δt_{reg} is much larger than the characteristic time scale of photo-ionization. So, whenever the number of absorbed photons accumulated in a cell reaches a pre-set limit, for example 30% of the total number of neutral atoms in the cell, we update the physical quantities of the cell with the appropriate integration time step $\Delta t_{\text{RT}} (< \Delta t_{\text{reg}})$.

When N_{ph} photon packets have been emitted, the integration time is synchronized as described in step 2, using Δt_{reg} for the particles which were not updated since last synchronization and with the time elapsed since the last update for the others. The relative values of the different time steps are specified in Sect. 3.2.1.

2.2. Ly- α line radiative transfer

Computing Ly- α transfer is necessary to evaluate accurately the Wouthuysen-Field effect (see Sect. 3.4) in the determination of the 21 cm brightness temperature.

The part of LICORICE which deals with the Ly- α line radiative transfer shares some features with its ionizing continuum counterpart: mainly the Monte Carlo approach and the adaptive grid. For the Ly- α transfer, $N_{\text{max}} = 12$ is used. This is a smaller value than for the ionizing continuum because Ly- α photons have no feedback on the gas: RT cells do not need to be updated at all. There is no direct CPU cost connected to using a smaller N_{max} .

The methods for resonant line scattering were presented in Semelin et al. (2007). The implementation is similar to those of other existing codes (Zheng & Miralda-Escudé 2002; Cantalupo et al. 2005; Dijkstra et al. 2006; Verhamme et al. 2006; Tasitsiomi 2006). Necessary improvements have been implemented in our code for the simulations presented in this paper. Let us describe them briefly.

2.2.1. Taking the full effect of expansion into account

Cosmological expansion is usually introduced in Ly- α transfer codes by including a Doppler shift associated with the Hubble flow velocities and by using a constant value for the expansion factor throughout the photon flight. This works well for simulation boxes of moderate size (a few 10 comoving Mpc). However, during reionization, a photon emitted just below Ly- β will travel several hundreds of comoving Mpc before it redshifts to Ly- α . Moreover, box sizes larger than 100 comoving Mpc are necessary to avoid underestimating the fluctuation power spectrum of the 21 cm line emission. Consequently we took the necessary

steps to include the full effect of cosmological expansion in our Ly- α simulations:

- we use the comoving frequency. The usual approach is to use the frequency in the reference frame of the center of the simulation box and convert back and forth to the frequency in the gas local rest frame by a Doppler shift including peculiar and Hubble flow velocities. Instead we use the frequency in the local comoving frame as the reference frequency and include only peculiar velocities in Doppler shifts. If a photon enters a cell with local comoving frequency ν_{in} at time t_{in} and exits the cell (or undergoes scattering) at time t_{out} , its outgoing local comoving frequency ν_{out} is simply given by the general formula:

$$\nu_{\text{out}} = \frac{a(t_{\text{in}})}{a(t_{\text{out}})} \nu_{\text{in}}, \quad (1)$$

where $a(t)$ is the expansion factor of the universe. As explained in Semelin et al. (2007), this avoids second order errors in $\frac{\delta a}{a}$ where δa is the variation of the expansion factor during the flight of the photon through the *whole* simulation box. However, between the incoming and outgoing comoving frequency in a cell, we do make a linear interpolation to compute the comoving frequency along the photon path. This is necessary to use Eq. (13) in Semelin et al. (2007) which allows a correct computation of the optical depth even when the photon redshifts all the way through the Ly- α line within the current cell. The point is that in the current version, errors do not add up from cell to cell;

- the second benefit of using this formulation is that we track the variation of the expansion factor $a(t)$ during the flight of the photon, and we can use the correct value at any given time to compute such quantities as the gas physical (non-comoving) density. This avoids first order errors in $\frac{\delta a}{a}$ when computing the optical depth for example.

In this framework, we naturally account for retarded time. The drawback is that we have to propagate over several box sizes (using periodic boundary conditions) some photons that were emitted more than 10 snapshots earlier. This is necessary for the reasons mentioned above but also because the source population changes drastically over such a time-scale.

2.2.2. Specific acceleration scheme

A photon which redshifts through the Ly- α line in a hydrogen medium at the universe average density at $z \sim 10$ faces an optical depth of $\tau \sim 10^6$ (Gunn & Peterson 1965; Loeb & Rybicki 1999). To compute 10^6 scatterings for the $\sim 10^9$ photons used in the simulations is impossible. An acceleration scheme has to be devised. The usual method is the core-skipping scheme (Avery & House 1968; Ahn et al. 2002). A photon entering the core of the line is systematically shifted out when it next scatters off a thermal atom. This scheme reduces the number of scatterings and CPU cost by several orders of magnitude while preserving the shape of the emerging spectrum. However, in this work, we do not need to compute the emerging spectrum. All we need is to know where the scatterings occur. Consequently we can use an even more drastic acceleration scheme. Although the few scatterings that occur in the blue wing of the line are important to determine in which location the photon enters the core of the line (Semelin et al. 2007), their contribution to the total number of scatterings is negligible. Consequently, the following method is used: we propagate the photon and compute scatterings until the local comoving frequency is shifted within 10 thermal

linewidths of the line center, in the blue wing, at a location \mathbf{x}_0 . Then we consider that the $\sim 10^6$ scatterings that this photon is bound to undergo all occur at \mathbf{x}_0 . At 10 thermal linewidths off the center, the mean free path of the photons is less than 1 kpc and much shorter than 1 pc in the core of the line. We can neglect the spatial diffusion while the photon remains within the 10 linewidth frequency range. As for the scatterings which occur outside the 10 linewidth range, there are just a few hundred of them and we can neglect their contribution to the total number of scatterings (but not their importance in determining where the core scatterings will occur).

One factor remains to be specified: exactly how this $\sim 10^6$ scattering number depends on the local state of the IGM. Looking at the optical depth computed for a redshifting photon, three variable quantities can influence the number of scatterings: the local neutral gas density, the local kinetic temperature of the gas and the current value of the Hubble constant. Escaping the line is achieved by a combination of frequency shifts from two sources: scattering off thermal atoms which produce a random walk in frequency, and the systematic shift to lower frequency between two scatterings due to cosmological expansion. How these two effects combine is not clear at first sight: although cosmological shifts are systematically redward, they are much smaller than the random thermal shifts when the photon is still near the core of the line. We ran a series of simulations without any acceleration scheme at different values of the local parameters, for a single source in a homogeneous medium, and we computed the average number of scatterings per photon. It turns out that changing the temperature in a reasonable range (1 K to 1000 K) has no influence on the average number of scatterings (variation less than that the statistical error for 1000 photons). The approach of Loeb & Rybicki (1999), developed in a 0 K medium, remains valid in the cosmological context. This means, as was checked numerically, that the average number of scatterings changes as $1/H(z)$. The number of scatterings per photon is obviously proportional to the overdensity of neutral hydrogen, however, in computing the 21 cm emission, we are interested in P_α , the average number of scatterings per atom per second. In P_α , the contribution of the overdensity cancels out. Consequently the following calibrated formula for N_{scat} , the number of scatterings for each photon, was used:

$$N_{\text{scat}} = 8 \times 10^5 \frac{H(z=10)}{H(z)}, \quad (2)$$

where $H(z)$ is the Hubble constant at redshift z . Many non-linear density structures at subgrid levels produce deviations from the above formula (Chuzhoy & Shapiro 2006).

3. Description of the simulations

3.1. Dynamics

The dynamical simulations have been run using a modified version of the parallel TreeSPH code Gadget2 (Springel 2005) which explicitly conserves both energy and entropy.

3.1.1. Initial conditions

The initial conditions are the reference conditions of the Horizon Project¹. They have been computed using the public version Graphic-2 code (Bertschinger 2001). The cosmological parameters are those of the concordance Λ CDM flat universe based on

¹ <http://www.projet-horizon.fr/>

Table 1. Mass and spatial resolution for the two simulations S20 and S100.

Simulations	L [h^{-1} Mpc]	m_{DM} [$h^{-1} M_{\odot}$]	m_{gas} [$h^{-1} M_{\odot}$]	ϵ [h^{-1} kpc]
S20	20	2.6×10^7	5.5×10^6	2
S100	100	3.2×10^9	6.9×10^8	10

WMAP3 data alone (Spergel et al. 2007): $\Omega_{\text{m}} = 0.24$, $\Omega_{\Lambda} = 0.76$, $\Omega_{\text{b}} = 0.042$, with a normalization of the density fluctuation power spectrum given by $\sigma_8 = 0.76$. The corresponding Hubble constant at the present epoch is $H_0 = 100 h \text{ km s}^{-1} \text{ Mpc}^{-1}$, with $h = 0.73$. The initial redshifts ($z = 42.7$ for the S20 and $z = 29.9$ for the S100 simulation) were chosen using the default prescription from Gadget-2. It relies on the Zel'dovich approximation to predict the growth of the smallest resolved structures until they enter the non-linear regime. Then the simulations start. Crocce et al. (2006) show that this approach leaves some spurious transients compared to the more accurate second-order Lagrangian perturbation theory. The corrections are of the order of a few percent on such quantities as the density power spectrum of the dark matter halo mass function. We believe that, in EoR simulations, other uncertainties connected to the source modeling outweigh this issue.

Using these cosmological parameters, we have run two simulations (S20 and S100) covering different comoving volumes, respectively $20^3 h^{-3} \text{ Mpc}^3$ and $100^3 h^{-3} \text{ Mpc}^3$. In both simulations, the number of particles is set to 2×256^3 ($\sim 33 \times 10^6$ particles), where half corresponds to gas particles and half to dark matter particles. The mass resolutions of dark matter and gas/stars particles, as well as the softening parameter, are given in Table 1. For comparison with other work, the minimum mass of resolved halos is $\sim 5 \times 10^{10} M_{\odot}$ for the S100 and $\sim 4 \times 10^8 M_{\odot}$ for the S20 simulations. However, let us emphasize that we do not need to identify halos with a halo finder code; sources are formed self-consistently in the dynamical code (see Sect. 3.1.2).

3.1.2. Gas physics

Additional gas physics has been added to the public version of Gadget-2. The cooling and heating of the gas are computed following the recipe proposed by Katz et al. (1996) where the gas is assumed to be optically thin and in ionization equilibrium with the UV background (the latter corresponds to updated values of the quasar radiation spectrum computed by Haardt & Madau 1996). In addition to the heating and cooling rates given by Katz et al. (1996), we also have taken into account the inverse Compton cooling using the formula in Theuns et al. (1998). These considerations apply to the dynamical simulation only, not to the radiative transfer simulations. Non equilibrium ionization and heating-cooling processes are recomputed independently in the radiative transfer simulations (see Sect. 2.1).

Star formation is taken into account by transforming gas particles into star particles. We have used the classical recipe that mimics a Schmidt law:

$$\frac{d\rho_{\star}}{dt} = \frac{\rho_{\text{g}}}{t_{\star}}, \quad (3)$$

where t_{\star} is defined by:

$$t_{\star} = t_{0\star} \left(\frac{\rho}{\rho_{\text{th}}} \right)^{-1/2}. \quad (4)$$

Following Springel & Hernquist (2003), we have set $t_{0\star} = 2.1$ Gyr for the S20 simulation and a physical density threshold of $\rho_{\text{th}} = 5.7 \times 10^{-25} h^2 \text{ g cm}^{-3}$. Moreover, it is required that the local gas overdensity exceeds 200 in order to form stars.

Supernova feedback is taken into account by simply injecting in the surrounding gas particles an amount of 10^{48} erg per unit solar mass formed. To avoid instantaneous dissipation by radiative cooling (Katz et al. 1996), 80% is ejected in kinetic form, and the rest is ejected in thermal form.

3.1.3. Calibration of the star formation history

To compare the 21 cm signals between the two simulations we need very similar star formation histories. However, the star formation rate non linearly depends on the numerical resolution, especially at high redshift (Springel & Hernquist 2003; Rasera & Teyssier 2006). To avoid an extremely CPU time consuming fine tuning of $t_{0\star}$ in the S100 simulation, we forced the star formation rate to follow the one obtained in S20. This was performed by adapting at each time step the parameter $t_{0\star}$, while relaxing the constraint on the minimum density needed to form stars.

3.1.4. Output frequency

Radiative transfer simulations are run as a post-treatment of the dynamical simulations, interpolating between the recorded snapshots. To obtain a reliable interpolation, 125 snapshots were recorded from $z = 41.66$ to $z = 5.92$. Conforming to the Horizon Project chosen rule, the interval between two snapshots is given in terms of the scale factor a by:

$$\Delta a = \frac{1}{2^{10}}. \quad (5)$$

3.2. Reionization

3.2.1. Initial conditions

The kinetic temperature of the gas is computed in the dynamical simulations assuming equilibrium for the ionization state with a uniform UV background. However, it is recomputed in the radiative transfer simulations using the photo heating and cooling rate for a non equilibrium ionization state. The radiative transfer for the S20 (resp. S100) simulation starts with the same initial temperature as the dynamical simulations, 34.7 K (resp. 17.3 K) computed with RECFAST (Seager et al. 1999). Using a uniform temperature is an approximation: from the epoch of decoupling ($z \sim 150$), different regions evolve adiabatically with different contraction/expansion factors due to the growth of density fluctuations. Moreover, the decoupling from the CMB is actually neither instantaneous nor homogeneous. Including these temperature fluctuations is not a simple task. We can estimate the rms amplitude of the fluctuations to be smaller than 10%. We chose to ignore them.

The initial ionization fraction of gas is set equal to zero. We used the recombination rate given by Spitzer (1978) and the collisional ionization in Cen (1992).

Our requirement for choosing the value of the reionization time step Δt_{reg} is that the relative variation of the gas temperature anywhere in the simulation box is less than 20%. This ensures that the recombination rate does not change too fast within Δt_{reg} . To meet this condition we used $\Delta t_{\text{reg}} = 1/40 \Delta t_{\text{snap}}$ (resp. $1/10 \Delta t_{\text{snap}}$) for S20 (resp. S100) and $\Delta t_{\text{cool}} = 1/100 \Delta t_{\text{reg}}$

(both for S20 and S100). Note that the S20 run required a smaller time step since it has a higher resolution.

3.2.2. Post-treatment of the dynamical simulations: the issue of gas heating

We use the snapshots of the dynamical runs as inputs for the radiative transfer simulation. Consequently, there is no feedback on the dynamics from the radiative heating of the gas. This has two opposite effects. First it slows down to some extent the propagation of the ionization fronts since the high gas pressure inside the Strömgen sphere is not effective. Second the source formation is not quenched by radiative feedback: stronger sources speed up the ionization front propagation. The net result of these two effects is unclear. In view of other important uncertainties, like the source modeling, the feedback of radiative transfer on the dynamics is neglected.

The second consequence of running the radiative transfer simulation in post-treatment of the dynamical simulation is that dynamical effects on the temperature of the gas due to shock heating are not included in the radiative transfer simulation.

Shock heating is a sensitive issue since it directly affects the 21 cm signal, possibly transforming absorption into emission by raising the gas temperature above the CMB temperature. For example, mini-halos with masses between 10^4 to $10^8 M_\odot$ form very early during the EoR and are dense and warm enough from shock heating during virialization to emit 21 cm radiation. Iliev et al. (2002) and Shapiro et al. (2006) show that the emission of mini-halos can dominate the 21 cm signal prior to the onset of Ly- α coupling. Furlanetto & Oh (2006), however, find that the contribution of diffuse regions dominates later on. The simulations presented here only marginally resolve the most massive of these mini-halos in the best case (S20 simulation), and we chose not to try to include them as subgrid physics. But we should keep in mind that shock heating both below and above our scale resolution may affect the 21 cm signal, as long as it occurs in neutral regions (mini-halos, filaments).

The adiabatic cooling of the gas by dynamical expansion in low density regions is also an important factor responsible for the possible strong absorption features in the 21 cm maps: we can take it into account easily during the post treatment. We use the fact that, below $T = 10^4$ K (always true in neutral, 21 cm emitting regions), the cooling rate of the primordial gas is negligible, and shock heating is limited in the low density diffuse regions of the IGM. Consequently, we approximate the thermal evolution of the gas in the dynamical simulation as adiabatic. We compute the variation of internal energy of a particle due to expansion or contraction between two consecutive snapshots from the variation of the density:

$$\Delta u = u_2 - u_1 = u_1 \left(\left(\frac{\rho_2}{\rho_1} \right)^{\gamma-1} - 1 \right), \quad (6)$$

where u is the internal energy and ρ is the gas density.

However, if the variation in density between two snapshots is large, applying it all at once results in numerical instabilities. This happens when particles pass through or collapse into a halo. To avoid this, the density is interpolated gradually between two snapshots.

The other cooling and heating processes are then included self-consistently in the radiative transfer simulation. We use the cooling-heating rates in Cen (1992), and a minimum gas temperature of 1 K.

Table 2. The total ionizing luminosity of a star particle and escape fraction of simulations.

Simulations	L_{tot} [erg/s]	f_{esc}
S20	4.60×10^{43}	0.08
S100	5.75×10^{45}	0.05

3.2.3. Source modeling

In this work we consider only stellar sources and do not study the influence of X-ray sources. The decline of the quasar luminosity function at redshift $z > 3$ suggests that stars were the dominant source of ionizing photons during the EoR (Shapiro & Giroux 1987; or Faucher-Giguère et al. 2008, for recent observational evidence). However, even in small quantities, X-ray sources have the potential to affect the 21 cm signal by heating the IGM. Indeed X-ray photons can have a mean free path of several 100 Mpc through neutral hydrogen during the EoR: they propagate through the ionization front out to the neutral regions. Using a homogeneous model Glover & Brand (2003) find that a modest number of X-ray sources can raise the temperature of the IGM by several tens of K. Moreover, Pritchard & Furlanetto (2007) show that the heating by X-rays is actually not homogenous: it produces fluctuations in the gas temperature which leave their own imprint on the 21 cm power spectrum. In this work, however, we want to focus on the specific influence of Ly- α pumping, X-ray sources will be included in a future work.

All baryon particles have the same mass: $7.6 \times 10^6 M_\odot$ (resp. $9.5 \times 10^8 M_\odot$) for the S20 (resp. S100) simulation. Accordingly, one star particle corresponds in fact to a star cluster or a dwarf galaxy so an IMF has to be assumed. We choose a Salpeter IMF, with masses in the range $1 M_\odot$ – $100 M_\odot$. Then we compute the total luminosity and spectral energy distribution (SED) for one star particle by integrating over the IMF. We use the table in Aller (1982) to obtain the radius and effective temperature of stars as a function of mass. The total ionizing luminosity (Table 2) of a star particle yields one or two photons per hydrogen atom at $z = 6.5$ (Fig. 2). The resulting SED is plotted in Fig. 3. It can be seen that it differs very little from a blackbody spectrum with 5×10^4 K effective temperature. Therefore our source model is roughly intermediate between PopII and PopIII stars.

3.2.4. Calibrating the global ionization history

Before making a global calibration using the escape fraction, we need to consider the effect of the time evolution of the stellar population within one source particle. Massive stars contribute the most to the ionizing luminosity of the source, but live for a shorter time. We use a simple model: when a new source particle is created, we assign it a random lifetime between 5 Myr and 20 Myr as a source of ionizing photons. The randomization is useful because we obtain new sources only with each new dynamical snapshot; a fixed lifetime for all sources and a discretely evolving number of sources with each new snapshot would produce distinct steps in the average ionizing flux. Globally, the average lifetime of the source is degenerate with the escape fraction as far as ionization history calibration is concerned, however, it allows us to account for the signature of local starbursts (in time and space) followed by quiescence. We plot the effect of considering a finite lifetime for the ionizing source on the star fraction history in Fig. 2. It can be seen that the young, ionizing star fraction fluctuates more strongly at high redshifts than

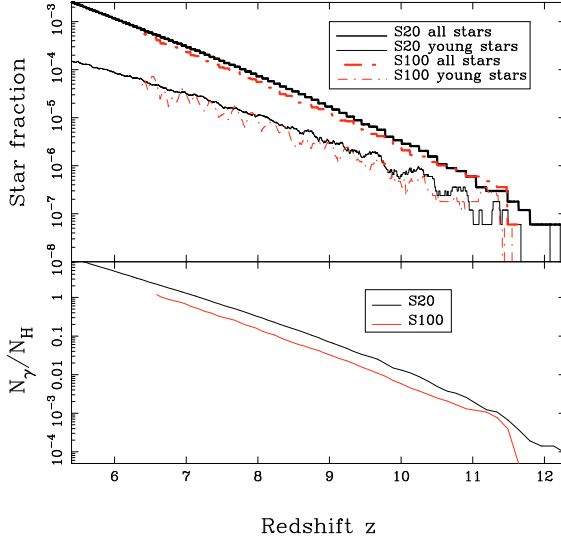


Fig. 2. *Top panel:* evolution of the fraction of baryonic mass locked into stars. Stars are considered young for the first 5–20 Myr. *Bottom panel:* number of emitted photons per hydrogen atom.

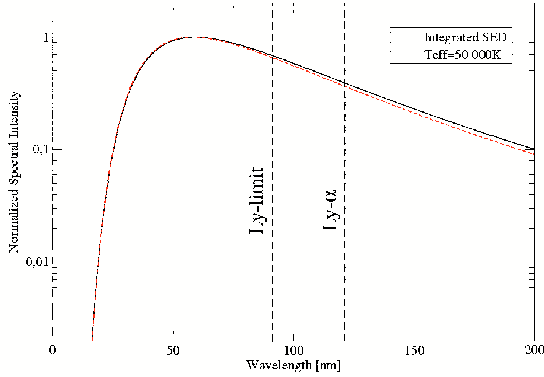


Fig. 3. Normalized spectral intensity as a function of wavelength.

the global star fraction. A combination of local starbursts followed by star formation quenching and insufficient mass resolution may be responsible for this effect.

By trial and error, we calibrated the escape fraction (Table 2) so that reionization is complete, at about $z \sim 6$.

3.3. Lyman- α transfer

We run the Lyman- α simulations as a further post-treatment of the reionization simulations. The time interval between two snapshots is typically 10 Myr at $z \sim 9$, during which the ionization fronts travel a few hundred comoving kpc at most. We consider that this time interval is small enough to permit a *de facto* interpolation of the quantities relevant for Lyman- α transfer: gas density and ionization state.

Potentially, Lyman series photons can heat up the gas (see references in Semelin et al. 2007). But heating occurs only at

low temperatures (~ 10 K), where the gas pressure is insignificant. Consequently, the feedback of Lyman- α photons on the dynamics is negligible. However, in models with soft source spectra, where the efficient heating of low density neutral regions by X-ray photons is absent, one consequence of including the heating by Lyman- α photons is to increase moderately the temperature in the coolest regions. We implemented a local Lyman- α heating using the following formula, derived from Eq. (47) and Fig. 3 in Furlanetto & Pritchard (2006):

$$\frac{dT_K}{dt} = \frac{0.8}{T_K^{1/3}} \frac{x_\alpha}{S_\alpha} \frac{10}{1+z} H(z) \quad \text{with} \quad S_\alpha \sim \left(1 - \frac{0.7}{\sqrt{T_K}}\right). \quad (7)$$

We checked that when the 21 cm signal is in absorption with an intensity in the 300 mK range, i.e. where the gas temperature is a few K, this small amount of heating can reduce the signal intensity by up to 100 mK.

Photons are emitted at frequencies between Ly- α and Ly- β . The spectrum and luminosity of the sources are computed with the method described in Sect. 2.2.3 for the ionizing continuum. In principle higher Lyman series photons also contribute. Indeed as soon as a photon emitted in the continuum hits an atom in a resonant upper Lyman line, it cascades locally down the levels and is transformed into a local Ly- α photon. These higher Lyman line photons are more concentrated around the sources since they need a smaller redshift before they resonate with a line (see e.g. Naoz & Barkana 2008). Overall, including the upper Lyman line photons would increase the number of Ly- α photons by a factor of less than 2. From the results of the simulations we estimate that this could shift the history of the average Ly- α coupling by $\Delta z = 0.3$. It would also add some limited amount of power in the fluctuations. In this work we include only the Ly- α line. Upper Lyman series lines will be included in a future work.

In the simulations, a fiducial number of $n_{\text{ph}} = 10^7$ photons is used between two dynamical snapshots. As the time interval between snapshots and the total source intensity varies, the physical content of the photons also varies. The value of $n_{\text{ph}} = 10^7$, dictated by the CPU cost of the simulations, is a lower limit for statistical significance: indeed, with our current grid resolution of less than 12 particles per cell, about 10% of the cells do not receive any photons between two snapshots. These cells are small and are mostly located in moderate density filaments and low flux environments, far from the sources. They are properly averaged with some of their neighbors when the fixed-grid maps are computed. To assess the impact of this limited sampling we also ran a simulation with 6×10^7 photons between two snapshots down to $z = 9.5$ for the $20 h^{-1}$ Mpc box. In this case the fraction of unsampled cells drops to $\sim 1\%$. It is only when maps are drawn with thin slices, $\sim 200 h^{-1}$ kpc, that a difference can be seen.

3.4. Physics of the 21 cm emission

To compute the differential brightness temperature of the 21 cm emission in the optically thin limit of the 21 cm line, we use the formula:

$$\delta T_b = 28.1 \text{ mK} x_{\text{HI}} (1 + \delta) \left(\frac{1+z}{10}\right)^{\frac{1}{2}} \frac{T_S - T_{\text{CMB}}}{T_S} \times \left(\frac{\Omega_b}{0.042} \frac{h}{0.73}\right) \left(\frac{0.24}{\Omega_m}\right)^{\frac{1}{2}} \left(\frac{1 - Y_p}{1 - 0.248}\right), \quad (8)$$

where δ is the local overdensity at redshift z , x_{HI} the neutral hydrogen fraction, T_S the neutral hydrogen spin temperature,

T_{CMB} the CMB radiation blackbody temperature at redshift z and Ω_b , Ω_m , h and Y_p are the usual cosmological parameters. In this formula, the contribution from the proper velocity gradients have been neglected (Barkana & Loeb 2005a). Mellema et al. (2006b) include this effect in computing 21 cm line of sight spectra. Analytic (McQuinn et al. 2006) and semi-numerical models (Mesinger & Furlanetto 2007) find that the contribution of proper velocity gradients to the 21 cm power spectrum is important only at $\langle x_{\text{HI}} \rangle < 0.5$ on scales smaller than the effective ionization bubble size. Since previous simulations did not include a proper treatment of the Ly- α pumping which is especially important during the early phase of reionization, it was not relevant to include the effect of proper velocity gradients. In this work, we include a full modeling of the Ly- α pumping. In a separate paper, the effect of proper velocity gradients will be studied.

The spin temperature of hydrogen T_S is coupled to the CMB temperature T_{CMB} by Thomson scattering of CMB photons, and to the kinetic temperature of the gas T_K by collisions and Ly- α pumping. As a result, the spin temperature can be written (Furlanetto et al. 2006):

$$T_S^{-1} = \frac{T_{\text{CMB}}^{-1} + x_c T_K^{-1} + x_\alpha T_C^{-1}}{1 + x_c + x_\alpha} \quad \text{with} \quad T_C \simeq T_K, \quad (9)$$

and

$$x_\alpha = \frac{4P_\alpha T_\star}{27A_{10}T_{\text{CMB}}}, \quad x_c = \frac{T_\star}{A_{10}T_{\text{CMB}}}(C_H + C_p + C_e), \quad (10)$$

where $T_\star = \frac{h\nu_0}{k_B} = 0.068 \text{ K}$ ($\nu_0 = 1420 \text{ MHz}$), $A_{10} = 2.85 \times 10^{-15} \text{ s}^{-1}$ is the spontaneous emission factor of the 21 cm transition, P_α is the number of scatterings of Ly- α photons per atom per second, and C_H , C_p and C_e are the de-excitation rates due to collisions with neutral atoms, protons and electrons. For the de-excitation rates we use the fitting formula given by Liszt (2001) and Kuhlen et al. (2006). The coupling coefficients x_α and x_c are computed for each gas particle from the simulation data. The final output is the value of the brightness temperature for each particle in each snapshot.

4. Analysis

We will focus our analysis on two aspects.

First, by comparing our two simulations, we will evaluate the effect of numerical resolution and box size. Numerical resolution truncates the physics at small scales: this mainly modifies the reionization history and geometry by removing small, dense structures with high recombination rates. The limited box size, on the other hand, truncates large scales and dampens the 21 cm brightness temperature power spectrum on corresponding wavenumbers.

The second axis of our analysis is to measure the effect of including an accurate treatment of the Wouthuysen-Field effect in computing the brightness temperature.

4.1. Evolution of sky-averaged quantities

4.1.1. Ionization fraction

The simplest way to characterize the global history of reionization is to compute the average ionization fraction as a function of redshift. The mass weighted ($\langle x_{\text{HI}} \rangle_{\text{mass}}$) and volume weighted ($\langle x_{\text{HI}} \rangle_{\text{vol}}$) average ionization fractions are shown in Fig. 4 for both simulations. For the volume (resp. mass) average we use the volume occupied by each particle derived from the SPH smoothing

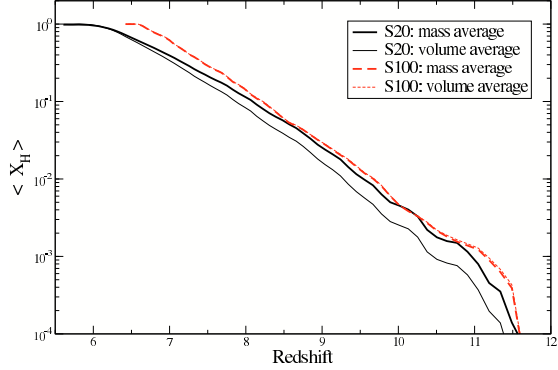


Fig. 4. Mass weighted and volume weighted averaged ionization fraction.

length (resp. the mass of each particle) as weights in the averaging procedure. The main feature of this plot is that the mass weighted averages are similar for the two simulations while the volume weighted averages differ. Indeed, the star formation histories of the two simulations were calibrated to produce the same number of ionizing photons at any redshift. As long as recombination is negligible, this should produce identical mass weighted ionization fractions. It can be checked in Fig. 4 that below redshift ~ 8 recombination becomes efficient in the S20 simulation, which contains denser small-scale structures due to higher resolution, and the mass weighted ionization fraction drops below its S100 counterpart.

The volume weighted ionization fractions differ at all redshifts between the two simulations, because highly ionized regions of identical mass, close to the sources, are denser and occupy a smaller volume in the more resolved S20 simulation. McQuinn et al. (2006) advocate the use of the volume-averaged ionization fraction as an evolution variable instead of redshift. Indeed, depending on arbitrary choices (all consistent with current observational constraints) for the source formation history and source nature, reionization can begin at $z = 12$, 15 or 20 and proceed differently. However, for a fixed average ionization fraction, McQuinn et al. (2006) show that the brightness temperature power spectrum depends weakly on the redshift at which this ionization fraction is achieved. This is true if a modification of the source formation efficiency is the main cause of the change in redshift for a fixed ionization fraction. If the change is caused by using a different source spectrum, or modifying the gas sub-grid physics (e.g. an inhomogeneous clumping factor), this may not be true anymore. We believe that the averaged ionization factor is indeed a more relevant measure of the evolution of reionization than redshift and we adopt their point of view. However, instead of the volume averaged ionization fraction, which is well suited to comparing different models with the same underlying gas density field, we will use the mass averaged ionization fraction which is better suited for the comparison of simulations with different mass resolution. While the mass averaged ionization fraction is a suitable quantity to track the progression of reionization, a volume average is more relevant to compute such observable quantities as the 21 cm brightness temperature. Consequently, all quantities other than the ionization fraction will be volume averaged.

We also computed the Thomson optical depth from the two simulations ignoring the presence of helium. The values are $\tau = 0.060$ and $\tau = 0.063$ for S20 and S100 simulations respectively,

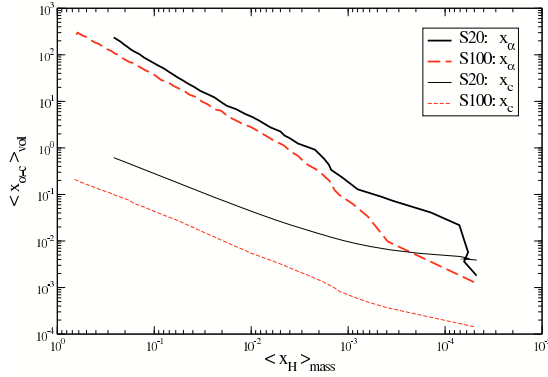


Fig. 5. Evolution of the volume averaged Lyman- α and collisional coupling coefficients as functions of the average ionization fraction for both simulations (see main text for a definition of the coefficients).

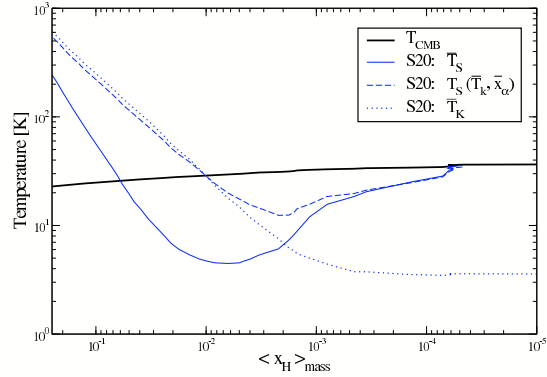


Fig. 6. Evolution of the neutral hydrogen spin temperature as a function of the average ionization fraction. The average is computed either directly from the particle spin temperatures or from the volume averaged values of T_K and x_α . The CMB temperature and volume averaged kinetic temperature are plotted for comparison.

i.e. within 1σ of the WMAP3 value $\tau = 0.0089 \pm 0.030$ (see Spergel et al. 2007).

4.1.2. Spin temperature coupling coefficients

The spin temperature of neutral hydrogen, T_S , is defined by Eq. (7) and depends on two coupling coefficients, x_α for the Wouthuysen-Field coupling and x_c for collisional coupling. Until now, x_α has never been computed consistently in simulations of the 21 cm emission. While x_α itself contains fluctuations which contribute to the power spectrum of the 21 cm signal, we study first the evolution of the average value of the coefficients which tells us at which stage in the reionization history the spin temperature can be considered fully coupled to the kinetic temperature of the gas. The evolution of the volume averaged coefficients $\langle x_\alpha \rangle_{\text{vol}}$ and $\langle x_c \rangle_{\text{vol}}$ is shown in Fig. 5, as a function of $\langle x_{\text{H}} \rangle_{\text{mass}}$. The first conclusion from Fig. 5 is that x_c is negligible compared to x_α except in the very early phase ($\langle x_{\text{H}} \rangle_{\text{mass}} \sim 10^{-4}$) for the S20 simulation. Logically, the S20 simulation, producing denser structures, has a higher x_c (indeed C_H , C_p and C_e in Eq. (8) depend on the density). With a better mass resolution and even denser structures than in the S20 simulation, x_c would still increase, and the ionization fraction when x_α starts to dominate would also increase. The second piece of information that can be derived is the magnitude of the error made by applying the usual assumption $x_\alpha = +\infty$. When $x_\alpha > 10$, the error made on δT_b by assuming $x_\alpha = +\infty$ is smaller than $\sim 10\%$. This corresponds to $\langle x_{\text{H}} \rangle_{\text{mass}} > 0.02$ for the S20 simulation and $\langle x_{\text{H}} \rangle_{\text{mass}} > 0.04$ for the S100 simulation. It may appear that the full coupling occurs very early on. Let us emphasize, however, that in this early phase there is a strong absorption signal (with our choice of source model) compared with the weaker emission signal observed later on. In a source model with a harder spectrum (to be studied in a future paper) we would have a weaker absorption signal. If the sources are still stars (e.g. using a more top-heavy IMF) the full coupling would also occur at a larger average ionization fraction since the ratio of ionizing to Lyman-alpha photons would be larger.

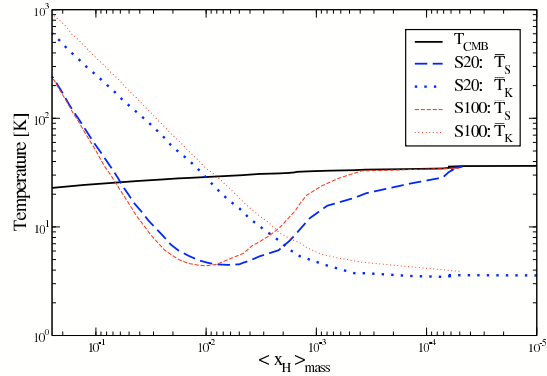


Fig. 7. The evolution of the volume averaged spin temperature, kinetic temperature, and CMB temperature is plotted as a function of the average ionization fraction. The quantities are plotted for both box sizes.

4.1.3. Spin temperature

Figure 6 displays the average spin temperature for the S20 simulation, with the average computed in two different ways. First the spin temperature is computed using the volume averaged quantities $\langle T_k \rangle_{\text{vol}}$, $\langle x_\alpha \rangle_{\text{vol}}$ (and $\langle x_c \rangle_{\text{vol}}$), following Furlanetto et al. (2006) and Gnedin & Shaver (2004). This quantity is denoted $T_S(\bar{T}_k, \bar{x}_\alpha)$. Then the more relevant value, \bar{T}_S , is computed, as the direct volume average on the particles of the spin temperature, i.e. $\bar{T}_S = \langle T_S \rangle_{\text{vol}}$. Figure 6 shows that there is a large difference between the two definitions. This is mainly due to the fact that the spin temperature is computed through the weighted average of *inverse* temperatures (Eq. (7)). This large difference propagates to the average brightness temperature. Consequently we strongly advocate replacing the Furlanetto et al. average traditionally used to define the emission and absorption regimes by the more relevant direct average of the spin/brightness temperature. Of course this is easily done only for simulations. Let us mention that with the direct average, the spin temperature remains below the CMB temperature at lower z .

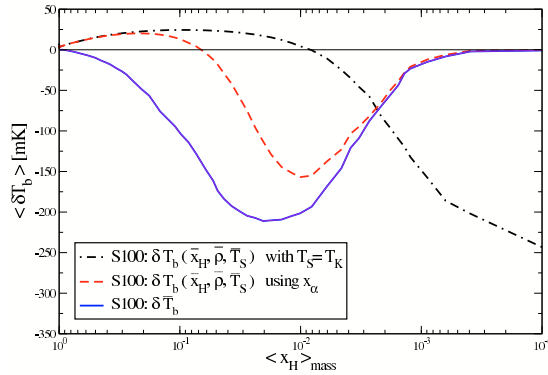


Fig. 8. Evolution of the average differential brightness temperature for the S100 simulation. The average is computed in three different ways (see main text and legend). The blue curve is the most relevant direct average of the particle brightness temperature.

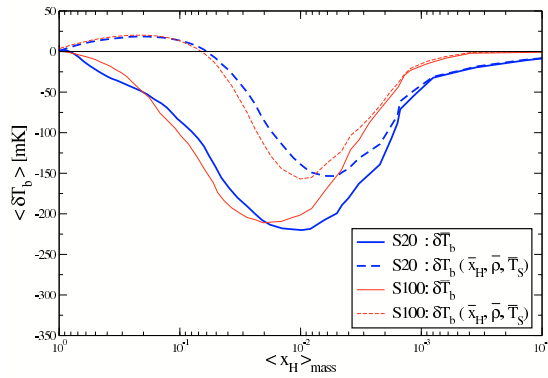


Fig. 9. Comparison of the evolution of the average differential brightness temperature for the two box sizes. The average is computed in two different ways (see main text).

Figure 7 compares the direct average of the particle spin temperature in the two simulations: the results are quite similar. The main difference is that the spin temperature starts to decouple from the CMB temperature later in the S100 simulation. Indeed, we use periodic boundary conditions in the simulations. Thus the Lyman- α sources are more homogeneously distributed in the $20 h^{-1}$ Mpc box, which lacks large scale modes, than in the $100 h^{-1}$ Mpc box (Barkana & Loeb 2005b). In the $100 h^{-1}$ Mpc box, large void regions receive little Lyman- α flux. There, the spin temperature remains coupled to the CMB at lower redshifts.

4.1.4. Differential brightness temperature

The differential brightness temperature is plotted in Fig. 8 for the S100 simulation. The average is computed in three different ways: $\delta T_b(\bar{x}_{\text{H}}, \bar{\rho}, \bar{T}_{\text{S}})$ with $T_{\text{S}} = T_{\text{K}}$ for each particle, $\delta T_b(\bar{x}_{\text{H}}, \bar{\rho}, \bar{T}_{\text{S}})$ computing T_{S} for each particle using x_{α} , and δT_b , using the same notations as for the spin temperature. In all these definitions we use a volume weighted average. The first definition uses the common $T_{\text{S}} = T_{\text{K}}$ assumption: as can be seen in

the plot, it fails at early times when the coupling is weak. The second definition (equivalent to Furlanetto et al. 2006) shows an emission and an absorption regime. However, with the more realistic third definition, δT_b , the emission regime disappears completely. Indeed, absorption regions have a strong signal which dominated over the weak, ~ 25 mK signal of the emitting regions. Of course, if X-ray sources were included, the cold neutral IGM would be pre-heated and the absorption regions contribution would shrink much faster: δT_b would show an emission regime and the absorption regime would be weaker. Including shock heating would go in the same direction although the magnitude of the change would be less homogenous and is more difficult to estimate.

To assess the effect of resolution and box size, we plot in Fig. 9 the direct δT_b and $\delta T_b(\bar{x}_{\text{H}}, \bar{\rho}, \bar{T}_{\text{S}})$ for both simulations. The overall behaviour is similar. In the S20 simulation the minimum of δT_b occurs at a 1% average ionization fraction compared to a 2% ionization fraction for the S100 simulation. This small difference is due in part to the slightly smaller coupling of the S100 simulation at equal ionization fraction. The values of the minimum δT_b are not very different either. We expect to find resolution effects and box size effects in the power spectra.

We have presented these average values to compare with previous studies. However, much information is erased when considering average quantities, which makes their interpretation of limited scope. We proceed now to present maps of the different quantities.

4.2. Maps

4.2.1. Ionization fraction

Maps of the ionization fraction of hydrogen are presented in Fig. 10 for both box sizes at a redshift when $\langle x_{\alpha} \rangle_{\text{vol}} = 1$, which we will call the Wouthuysen-Field coupling redshift (hereafter WFCR), and at a redshift when $\langle x_{\text{H}} \rangle_{\text{mass}} = 0.5$, which we will call the half reionization redshift (HRR). We can see that the WFCR correspond to an early stage in the reionization history. The maps are presented for two different slice thicknesses: $2 h^{-1}$ Mpc and $200 h^{-1}$ kpc. The $2 h^{-1}$ Mpc slice corresponds to a bandwidth $\delta\nu \sim 0.15$ MHz at a redshift between 6 and 10, an acceptable value for SKA. The $200 h^{-1}$ kpc slice is plotted to give a feeling of how much power would be added at small scales by using narrower bandwidth: indeed, sharper ionization fronts are found in this case. Also as expected the S100 maps show coherent structures on scales up to $50 h^{-1}$ Mpc which cannot be accounted for in the S20 maps.

Usual effect of a lower mass resolution (S100 vs. S20) is to delay reionization. Indeed small mass halos form first and make a large contribution to the ionizing photon budget at early times (see Iliev et al. 2007). In our treatment, the delay is removed because we calibrated the source formation history of the S100 simulation on the S20 simulation by boosting the formation efficiency. However, this procedure can only account for unresolved halos located within more massive, resolved, proto-halos. The contribution from unresolved halos located in comparatively underdense regions could modify the morphology of the ionization maps during the early reionization history.

4.2.2. Lyman- α coupling

The influence of including a proper treatment of the Wouthuysen-Field effect on the 21 cm signal is twofold. First, it simply modifies the intensity of the signal, especially in the

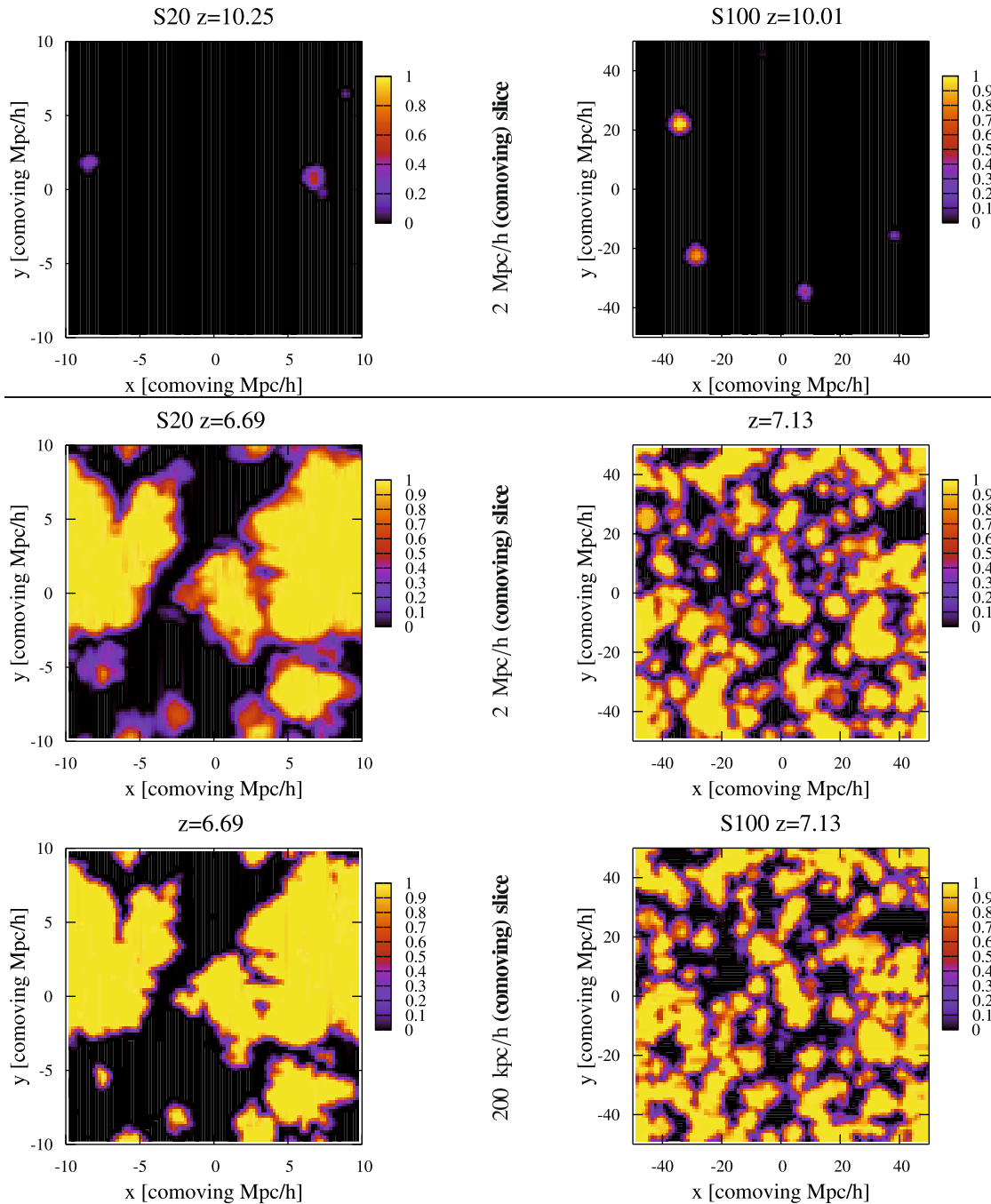


Fig. 10. Maps of the ionization fraction for the two simulations (right and left) at two different stages of reionization (above and below line), the WFCR and the HRR (see text for definition) and for two slice thicknesses (as labeled). The color scale is a linear function of the ionization fraction.

regions seen in absorption. This will be obvious in the brightness temperature maps shown in Sect. 4.2.3. The second effect is to introduce a new source of fluctuations in the signal, associated

with the fluctuations in the local Ly- α flux. Figure 11 presents maps of the x_α coefficient for both simulations at the WFCR. Around the WFCR, the additional fluctuations to the brightness

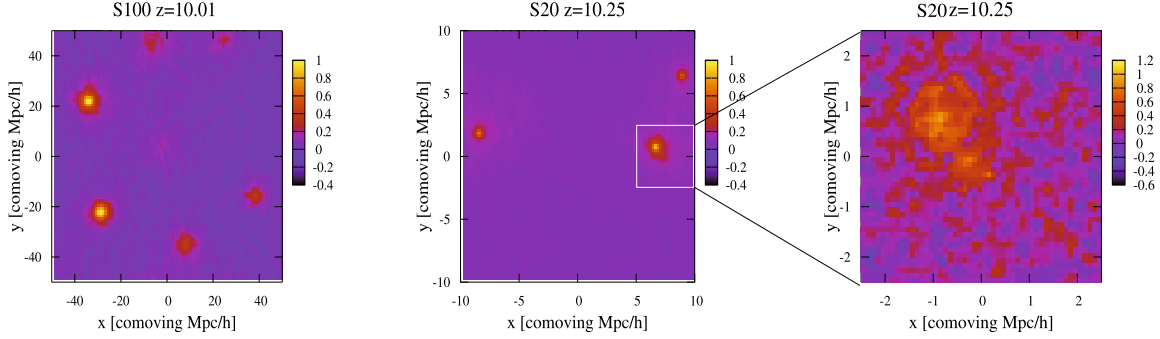


Fig. 11. Maps of the x_α coupling coefficient. We use a logarithmic color scale, and choose the redshift in each simulation (S20 and S100) such that $\langle x_\alpha \rangle = 1$ (10.25 for S20 and 10.01 for S100). The thickness of the slice is $2h^{-1}$ Mpc for the two panels on the left and $100h^{-1}$ kpc for the right panel.

temperature are expected to be maximal. On a large scale, the maps boil down to strong coupling regions around sources, superimposed on a uniform weak coupling background. The signature of the added brightness temperature fluctuations will be based on the typical sizes of the strong coupling regions and on the clustering and Poisson noise in the source distribution. Keeping this in mind, it is interesting to notice that the strong coupling regions appear to be much smaller, $\sim 2h^{-1}$ Mpc, in the S20 simulation than in the S100 simulation where they extend over $\sim 10h^{-1}$ Mpc. To understand this let us remember that we apply periodic boundary conditions to the radiative transfer code. As a result, any point in the S20 simulation is surrounded by a rather homogeneous distribution of sources, with the closest source at most $\sim 10h^{-1}$ Mpc away. This dampens the fluctuations in the Ly- α flux and washes out the outer parts of the strong coupling regions. As a result, we expect to find more power at large scales in the added brightness temperature fluctuations in the S100 simulation than in the S20 simulation.

The zoom on the source in the S20 simulation shows that the apparent spherical symmetry of the strong coupling regions breaks down at small scales. Semelin et al. (2007) have shown that substantial asymmetry can be expected if the density field of the gas is not homogeneous (e.g. presence of filaments). Let us notice, however, that the slice thickness for the zoom is $100h^{-1}$ kpc, while it is $2h^{-1}$ Mpc for the other maps. With such a thin slice the noise in the x_α evaluation (resulting of the finite number of photons used in the Monte Carlo scheme) is not smoothed out at all. Any structure outside the main strong coupling region is mostly noise (visible on the color version only). If structures exist in the x_α maps at scales smaller than $1h^{-1}$ Mpc and with an amplitude of less than a factor of 3 above or below the background, we will miss them in the noise or smooth them out. From a theoretical point of view it would be interesting (but very costly) to produce maps with a lower noise level. However, from a practical point a view, these scales are below the projected resolution of SKA.

4.2.3. Brightness temperature maps

The most common (and most drastic) approximation used to compute the brightness temperature is $T_S \gg T_{\text{CMB}}$ (case 1). In this approximation no absorption region can exist. The second approach is to assume full Lyman- α coupling ($x_\alpha = \infty$) (case 2). The third approach, the one used in this paper, is to compute self-consistently the local values of x_α and derive

accordingly the local values of T_S and T_b (case 3). We plot maps of the differential brightness temperature for all three cases and for both simulation boxes at the WFCR in the 6 top panels of Fig. 12. The thickness of the slice is $2h^{-1}$ Mpc. At this early redshift, when the two first approximations are hardly reliable, the differences are striking. Not surprisingly case 1 fails completely: it is not tailored to handle absorption regions and predicts only emission. More interesting, but also expected, case 2 overpredicts the strength of the absorption compared to case 3 (300 mK instead of 200 mK) by assuming full Wouthuysen-Field coupling. We used the same color scale for all maps to emphasize these differences. The strong absorption signal observed in cases 2 and 3 is the consequence of our choice of rather soft-spectrum sources. The neutral IGM undergoes very little preheating by UV and X rays. Let us emphasize that the strength of the absorption signal is very sensitive to the thermal modeling of the gas when $T_K \ll T_{\text{CMB}}$, which is not uncommon at this redshift with our choice of sources. Indeed, the included Ly- α heating, although very weak (at most a few K over the EoR), decreases the strength of the absorption signal by 50 to 100 mK. If even a small fraction of hard-spectrum sources was included, the absorption strength would decrease and turn to emission at later redshifts.

The six bottom panels of Fig. 12 shows the same maps for the HRR. At this redshift we have $\langle x_\alpha \rangle > 200$ for both simulations. Consequently the maps for cases 2 and 3 are almost identical. Comparing with Fig. 10 it can be checked that the regions which are still seen in absorption are the neutral regions not too close to the ionization fronts. Comparing the absorption regions in the S20 and in the S100 maps, it can be seen that the signal is somewhat stronger in the S20 simulation. We have determined that a lower gas kinetic temperature in the S20 simulation, in the voids, is responsible for this effect. Since we are talking about temperatures lower than 10 K, a difference of a few K produce a large effect on the differential brightness temperature. The S20 simulation has a higher mass resolution which creates higher density contrasts. In the voids, the density is lower and the adiabatic expansion stronger: the resulting temperature is lower.

Obviously, in case 1, the absorption regions turn to emission. Since emission saturates quickly at a few tens of mK, the statistical property of the signal such as the average rms fluctuations of the brightness temperature will be weaker. At such an advanced stage in the reionization history the assumption made in case 1

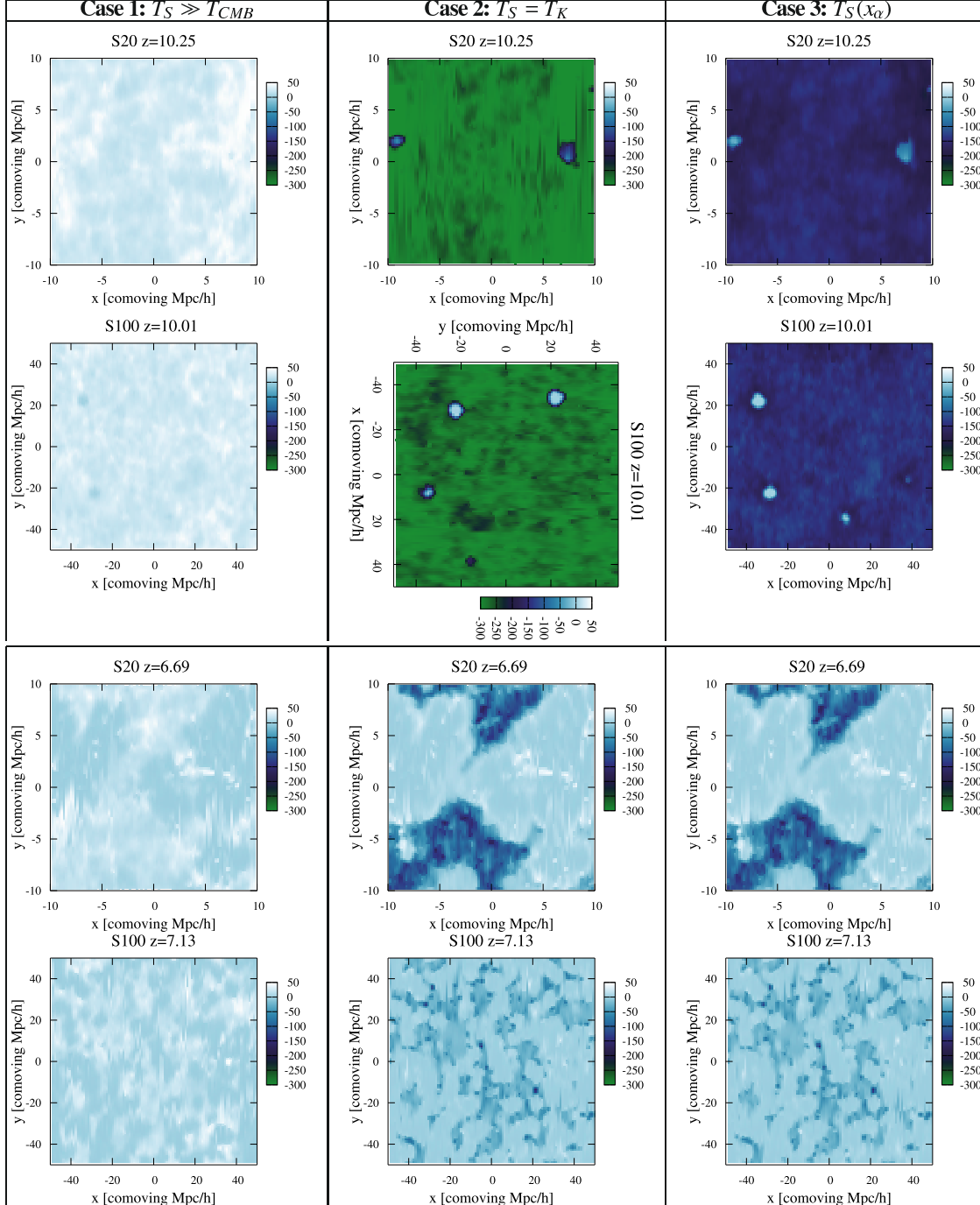


Fig. 12. Differential brightness temperature maps for both box sizes and 3 different hypotheses for computing the spin temperature (see main text and description in the figure). The redshift of the 6 top panels is chosen such that $\langle x_\alpha \rangle = 1$, the redshift of the 6 bottom panels is such that $\langle x_\alpha \rangle = 0.5$. The temperature color scale is linear, in mK. The thickness of the slice is $2h^{-1}$ Mpc.

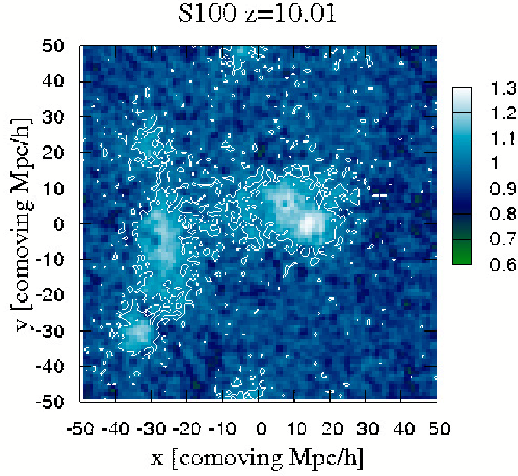


Fig. 13. Ratio of the differential brightness temperature computed with the fluctuating local value of x_α on the one hand and the average value of x_α on the other hand. The color scale is linear. The contour is computed from the x_α field for the $x_\alpha = 1$ value.

may actually be more realistic: cases 2 and 3 would probably look more like case 1 if we included X-ray sources.

Using a homogeneous average value for x_α to account for the Wouthuysen-field effect (for example a calibrated function of x_H) is much easier than computing the full radiative transfer in the line. So it is important to assess the benefit reaped from doing the full treatment. The x_α field induces its own fluctuation in the brightness temperature signal. Figure 13 illustrates this point. It shows a map of the ratio of the differential brightness temperatures computed with the fluctuating local value of x_α on the one hand and the homogeneous, average value of x_α on the other hand. This map is computed at the WFCR, for the S100 simulation. As expected, the ratio is mostly larger than one inside the $x_\alpha = 1$ contour and lower outside. Moreover the two differential brightness temperatures differ by up to 30%. Consequently it appears that, at these early redshifts when the Lyman- α coupling is not full, it is worth doing the full Lyman- α transfer.

5. Power spectrum

Using the power spectrum as a statistical tool for analyzing the EoR 21 cm signal is natural because it can be directly computed from the visibilities measured by the radio interferometers such as LOFAR, MWA or SKA. Morales & Hewitt (2004) have shown that using the full 3D power spectrum rather than the 2D angular power spectrum will improve the sensitivity of the observations and make the process of foreground removal easier.

Strength of the Lyman- α coupling fluctuations

Figure 14 shows the power spectrum of the quantity $z_\alpha = \frac{x_\alpha}{1+x_\alpha}$ for both simulations at the WFCR. Indeed directly plotting the spectrum of x_α is not interesting: the x_α field is dominated by the very strong values near the sources and has a power spectrum similar to that of a distribution of Dirac functions. However, these very high values of x_α are not especially interesting: they

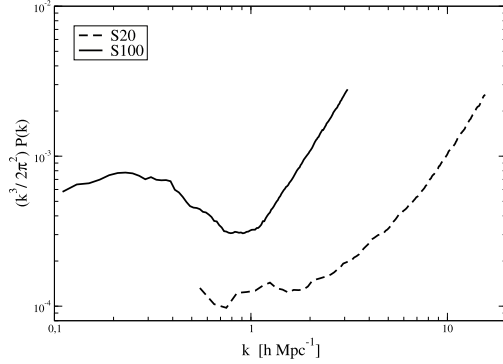


Fig. 14. 3D isotropic power spectrum of $\frac{x_\alpha}{1+x_\alpha}$. The spectra are plotted for both simulations, S20 and S100, at the redshift when $\langle x_\alpha \rangle = 1$.

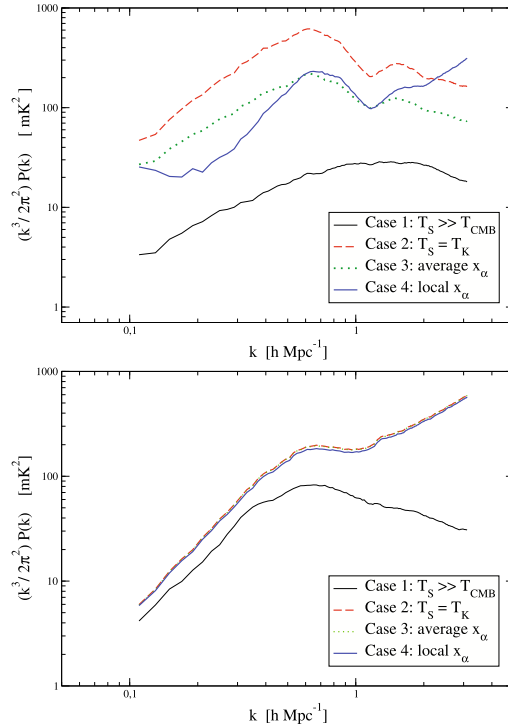


Fig. 15. Comparison of the 3D isotropic dimensional power spectrum of the differential brightness temperature with 4 different assumptions used to compute the spin temperature (see legend and main text). The spectra are computed for the S100 simulation. *The top panel* is for the redshift when $\langle x_\alpha \rangle = 1$, and *the bottom panel* is for the redshift when $\langle x_H \rangle = 0.5$.

are just values for which the coupling saturates. z_α , which is just the weight applied to the inverse kinetic temperature in Eq. (9) (neglecting the contribution of x_c), varies between 0 and 1 and contains more relevant information about the magnitude of the coupling. As can be seen in Fig. 14, the point sources still dominate the small scales. More interesting is the increase of the power spectrum toward large scales, which is barely visible for

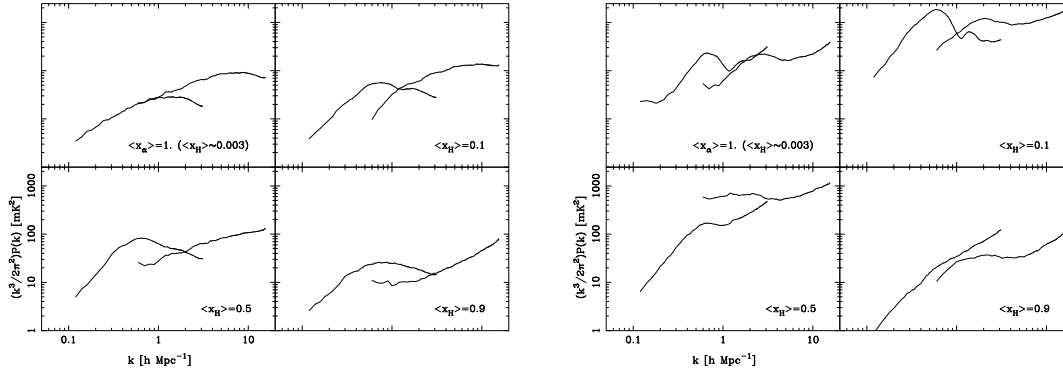


Fig. 16. 3D isotropic dimensional power spectrum of the differential brightness temperature for the two box sizes. The stage of reionization is indicated in each panel. The four left panels assume $T_S \gg T_{\text{CMB}}$ while the four right panels compute T_S exactly using the local values of x_α .

the S20 simulation but obvious in the S100 simulation. It is likely that this increase tracks the Poisson noise in the large scale clustering of the sources and void distribution. For the S100 simulation, the spectrum shows a local maximum at scales $\sim 30 h^{-1}$ Mpc. Whether this maximum is real or only the effect of the box size is an interesting question. Only simulations with larger boxes will give the answer.

Differential brightness temperature

In this section, we will compute directly the *dimensional* power spectrum of δT_b . Various authors, studying the emission regime, compute the power spectrum of δT_b divided by the average, redshift dependent, emission temperature $T_0 \sim 28 \left(\frac{1+z}{10}\right)^{1/2}$. When we include the absorption regime, T_0 has no special significance. Using the actual average δT_b of the box would be no better: having both emission and absorption, it holds no information about the amplitude of the fluctuations and may even be zero at some redshift. Using the actual rms average at each redshift would indeed be more relevant as it does reflect the amplitude of the fluctuations. However it would erase the information about the absolute amplitude at a given scale, at different redshifts. Consequently, we decided to plot the direct dimensional power spectrum of the differential brightness temperature.

Figure 15 shows the three-dimensional isotropic power spectrum of δT_b as defined by Eq. (8) for the S100 simulation, at the WFCR (top panel) and the HRR (bottom panel), in four different cases for the computation of the spin temperature. In case 1, we assume that $T_S \gg T_{\text{CMB}}$, in case 2 $T_S = T_K$, in case 3 we use Eq. (9) with the box averaged value of x_α , and finally in case 4, we use Eq. (9) with the local values of x_α . As expected, the larger differences appear at the WFCR, where the amplitude of the power spectrum changes by more than a factor of 10 depending on the case. Case 1, ignoring the possibility of absorption, strongly underestimates the amplitude of the power spectrum, while case 2, assuming full coupling between spin temperature and gas kinetic temperature, overestimates the amplitude. The amplitudes for cases 3 and 4 are similar (and more realistic). However, case 4 shows more power at small scales and less power at large scales than case 3. Indeed, as illustrated in Fig. 13, case 3 uses a larger value of x_α far from the sources, thus produces a stronger absorption in large scale voids and more power at large scale in the spectrum than case 4. The behaviour

at small scales arises from the presence of the Ly- α halos around the sources in case 4. Semelin et al. (2007) have shown that the profile of these halos can be as steep as r^{-3} if the gas has an isothermal profile. Even at distances of a few comoving Mpc, where the gas profile flattens, the Ly- α halo profile behaves as $\sim r^{-2.3}$ (Semelin et al. 2007; Chuzhoy & Zheng 2007). The contribution from these sharp x_α fluctuations explains the increase in the case 4 power spectrum at small scales. At the HRR (bottom panel) the situation is simpler. The Wouthuysen-Field coupling is very strong and cases 2, 3 and 4 are almost indistinguishable. All three have much larger amplitude than case 1 which is related to the fact that absorption can produce a larger absolute signal than emission, thus larger fluctuations. It is interesting to notice that the difference in amplitude is especially large at small scales. The contribution of the regions straddling the sharp ionization front is presumably responsible for this feature. In case 1, the brightness temperature rises from ~ 0 mK in the fully ionized region inside the ionization front to a moderate ~ 20 mK emission outside of the front. In all other cases, the temperature first rises to a moderate emission in the regions just outside the ionization front, preheated above the CMB temperature by the hard part of the source spectrum, then drops to strong absorption farther out in the cool voids. The thickness of the preheated regions depends strongly on the source modeling: in our case it is less than $1 h^{-1}$ Mpc. With a harder spectrum these regions would be thicker, and with X-ray sources they would be erased and the corresponding feature absent in the power spectrum.

Figure 16 shows the δT_b power spectrum of both the S20 and S100 simulations at four different stages of reionization (the WFCR, $\langle x_H \rangle = 0.1$, $\langle x_H \rangle = 0.5$, and $\langle x_H \rangle = 0.9$), for case 1 (the four panels on the left) and case 4 (the four panels on the right). Let us first comment on how the spectra for the two simulations connect. In most cases the large scales in the S20 simulation have less power than the same scales in the S100 simulation. This is the reason why EoR simulations have to use large boxes: to sample well enough the large scale clustering properties of the source distribution. There is however one exception, the $\langle x_H \rangle = 0.5$ (HRR) in case 4, where the S20 simulation has more power even on its large scales. This is related to the fact, already discussed in Sect. 4.2.3, that the absorption in the voids is stronger in the S20 simulation and thus the fluctuations are amplified. A second point is that at the WFCR the case 4 spectra have a more complex signature and a larger amplitude than the case 1 spectra which merely track the density fluctuations.

Taking absorption and Ly- α coupling correctly into account is essential at this early redshift. A third point is that we reproduce the behaviour noted by Mellema et al. (2006b) and Lidz et al. (2007b), that at scales of a few comoving Mpc the amplitude of the power spectrum reaches a maximum at the HRR, then decreases. This is true for case 1, which was used by Lidz et al. In case 4, with the full Ly- α modeling, it looks like the maximum shifts to smaller values of the average ionization fraction.

6. Conclusions

In this work, we have presented simulations of the 21 cm emission from the EoR. The first hydrodynamic simulations were run in cosmological boxes of sizes $20 h^{-1}$ Mpc and $100 h^{-1}$ Mpc with 2×256^3 particles. Then, using our adaptive Monte-Carlo code LICORICE, we ran, in post-treatment, radiative transfer simulations for the ionizing continuum. Finally cosmological radiative transfer simulations in the Lyman- α line were performed. The latter are necessary to compute the neutral hydrogen spin temperature without making any assumption about the strength of the coupling. This approach has not been followed before. We model the sources of both ionizing continuum and Lyman- α photons as stars, using a Salpeter IMF cut off at $100 M_{\odot}$. The $100 h^{-1}$ Mpc simulation star formation history is calibrated on the $20 h^{-1}$ Mpc. The photon escape fraction is calibrated independently in both simulations to produce a Thomson scattering optical depth of CMB photons within 1σ of the WMAP3 value, and a complete reionization at redshift $z \sim 6$. We have not included X-ray sources. If we had they would heat up the IGM and reduce the contribution of absorption vs emission in the signal.

We first computed the evolution of a number of box-averaged quantities as functions of the average ionization fraction. We find that, with our source modeling, the average Lyman- α coupling coefficient x_{α} reaches 1 for small values of the ionization fraction (a few 10^{-3}). However full coupling ($x_{\alpha} \gg 1$) is achieved only for ionization fractions greater than 10^{-1} . This is in line with expectations. Next we plotted the average spin temperature and differential brightness temperature. It was shown that the results are very different depending on how the average is computed: directly on the spin/brightness temperature of the particles, or from the volume-averaged values of the gas kinetic temperature and coupling coefficients. The latter is often used, but the former is more relevant. The direct average tends to erase the signal as regions in absorption have a much stronger signal than regions in emission. Maps of the 21 cm emission confirm that the different assumptions made in computing the spin temperature lead to very different levels of the signal. The $T_S \gg T_{\text{CMB}}$ assumption is not relevant at all for our choice of source modeling. It would be more relevant at not-too-early redshifts if we included X-ray sources. As expected the full coupling assumption, $x_{\alpha} = \infty$, is reasonable except in the early phase of reionization. In this early phase, we illustrate how computing the local values of x_{α} produces large fluctuations in the brightness temperature compared to using a redshift-dependent uniform value.

Finally the 3D dimensional power spectrum of the differential brightness temperature was plotted, with different assumptions in computing the spin temperature, at various stages of reionization and for the two box sizes. The first important (and expected) result is that including the possibility of a signal seen in absorption adds a large amount of amplitude to the power spectrum. This obviously depends on the choice of the source model. Then, in the early phase of reionization ($\langle x_{\text{H}} \rangle < 0.1$), using the local value of the Lyman- α coupling changes the spectrum by transferring power from large scales to small scales. We

reproduce the behaviour shown by Mellema et al. (2006b) and Lidz et al. (2007b): a maximum of the amplitude at $\langle x_{\text{H}} \rangle = 0.5$ for the scales around $10 h^{-1}$ Mpc. However, when absorption and the exact computation of the Lyman- α coupling are included, this maximum is shifted to smaller ionization fractions.

As mentioned several times, the first modification to our model that will be investigated is a modification of the source model. Including even a limited number of X-ray sources such as quasars would more efficiently preheat the regions outside of the ionization front, reducing the strength of the absorption regime, or even turning it to emission. This will be investigated in a forthcoming paper.

Another interesting development of this work is to include the anisotropic effect of the peculiar velocities on the 21 cm emission (Barkana & Loeb 2005a). Using the anisotropy, it is possible to separate the contribution of the velocities to the 21 cm fluctuations from the other contributions and to derive constraints on the cosmological parameters. Since this effect is important mostly in the early reionization phase and on small scales, it is a logical follow-up of including the full modeling of the Lyman- α coupling.

The implication of this work for the design of the future radio interferometers is simply to emphasize the potential for the detection of the signal during the early phase of reionization when the fluctuations in the signal are strong. Unfortunately, translating ‘‘early phase’’ into a numerical value for the redshift depends crucially on the star formation history at these high redshifts, of which very little is known. From the value of the Thomson scattering optical depth, it is likely, however, that this early phase occurs at $z > 12$.

Acknowledgements. This work was realized in the context of the SKADS and HORIZON projects. PDM acknowledges support from a SKADS post-doctoral fellowship. The author thanks the anonymous referee for helpful comments and improvements.

References

- Ahn, S.-H., Lee, H.-W., & Lee H. M. 2001, *ApJ*, 554, 604
- Ahn, S.-H., Lee, H.-W., & Lee, H. M. 2002, *ApJ*, 567, 922
- Aller, L. H. Numerical Data and Functional Relationships in Science and Technology – New Series Gruppe/Group 6 Astronomy and Astrophysics Volume 2 (Berlin, Heidelberg, New York: Springer-Verlag)
- Altay, G., Croft, R. A. C., & Pelupessy, I. 2008, *MNRAS*, 386, 1931
- Avery, L. W., & House, L. L. 1968, *ApJ*, 152, 493
- Barkana, R., & Loeb, A. 2004, *ApJ*, 609, 474
- Barkana, R., & Loeb, A. 2005a, *ApJ*, 624, L65
- Barkana, R., & Loeb, A. 2005b, *ApJ*, 626, 1
- Bertschinger, E. 2001, *ApJS*, 137, 1
- Cantalupo, S., Porciani, C., Lilly, S., & Miniati, F. 2005, *ApJ*, 628, 61
- Cen, R. 1992, *ApJS*, 78, 341
- Chuzhoy, L., & Shapiro, P. R. 2006, *ApJ*, 651, 1
- Chuzhoy, L., & Zheng, Z. 2007, *ApJ*, 670, 912
- Ciardì, B., & Madau, P. 2003, *ApJ*, 596, 1
- Ciardì, B., Scannapieco, E., Stoehr, F., et al. 2006, *MNRAS*, 366, 689
- Crocce, M., Pueblas, S., & Scoccimarro, R. 2006, *MNRAS*, 373, 369
- Dijkstra, M., Haiman, Z., & Spaans, M. 2006, *ApJ*, 649, 14
- Fan, X., Carilli, C. L., & Keating, B. 2006, *ARA&A*, 44, 415
- Faucher-Giguère, C.-A., Lidz, A., Hernquist, L., & Zaldarriaga, M. 2008, *ApJ*, 682, L9
- Field, G. B. 1958, *Proc. IRE*, 46, 240
- Furlanetto, S. R., & Oh, S. P. 2006, *ApJ*, 652, 849
- Furlanetto, S. R., & Pritchard, J. R. 2006, *MNRAS*, 372, 1093
- Furlanetto, S. R., Sokasian, A., & Hernquist, L. 2004, *MNRAS*, 347, 187
- Furlanetto, S. R., Oh, S. P., & Briggs, F. H. 2006, *PhR*, 433, 181
- Glover, S. C. O., & Brand, P. W. J. L. 2003, *MNRAS*, 340, 210
- Gnedin, N. Y., & Ostriker, J. P. 1997, *ApJ*, 486, 581
- Gnedin, N. Y., & Abel, T. 2001, *NewA*, 6, 437
- Gnedin, N. Y., & Shaver, P. A. 2004, *ApJ*, 608, 611
- Haardt, F., & Madau, P. 1996, *ApJ*, 461, 20
- Gunn, J. E., & Peterson, B. A. 1965, *ApJ*, 142, 1633

- Hernquist, L., & Katz, N. 1989, *ApJS*, 70, 419
- Iliev, I. T., Shapiro, P. R., Ferrara, A., & Martel, H. 2002, *ApJ*, 573, L123
- Iliev, I. T., Mellema, G., Pen, U.-L., et al. 2006, *MNRAS*, 369, 1625
- Iliev, I. T., Mellema, G., Shapiro, P. R., & Pen, U. 2007, *MNRAS*, 376, 534
- Iliev, I. T., Mellema, G., Pen, U.-L., Bond, J. R., & Shapiro, P. R. 2008, *MNRAS*, 384, 863
- Katz, N., Weinberg, D. H., & Hernquist, L. 1996, *ApJS*, 105, 19
- Komatsu, E., Dunkley, J., Nolta, M. R., et al. 2008 [arXiv:0803.0547]
- Kuhlen, M., Madau, P., & Montgomery, R. 2006, *ApJ*, 637, L1
- Lidz, A., Zahn, O., McQuinn, M., et al. 2007a, *ApJ*, 659, 865
- Lidz, A., Zahn, O., McQuinn, M., Zaldamaga, M., & Hernquist, L. 2007b [arXiv:0711.4373]
- Liszt, H. 2001, *A&A*, 371, 698
- Loeb, A., & Rybicki, G. 1999, *ApJ*, 524, 527
- Madau, P., Meiksin, A., & Rees, M. J. 1997, *ApJ*, 475, 429
- Maselli, A., Ferrara, A., & Ciardi, B. 2003, *MNRAS*, 345, 379
- McQuinn, M., Zahn, O., Zaldamaga, M., Hernquist, L., & Furlanetto, S. 2006, *ApJ*, 653, 815
- McQuinn, M., Lidz, A., Zahn, O., et al. 2007, *MNRAS*, 377, 1043
- Mellema, G., Iliev, I. T., Alvarez, M. A., & Shapiro, P. R. 2006a, *NewA*, 11, 374
- Mellema, G., Iliev, I. T., Pen, U.-L., & Shapiro, P. R. 2006b, *MNRAS*, 372, 679
- Metcalf, R. B., & White, S. D. M. 2007, *MNRAS*, 381, 447
- Mesinger, A., & Furlanetto, S. 2007, *ApJ*, 669, 663
- Monaghan, J. J. 1992, *ARA&A*, 30, 543
- Morales, M., & Hewitt, J. 2004, *ApJ*, 615, 7
- Nakamoto, T., Umemura, M., & Susa, H. 2001, *MNRAS*, 321, 593
- Naoz, S., & Barkana, R. 2008, *MNRAS*, 385, L63
- Pawlik, A. H., & Schaye, J. 2008, *MNRAS*, 389, 651
- Pritchard, J., & Furlanetto, S. R. 2007, *MNRAS*, 376, 1680
- Rasera, Y., & Teyssier, R. 2006, *A&A*, 445, 1
- Razoumov, A. O., & Cardall, C. Y. 2005, *MNRAS*, 362, 1413
- Rijkhorst, E.-J., Plewa, T., Dubey, A., & Mellema, G. 2006, *A&A*, 452, 907
- Salvaterra, R., Ciardi, B., Ferrara, A., & Baccigalupi, C. 2005, *MNRAS*, 360, 1063
- Santos, M. G., Amblard, A., Pritchard, J., et al. 2007 [arXiv:0708.2424]
- Seager, S., Sasselov, D., & Scott, D. 1999, *ApJ*, 523, L1
- Semelin, B., Combes, F., & Baek, S. 2007, *A&A*, 474, 365
- Shapiro, P. R., & Giroux, M. L. 1987, *ApJ*, 321, L107
- Shapiro, P. R., Ahn, K., Alvarez, M. A., et al. 2006, *ApJ*, 646, 681
- Spiegel, D. N., Bean, R., Doré, O., et al. 2007, *ApJS*, 170, 377
- Spitzer, L. 1978, *Physical Processes in the Interstellar Medium* (New York: Wiley)
- Springel, V., & Hernquist, L. 2003, *MNRAS*, 339, 289
- Springel, V. 2005, *MNRAS*, 364, 1105
- Susa, H. 2006, *PASJ*, 58, 445
- Tasitsiomi, A. 2006, *ApJ*, 645, 792
- Theuns, T., Leonard, A., Efstathiou, G., Pearce, F. R., & Thomas, P. A. 1998, *MNRAS*, 301, 478
- Trac, H., & Cen, R. 2007, *ApJ*, 671, 1
- Valdés, M., Ciardi, B., Ferrara, A., Johnston-Hollitt, M., & Röttgering, H. 2006, *MNRAS*, 369, L66
- Verhamme, A., Schaerer, D., & Maselli, A. 2006, *A&A*, 460, 397
- Whalen, D., & Norman, M. L. 2006, *ApJS*, 162, 281
- Wouthuysen, S. A. 1952, *AJ*, 57, 31
- Zahn, O., Lidz, A., McQuinn, M., et al. 2007, *ApJ*, 654, 12
- Zheng, Z., & Miralda-Escudé, J. 2002, *ApJ*, 578, 33

Chapter 4

The simulated 21 cm signal II

Stars are considered as the main photoionizing source during the reionization. However even small quantities of X-rays from various type of sources (e.g. quasars, X binaries, SN remnants etc) can affect the evolution of the gas temperature. With a much smaller photoionizing cross section, X-rays penetrate the ionization front farther than UV photons and raise the temperature in the neutral voids. Glover & Brand (2003) show that a modest number of X-ray sources can heat the temperature of the IGM by several tens of K using a homogeneous analytic model.

Pritchard & Furlanetto (2007) find that X-rays heat the gas more strongly around the sources rather than heating the gas homogeneously. Moreover, high-redshift sources are highly clustered and these fluctuating X-ray fluxes leave their own imprint on the 21 cm power spectrum.

We used a more refined source model for this study including X-rays. In addition, we did ray-tracing for these X-rays to investigate their inhomogeneous effect on the 21cm power spectrum.

We also study the effect of Helium reionization on the 21-cm signal and compare with the case of hydrogen only reionization.

4.1 Source Model

The numerical methods used in this study are quite similar to those presented in Baek et al. (2009) (hereafter Paper I) The dynamical simulations have been run with GADGET2 (Springel, 2005) and post-processed with UV continuum radiative transfer further processed with Ly- α transfer using LICORICE. The same cosmological parameters and number of particles are used and we refer the reader to Paper I for details related to the numerical method and parameters. The main improvement on the previous work is using a more realistic source model including soft X-rays. We present the source model below.

4.1.1 Star Formation Rate

Unlike in the previous work, we computed the star formation in the radiative transfer part of LICORICE. LICORICE uses the classical recipe that mimics a Schmidt law:

$$\frac{d\rho_*}{dt} = \frac{\rho_g}{t_*}, \quad (4.1)$$

where t_* is defined by :

$$t_* = t_{0*} \left(\frac{\rho}{\rho_{th}} \right). \quad (4.2)$$

We have set the parameters t_* and ρ_{th} so that the evolution of the global star fraction follows the S20 simulation ($20h^{-1}$ Mpc) in Paper I. All simulations in this study have a $100h^{-1}$ Mpc box size. Following the above equations, a gas particle whose local density exceeds the threshold ($\rho > 5\rho_{\text{ctirical}}$) increases its star fraction, f_* .

Since the first stars at the epoch of reionization are very massive, they have very short life time and their luminosity is closely related to the star formation rate. The Lyman-Werner band emission is dominated by massive, short-lived OB stars and declines rapidly once star formation comes to an end (Glover & Brand 2003). Consequently we computed the increase in the amount of star fraction, Δf_* , between two consecutive snapshots for each particle. If $\Delta f_* > 0.01$ we considered the particle as a source, and computed total luminosity emitted from mass $m_{\text{gas}}\Delta f_*$. If the particle reaches $\Delta f_* = 1$, we turn off the source.

The first source appears earlier than in an previous work, since a particle with the star fraction $\Delta f_* > 0.01$ are considered as a source. The number of particles whose star fraction $\Delta f_* < 0.01$ is not significant except the end of simulations.

4.1.2 Luminosity and SED of the stellar sources

All baryon particles have the same mass of $9.5 \times 10^8 M_\odot$. The amount of young stars in a particle, $m_{\text{gas}}\Delta f_*$, corresponds to a star cluster of a dwarf galaxy so an IMF should be taken into account. We choose a Salpeter IMF, with masses in the range $1.6M_\odot - 120M_\odot$. Then we compute the total luminosity and the spectral energy distribution (SED) for a star particle. We interpolated linearly the data in Meynet & Maeder (2005); Hansen & Kawaler (1994) to obtain the total luminosity, effective temperature and life time of massive star of low metallicity as a function of star mass (see Tab. 4.1).

Then we obtained the averaged value of total luminosity, the SED and the life time of the source by integrating over the different bins of mass. The total luminosity and the life time depending on the spectral band are given in tab. 4.2 and the resulting SED is plotted in Fig. 4.1.

mass [M_{\odot}]	$\log(L/L_{M_{\odot}})$	$\log(T_{eff})$	$t_{life}[Myr]$
120	6.3	4.7	3
60	5.8	4.6	4.5
40	5.6	4.5	6
30	5.2	4.5	7
20	4.8	4.45	10
15	4.65	4.4	14
12	4.2	4.37	20
9	3.8	4.3	34
5.9	2.92	4.18	120
2.9	1.73	3.97	700
1.6	0.81	3.85	3000

Table 4.1: Physical properties of low metallicity ($Z = 0.004Z_{\odot}$) MS stars

Energy band	$10.24 \text{ eV} \leq E < 13.6 \text{ eV}$	$E \geq 13.6 \text{ eV}$
Luminosity[erg/s]	6.32×10^{44}	2.14×10^{45}
Life time[Myr]	20.36	8.03

Table 4.2: Averaged luminosities and life times of our source model depending on the energy band.

4.1.3 X-ray source model

X-rays can have a significant effect on the 21 cm brightness temperature. The X-ray photons, having a smaller ionizing cross-section, can penetrate neutral hydrogen further than UV photons and heat the gas above the cosmic microwave background temperature. This X-ray heating effect on the IGM is often assumed to be homogeneous because of X-rays' long mean free path. In reality, the X-ray flux is stronger around the sources and the inhomogeneous X-ray flux can bring on extra fluctuations for the 21 cm brightness temperature. We choose QSO type sources as the main X-ray sources and use ray-tracing for X-ray photons. This enables us to investigate the effect of inhomogeneous X-ray heating on the signal.

Luminosity

First, we need to determine the total luminosity and the number density of X-ray sources. We simply divided the total luminosity, L_{tot} , of the source particle into a stellar contribution, L_{star} , and a QSO contribution, L_{QSO} . We follow Glover & Brand (2003) to determine the fraction L_{QSO} of L_{tot} . Therefore, L_{QSO} depends on the star formation rate, since L_{tot} itself is proportional to the increment of the star fraction between two snapshots of the dynamic simulation.

One reason for this approach is that X-ray binaries and supernova remnants con-

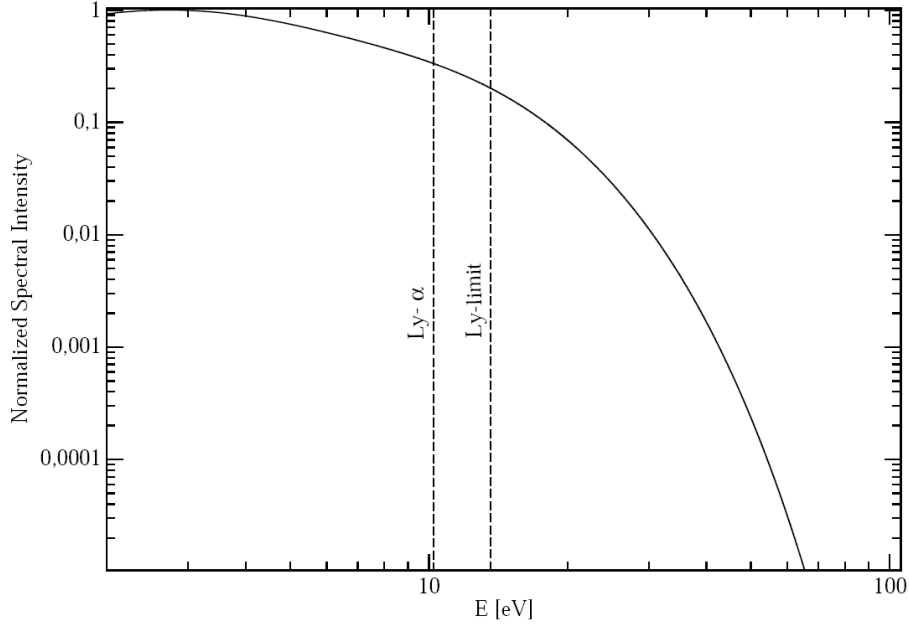


Figure 4.1: Normalized spectral intensity of our source model.

tribute to X-ray sources as well as quasars and they are strongly related to the star formation rate. Following the work of Glover & Brand (2003), we took 0.1% of L_{tot} as the fiducial X-ray source luminosity, L_{QSO} . However, considering that they assumed a simple and empirically motivated model we have also run simulations with different values L_{QSO} , 1% and 10% of L_{tot} . The quasar luminosity fraction less than 0.1% is not of interest to us, since its heating effect is negligible.

Soft X-rays

First, we have to choose the photon energy range since hard X-ray photons have a huge mean free path which costs a lot for ray-tracing computation. The comoving mean free path of an X-ray with energy E is (Furlanetto, 2006)

$$\lambda_X = 4.9 \bar{x}_{\text{HI}}^{-1/3} \left(\frac{1+z}{15} \right)^{-2} \left(\frac{E}{300 \text{eV}} \right)^3 \text{ Mpc}. \quad (4.3)$$

All photons with energy below $E \sim 2[(1+z)/15]^{1/2} \bar{x}_{\text{HI}}^{-1/3} \text{ keV}$ are absorbed within a Hubble length and the E^{-3} dependence of the cross-section means that heating is dominated by soft X-rays, which do fluctuate on small scales (Furlanetto 2006). Therefore, we used an energy range for X-ray photons from 0.1keV to 2keV. The photons with energy higher than 2keV have a large mean free path so that their propagating time is comparable to the simulation time. They are not absorbed until

the end of simulation at $z \approx 6$. Furthermore, the fraction of ionizing photon over $2keV$ is small. 99% percent of L_{QSO} is included in the energy band from $0.1keV$ to $2keV$, which is the soft X-ray range.

QSO spectral Index

We compute the specific luminosity within the band $0.1keV$ to $2keV$ using a power-law with index α . We assume a power law spectrum form

$$L_\nu = k \left(\frac{\nu}{\nu_0} \right)^{-\alpha}, \quad (4.4)$$

where k is a normalization constant so that

$$L_{QSO} = \int_{\nu_1}^{\nu_2} L_\nu d\nu, \quad (4.5)$$

where $h\nu_1 = 0.1 keV$ and $h\nu_2 = 2 keV$. The amount of X-ray heating is sensitive to the spectrum of QSOs but there exists a large observational uncertainty in the mean and distribution of α . The power index α has been measured by Telfer et al. (2002) to be ≈ 1.6 , but with a large Gaussian standard deviation of 0.86. Recently Scott et al. (2004) derived an average value of $\alpha = 0.6$ from a sample of FUSE and HST quasars. We choose $\alpha = 1.6$ as our fiducial case, and used $\alpha = 0.6$ for comparison.

Secondary Ionization

X-rays deposit energy in the IGM by photoionization through three channels. The primary electron from hydrogen and helium atom distributes its energy by 1) collisional ionization, producing secondary electrons, 2) collisional excitation of H and He and 3) Coulomb collision with thermal electrons. We used the fitting formula in Shull & van Steenberg (1985) to compute the fraction of secondary ionization and heating. (see Fig. 4.2)

4.2 Simulations

4.2.1 Initial condition

The dynamic simulations have been run using a modified version of the parallel TreeSPH (Springel 2005). All initial conditions are equal to the S100 simulation of Paper I. They have the linear box size of $100 Mpc h^{-1}$ and the same mass resolution. The cosmological parameters are those of the concordance Λ CDM flat universe based on WMAP3 data (Spergel et al., 2007). There is only one difference between

$$\text{Form 1: } y = C[1 - (1 - x^a)^b],$$

$$\text{Form 2: } y = C(1 - x^a)^b.$$

FITTING COEFFICIENTS^a

Form	Parameter	C	a	b
1.....	Heat/ E_0	0.9971	0.2663	1.3163
2.....	ϕ (H I) (I/E_0)	0.3908	0.4092	1.7592
2.....	ϕ (He I) (I/E_0)	0.0554	0.4614	1.6660
2.....	E (H I) (I/E_0)	0.4766	0.2735	1.5221
2.....	E (He I) (I/E_0)	0.0246	0.4049	1.6594

^a Coefficients for analytic fits (eqs. [1] and [2]) to heat, secondary ionizations ϕ , and secondary excitations E of H I or He I. Here, I is the appropriate excitation or ionization energy: 10.2 or 13.6 eV for H I; 19.95 or 24.58 eV for He I. These formulae are only accurate for $E_0 > 100$ eV (see Fig. 3).

Figure 4.2: Fittig formula and coefficients from Shull & van Steenberg (1985). x is ionization fraction. Form 1 is for the fraction of energy (E_0) deposited as heat, Form 2 is for the fractional energies going into H and He excitation or ionization.

the S100 simulation of Paper I and this work. We do not use the source formation provided by Gadget2, but re-compute it with LICORICE during the radiative transfer process. We compute the star formation rate using the density difference between two consecutive snapshots.

We post-processed radiative transfer simulations for 7 different models. The different parameters for each model are listed on table 4.3. Our first case, S1 simulation, assumes only stellar type sources. S2 and S3 simulations both contain helium while the other simulations have been run with only hydrogen. S2 contains only the stellar type sources whereas S3 includes quasar type sources. Both the fourth (S4) and fifth (S5) cases use 0.1% of the total luminosity for the quasar type sources, but they use different quasar spectral index : $\alpha = 1.6$ and $\alpha = 0.6$ (Eq.1.8). The S6 and S7 cases use 1% and 10% of the total luminosity for the quasar type sources, both with $\alpha = 1.6$.

4.2.2 Global history of reionization

The mass weighted ($\langle x_H \rangle_{mass}$) and volume weighted ($\langle x_H \rangle_{vol}$) average ionization fractions of S1 and S2 are shown in Fig. 4.3. The global evolution of the ionization fraction depends mostly on the content (He or H only) of the IGM rather than the type of sources. All simulations with only hydrogen (S4, S5, S6 and S7) are very close to the evolution of S1, and S3 (Helium) is very similar to the case of S2.

Model	Helium	L_{star}	L_{QSO}	spectral index
S1	No	100 %	0 %	-
S2	Yes	100 %	0 %	-
S3	Yes	99.9 %	0.1 %	$\alpha=1.6$
S4	No	99.9 %	0.1 %	$\alpha=1.6$
S5	No	99.9 %	0.1 %	$\alpha=0.6$
S6	No	99 %	1 %	$\alpha=1.6$
S7	No	90 %	10 %	$\alpha=1.6$

Table 4.3: Simulation parameters and different models

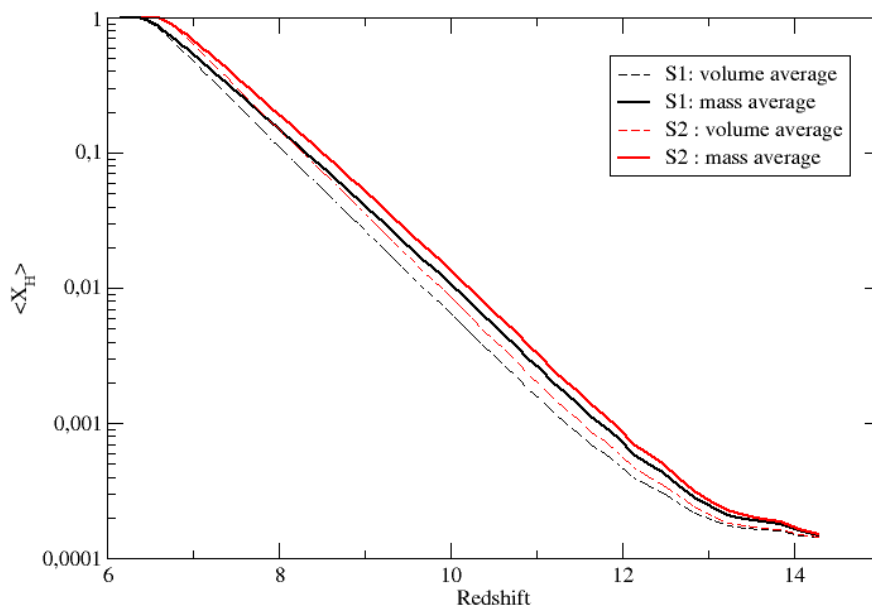


Figure 4.3: The mass weighted and volume weighted averaged ionization fraction.

The first source appears at $z \approx 14$ which is earlier than in the S100 simulation of Paper I, since we consider a particle as a source if the new star fraction $\Delta f_* > 0.01$. S1 reaches the end of reionization a little bit earlier ($\Delta z \approx 0.25$) than S2. The number of emitted photons are equal for both simulations, but S2 has less absorbers than S1 (about 80%) since S2 contains Helium which occupies 25% of the IGM in mass. Even if the helium atoms can absorb two photons, almost all the helium atoms of IGM remain as He^+ until the end of reionization $z \approx 6$, because the photoionization potential for He^+ is 54.4eV, which is much higher than H^+ (13.6 eV) and He^0 (24.6 eV). Thus simulations with helium shows fast evolution of the HII region, because including Helium keeping the same mass density for the IGM decreases the number density and the absorption probability only depends on the number density of the absorbers.

Maps of the ionization fraction of hydrogen and kinetic temperature of gas of all

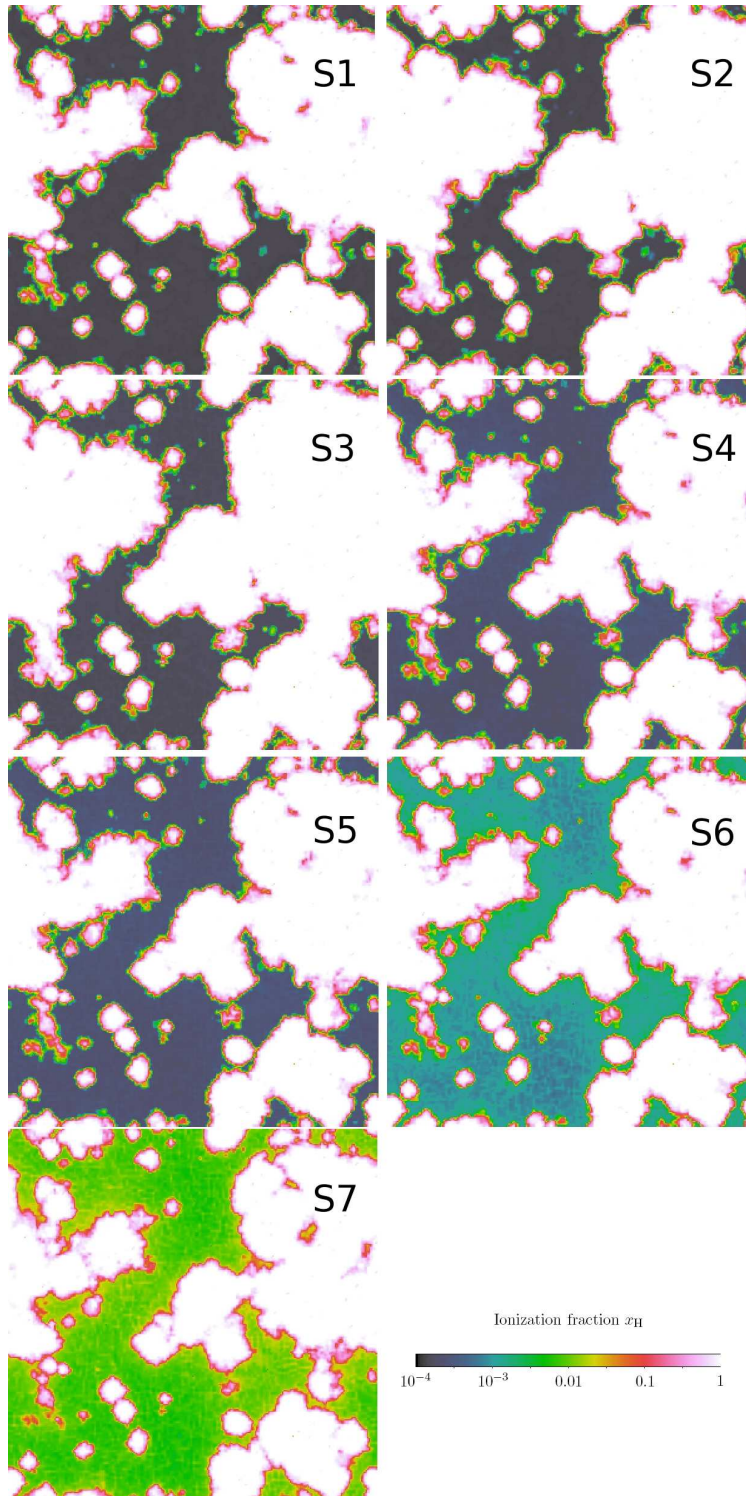


Figure 4.4: Maps of the ionization fraction for the seven simulations when $\langle x_{\text{H}} \rangle_{\text{mass}}$ of S1 simulation is equal to 0.5 ($z = 7.00$). The color is presented in logarithmic scale and the slice thickness is 1.2 comoving Mpc.

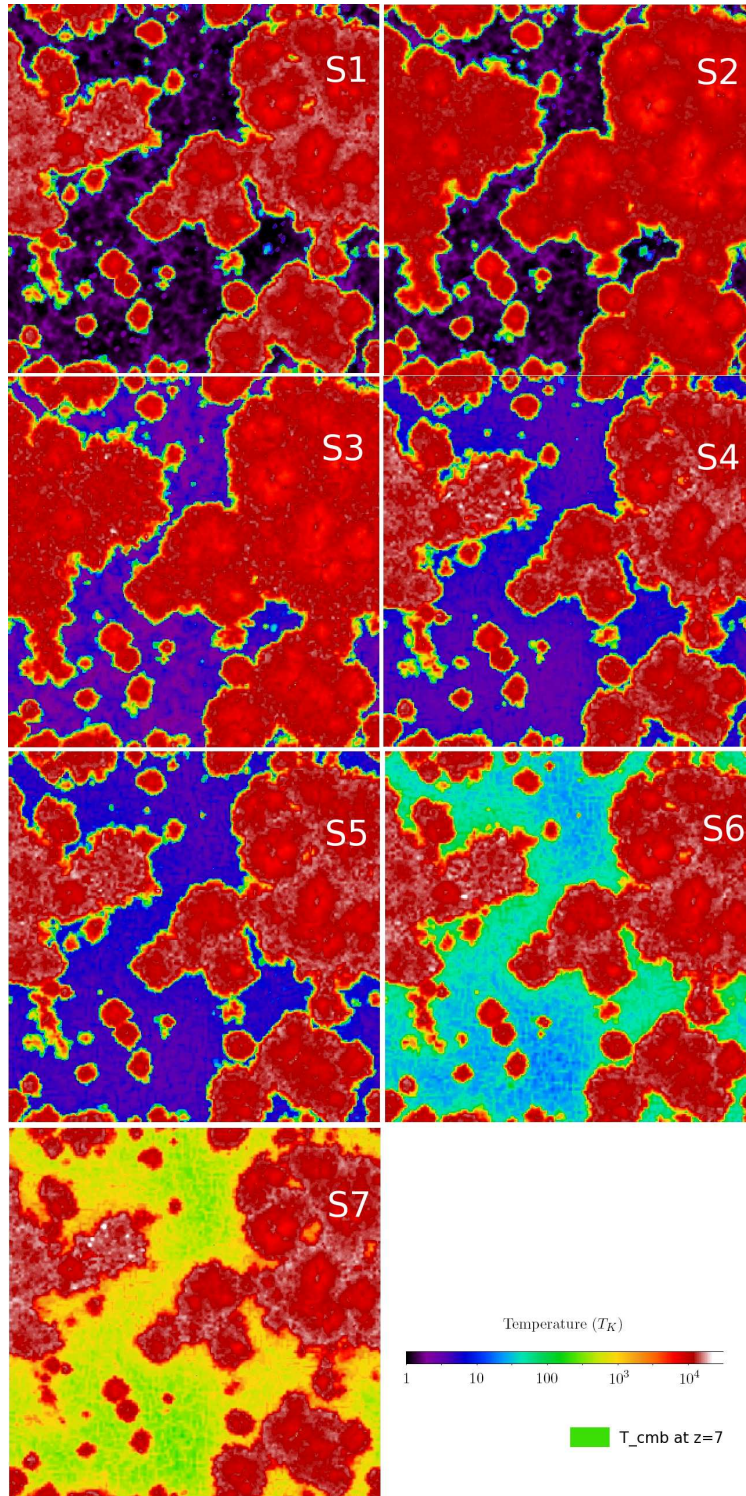


Figure 4.5: Maps of the kinetic temperature for the seven simulations when $\langle x_H \rangle_{mass}$ of S1 simulation is equal to 0.5 ($z = 7.00$). The color is presented in logarithmic scale and the slice thickness is 1.2 comoving Mpc.

7 models are presented in Fig. 4.4 and Fig. 4.5. All maps are presented for a slice thickness of $1.2 \text{ comoving } h^{-1}\text{Mpc}$ at a redshift when the mass weighted ionization fraction of S1 (S2) is 0.5 (0.6).

The global morphology of reionization is more similar to the S20 case of Paper I than S100. In order to calibrate the source formation of S100 on S20, S100 removed the threshold of density. It caused some degree of source formation in voids. The source formation of this work is more realistic, sources are highly clustered and the distribution of the HII bubbles is more inhomogeneous than in the S100 simulation and show coherent structure on scales up to $50 h^{-1} \text{ Mpc}$.

4.3 Helium reionization

We have run two simulations with Helium, S2 and S3. S2 has only stellar type sources, while S3 uses 0.1% of L_{total} for the quasar type sources. The cross-sections for ionization (H, He, He^+) are calculated using the fits of Verner et al. (1996).

The main noticeable result of models using Helium is the fast evolution of the HII region with respect to hydrogen reionization. The initial ionization fraction of hydrogen is given by RECFAST (Seager et al., 1999) as $x_{\text{H}^+}=1.5 \times 10^{-4}$ while x_{He^+} and $x_{\text{He}^{++}}$ are set to zero.

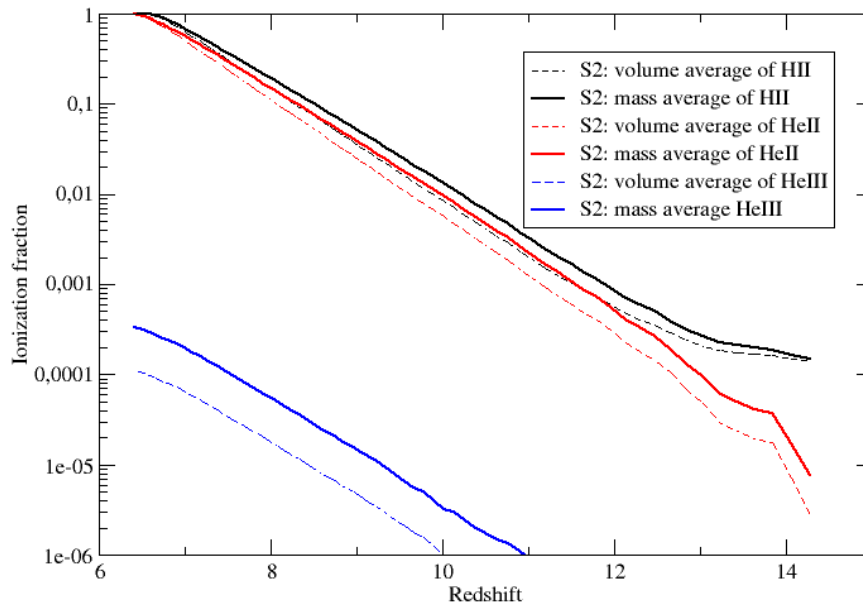


Figure 4.6: The volume weighted and mass weighted averaged ionization fraction of HII, HeII and HeIII.

Fig. 4.6 shows the evolution of the averaged ionization fraction. The evolution of $\langle x_{\text{He}^+} \rangle$ follows $\langle x_{\text{H}^+} \rangle$ with decreasing gaps between them and reaches the

end of reionization a little bit later than $\langle x_{\text{H}^+} \rangle$. The ionizing potential of neutral helium (24.6 eV) is 2 times larger than hydrogen (13.6 eV), and the emitted number of photons above 24.6 eV are less than the photons above 13.6 eV (see Fig. 4.1). Therefore helium reionized later than hydrogen.

However $\langle x_{\text{He}^{++}} \rangle$ remains almost negligible during the whole simulation time. In all three species, the volume averaged value is smaller than the mass averaged value, since highly ionized regions of identical mass, close to the sources, are denser and occupy a smaller volume. The difference of these two averaged values is largest for the $\langle x_{\text{He}^{++}} \rangle$ case. Since a small fraction of $\langle x_{\text{He}^{++}} \rangle$ appears only around the sources which are embedded in dense regions. (see also the Fig. 4.7)

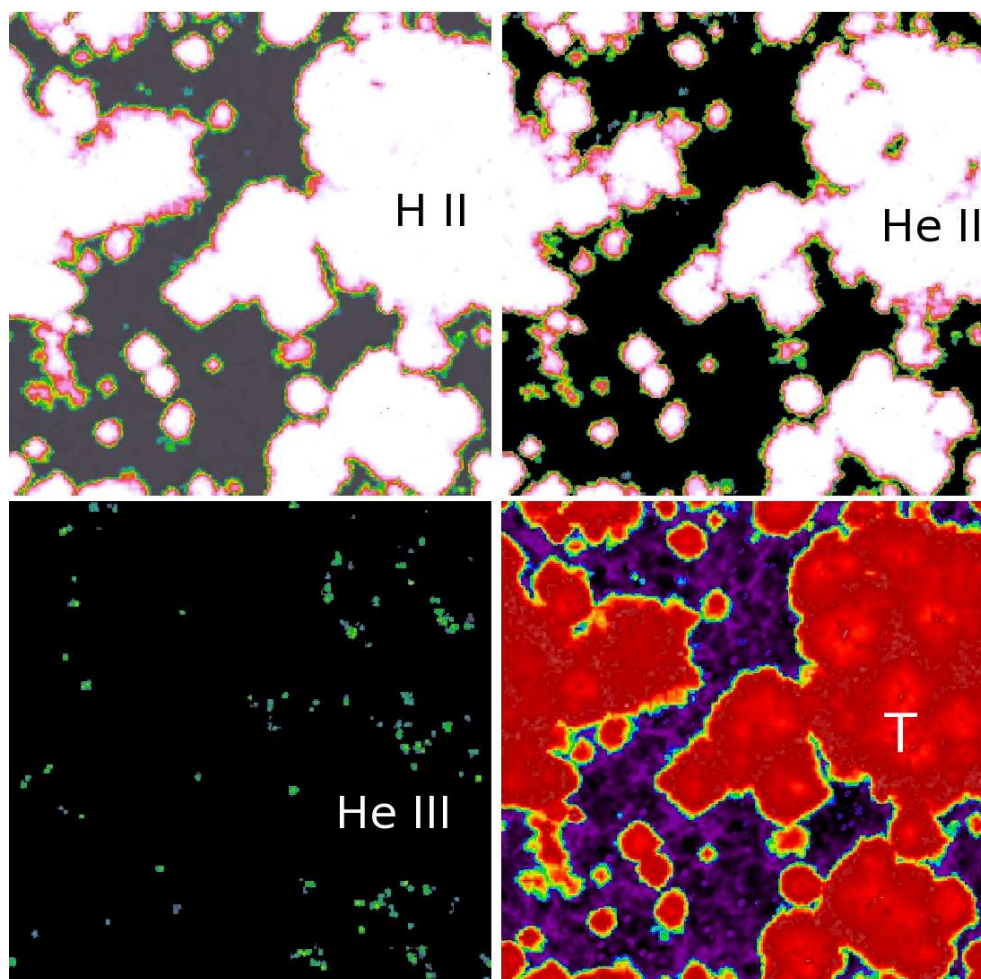


Figure 4.7: Maps of the ionization fraction of $\langle x_{\text{H}^+} \rangle$, $\langle x_{\text{H}^+} \rangle$, $\langle x_{\text{He}^{++}} \rangle$ and the kinetic temperature T_K when the $\langle x_{\text{H}} \rangle$ of S2 is equal to 0.5 (at redshift $z = 7.13$). All color scales are the same as in Fig. 4.4 and Fig. 4.5

The second noticeable result of Helium reionization is the slightly lower kinetic temperature of the ionized region. We can see this difference in Fig. 4.5 by comparing

(S1,S2) or (S3,S4). First, it can be explained by that higher ionization potential of helium ($h\nu_{\text{He}} \approx 24.6\text{eV}$; $h\nu_{\text{He}^+} \approx 54.4\text{ eV}$) than that of hydrogen ($h\nu_{\text{H}} \approx 13.6\text{ eV}$). He and He^+ need more energy to be ionized and only the remaining energy is converted into the gas heating. In addition, the photoionizing cross section of He is $\sigma_{\text{He}} \propto \nu^{-2}$ ($h\nu \geq 24.6\text{ eV}$) while that of hydrogen is $\sigma_{\text{H}} \propto \nu^{-3}$ ($h\nu \geq 13.6\text{ eV}$). Thus the helium prefers energetic photons for being photoionized, leaving less energy for heating.

On the other hand, we averaged the gas temperature of S2, S3 and S4 in the void where the ionization fraction is $x_{\text{H}} < 0.001$ at $z = 7.00$ (maps shown in Fig. 4.5). The averaged temperature in the void is 1.72 K, 3.21 K and 4.06 K for S2,S3 and S4. We can explain the higher temperature of S3 with respect to S2 as the effect of X-ray heating in the void. Both S3 and S4 use X-rays, and we can explain the higher temperature of S4 (only hydrogen) compared to S3 (with helium) by the larger cross section of helium ionization for energetic photons.

4.4 QSO index

As we discussed in the above section 4.1, there is the large observational uncertainty in the mean and distribution of quasar spectral index α . Our fiducial model assumes $\alpha = 1.6$. Fig. 4.8 shows the spectral intensity of the different quasar spectral index.

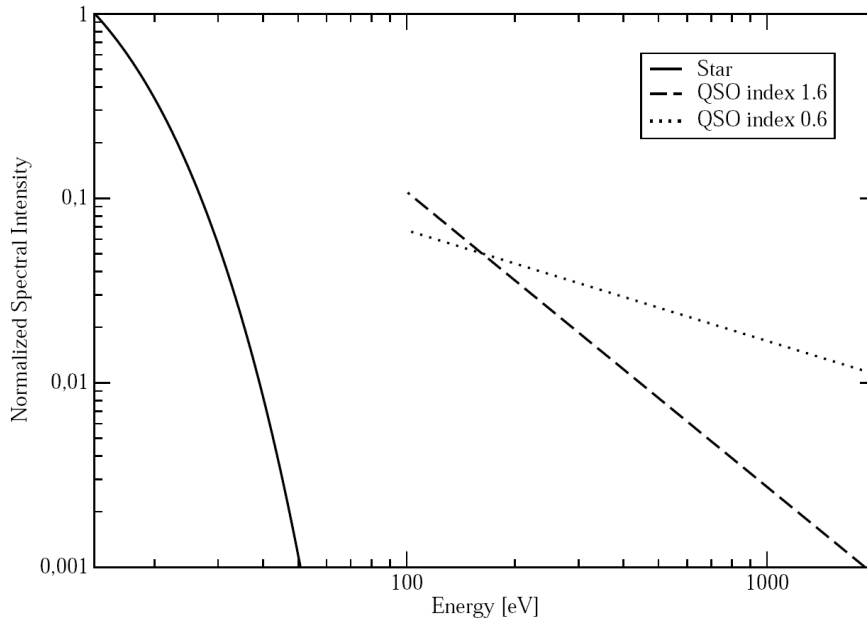


Figure 4.8: Normalized spectral intensity of stellar and quasar type sources. Integrated energy of quasar type sources are 0.1% of that of stellar type source.

As shown in Fig. 4.4, S4 and S5 shows almost the same ionization fraction. S4 uses a QSO index of $\alpha = 1.6$ and S5 uses $\alpha = 0.6$. Since the total emitted energy is fixed, the X-ray photons of S5 are more energetic and S5 has a smaller number of photons. However, the difference in the number of photons is negligible and the ionization fraction as well as the propagation of the ionization fronts do not show noticeable differences.

On the other hand, the gas temperature for S5 in the voids is slightly higher than for S4 (see Fig. 4.5). S5 has more energetic X-ray photons which can penetrate the ionization fronts and heat the neutral voids. However, the temperature in the neutral voids of S5 is not always higher than S4. We computed the evolution of the gas temperature in the void for two cases in Fig. 4.9. At each snapshot, we made the list of particles whose ionization fraction is simultaneously less than 0.01 in both cases, and averaged for each simulation.

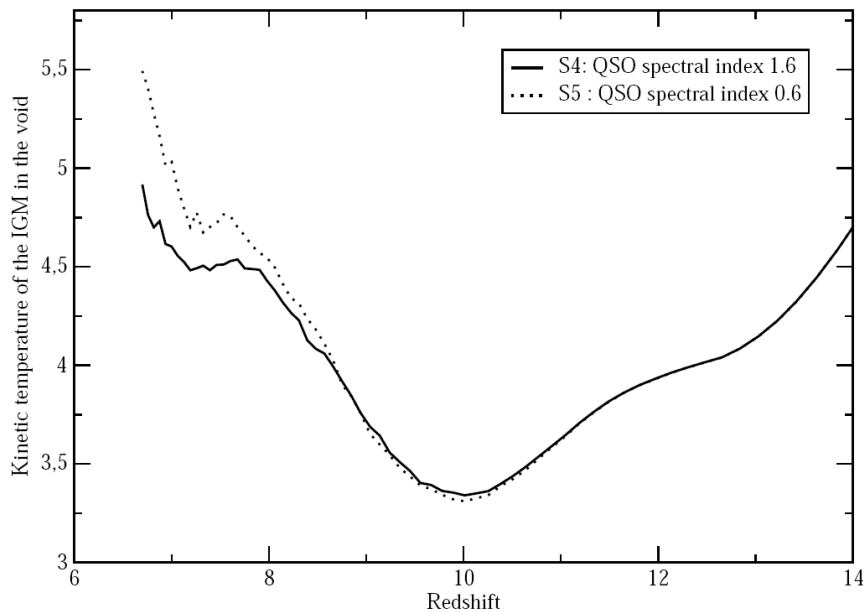


Figure 4.9: The evolution of the gas temperature in the void.

From the beginning of the reionization $z \approx 14$, the temperature of S4 is slightly higher than S5 until $z \approx 9$. The temperature curves cross around $z \approx 9$, S5 begins to dominate S4 with an increasing gap between them.

This can be explained by the long mean free path of energetic photons. In both cases, quasar type sources emit the same energy, but S4 emits softer photons while S5 emits harder photons. Softer photons are absorbed quickly while harder photons are not absorbed quickly because of their longer mean free path. At the beginning, S4 absorbs more photons than S5, and that is why its temperature is higher than S5.

During the simulation time, harder photons are redshifted along the long path. Around $z \approx 9$, harder photons emitted at the beginning of the simulation start to be absorbed and heat the gas.

Therefore, we can conclude that using the harder quasar spectrum index increases the gas temperature in the void but it takes time. The amount of the additional heating is not large.

4.5 Luminosity of the QSO

The main goal of this study is to investigate the effect of X-ray heating on the 21-cm signal. We have run several simulations varying the luminosity of X-rays, L_{QSO} , for a fixed total luminosity. We find that the global evolution of ionization fraction and HII regions are quite similar for all simulations, but the gas temperature in the void varies a lot depending on the L_{QSO} . In order to follow the evolution of the gas temperature of neutral hydrogen in the void, we find the particles whose ionization fraction are simultaneously less than 0.01 for S1, S4, S5, S6 and S7. We plotted the evolution against the CMB temperature in Fig. 4.10.

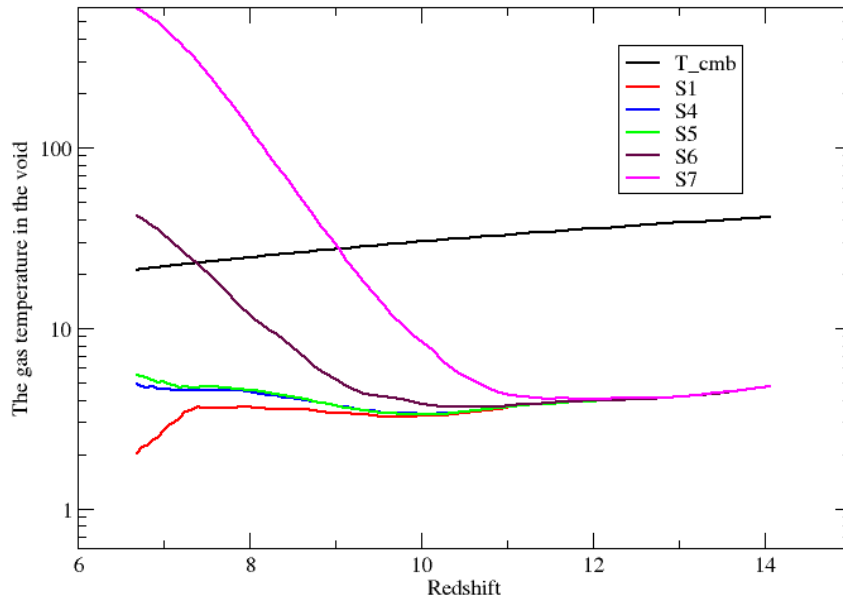


Figure 4.10: The evolution of gas temperature in the void.

S4 and S5, which use 0.1% of the total energy for L_{QSO} show similar curves. The temperature of all simulations in Fig. 4.10 decreases because of the adiabatic expansion until $z \approx 12$. After, S7 starts to increase first. Our fiducial model was S4, using 0.1% of the total energy for L_{QSO} , but the temperature in the voids of S4

is always under the CMB temperature. Even for S7, the gas temperature of neutral hydrogen in the void is still under the CMB temperature until $z \approx 9$. This means that the X-ray heating needs time to heat the IGM above CMB temperature, and the 21 cm signal can be observed in absorption during the early epoch of reionization.

4.6 The 21-cm signal

We have run three Lyman- α simulations for S1, S4 and S7 as a further post-treatment to obtain the 21-cm signal. With the local Lyman- α flux obtained in the simulations, we recompute the kinetic temperature in order to include Lyman- α heating. We implement Lyman-alpha heating only for the particles whose ionization fraction is less than 10^{-3} , otherwise photo heating dominates over the Lyman- α heating.

We use the following formula from Furlanetto & Pritchard (2006) for the Lyman-alpha heating :

$$\frac{dT_k}{dt}|_{\text{Lyman}} = \frac{0.8}{T_k^{1/3}} \frac{x_\alpha}{S_\alpha} H(z) \quad \text{with } S_\alpha \sim \left(1 - \frac{0.7}{\sqrt{T_k}}\right). \quad (4.6)$$

We suppose that the thermal evolution of the particles in the coolest regions ($x_H < 10^{-3}$) depends only on the adiabatic expansion, Lyman- α heating and X-ray heating (for S4 and S7). Radiative cooling remains negligible in this region. So the variation of temperature between two snapshots becomes,

$$\frac{dT_k}{dt} = \Delta T_{\text{Lyman}} + \Delta T_{\text{adiabatic}} + \Delta T_{\text{X-ray}}. \quad (4.7)$$

$\Delta T_{\text{X-ray}}$ is estimated by

$$\Delta T_{\text{X-ray}} = \Delta T_{\text{RT}} - \Delta T'_{\text{adiabatic}}, \quad (4.8)$$

where ΔT_{RT} is the temperature difference between two snapshot from the UV radiative transfer simulation, and $\Delta T'_{\text{adiabatic}}$ is due to adiabatic expansion in the dynamical simulation.

The S20 and S100 simulations in Paper I show a moderate increase of the temperature due to Lyman heating, a few K. However, the new source model in this work has a stronger luminosity in the Lyman band ($\text{Ly-}\alpha < E < \text{Ly-limit}$) than in the previous work (compare the spectral intensity in Fig.3 of PaperI and in Fig. 4.1). The ratio of the integrated luminosity in the Lyman band with respect to the ionizing band, $L_{\text{Lyman}}/L_{\text{ion}}$, is ~ 10 times larger than the previous one, since we consider now the finite life time of stars, which results in strong Lyman heating for a normalized ionizing flux. In addition, Lyman- α flux is overestimated in this work, since we com-

pressed the total energy ($10.24\text{eV} \leq E < 13.6\text{eV}$) emitted during the averaged life time (20.36 Myr, see Tab. 4.2) into the time between two snapshots (6-10 Myr).

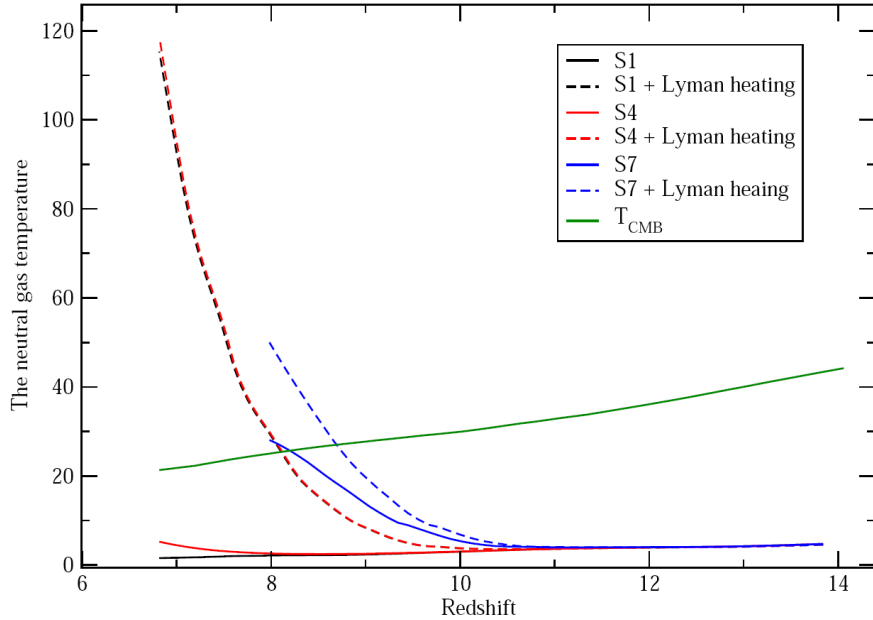


Figure 4.11: The evolution of neutral gas temperature ($x_H < 10^{-3}$).

Fig. 4.11 shows the evolution of the neutral gas temperature with and without Ly- α heating. S7 does not have a sufficient sample of particles with $x_H < 10^{-3}$ at $z < 8$, so we stop the curve. Lyman- α heating is negligible until redshift $z \sim 10.5$, but then it increases rapidly above the CMB temperature. At $z \sim 7$, where the averaged ionization fraction is 0.5, the Lyman- α heating dominates over the X-ray heating which makes the X-ray effects negligible. The differential brightness temperature maps are shown in Fig. 4.12. Maps in the left column present the signal when $\langle x_\alpha \rangle_{mass}=1$, which we call the Wouthuysen-Field coupling redshift (hereafter WFCR), and maps in the right column present the signal when $\langle x_H \rangle_{mass}=0.5$, which we call the half reionization redshift (HRR). At the WFCR ($z \sim 11.64$), neither X-ray heating nor Lyman- α heating are inefficient, and all maps show a similar pattern. However, if we compare these maps (S1 and S4) at WFCR with the signal of Paper I (Fig.12 of Paper I), we see a stronger absorption signal around HII bubbles. Since the ratio of the luminosity, L_{Lyman}/L_{ion} , is much larger than in the previous work, we find larger halos of Lyman- α coupled regions, which we call Lyman- α halos. The spin temperature inside the Lyman- α halo is highly coupled to the gas temperature. If the HII bubble is smaller than the Lyman- α halo, the region outside of HII bubble but inside Lyman- α halo have a signal in strong absorption, where the spin temperature is very low. On the other hand, the signal of S7 at WFCR does not show such a strong

absorption around the sources, since X-ray heating already increased the gas temperature in these regions. Thus it may be possible to constrain the spectral property of the sources (L_{Lyman}/L_{ion} and L_{X-rays}/L_{ion}) using the average radial profile of δT_b around the sources.

Maps in the right column of Fig. 4.12 show the differential brightness temperature at the HRR. At this redshift, Lyman- α heating is so strong that the spin temperature is higher than the CMB temperature. The high spin temperature begin to saturate the term $1 - \frac{T_{cmb}}{T_s}$ of Eq.(3.7), and turns the 21-cm signal into emission. Lyman- α heating dominates over the X-ray heating, so the X-ray effect on the signal (S4) is not noticeable with respect to S1, which does not have X-ray sources. However, the X-ray luminosity for S7 is 1000 times larger than for S4, and it heats the neutral gas even more. The X-ray heating of S7 increases the value of the term $1 - \frac{T_{cmb}}{T_s}$ by 20% with respect to S4, so it amplifies the intensity of the emission.

We averaged the differential brightness signal over the simulation box and present the result as a function of redshift in Fig. 4.13. S1 and S4 have the maximum intensity in absorption when the averaged ionization fraction is ~ 0.01 at $z \sim 10$. The maximum intensity ($|\delta T_b|$) and the averaged ionization fraction at the corresponding redshift is coherent with the S100 simulation of Paper I. At this redshift, Lyman- α heating is still negligible. Later, Lyman- α heating becomes much more important than the X-ray heating. Even with the strong X-ray and the Lyman- α heating of S7, the averaged signal still shows a strong absorption down to ~ -150 mK.

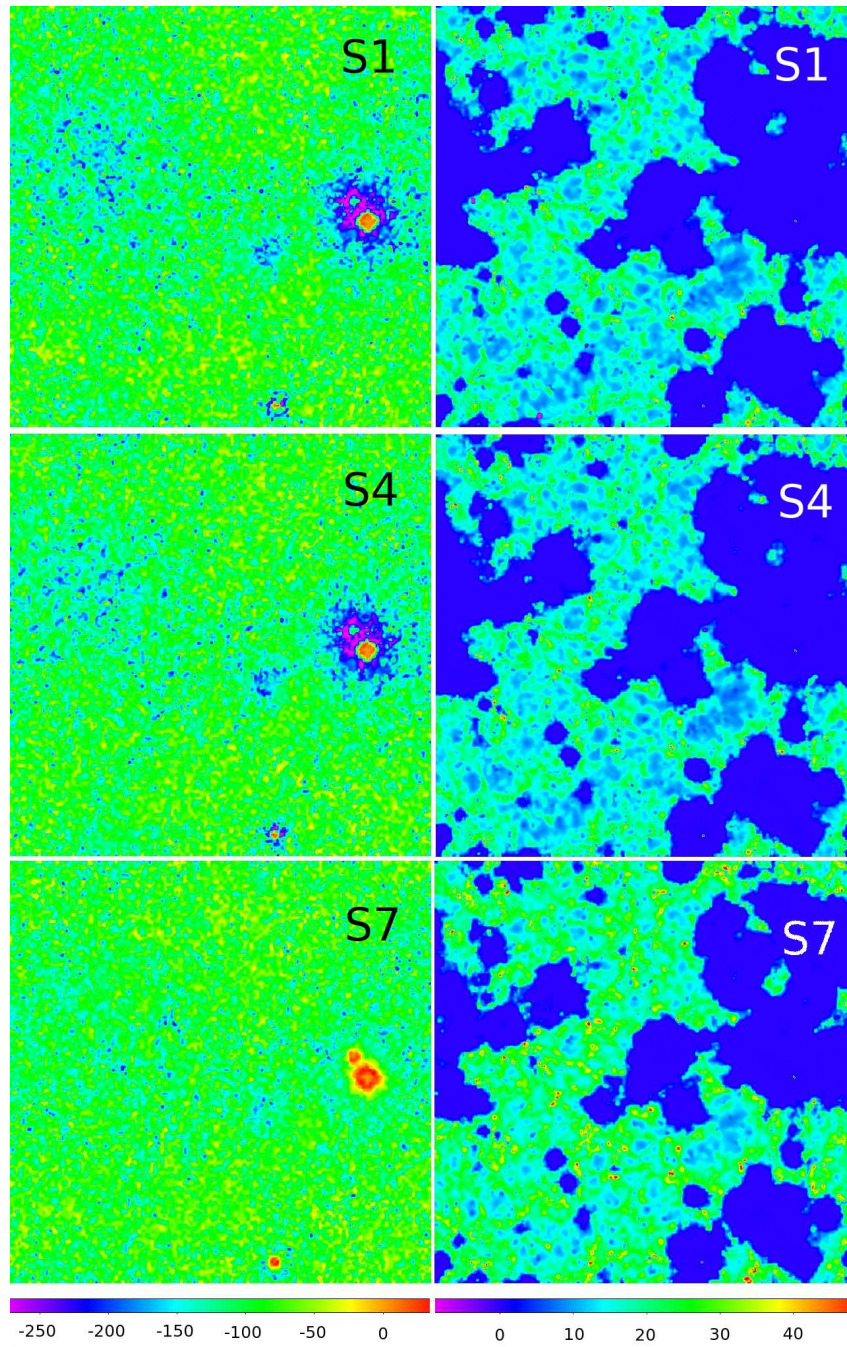


Figure 4.12: Left column : Maps of the differential brightness temperature when $\langle x_\alpha \rangle = 1$ ($z = 11.64$). Right column : Maps of the differential brightness temperature when $\langle x_H \rangle = 0.5$ ($z = 7.00$). The color is presented in linear scale and the slice thickness is 2 comoving Mpc.

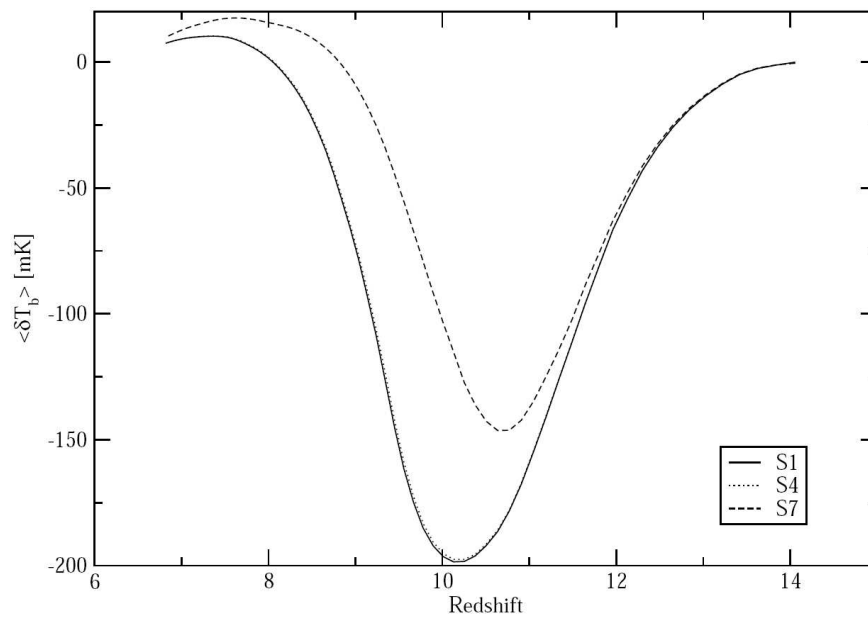


Figure 4.13: The evolution of the averaged 21-cm signal.

Chapter 5

Galaxy formation with LICORICE

The formation and evolution of galaxies are very complex processes. Among others, the thermal evolution of the gas is important for structure formation. Cooling and heating of the IGM lead to the condensation of gas in the dark matter potential wells where it forms stars and galactic disks. Including all these physical processes self-consistently in the simulations is very expensive in terms of computational costs and memory, so they are usually treated with semi-analytical methods.

We intend to model the formation and evolution of galaxies in a cosmological context through hydrodynamic radiative transfer simulations using LICORICE. Our aim in this work is to evaluate the exact state of the ionization fraction and temperature of the gas with radiative hydrodynamic simulations. Then we compare the thermal evolution of gas and structure formation for different simulations with and without radiative feedback. The work is still in progress, but I present some results and prospects here.

5.1 Initial conditions

The goal is to explore the physics of primordial galaxies ($z \sim 3$), considering radiative feedback on hydrodynamics. To resolve galactic disks, we need at least $\sim 10^4$ baryon particles. Mayer et al. (2008) argue that high mass and spatial resolution is a necessary condition in order to obtain large observable spiral disks avoiding spurious dissipation of the angular momentum. In addition, cosmological simulations of disk formation must follow the nonlinear development of structures in a large volume, of several tens of Mpc to properly compute the tidal torques that generate the angular momentum of the galaxy sized halos. However, radiative hydrodynamical simulations are very expensive in terms of CPU time and memory if they have to satisfy simultaneously the two above conditions. Therefore, we use the zooming technique with 4 layers of mass resolutions in the initial conditions as shown in Fig. 5.1. The zooming

Model	x_{H}	Computation	Radiative transfer
G1		No	No
G2		Yes	No
G3		Yes	Yes

Table 5.1: Simulation parameters and different models

technique is presented by Navarro & White (1994).

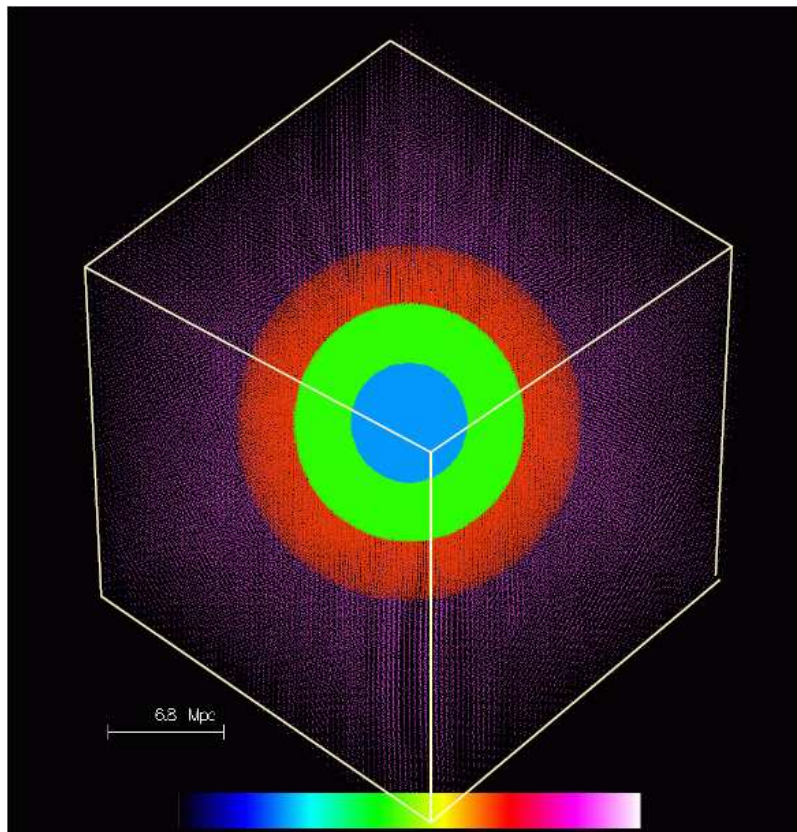


Figure 5.1: Initial particle distribution at $z \sim 42$ using the public Gific-2 code.(Bertschinger, 2001)

It results in about 2.5 millions of baryon and dark matter particles for a $20 h^{-1}$ Mpc cubic box. The magenta particles in Fig. 5.1 are distributed with 64^3 resolution, red particles with 128^3 , green particles with 256^3 and blue particles with 512^3 resolution giving the highest mass resolution of $1.8 \times 10^6 M_{\odot}$ per particle. The cosmological parameters are the same as in the previous work, using the WMAP3 data from Spergel et al. (2007). Simulations start at redshift $z \sim 40$ and continue until the first large disks are formed at about redshift $z \sim 3$. Three different simulations are listed in Tab. 5.1.

G1 assumes that all gas particles are in equilibrium state for the collisional ioniza-

tion. In the absence of UV photons, x_H depends only on the gas temperature. Then cooling rates are obtained from x_H and the temperature. G2 computes the x_H without the collisional equilibrium assumption. From the initial ionization fraction at $z \sim 40$ given by RECFAST (Seager et al., 1999), x_H is recomputed with Eq.(2.18). Usually, hydrodynamic simulations without radiative transfer, e.g. Gadget2 (Springel, 2005), assume collisional ionization equilibrium. We can test the assumption by comparing the results of G1 and G2. G3 computes the x_H and includes radiative transfer in order to study the 3D radiative feedback on galaxy formation. G3 has not been done yet, but will be finished in the near future.

5.2 Cooling rate and collisional equilibrium

Not all simulations have been done yet, and there remain some tests to do, but we find some interesting preliminary results especially for the cooling rate of primordial gas. We define the characteristic time of ionization and cooling as

$$\tau_{ion} = \frac{x_H}{\frac{dx_H}{dt}}, \quad \tau_{cool} = \frac{T}{\left(\frac{dT}{dt}\right)_{cool}}, \quad (5.1)$$

where $\left(\frac{dT}{dt}\right)_{cool}$ means the temperature variation by cooling per unit time interval. We compute the ratio between two characteristic times, $\frac{\tau_{ion}}{\tau_{coll}}$ for various pairs of (T, x_H) and present the results in Fig. 5.2. The ratio is expressed in different colors in logarithmic scale with 6 different contours. Both τ_{ion} and τ_{coll} are proportional to the density n_H , so the ratio $\frac{\tau_{ion}}{\tau_{coll}}$ is independent of the density.

As shown in Fig. 5.2, the particles which are in the relevant range of (T, x_H) have very high ratio of $\frac{\tau_{ion}}{\tau_{coll}}$. That means the ionization fraction varies slowly compared to the temperature, and is easily out of equilibrium when the temperature changes suddenly in a hydro shock for example.

Once the ionization fraction is out of equilibrium, the cooling rate increases a lot with respect to the equilibrium case.

Fig. 5.3 shows how the cooling rate changes depending on the ionization fraction. The black curve is the hydrogen atomic cooling rate of simulations with ionization fraction in equilibrium, x_{eq} and the blue curve is the same rate for the ionization fraction, $x_H = 0.9x_{H,eq}$. The blue curve is much higher than the cooling rate with metal cooling of Sutherland & Dopita (1993). Therefore, the cooling effect might be underestimated under the assumption of collisional equilibrium of x_{eq} . If we include radiative transfer, τ_{ion} can be reduced since $\frac{dx_H}{dt}$ becomes large through photoionization. It also changes the cooling rate and gas temperature. Therefore, in order to properly follow the thermal evolution of the gas, we have to include both ionization

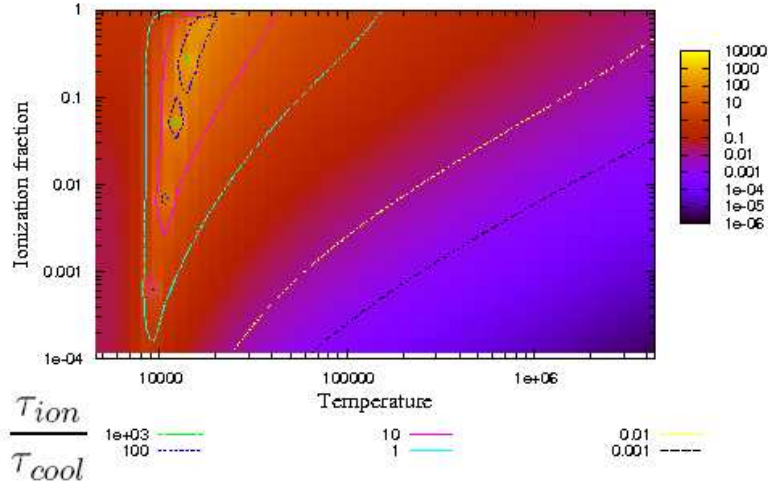


Figure 5.2: $\frac{\tau_{ion}}{\tau_{coll}}$ ratio for various pairs of (T, x_H) .

equation and radiative transfer into simulations.

5.3 Snapshot of the simulation

Fig. 5.4 is a snapshot of the G2 simulation at redshift $z = 4.8$. We see the filament structure in the center with high resolution. The resolution gets worse going outward from the center. We recenter the simulation box at the densest region of the particle distribution.

Fig. 5.5 is temperature maps of G1 and G2 at $z = 3.3$. Both maps are zoomed by 4. G2 temperature in halos or filaments is lower than G1 because of strong cooling rate with ionization fractions out of equilibrium. Once again, including photoheating could modify the picture.

5.4 Discussion and prospects

We find that the cooling rate of the gas strongly increases when out of equilibrium ionization is taken into account. The characteristic time scale of ionization is larger than that of cooling, so a large part of gas particles ($\sim 30-40\%$) are out of equilibrium for collisional ionization. This affects the thermal evolution and accretion rate of the gas.

However, the photoionization process can reduce the characteristic time scale of ionization and the cooling rate and accretion rate can be different with radiative

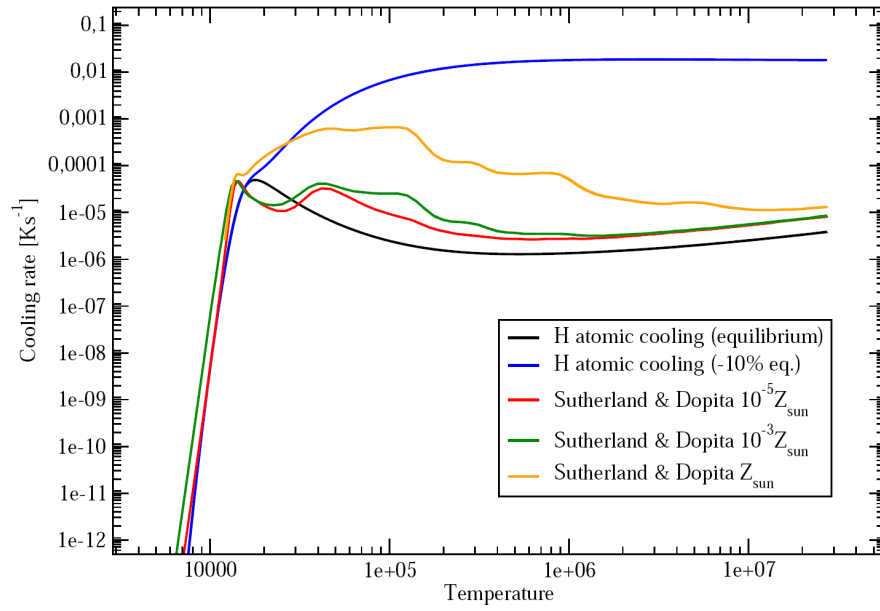


Figure 5.3: Various cooling rate.

transfer. We will compare the different thermal evolution with the G3 simulation in a near future.

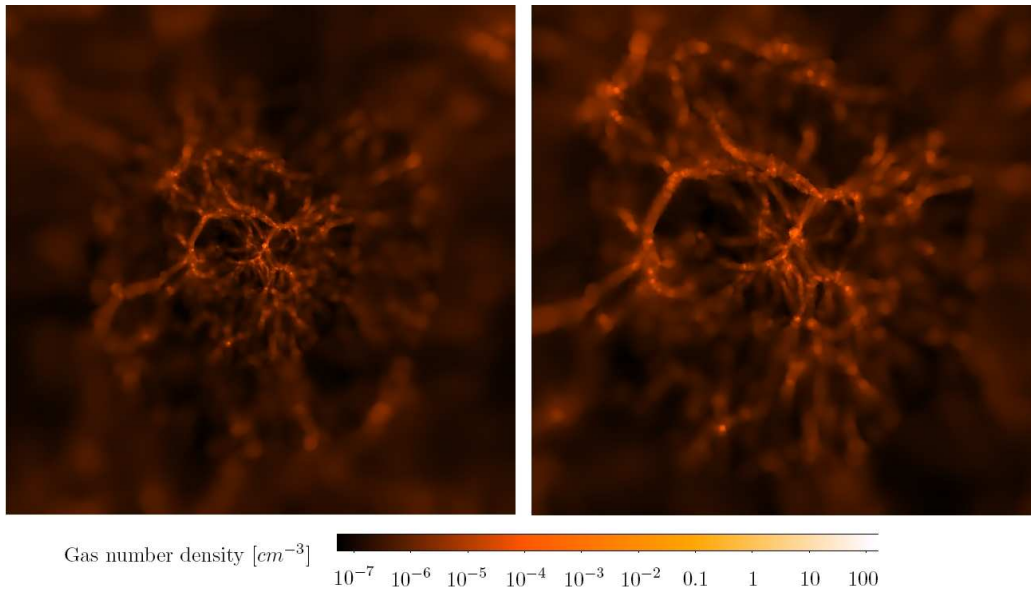


Figure 5.4: The number density (comoving) map of G2 at $z = 4.8$. The right map is zoom by 2 at the center of the left map.

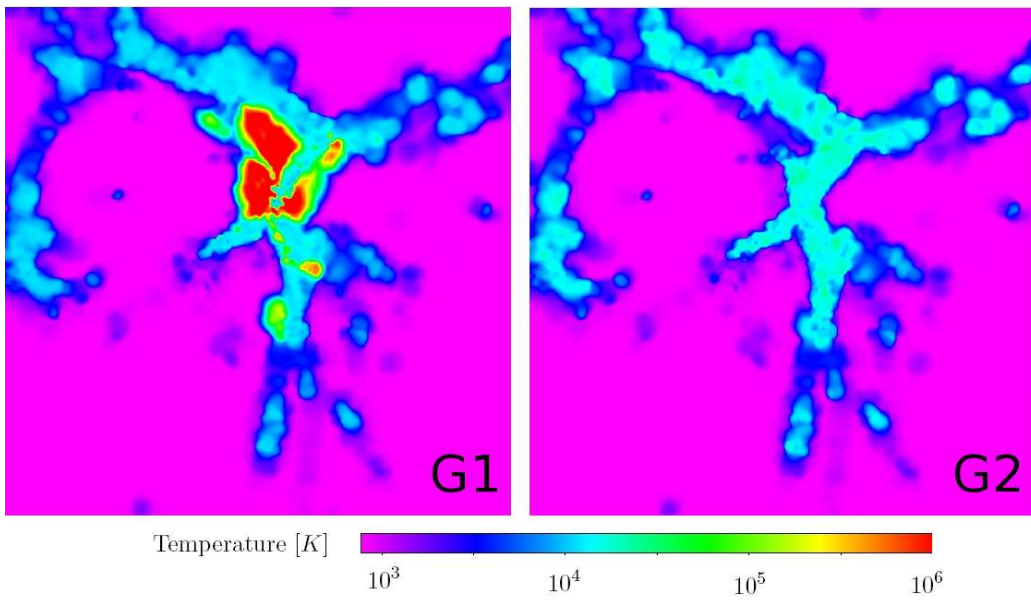


Figure 5.5: The temperature maps of G1 and G2 at $z = 3.3$.

Chapter 6

Conclusion

One of the principal tasks during my thesis was to study the epoch of reionization with numerical simulations, where radiative transfer is an essential tool. First, the work was started by developing a 3D ray-tracing module for the LICORICE code. We implemented the Monte Carlo scheme, introduced by Maselli et al. (2003), into an adaptive grid. The Monte Carlo method has the advantage of being able to handle various physical processes. The method is relevant to study the 21 cm signal from the epoch of reionization, since many physical processes contribute to the 21 cm signal. However, it is relatively slower than other methods due to the slow decrease of the statistical errors from random sampling, so good implementation and optimization are continuously required for LICORICE.

We reproduced the tests described in the Cosmological Radiative Transfer Code Comparison Project by Iliev et al. (2006a), and LICORICE shows good agreement with the other codes. Then we improved LICORICE by participating in the second comparison project (Iliev et al, in prep) for radiative hydrodynamic problems.

We have performed simulations of cosmic reionization by post-processing N-body and SPH hydrodynamic simulations. Unlike other works (e.g. Iliev et al. (2006b); Trac & Cen (2007); McQuinn et al. (2007b); Zahn et al. (2007) etc.), we did not assume a constant baryon fraction Ω_b/Ω_m for the baryon density field. The baryons are tracers of the dark matter on large linear scales and the gravitation is the main driving force of structure formation. On a small scale however, where gravitational collapse occurs and star forms, the hydrodynamic pressure becomes important and the dynamic gets even more complex with the influence of radiative cooling and heating.

In order to satisfy the two requirements of the simulations of reionization : high mass resolution and large volume simulations, we used two different box sizes. High mass resolution is required to resolve the halos down to the scale of $\sim 10^8 M_\odot$, where the majority of photoionizing sources are formed at high redshift. Moreover, high resolution is necessary to obtain realistic, non-spherical ionized regions arising from

the high photon consumption by recombination in small dense clumps. The minimum mass of resolved halos in S20 is $\sim 4 \times 10^8 M_\odot$, which allows for a convincing star formation treatment. The lower mass resolution of the S100 simulation delays the beginning of reionization because the star formation rate depends non linearly on the numerical resolution. To correct the star formation rate of the large volume simulation, we calibrate the source formation history of S100 on S20 by boosting the formation efficiency. As expected, S20 consumes about 5 times more photoionizing photons until the end of reionization. However, S100 shows HII regions on large scales ($\sim 50 h^{-1} \text{Mpc}$) which can not be obtained in the S20 simulation.

Including X-ray sources does not change a lot the evolution and global morphology of HII regions due to the weak X-ray luminosity compared to the stellar sources. However, X-rays can play an important role for the physical state of the gas in the voids. X-rays travel in neutral hydrogen with a very large mean free path, several hundreds of comoving Mpc, sometimes comparable to the Hubble length. They penetrate into the neutral gas regions in the voids and change the temperature of the gas. The S4 simulation contains X-ray sources and shows an increment of $\sim 3 \text{ K}$ with respect to S1 which contains only the stellar sources, when the average ionization fraction is 0.5. The X-ray luminosity of S4 is based on the work by Glover & Brand (2003), 0.1% of the total luminosity. S7 which includes 10% of the total luminosity as X-rays heats efficiently the temperature of neutral gas, but the averaged temperature is still less than the CMB temperature until $z \sim 9$.

To obtain the 21-cm signal, we further post-processed the simulations of reionization with Lyman α ray-tracing. The effect of Ly- α scattering on the 21-cm signal has not been fully considered until now. The Ly- α flux was assumed to be strong enough and homogeneous during the whole epoch of reionization. We find that the Ly- α flux is not homogeneous and the coupling is weak during the early phase of reionization. The fluctuation in the Lyman- α flux can imprint additional power on the power spectrum of the 21-cm signal and change the overall amplitude of the 21-cm signal.

The spectrum of the sources used in Baek et al. (2009) increases moderately the temperature in the void regions by Lyman- α heating, but the second spectrum used in following work changed significantly the amount of Lyman- α heating. The new spectrum was averaged, taking into account both the IMF and the variation of the source life time with mass, which results in a higher luminosity between Lyman-limit and Lyman- α . The Lyman- α heating dominates over the X-ray heating in the S4 case, but it still takes time to heat the gas above the CMB temperature, which occurs at redshift $z \sim 8$. Combined with the various initial mass functions, the study of the Lyman- α effect on the reionization will give constraints on the properties of the source of the EoR. Even with the strong X-ray and Lyman- α heating of the S7 simulation,

we found a signal in strong absorption during the early phase of reionization.

Shock heating from the cosmological structure formation is ignored in the current work, but it has the potential to affect the 21-cm signal by increasing the gas temperature above the CMB temperature. It is not sure whether shocks are strong enough in the filaments of the neutral regions to affect the 21-cm signal. Mini-halos ($\sim 10^4 - 10^8 M_\odot$) form very early during the EoR and are dense and warm enough from shock heating during virialization to emit the 21 cm signal, but Furlanetto & Oh (2006) find that the contribution of mini-halos will not dominate, because of the limited resolution of instrumentation. However, shock heating is worth investigating with coupled radiative hydrodynamic simulations with higher mass resolution.

In spite of the physics encoded in the 21-cm signal, observational challenges such as foreground contaminations, ionosphere effects, terrestrial interferences are important and the technical strategies should be fully examined. Just as the CMB observations constrained a lot the basic cosmological parameters which are necessary to understand structure formation, we hope that the 21-cm signal will reveal many unknowns of the high-redshift Universe. For example, what is the nature of the first sources and how are they formed, how do they evolve, how do their feedback affect the IGM, etc.

Through the radiative transfer of LICORICE coupled with its dynamic part, we can study various interesting problems of astrophysics and cosmology. Formation and evolution of galaxy with radiative feedback on hydrodynamics is one example. Galaxy formation is a very complex process, and many other processes are potentially of importance. Until now, photoionization and radiative cooling/heating have usually been included as a semi-analytic way because of high computational cost of radiative transfer simulations. Now three-dimensional radiative transfer with hydrodynamics at cosmological scale is the cutting edge of numerical astrophysics, and will be used to study structure formation in order to re-examine several problems of standard Λ CDM cosmology, such as the missing angular momentum problem and the missing satellite problem.

Appendix A

Cross-sections and rate coefficients

Cross-sections

The photoionization cross-sections $\sigma(E)$ are given by the fitting formula from Verner et al. (1996) :

$$\sigma(E) = \sigma_0 F(y) \text{ Mb}, \quad x = \frac{E}{E_0} - y_0, \quad y = \sqrt{x^2 + y_1^2},$$

$$F(y) = [(x - 1)^2 + y_w^2] y^{0.5P-5.5} (1 + \sqrt{t/t_a})^{-P}, \quad (\text{A.1})$$

where E is photon energy in eV, and σ_0 , E_0 , y_w , y_a , P , y_0 , and y_1 are the fit parameters (1 Mb = 10^{-18}cm^2 , see Tab. A.1).

Ion	E_{th} [eV]	E_{max} [eV]	E_0 [eV]	σ_0 [Mb]	y_a	P	y_w	y_0	y_1
H I	1.360E+1	5.000E+4	4.298E-1	5.475E+4	3.288E+1	2.963E+0	0.000E+0	0.000E+0	0.000E+0
He I	2.459E+1	5.000E+4	1.361E+1	9.492E+2	1.469E+0	3.188E+0	2.039E+0	4.434E-1	2.136E+0
He II	5.442E+1	5.000E+4	1.720E+0	1.369E+4	3.288E+1	2.693E+0	0.000E+0	0.000E+0	0.000E+0

Table A.1: Fit parameters for photoionization cross-sections

Recombination Rate¹ [$\text{cm}^3 \text{s}^{-1}$]

- Case A : $\alpha_{\text{H}^0}(T) = 8.40 \times 10^{-11} T^{-1/2} \left(\frac{T}{10^3}\right)^{-0.2} \times \left[1 + \left(\frac{T}{10^6}\right)^{0.7}\right]^{-1}$ (Cen, 1992)
- Case B : $\alpha_{\text{H}^0}(T) = 2.59 \times 10^{-13} (T/10^4)^{-3/4}$ (Spitzer, 1978)
- $\alpha_{\text{He}^0}(T) = 1.50 \times 10^{-10} T^{-0.6353}$ (Cen, 1992)
- $\alpha_{\text{He}^+}(T) = 3.36 \times 10^{-10} T^{-1/2} \left(\frac{T}{10^3}\right)^{-0.2} \times \left[1 + \left(\frac{T}{10^6}\right)^{0.7}\right]^{-1}$ (Cen, 1992)

¹H⁰ denotes the neutral hydrogen and He⁰ denotes the neutral helium

Collisional ionization rates [cm^3s^{-1}]

- $\gamma_{\text{H}^0}(T) = 5.85 \times 10^{-11} T^{1/2} \left[1 + \left(\frac{T}{10^5} \right)^{1/2} \right]^{-1} e^{-157809.1/T}$ (Cen, 1992)
- $\gamma_{\text{He}^0}(T) = 2.38 \times 10^{-11} T^{1/2} \left[1 + \left(\frac{T}{10^5} \right)^{1/2} \right]^{-1} e^{-285335.4/T}$ (Cen, 1992)
- $\gamma_{\text{He}^+}(T) = 5.68 \times 10^{-12} T^{1/2} \left[1 + \left(\frac{T}{10^5} \right)^{1/2} \right]^{-1} e^{-631515/T}$ (Cen, 1992)

Collisional ionization cooling [$\text{erg cm}^3\text{s}^{-1}$]

- $\zeta_{\text{H}^0}(T) = 1.27 \times 10^{-21} T^{1/2} \left[1 + \left(\frac{T}{10^5} \right)^{1/2} \right]^{-1} \times e^{-157809.1/T}$ (Cen, 1992)
- $\zeta_{\text{He}^0}(T) = 9.38 \times 10^{-22} T^{1/2} \left[1 + \left(\frac{T}{10^5} \right)^{1/2} \right]^{-1} \times e^{-285335.4/T}$ (Cen, 1992)
- $\zeta_{\text{He}^+}(T) = 4.95 \times 10^{-22} T^{1/2} \left[1 + \left(\frac{T}{10^5} \right)^{1/2} \right]^{-1} \times e^{-631515/T}$ (Cen, 1992)

Recombination cooling [$\text{erg cm}^3\text{s}^{-1}$]

- $\eta_{\text{H}^0}(T) = 8.70 \times 10^{-27} T^{1/2} \left(\frac{T}{10^3} \right)^{-0.2} \times \left[1 + \left(\frac{T}{10^6} \right)^{0.7} \right]^{-1}$ (Cen, 1992)
- $\eta_{\text{He}^0}(T) = 1.55 \times 10^{-26} T^{0.3647}$ (Cen, 1992)
- $\eta_{\text{He}^+}(T) = 3.48 \times 10^{-26} T^{1/2} \left(\frac{T}{10^3} \right)^{-0.2} \times \left[1 + \left(\frac{T}{10^6} \right)^{0.7} \right]^{-1}$ (Cen, 1992)

Collisional excitation cooling

- $\psi_{\text{H}^0}(T) = 7.5 \times 10^{-19} \left[1 + \left(\frac{T}{10^5} \right)^{1/2} \right]^{-1} \times e^{-118348/T}$ [$\text{erg cm}^3\text{s}^{-1}$] (Cen, 1992)
- $\psi_{\text{He}^0}(T) = 5.54 \times 10^{-17} T^{-0.397} \left[1 + \left(\frac{T}{10^5} \right)^{1/2} \right]^{-1} \times e^{-473638/T}$ [$\text{erg cm}^3\text{s}^{-1}$] (Cen, 1992)

- $\psi_{\text{He}^+}(T) = 9.10 \times 10^{-27} T^{-0.1687} \left[1 + \left(\frac{T}{10^5} \right)^{1/2} \right]^{-1} \times e^{-13179/T} \text{ [erg cm}^6\text{s}^{-1}\text{]} \text{ (Cen, 1992)}$

Bremsstrahlung cooling [erg cm³s⁻¹]

$$\beta(T) = 1.42 \times 10^{-27} T^{1/2} [n_{\text{H}^+} + n_{\text{He}^+} + n_{\text{He}^{++}}] n_e \text{ (Black, 1981)}$$

Compton cooling/heating [erg cm³s⁻¹]

$$\varpi(T) = 1.017 \times 10^{-37} T_\gamma^4 [T - T_\gamma] n_e$$

Bibliography

- Abel, T., & Wandelt, B. D. 2002, MNRAS, 330, L53
- Ahn, S.-H., Lee, H.-W., & Lee, H. M. 2002, ApJ, 567, 922
- Avery, L. W., & House, L. L. 1968, ApJ, 152, 493
- Baek, S., di Matteo, P., Semelin, B., Combes, F., & Revaz, Y. 2009, A&A, 495, 389
- Barkana, R., & Loeb, A. 2004, ApJ, 609, 474
- . 2005, ApJ, 626, 1
- Barnes, J., & Hut, P. 1986, Nature, 324, 446
- Becker, R. H., et al. 2001, AJ, 122, 2850
- Bertschinger, E. 2001, ApJS, 137, 1
- Black, J. H. 1981, MNRAS, 197, 553
- Boisse, P. 1990, A&A, 228, 483
- Bowman, J. D., Morales, M. F., & Hewitt, J. N. 2006, ApJ, 638, 20
- Cantalupo, S., Porciani, C., Lilly, S. J., & Miniati, F. 2005, ApJ, 628, 61
- Cen, R. 1992, ApJS, 78, 341
- Cen, R., & McDonald, P. 2002, ApJ, 570, 457
- Ciardi, B., Ferrara, A., Marri, S., & Raimondo, G. 2001, MNRAS, 324, 381
- Ciardi, B., Ferrara, A., & White, S. D. M. 2003a, MNRAS, 344, L7
- Ciardi, B., Stoehr, F., & White, S. D. M. 2003b, MNRAS, 343, 1101
- Dawson, S., Rhoads, J. E., Malhotra, S., Stern, D., Wang, J., Dey, A., Spinrad, H., & Jannuzi, B. T. 2007, ApJ, 671, 1227

- Di Matteo, T., Perna, R., Abel, T., & Rees, M. J. 2002, *ApJ*, 564, 576
- Dijkstra, M., Haiman, Z., & Spaans, M. 2006, *ApJ*, 649, 14
- Doré, O., Holder, G., Alvarez, M., Iliev, I. T., Mellema, G., Pen, U.-L., & Shapiro, P. R. 2007, *Phys. Rev. D*, 76, 043002
- Fan, X., et al. 2001, *AJ*, 122, 2833
- Fan, X., Narayanan, V. K., Strauss, M. A., White, R. L., Becker, R. H., Pentericci, L., & Rix, H.-W. 2002, *AJ*, 123, 1247
- Fan, X., et al. 2006, *AJ*, 132, 117
- Field, G. B. 1959, *ApJ*, 129, 536
- Furlanetto, S. R. 2006, *MNRAS*, 371, 867
- Furlanetto, S. R., & Briggs, F. H. 2004, *New Astronomy Review*, 48, 1039
- Furlanetto, S. R., & Oh, S. P. 2006, *ApJ*, 652, 849
- Furlanetto, S. R., Oh, S. P., & Briggs, F. H. 2006, *Phys. Rep.*, 433, 181
- Furlanetto, S. R., & Pritchard, J. R. 2006, *MNRAS*, 372, 1093
- Furlanetto, S. R., Sokasian, A., & Hernquist, L. 2004, *MNRAS*, 347, 187
- Gingold, R. A., & Monaghan, J. J. 1977, *MNRAS*, 181, 375
- Glover, S. C. O., & Brand, P. W. J. L. 2003, *MNRAS*, 340, 210
- Gnedin, N. Y. 2004, *ApJ*, 610, 9
- Górski, K. M., Banday, A. J., Hivon, E., & Wandelt, B. D. 2002, in *Astronomical Society of the Pacific Conference Series*, Vol. 281, *Astronomical Data Analysis Software and Systems XI*, ed. D. A. Bohlender, D. Durand, & T. H. Handley, 107–+
- Gunn, J. E., & Peterson, B. A. 1965, *ApJ*, 142, 1633
- Hansen, C. J., & Kawaler, S. D. 1994, *Stellar Interiors. Physical Principles, Structure, and Evolution.*, ed. C. J. Hansen & S. D. Kawaler
- Hogan, C. J., & Rees, M. J. 1979, *MNRAS*, 188, 791
- Hu, W., & Dodelson, S. 2002, *ARA&A*, 40, 171

- Iliev, I. T., et al. 2006a, MNRAS, 371, 1057
- Iliev, I. T., Mellema, G., Pen, U.-L., Bond, J. R., & Shapiro, P. R. 2008, MNRAS, 384, 863
- Iliev, I. T., Mellema, G., Pen, U.-L., Merz, H., Shapiro, P. R., & Alvarez, M. A. 2006b, MNRAS, 369, 1625
- Iliev, I. T., Mellema, G., Shapiro, P. R., & Pen, U.-L. 2007, MNRAS, 376, 534
- Iliev, I. T., et al. 2009, ArXiv e-prints
- Jeans, J. H. 1928, Astronomy and cosmogony, ed. J. H. Jeans
- Jelić, V., et al. 2008, MNRAS, 389, 1319
- Kaiser, N. 1984, ApJ, 282, 374
- Katz, N. 1992, ApJ, 391, 502
- Katz, N., Weinberg, D. H., & Hernquist, L. 1996, ApJS, 105, 19
- Kawai, N., et al. 2006, Nature, 440, 184
- Knox, L. 2003, New Astronomy Review, 47, 883
- Lee, K.-G., Cen, R., Gott, J. R. I., & Trac, H. 2008, ApJ, 675, 8
- Lidz, A., Hui, L., Zaldarriaga, M., & Scoccimarro, R. 2002, ApJ, 579, 491
- Lidz, A., Zahn, O., McQuinn, M., Zaldarriaga, M., Dutta, S., & Hernquist, L. 2007, ApJ, 659, 865
- Loeb, A., & Barkana, R. 2001, ARA&A, 39, 19
- Loeb, A., & Rybicki, G. B. 1999, ApJ, 524, 527
- Martin, C. L., & Kennicutt, Jr., R. C. 2001, ApJ, 555, 301
- Maselli, A., Ciardi, B., & Kanekar, A. 2009, MNRAS, 393, 171
- Maselli, A., Ferrara, A., & Ciardi, B. 2003, MNRAS, 345, 379
- Mayer, L., Governato, F., & Kaufmann, T. 2008, Advanced Science Letters, 1, 7
- McQuinn, M., Furlanetto, S. R., Hernquist, L., Zahn, O., & Zaldarriaga, M. 2005, ApJ, 630, 643

- McQuinn, M., Lidz, A., Zahn, O., Dutta, S., Hernquist, L., & Zaldarriaga, M. 2007a, *MNRAS*, 377, 1043
- . 2007b, *MNRAS*, 377, 1043
- McQuinn, M., Zahn, O., Zaldarriaga, M., Hernquist, L., & Furlanetto, S. R. 2006, *ApJ*, 653, 815
- Mellema, G., Iliev, I. T., Alvarez, M. A., & Shapiro, P. R. 2006a, *New Astronomy*, 11, 374
- Mellema, G., Iliev, I. T., Pen, U.-L., & Shapiro, P. R. 2006b, *MNRAS*, 372, 679
- Merz, H., Pen, U.-L., & Trac, H. 2005, *New Astronomy*, 10, 393
- Meynet, G., & Maeder, A. 2005, *A&A*, 429, 581
- Mihos, J. C., & Hernquist, L. 1994, *ApJ*, 437, 611
- Monaghan, J. J. 1992, *ARA&A*, 30, 543
- Monaghan, J. J., & Lattanzio, J. C. 1985, *A&A*, 149, 135
- Morales, M. F. 2005, *ApJ*, 619, 678
- Navarro, J. F., & White, S. D. M. 1993, *MNRAS*, 265, 271
- . 1994, *MNRAS*, 267, 401
- Oh, S. P., & Furlanetto, S. R. 2005, *ApJ*, 620, L9
- Ostriker, J. P., & Vishniac, E. T. 1986, *ApJ*, 306, L51
- Page, L., et al. 2007, *ApJS*, 170, 335
- Peebles, P. J. E. 1993, *Principles of physical cosmology* (Princeton Series in Physics, Princeton, NJ: Princeton University Press, —c1993)
- Pritchard, J. R., & Furlanetto, S. R. 2006, *MNRAS*, 367, 1057
- . 2007, *MNRAS*, 376, 1680
- Santos, M. G., Amblard, A., Pritchard, J., Trac, H., Cen, R., & Cooray, A. 2008, *ApJ*, 689, 1
- Santos, M. G., Cooray, A., Haiman, Z., Knox, L., & Ma, C.-P. 2003, *ApJ*, 598, 756
- Santos, M. G., Cooray, A., & Knox, L. 2005, *ApJ*, 625, 575

- Santos, M. R. 2004, MNRAS, 349, 1137
- Scott, J. E., Kriss, G. A., Brotherton, M., Green, R. F., Hutchings, J., Shull, J. M., & Zheng, W. 2004, ApJ, 615, 135
- Seager, S., Sasselov, D. D., & Scott, D. 1999, ApJ, 523, L1
- Semelin, B., & Combes, F. 2002, A&A, 388, 826
- . 2005, A&A, 441, 55
- Semelin, B., Combes, F., & Baek, S. 2007, A&A, 474, 365
- Shimasaku, K., et al. 2006, PASJ, 58, 313
- Shin, M.-S., Trac, H., & Cen, R. 2008, ApJ, 681, 756
- Shull, J. M., & van Steenberg, M. E. 1985, ApJ, 298, 268
- Sokasian, A., Abel, T., & Hernquist, L. E. 2001, New Astronomy, 6, 359
- Songaila, A. 2004, AJ, 127, 2598
- Songaila, A., & Cowie, L. L. 2002, AJ, 123, 2183
- Spergel, D. N., et al. 2007, ApJS, 170, 377
- Spitzer, L. 1978, Physical processes in the interstellar medium (New York Wiley-Interscience, 1978. 333 p.)
- Springel, V. 2005, MNRAS, 364, 1105
- Springel, V., & Hernquist, L. 2003, MNRAS, 339, 312
- Springel, V., Yoshida, N., & White, S. D. M. 2001, New Astronomy, 6, 79
- Strömgren, B. 1939, ApJ, 89, 526
- Sunyaev, R. A. 1978, in IAU Symposium, Vol. 79, Large Scale Structures in the Universe, ed. M. S. Longair & J. Einasto, 393–402
- Susa, H., & Umemura, M. 2000, ApJ, 537, 578
- Sutherland, R. S., & Dopita, M. A. 1993, ApJS, 88, 253
- Taniguchi, Y., et al. 2005, PASJ, 57, 165
- Tasitsiomi, A. 2006, ApJ, 645, 792

- Telfer, R. C., Zheng, W., Kriss, G. A., & Davidsen, A. F. 2002, *ApJ*, 565, 773
- Thomas, R. M., et al. 2009, *MNRAS*, 393, 32
- Trac, H., & Cen, R. 2007, *ApJ*, 671, 1
- Trac, H., Cen, R., & Loeb, A. 2008, *ApJ*, 689, L81
- Trac, H., & Pen, U.-L. 2006, *New Astronomy*, 11, 273
- Verhamme, A., Schaerer, D., & Maselli, A. 2006, *A&A*, 460, 397
- Verner, D. A., Ferland, G. J., Korista, K. T., & Yakovlev, D. G. 1996, *ApJ*, 465, 487
- Zahn, O., Lidz, A., McQuinn, M., Dutta, S., Hernquist, L., Zaldarriaga, M., & Furlanetto, S. R. 2007, *ApJ*, 654, 12
- Zheng, Z., & Miralda-Escudé, J. 2002, *ApJ*, 578, 33